Modelling chromosomal instability in high-grade serous ovarian cancer

A thesis submitted to the University of Manchester
for the degree of Doctor of Philosophy
in the Faculty of Biology, Medicine and Health

2021

Daniel K. Bronder

School of Medical Sciences
Division of Cancer Sciences

Table of contents

Word count: 43,543

List of tables

List of figures

List of abbreviations

184-*hTERT*	*hTERT*-immortalized, non-transformed mammary epithelial cells
2c	Diploid
4c	Tetraploid
8c	Octoploid
Apc	Adenomatous polyposis coli
APC/C	Anaphase progression complex/cyclosome
BMP	Bone morphogenic protein
BRCA1	Breast cancer gene/protein 1
Brca1	Mouse homologue of *BRCA1*
BRCA2	Breast cancer gene/protein 2
Brca2	Mouse homologue of *BRCA2*
BSA	Bovine serum albumin
BUB1B	BUB1 mitotic checkpoint serine/threonine kinase B
C class	Cancers classified by chromosomal copy number changes
Cas9	CRISPR associated protein 9
CCNB1	Cyclin B1
CD19	Cluster of differentiation 19 protein
CD45	Cluster of differentiation 45 protein
CDK	Cyclin dependent kinase
CDK2	Cyclin dependent kinase 2
CDK4/6	Cyclin dependent kinase 4/6
CDKN1A	Cyclin dependent kinase inhibitor 1A
CDKN2A	Cyclin dependent kinase inhibitor 2A
cDNA	Complementary DNA
CENP-E	Centromere protein E
CENP-Ei	GSK923295, an inhibitor of CENP-E
CENPF	Centromere protein F
CEP57	Centrosomal protein 57
cGAMP	2′3′-cyclic GMP-AMP
cGAS	2′3′-cyclic GMP-AMP synthase
CIN	Chromosomal instability
CPM	Counts per million
CRISPR	Clustered regularly interspaced short palindromic repeats
CRUK	Cancer research United Kingdom
DAPI	4′,6-diamidino-2-phenylindole

DEG	Differentially expressed gene
DLD-1	Human, microsatellite unstable colorectal cancer cells
DMEM	Dulbecco's modified eagle medium
DNA	Deoxyribonucleic acid
E1a	Adenovirus early region 1A
EGF	Epidermal growth factor
EV	Empty vector
FACS	Fluorescence-activated cell sorting
FBS	Foetal bovine serum
FISH	Fluorescence *in situ* hybridization
FNE1	Human, fallopian tube-derived, *hTERT* immortalized cells
FOMI	Fallopian ovary modified Ince medium
g*BRCA1*	Guide RNA targeting *BRCA1*
GEMM	Genetically engineered mouse model
GI	Genomic instability
gRNA	Guide RNA
GSEA	Gene set enrichment analysis
GSVA	Gene set variation analysis
g*TP53*	Guide RNA targeting *TP53*
HCT116	Human, microsatellite unstable colorectal cancer cells
HGSOC	High-grade serous ovarian cancer
HR	Homologous recombination
Hras	Harvey rat sarcoma virus oncogene
HRD	Homologous recombination deficiency
IACUC	Institutional animal care and use committee
KEGG	Kyoto encyclopaedia of genes and genomes
LB	Luria-Bertani
M class	Cancers classified by nucleotide mutations
M-FISH	Multiplex fluorescence *in situ* hybridization
MAD2L1	Mitotic arrest deficient 2 like 1
MEF	Mouse embryonic fibroblast
miFISH	Multiplexing interphase fluorescence *in situ* hybridization
mRNA	Messenger RNA
MYC	Human homologue of an avian Myelocytomatosis oncogene
NCI	National cancer institute
NeoR	Neomycin resistance cassette
NES	Normalized enrichment score

NGS	Next generation sequencing
NIH	National institutes of health
NSG	Non-obese diabetic, severe combined immunodeficiency, gamma mouse
OCMI	Ovarian carcinoma modified Ince medium
OMIM	Online mendelian inheritance in man
P	*TP53* single-mutant FNE1 subclones
PARP	Poly (ADP-ribose) polymerase
PARPi	Olaparib, an inhibitor of PARP
PB	*TP53,BRCA1* double-mutant FNE1 subclones
PBS	Phosphate-buffered saline
PBS-B	PBS supplemented with 1% (wight/volume) BSA
PBS-T	PBS supplemented with 0.1% Triton-X-100
PC	Principal component
PCA	Principal component analysis
PCR	Polymerase chain reaction
PDMR	Patient-derived model repository
PDX	Patient-derived xenograft
PLK1	Polo like kinase 1
PLK4	Polo like kinase 4
PM	*TP53* mutant, *MYC* overexpressing FNE1 subclones
PTC	Premature termination codon
Pten	Mouse homologue of *PTEN*
PTEN	Phosphatase and tensin homologue
RE	p53 response element
RNA	Ribonucleic acid
RNAi	RNA interference
RPE-1	Retinal pigment epithelial cells
RPM	Rounds per minute
SAC	Spindle assembly checkpoint
SCID	Severe combined immunodeficiency mouse
scWGS	Single-cell whole genome sequencing
SDS	Sodium dodecyl sulphate
SEER	Surveillance, epidemiology and end results programme
SKY	Spectral karyotyping
SSC	Saline sodium citrate
STIC	Serous tubal intraepithelial carcinoma
STING	Stimulator of interferon genes

STR	Short tandem repeat
SV40 TAg	Simian virus 40 Large T antigen oncoprotein
TBE	Tris, borate, EDTA buffer
TBS-T	Tris-buffered saline supplemented with 0.1% Tween-20
TCGA	The cancer genome atlas research network
TERC	Telomerase RNA component
TGFβ	Transforming growth factor beta
TP53	Tumour protein 53
TRIP13	Thyroid hormone receptor interactor 13
Trp53	Mouse homologue of *TP53*
Ttk	TTK protein kinase
UK	United Kingdom
US	United States
WGD	Whole genome doubling
WHO	World health organization

Abstract

High Grade Serous Ovarian Cancer (HGSOC) originates in the fallopian tube and is characterized by near-ubiquitous *TP53* mutations. High levels of chromosomal instability (CIN) and resulting chromosomal copy number changes (aneuploidy) are another defining feature. Consequences of CIN in cancer cells are intratumoural genetic heterogeneity, cancer genome evolution, therapy resistance and a propensity for metastasis. CIN describes the perpetual mis-segregation of chromosomes as a result from errors in mitosis or interphase DNA replication stress.

Since mutations in mitosis and DNA replication controlling genes are rare in HGSOC, I aimed to assess if genetic aberrations characteristic of HGSOC, specifically in *TP53*, *BRCA1* and *MYC*, are sufficient to induce CIN. For this purpose, I first validated the human, fallopian tube-derived, non-transformed, *hTERT*-immortalized cell line FNE1 as a useful model system. Importantly, FNE1 cells are p53-proficient, chromosomally stable and near-diploid.

Subsequently, I mutagenized the tumour suppressor genes *TP53* and *BRCA1* and overexpressed the oncogene *MYC* using CRISPR/Cas9 in combination with lentiviral vectors. This led to the establishment of *TP53* single-, *TP53/BRCA1* and *TP53/MYC* double- and *TP53/BRCA1/MYC* triple-mutant FNE1 subclones. Mutant FNE1 cells were then subjected to analyses of their genome by multiplex interphase Fluorescence *in situ* Hybridization (miFISH) and single-cell, shallow depth whole genome sequencing (scWGS). Analyses of two *TP53/BRCA1/MYC* triple-mutant FNE1 subclones revealed the emergence of tetraploidy and diverse gains and losses in comparison to wild-type FNE1 cells which suggests on-going CIN. Strikingly, an increase in aneuploidy could already be observed in *TP53* single-mutant cells.

To elucidate potential mechanisms causing CIN in the mutant subclones, RNA sequencing was performed. Gene set variation analysis (GSVA) revealed increased enrichment scores of Mitotic spindle, G2/M checkpoint, E2F targets and DNA replication gene sets in *TP53* single-mutant cells alone suggesting early cell cycle deregulation as a result of p53 loss. Indeed, the G2/M checkpoint and E2F target gene sets were further enriched in *TP53/BRCA1* and *TP53/MYC* double- and *TP53/BRCA1/MYC* triple-mutant FNE1 subclones.

Taken together, these data suggest transcriptional rewiring of the cell cycle upon p53-loss, which is exacerbated by additional *BRCA1* perturbation and *MYC* overexpression, as a cause of CIN in HGSOC.

Declaration

I hereby declare that no portion of the work referred to in this thesis has been submitted in support of another degree or qualification of this or any other university or other institute of learning.

Copyright statements

i. The author of this thesis (including any appendices and/or schedules to this thesis) owns certain copyright or related rights in it (the “Copyright”) and s/he has given The University of Manchester certain rights to use such Copyright, including for administrative purposes.

ii. Copies of this thesis, either in full or in extracts and whether in hard or electronic copy, may be made only in accordance with the Copyright, Designs and Patents Act 1988 (as amended) and regulations issued under it or, where appropriate, in accordance with licensing agreements which the University has from time to time. This page must form part of any such copies made.

iii. The ownership of certain Copyright, patents, designs, trademarks and other intellectual property (the “Intellectual Property”) and any reproductions of copyright works in the thesis, for example graphs and tables (“Reproductions”), which may be described in this thesis, may not be owned by the author and may be owned by third parties. Such Intellectual Property and Reproductions cannot and must not be made available for use without the prior written permission of the owner(s) of the relevant Intellectual Property and/or Reproductions.

iv. Further information on the conditions under which disclosure, publication and commercialisation of this thesis, the Copyright and any Intellectual Property and/or Reproductions described in it may take place is available in the University IP Policy (see http://documents.manchester.ac.uk/DocuInfo.aspx?DocID=2442 0), in any relevant Thesis restriction declarations deposited in the University Library, The University Library’s regulations (see http://www.library.manchester.ac.uk/about/regulations/) and in The University’s policy on Presentation of Theses.

About the author

Daniel graduated from the University of Glasgow in 2016 with a Bachelor's (Honours) degree in genetics. The same year, Daniel started his thesis work with Prof. Stephen Taylor at the Manchester Cancer Research Centre as part of the Wellcome Trust/National Institutes of Health (NIH) PhD programme. After two years in Manchester, Daniel moved to Dr Thomas Ried's laboratory at the National Cancer Institute (NCI) in Bethesda, Maryland, where he continued to work towards his thesis.

Acknowledgements

First, I thank Stephen and Thomas for their teaching, continued support and the opportunity to pursue a PhD working in their labs. Stephen for teaching me how to design and execute careful experiments. Thomas for introducing me to the field of aneuploidy and chromosomal instability as well as guiding me on my path. Together, they taught me how to do rigorous science.

An important thanks goes out to the members of both labs I spent time in. Day to day support from, discussions with and shared cake, tea and coffee with Susana, Anthony, Livi, Louisa, Sam, Paul, Dara, Rachel, Kerstin, Danny, Wei-Dong and Daniela are gratefully appreciated. Many thanks to Nisha and Anya, who started with me in Manchester, and Markus, who was already working in Bethesda, for sharing the lows and highs of my PhD experience. Additional thanks go to Gordon, Nisha, Stephen and Thomas for help with proofreading of this thesis. For assistance with mouse work, I have to thank Maria and Josh. Also, many thanks to my collaborators Dali for *BRCA1* discussions, Josh for help with RNA sequencing as well as Floris and his team for help with single-cell sequencing.

I owe a very special thanks to the NIH OxCam community, especially Katie, who supported me in too many ways to name, but mainly by introducing me to many new friends when I arrived in Bethesda. Additionally, I gratefully acknowledge two micrograntsfrom the OxCam office and extracurricular support from the International Biomedical Research Alliance.

Thank you to the Wellcome Trust and NIH's intramural training programme for funding through the Wellcome Trust/NIH PhD programme and Danny for his encouragement and mentorship since I decided to apply.

I am indebted to my family and friends as well as Alex for their continued understanding, unwavering support and unconditional positivity. Lastly, I am dedicating this work to Wiesława Sibinska and Sebastian Bronder.

Other contributors

Spectral karyotyping (SKY), which is reported in Figures 3.1 and 3.2, was performed by Dr Darawalee Wangsa Zong. Single-cell shallow-depth whole genome sequencing (scWGS), which is reported in Figures 3.1, 4.5 and 4.6, was performed by Dr Floris Foijer and his laboratory. RNA sequencing was performed at the Center for Cancer Research's Office of Science and Technology Resource's Sequencing Facility. Subsequent analyses, which form the basis of Chapter 5, were performed with the help of Dr Thomas J. Meyer.

Chapter 1: Introduction

1.1: Overview

Cancer is a leading cause of death worldwide. In 2018, an estimated 9.6 million deaths were caused by cancer, second only to ischaemic heart disease (WHO, 2021). As a disease, cancer comprises many distinct types and can arise in most normal tissues (Weinberg, 2014). Depending on the tissue of origin, tumours are referred to as carcinomas of epithelial, sarcomas of bone, fat, muscle or fibroblast cell origin or as leukaemias and lymphomas which are of haematopoietic origin. Lastly, individual cell lineages in the brain can also give rise to a variety of cancers. The most common kinds of cancer, however, are of epithelial origin which can be further divided into squamous cell carcinomas and adenocarcinomas originating from the protective, epithelial sheet cells and more specialized secretory epithelial cells, respectively.

Two landmark reviews defined the *hallmarks of cancer* as a collection of unifying phenotypes characteristic of all cancer cells (Hanahan and Weinberg, 2000, 2011). In its first edition, six features were defined. Four of these features relate to unrestrained growth and avoidance of growth suppression, angiogenesis and metastasis complete the first set of the *hallmarks of cancer* (Hanahan and Weinberg, 2000). More recently, energetic dysregulation, immune evasion, tumourigenic inflammation and genomic instability (GI) were added (Hanahan and Weinberg, 2011). While all ten hallmarks discriminate normal from cancerous cells, GI, as the name suggests, manifests on the genetic level of cancer cells and thus has the potential to impact all cellular processes.

GI can be divided into two classes (Fig. 1.1). One is driven by nucleotide mutations impacting the DNA sequence (M class) (Ciriello et al., 2013). The causes for these mutations can be endogenous or exogenous and several environmental and genetic factors have been identified as drivers of specific mutational signatures, which are reoccurring abnormalities in the DNA sequence and can be thought of as genomic scars of mutagenic processes (Fig. 1.1A-C) (Tubbs and Nussenzweig, 2017). The first pan-cancer analysis identified 21 mutational signatures and the authors were able to assign eleven mutational signatures directly to dysfunctional DNA repair mechanisms, age or environmental toxins such as exposure to tobacco smoke, ultraviolet light and temozolomide (Alexandrov et al., 2013). Advances in next generation sequencing (NGS) technology and downstream bioinformatics tools have galvanized the analyses of cancer genomes and follow-up studies have described several additional mutational signatures (Alexandrov et al., 2020). The mechanisms underpinning

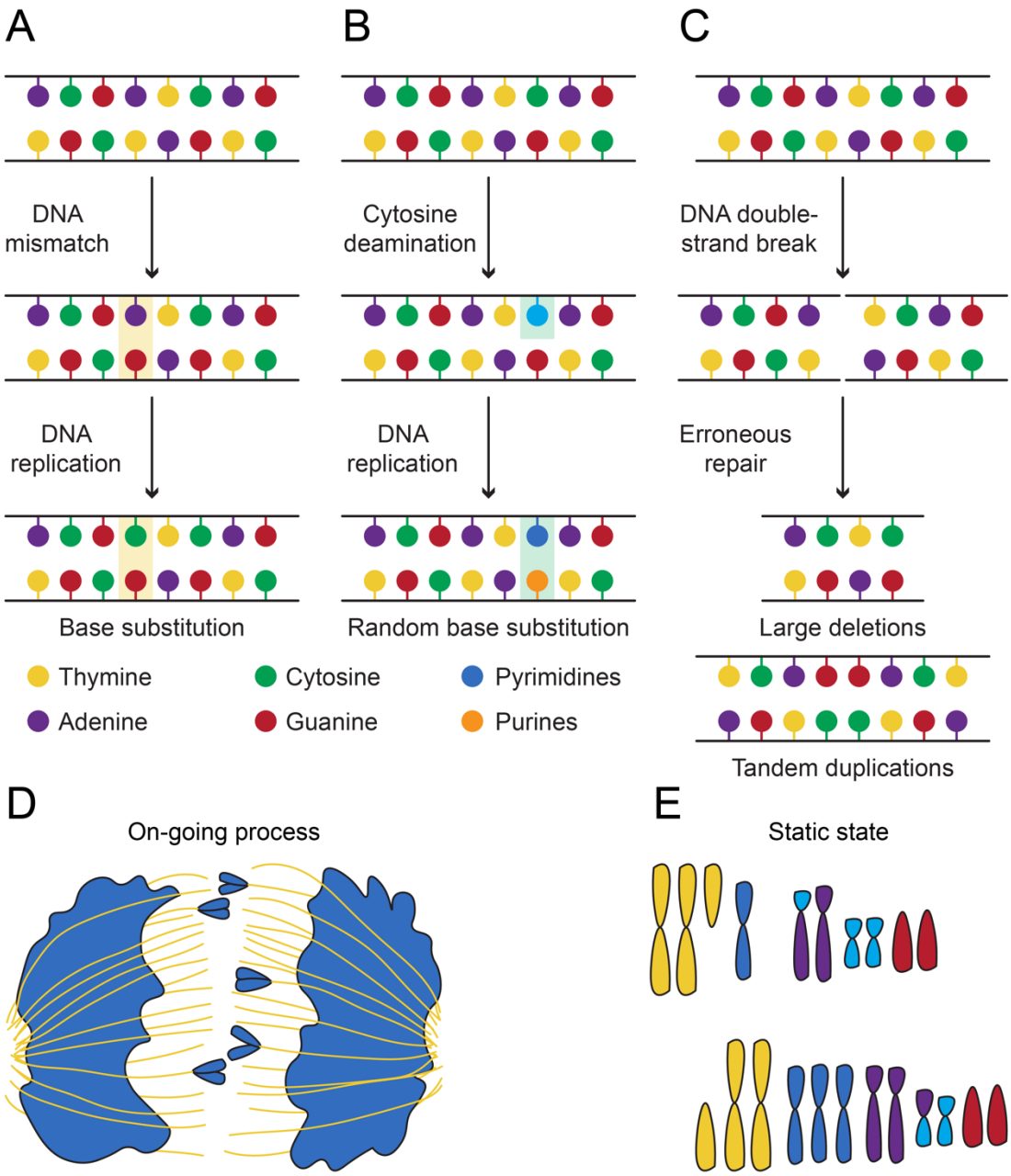

Figure 1.1: M and C classes of genomic instability in cancer
M and C classes of genomic instability were defined by Ciriello et al. (2013). **A, B** and **C** Depiction of DNA mismatch repair deficiency, aberrant APOBEC cytosine deaminase activity and homologous recombination deficiency, respectively, which are mutagenic processes underlying the M class of genomic instability. DNA damage associated with the respective processes and resulting genomic scars are indicated. **D** Schematic of chromosomal instability as the perpetual mis-segregation of chromosomes during mitosis. **E** Illustration of two static, aneuploid karyotypes.

many of these mutational signatures remain to be determined, but as mentioned above, those mutational signatures associated with exposure to tobacco smoke or ultraviolet light are predominantly observed in lung and exclusively observed in skin cancers, respectively.

The other class of GI encompasses large scale changes in DNA copy number rather than nucleotide sequence (C class; Fig. 1.1D-E) (Ciriello et al., 2013). Copy number alterations are defined as an increase or decrease in DNA sequences containing multiple genes whereas gains and losses of chromosomes or chromosome arms are defined as whole chromosome or partial aneuploidy, respectively, which has been defined as a deviation in chromosome number from the haploid genome content (Ben-David and Amon, 2020). In human cancers, aneuploidy is observed in 88% of cases (Taylor et al., 2018). In fact, aneuploidy is a feature characteristic of solid tumours and far less common in haematological malignancies (Shukla et al., 2020). Similar to the M class, qualitative and quantitative differences in aneuploidy exist in the C class. The most prominent example of qualitative differences between tumour entities are the idiosyncratic aneuploidies of chromosome 7 and 10 (gain and loss, respectively) which occur with very high penetrance in glioblastoma multiforme and the gain of chromosome 13 exclusively observed in gastrointestinal cancers (Taylor et al., 2018). Quantitatively, the extent to which the cancer genome is impacted by copy number alterations also varies between cancer entities. Indeed, the landmark study first describing the C and M classes of tumours had relied on the separation of eleven cancer types by either high levels of mutations or chromosomal copy number changes (Ciriello et al., 2013). Subsequent analyses of increasing numbers of cancer types and tumour samples have largely reproduced these initial findings (Shukla et al., 2020; Taylor et al., 2018). Thyroid carcinoma, thymoma, prostate adenocarcinoma and lower grade glioma have consistently been found to display low levels of aneuploidy. At the other end of the spectrum, testicular germ cell tumour, adrenocortical carcinoma, lung squamous cell carcinoma and ovarian cancer have likewise been identified to display high levels of aneuploidy. In fact, ovarian cancer was initially identified as the tumour type with most cases classified as C class by Ciriello et al. (2013).

In the analyses outlined above ovarian cancer refers to high-grade serous ovarian cancer (HGSOC) specifically which was the second cancer genomics study published by the cancer genome atlas research network (TCGA) in 2011. At that time, our understanding of cancer genomics was in its infancy, however, underlying genetics in other cancer types were being explored and studied while knowledge about HGSOC was very limited. The TCGA's analysis of HGSOC thus lent novel, long awaited

insight into the disease. The most striking discoveries made in that study are the high levels of copy number changes, the near-ubiquitous mutations in *TP53* and the absence of other mutations (TCGA, 2011). The absence of characteristic secondary mutations is in contrast to other cancer types where multiple genes are mutated in addition to *TP53*. These insights have inspired discovery-driven science to better our understanding of HGSOC with the goal of a positive impact on patient treatments and outcomes, yet many fundamental questions remain unanswered.

The introduction of this thesis will outline our current knowledge of HGSOC genesis and the genetic aberrations at play with a focus on *TP53*, *BRCA1* and *MYC*. An in-depth account of aneuploidy and its major cause, chromosomal instability (CIN), will also be given due to its pertinence in HGSOC. Additionally, relevant model systems for the study of HGSOC and methodologies for the study of aneuploidy and CIN will be introduced. Lastly, the rationale and aims for this thesis will be defined.

1.2: High-grade serous ovarian cancer

Ovarian cancer was the leading cause of death from gynaecological malignancies and the fifth most common cause of cancer death in women in 2020 in the United States (US) (Siegel et al., 2020). A similar picture presents in the United Kingdom (UK) where it was the sixth most common cause of cancer death in women in 2017 (CRUK, 2020a). Survival at five years after diagnosis in both the US and the UK has improved over the last decades, however, remains at 48.6% and 42.6%, respectively (CRUK, 2020b; SEER, 2020). Like many other cancers, ovarian cancer is a summary term for multiple distinct diseases which I will introduce in the following section before I focus on HGSOC specifically.

1.2.1: Overview of ovarian cancers

Ovarian cancer summarizes multiple histopathological subtypes of non-epithelial and epithelial origin. Ovarian cancers of non-epithelial origin are typically less aggressive in presentation and encompass sex-cord stromal, germ cell, small cell carcinoma (hypercalcaemic and non-hypercalcaemic types) and ovarian sarcoma, the former two subtypes account for 2% and 3% of all ovarian cancers, respectively, and the latter two are extremely rare (Torre et al., 2018). On the other hand, ovarian cancers of epithelial origin account for more than 90% of ovarian cancer cases and one particular subtype is highly aggressive.

For epithelial ovarian cancers, Kurman and Shih Ie (2016) have proposed a dualistic model of tumourigenesis: type I cancers are endometrial, mucinous, clear cell and

low-grade serous ovarian cancers and type II is effectively only HGSOC. This typing of epithelial ovarian cancers is based on a combination of clinical, pathological and molecular characteristics of the respective diseases. Type I epithelial ovarian tumours are frequently detected as early stage disease, progress slowly and have low proliferative activity. Specifically, 67-75% of endometrial, mucinous and clear cell ovarian cancers were diagnosed as stage 1 or 2 in the US between 2007 and 2013 (Torre et al., 2018). In striking contrast, only 16% of HGSOCs were diagnosed as stage 1 or 2. It follows that HGSOC is mostly diagnosed at stage 3 or 4 which, together with the regular occurrence of ascites in HGSOC patients, illustrates its aggressiveness (Kurman and Shih Ie, 2016). Survival five years after diagnosis with HGSOC is dismal at 43% compared with 66%-82% for the other above-mentioned subtypes of epithelial origin.

Importantly, HGSOC represents 52% of all ovarian cancer cases making it the commonest and combined with its poor prognosis, regular recurrence following therapy and general, aggressive behaviour also the most lethal. In addition to the clinical and pathological characteristics differentiating type I and II epithelial ovarian cancers, molecular genetic characteristics will be described in the following section that set HGSOC apart from other ovarian malignancies and also other cancer types.

1.2.2: Genomics of high-grade serous ovarian cancer

In December 2005, TCGA was launched by the National Institutes of Health (NIH) with the intention to catalogue and understand the genomic changes that underpin all major types of human cancers. Less than a year later, in September 2006, TCGA announced that lung, brain and ovarian cancers were selected to be analysed first. The glioblastoma multiforme study was published first and the study on HGSOC was second (TCGA, 2008, 2011).

The sequencing of 316 HGSOC samples by TCGA revealed near-ubiquitous mutations in the tumour suppressor gene *TP53* and recurrent mutations in the tumour suppressor genes *BRCA1* and *BRCA2* in 12% and 11% of cases, respectively (Fig. 1.2A) (TCGA, 2011). Upon re-examination of the cases devoid of *TP53* mutations, a follow-up study showed that miscalling of sequencing reads and misclassification of tumour samples as HGSOC meant that in fact all *bona fide* HGSOC samples harboured mutations in *TP53* (Vang et al., 2016). Indeed, an independent study focusing on *TP53* mutations exclusively had already shown the presence of ubiquitous *TP53* mutations in HGSOC (Ahmed et al., 2010). Apart from the aforementioned mutations in tumour suppressor genes, the HGSOC genome is characterized by copy number

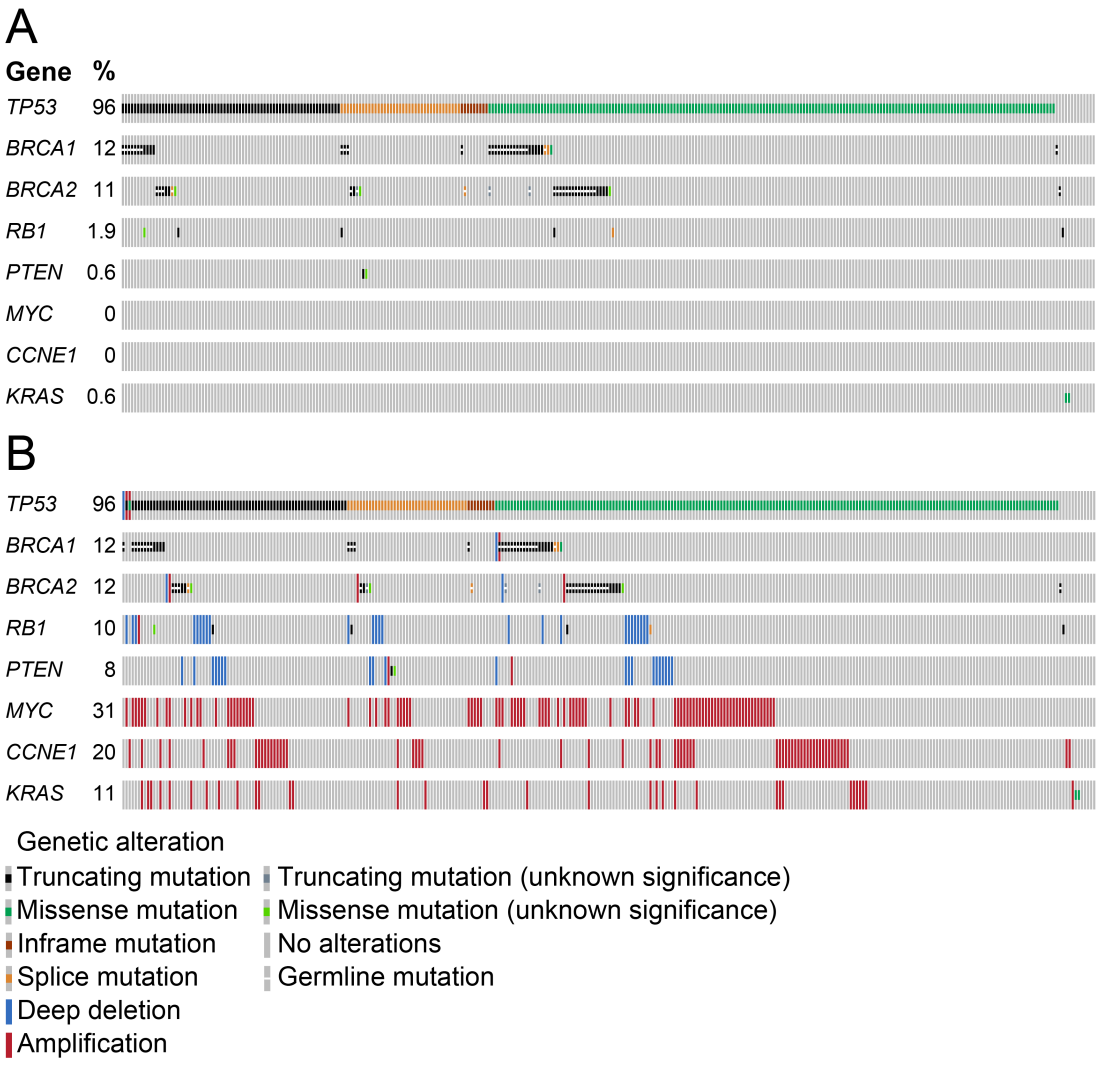

Figure 1.2: The cancer genome atlas genomics of high-grade serous ovarian cancer
A Mutations detected in 316 high-grade serous ovarian cancer samples. **B** Mutations, deletions and amplifications detected in 316 high-grade serous ovarian cancer samples.
Gene symbols and frequency of mutations are indicated. Each column reflects a single sample.

aberrations. Other tumour suppressor genes such as *RB1* and *PTEN* are only mutated in 2% and 0.6% of cases, respectively (Fig. 1.2A) (Cerami et al., 2012; Gao et al., 2013; TCGA, 2011). When taking into account copy number changes, however, 10% and 8% of cases show copy number losses of *RB1* and *PTEN*, respectively (Fig. 1.2B). A similar picture emerges with regards to oncogenes. *KRAS*, *CCNE1* and *MYC* are gained in 11%, 20% and 31% of cases. Of note, not a single sample showed mutations in *CCNE1* or *MYC* (Fig. 1.2B) (Cerami et al., 2012; Gao et al., 2013; TCGA, 2011). These copy number changes and aneuploidies of whole or partial chromosomes are a consequence of constant chromosome mis-segregation events during mitosis referred to as CIN, whose causes and consequences will be discussed in *1.3: Chromosomal instability and aneuploidy* (Bakhoum and Cantley, 2018). In addition to the assessment of mutations and numerical changes in individual genes, genomic scars resulting from on-going mutagenic processes, such as CIN, have also been utilized to characterize HGSOC in more detail. Foldback inversions (FBI) and homologous recombination deficiency (HRD) have been described as the main sources of the genomic scars observed in HGSOC (Fig. 1.3A) (Wang et al., 2017). The latter will be discussed in more detail in *1.4.2: Homologous recombination deficiency in BRCA1/2-mutated cases*.

The molecular genetic characteristics of HGSOC have also been described as distinguishing features of the aforementioned types I and II of epithelial ovarian cancer. The presence of *TP53* mutations and CIN is a feature ubiquitously observed in HGSOC but only rarely observed in other epithelial ovarian cancers (Kurman and Shih Ie, 2016).

1.2.3: Cellular origin of high-grade serous ovarian cancer

The origin of HGSOC can be considered bimodal. The ovarian surface epithelium had long been considered to be the tissue of origin, however, more than a century ago, it had already been suggested that the origin of ovarian or peritoneal tumours from the fallopian tube could not be ruled out (Doran, 1884). Therefore, the fallopian tube epithelium also has to be considered the HGSOC tissue of origin.

Histopathological analyses of samples collected after prophylactic salpingo-oophorectomies showed that early-stage lesions, known as p53 signatures, and more advanced serous tubal intraepithelial carcinomas (STIC) occurred at similar frequency in both control fallopian tube samples and in samples from patients with known *BRCA1* or *BRCA2* mutations (Shaw et al., 2009). It was also shown that CIN occurred early in HGSOC precursors and resulting genetic copy number aberrations were

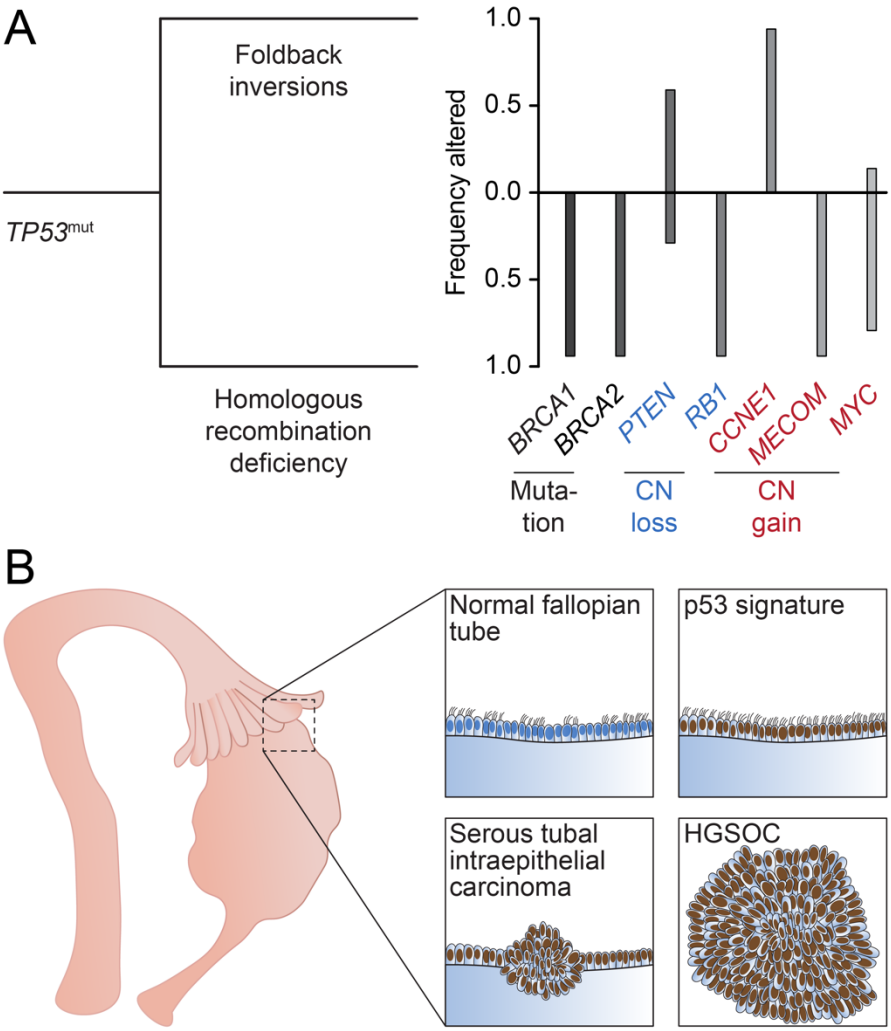

Figure 1.3: Genomic classification and origin of high-grade serous ovarian cancer

A Following the truncal *TP53* mutation, high-grade serous ovarian cancers were classified into two groups based on genomic features by Wang et al. (2017). These two groups are based on either a high prevalence of foldback inversions or homologous recombination deficiency. These characteristics were found to co-occur with mutations, copy number (CN) gains and losses of certain genes. **B** High-grade serous ovarian cancer originates from the fallopian tube epithelial, non-ciliated, secretory cell type and early stages of tumourigenesis are p53 signatures and serous tubal intraepithelial carcinomas. Figure inspired by Bowtell et al. (2015).

frequently congruent between early and late-stage lesions (Salvador et al., 2008). Since entering the genomics era, sequencing-based approaches were used to decipher the complex origin of HGSOC by analysing matched early stage p53 signatures, STIC lesions and HGSOCs (Fig. 1.3B) (Kuhn et al., 2012; Labidi-Galy et al., 2017). In all cases, mutations in *TP53* were observed across lesions of all stages corroborating its role as a driver mutation in HGSOC (Labidi-Galy et al., 2017). It is important to appreciate, however, that metastases from a primary tumour in the ovary to the fallopian tube have also been reported which illustrates the complexity of HGSOC origin (Eckert et al., 2016). From a more functional perspective, comparison of transcriptomic features of HGSOCs have been shown to most frequently correlate with transcriptomes of the fallopian tube which led to the consensus that most HGSOCs (88%) arise from the fallopian tube (Ducie et al., 2017).

To delineate which cell type specifically gives rise to HGSOC genetically engineered mouse models (GEMMs) were employed. Ultimately, the epithelial, non-ciliated, secretory, PAX8-expressing cell type at the distal fallopian tube was identified as the cell of origin and has been validated in GEMMs and a variety of human systems. Mice expressing the Cre recombinase in a *Pax8* specific, tetracycline dependent manner were shown to develop HGSOC when conditional *Trp53*, *Pten* and *Brca1/2* alleles were mutated *in vivo* (Perets et al., 2013). Furthermore, mice harbouring conditional *Trp53*, *Brca1*, and *Rb1*, or *Nf1* or *Rb1* and *Nf1* alleles were shown to develop STIC lesions and HGSOC in a tamoxifen dependent manner activating Cre^{ERT2} driven by the *Ovgp1* promoter (Sherman-Baust et al., 2014; Zhai et al., 2017). In addition to these GEMMs, multiple human fallopian tube-derived model systems have been described and showed that HGSOC can originate from the epithelial, secretory cells of the fallopian tube in human model systems. Additional GEMMs and the briefly mentioned, human fallopian tube-derived cell lines will be introduced in more detail in section *1.5: Approaches to study high-grade serous ovarian cancer*.

1.3: Chromosomal instability and aneuploidy

As mentioned briefly, aneuploidy is observed in up to 88% of human cancers, but also manifests in other diseases and only rarely in health tissue (Santaguida and Amon, 2015; Taylor et al., 2018). The underlying cause of aneuploidy in cancer is CIN which describes a phenotype characterized by the perpetual mis-segregation of chromosomes during mitosis and was first described in near-diploid and aneuploid colorectal cancer cell lines and (Lengauer et al., 1997). However, it is important to distinguish aneuploidy, as a genomic scar and static state of numerical chromosomal

imbalances, from the process of constant chromosome mis-segregation during mitosis, CIN. Thus, I will outline the processes preceding and governing cell division as well as fundamental insights into aneuploidy in health, disease and cancer in this section. Furthermore, I will describe causes and consequences of aneuploidy and CIN as well as approaches for the study of these two phenomena.

1.3.1: The cell cycle and mitosis

During physiological processes, such as organismal growth, tissue regeneration and wound healing, cells proliferate. As part of proliferation cells duplicate their genome and subsequently divide it between two daughter cells. The eukaryotic cell cycle, which underlies proliferation, is divided into four distinct phases, two gap phases, G1 and G2, which sandwich the DNA synthesis phase, S-phase, and are collectively referred to as interphase. As the name suggests, in S-phase new DNA is synthesized to double the cell's genome. The final fourth stage, disconnecting G2 and G1, of the cell cycle is mitosis during which the newly synthesized DNA is divided equally into two daughter cells. On the whole, the cell cycle is a tightly controlled process with checkpoints in place at the key transition points to maintain cell cycle fidelity and genomic integrity (Weinberg, 2014).

After mitosis, cells are typically rendered in a static, quiescent state referred to as G0 which they can exit from to enter G1 upon dephosphorylation of the retinoblastoma protein (RB1, encoded by *RB1*; Fig. 1.4A) (Sherr and Bartek, 2017). During this early time in G1, endogenous and exogenous mitogens stimulate cell growth by signalling through cyclin D-dependent kinases (CDK) 4 and 6 (CDK4/6). Over the course of G1, cells acquire the required nutrients, increase in size and progressively phosphorylate RB1 in a dynamic, CDK4/6-dependent manner at first. The continued phosphorylation of RB1, supported by cyclin E and CDK2 in late G1, results in the successive release of its target protein the E2F transcription factor. However, if cells sense stress early and late during G1 RB1 phosphorylation activity by CDKs is inhibited by the CDK inhibitors p16 (*CDKN2A*) and p21 (*CDKN1A*). Upstream of p21, the stress response is directly initiated by *CDKN1A* transcriptional activation through p53. In the absence of p53-p21 activation and upon hyperphosphorylation of RB1 cells can progress through G1 normally and enter S-phase in an E2F-dependent manner.

The transition from G1- to S-phase also marks the G1 checkpoint which ensures integrity of DNA prior to replication initiation as S-phase entry in the presence of DNA damage can be detrimental. The core mediator of S-phase entry is the transcription factor E2F which initiates the expression of DNA polymerases, DNA helicases, DNA

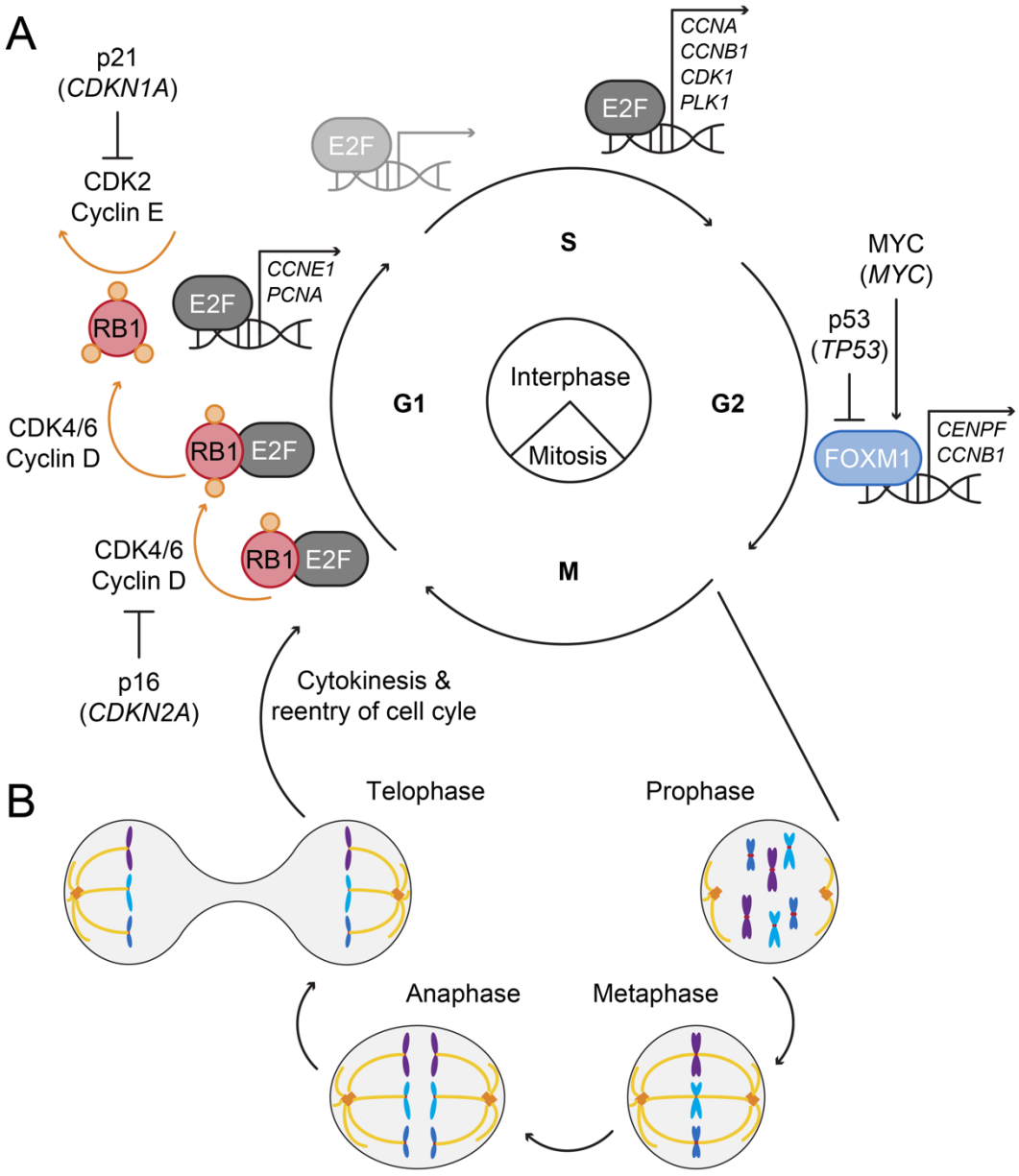

Figure 1.4: The cell cycle and mitosis
A Schematic of the cell cycle with key proteins involved in pertinent transitions. Over the course of G1 the mediator of S-phase entry, E2F, is liberated from its binding partner RB1 by cyclin dependent kinase mediated phosphorylation of RB1. In late G1, E2F initiates transcription of targets required for S-phase entry. In early S-phase, E2F transcribes genes required for nucleotide synthesis, helicases, ligases and DNA replication factors. In late S-phase, E2F dependent transcription of mitotic factors is initiated. FOXM1 transcribes additional mitotic factors to facilitate M-phase entry. Individual promoters and suppressors of transcription factors and cyclin dependent kinases are indicated. Figure inspired by Sherr & Bartek (2017). **B** Illustration of the four stages of mitosis. Chromosomes are indicated in blue and purple, centromeres in red, microtubules in yellow and centrosomes in orange.

ligases, topoisomerase, additional cell cycle regulators and also initiates the duplication of the centrosome (Fig. 1.4A) (Nigg and Holland, 2018; Otto and Sicinski, 2017). During S-phase, DNA is first unwound and then synthesized with 5' to 3' directionality. This means that one strand is synthesized continuously (leading strand) and one strand is synthesized in a step-wise manner (lagging strand). On the lagging strand, RNA primers hybridize to the DNA which prompt synthesis generating so called Okazaki fragments which are ligated once fully synthesized (Limas and Cook, 2019). DNA replication occurs at the replication fork in a highly dynamic manner and can easily be disrupted by an encounter of the replication machinery with a damaged DNA strand. Untimely resolution of a DNA single-strand break can result in the formation of a DNA double-strand break which in the presence of replicated DNA is repaired by homologous recombination (HR), described in more detail in *1.4.2: Homologous recombination deficiency in BRCA1/2-mutated cases* due to its importance in HGSOC.

Once DNA replication is completed, cells are in G2 and mitosis is initiated in a manner dependent on FOXM1-mediated transcriptional activation of mitotic regulators such as *CCNB1*, *CENPF* and *PLK1* during G2 (Fig. 1.4A) (Laoukili et al., 2005). Again, prior to the commitment to the next stage of the cell cycle, genomic integrity is ensured at the end of G2 to prevent cell death following mitotic entry in the presence of DNA damage (Blank et al., 2015). Upon entry into prophase, the first stage of mitosis, the nuclear envelope disassembles and chromosomes condense so that sister chromatids are held together at the kinetochore (Fig. 1.4B). During prometaphase, the chromosomes' kinetochore is attached to spindle microtubules which are anchored at spindle poles formed by the previously duplicated centrosomes. Subsequently, the chromosomes are moved from the spindle poles to the metaphase plate. This step is in part facilitated by the mitotic kinesin CENP-E which is required for proper kinetochore-microtubule attachments and chromosome movement towards the metaphase plate (Putkey et al., 2002). In the process of forming the metaphase plate, all chromosomes need to be attached correctly to microtubules and aligned otherwise the spindle assembly checkpoint (SAC) cannot be satisfied. Upon SAC satisfaction, the anaphase promoting complex or cyclosome (APC/C) is activated. The APC/C is an E3 ubiquitin ligase that tags multiple mitotic proteins, such as cyclin B, for degradation thus initiating anaphase onset and exit from mitosis (Lara-Gonzalez et al., 2012). During anaphase, the chromosomes are separated and pulled towards the spindle poles. In the subsequent telophase, the nuclear envelope is established and chromosomes begin to decondensate. Lastly, to complete mitosis, the cytoplasmic connection of the new daughter cells is cut during cytokinesis.

At this point the previous cell cycle is complete and each daughter cell re-enters at G0/1. Faithful genome duplication and division should prevent any potential downstream stresses in the daughter cells. Consequences of acute chromosome segregation errors will be introduced in more detail in *1.3.6: Consequences of chromosomal instability other than aneuploidy* and *1.3.7: Consequences of aneuploidy*.

1.3.2: Aneuploidy in diseases other than cancer

Since cellular diploidy is robustly controlled by the mechanisms outlined in the previous section, it is important to note that it is infrequently observed in healthy tissues (Knouse et al., 2014). Rare aneuploidies that occur as a result of chromosome segregation errors during gametogenesis manifest in the embryo's genome as trisomies or monosomies. Sex chromosome aneuploidies such as Turner syndrome (X0), Klinefelter syndrome (XXY), Trisomy X, XYY and XXYY occur rarely; the most frequent is Klinefelter syndrome seen in 1 of 750 live births (Skuse et al., 2018). In contrast to sex chromosome aneuploidies, autosomal trisomies almost uniformly lead to spontaneous abortions or stillbirths. Only three constitutional, autosomal trisomies are observed in live births: Patau syndrome (trisomy 13), Edwards syndrome (trisomy 18) and Down syndrome (trisomy 21) (Jackson-Cook, 2011). While survival of children born with Patau and Edwards syndrome is less than 10% at one year of age, Down syndrome patients have normal life expectancy, but display developmental defects (NHS, 2019). Constitutional whole chromosome monosomies, with the exception of Turner syndrome, have not been reported, however, partial or whole deletion of chromosome arm 18q leads to 18q deletion syndrome.

An important contributor of phenotype severity in patients with constitutional aneuploidy disorders is mosaicism where a fraction of cells remains diploid which alleviates disease severity. Indeed, it was shown in mouse pre-implantation embryos that pharmacologically induced, aneuploid cells would be outcompeted by euploid cells thus rescuing potential developmental defects due to aneuploidy (Bolton et al., 2016). Mosaic variegated aneuploidy is a group of hereditary, recessive diseases caused by biallelic mutations in *BUB1B*, *CEP57* and *TRIP13* which encode for proteins important for chromosome segregation (Hanks et al., 2004; Snape et al., 2011; Yost et al., 2017). Mosaic variegated aneuploidy causes mosaicism of aneuploidy, consequently patients suffer, with varying penetrance, from growth retardation, microcephaly, developmental delays, seizures and a predisposition to cancers. These observations illustrate that aneuploidy is only partially compatible with cellular or organismal health.

1.3.3: Aneuploidy in cancer

The vast majority of human solid tumours are aneuploid and the degree of aneuploidy varies between tumour types (Ciriello et al., 2013; Shukla et al., 2020; Taylor et al., 2018). A potential link between aneuploidy, deregulated mitosis and cancer had first been suggested more than a century ago by Hansemann (1890) and raised again later by Boveri (1914). Indeed, studies comparing aneuploidy profiles of pre-neoplastic and cancerous lesions using comparative genomic hybridization have shown that aneuploidy manifests early and that the number of aneuploid chromosomes increases as the diseases progresses. Work on cervical cancer and its pre-cursor lesions revealed an increase in gains of chromosome arm 3q during tumourigenesis as a defining feature differentiating low and moderate dysplasia from severe dysplasia and carcinoma *in situ* (Heselmeyer et al., 1996). These observations were confirmed using Fluorescence *in situ* Hybridization (FISH) targeting the *TERC* locus which maps to chromosome arm 3q. This approach showed that only a small number of atypical squamous cells and low-grade dysplasia lesions had gained *TERC*, but up to 63% and 76% of moderate- and high-grade dysplasia lesions had gained *TERC*, respectively (Heselmeyer-Haddad et al., 2003). This observation is not unique to cervical cancer, similar work done on colorectal cancer using comparative genomic hybridization showed that over the course of progression from low- to high-grade adenoma and ultimately to carcinoma several chromosomal gains and losses occurred in a step-wise manner (Ried et al., 1996). More recently, a prospective study focusing on lung cancer showed that carcinomas *in situ* displaying high levels of copy number changes were more likely to progress to carcinoma (Teixeira et al., 2019). Lastly, a pan-cancer analysis of aneuploidy in TCGA samples showed a stage-dependent increase in copy number changes in carcinomas (Shukla et al., 2020). Taken together these data illustrate that aneuploidy increases over the course of cancer development.

In addition to whole chromosome and chromosome arm aneuploidy, the duplication of the entire chromosome complement has also been described during cancer development. The first observation of these so called whole genome doubling (WGD) events was made in studies of Barrett's oesophagus, a neoplastic precursor of oesophageal cancer (Galipeau et al., 1996). This particular study found that WGD co-occurred with inactivation of *TP53* and led to the development of aneuploidy. Indeed, retrospective NGS studies of Barrett's oesophagus patients who either progressed within one year or did not progress over three years showed that aneuploidy, determined by shallow-depth whole genome sequencing, was predictive of disease progression (Killcoyne et al., 2020). Large scale, pan-cancer analyses of WGD have also

shown that it occurs as disease progresses and is associated with mutations in *TP53* (Bielski et al., 2018; Zack et al., 2013). In the same manner that aneuploidy is more prominent in solid than haematological malignancies, WGD events were also found be more frequent in solid than haematological tumours (Shukla et al., 2020). Furthermore, its occurrence is more prominent in metastatic than in primary tumours suggesting that it increases with disease aggressiveness (Priestley et al., 2019). I will describe WGD in more detail as a cause of CIN below.

Aneuploidy is also readily observed in precursor lesions of HGSOC. In fact, the observation that numerical chromosomal imbalances were congruent between p53 signatures, STIC lesions, HGSOCs and metastases provided evidence to support the notion of a fallopian tube origin of HGSOC (Salvador et al., 2008). This illustrates that together with *TP53* mutations, aneuploidy is observed early in HGSOC specifically.

1.3.4: The aneuploidy paradox

The observations that aneuploidy is rarely observed in normal tissues and detrimental for development yet a defining feature of cancers raise a paradox, first described and later reviewed by Williams et al. (2008) and Sheltzer and Amon (2011), respectively. The paradoxical relationship stems on the notion that cancer cells somehow evade or overcome a fitness cost brought about by aneuploidy. In addition, to the clinical observations of Patau, Edwards and Down syndrome, experimental observations showing proliferation, metabolism and immortalization defects were first made in yeast and later confirmed in mouse embryonic fibroblasts (MEFs) (Torres et al., 2007; Williams et al., 2008). MEFs were generated from mice bred to generate a single, specific trisomy in offspring and subsequently subjected to a number of cell biological assays. These found that RNA expression from the trisomic chromosome followed gene dosage, trisomic cells had increased volume and proliferated more slowly compared with euploid control cells (Williams et al., 2008). In a similar study also using trisomic MEFs, additional ectopic expression of oncogenes only partially rescued the proliferative defect incurred by aneuploidy. In all cases ectopic expression of oncogenes increased the proliferation of trisomic cells, however, failed to match wildtype MEFs also ectopically expressing oncogenes. Strikingly, in most cases trisomic MEFs ectopically expressing oncogenes also failed to match the proliferation of wildtype MEFs transduced with the control vector construct (Sheltzer et al., 2017). Furthermore, in models of cancer, aneuploidy has also been shown to impair malignant phenotypes. In particular, trisomic HCT116 colorectal cancer cells (otherwise near-diploid) were subjected to *in vitro* migration and invasion as well as *in vivo* metastasis

assays which found that five out of the six tested trisomies suppressed metastatic behaviour (Vasudevan et al., 2020). A more detailed account of the role of aneuploidy in promoting or suppressing cancer phenotypes has recently been given by Vasudevan et al. (2021).

A clue about the potential reasons why aneuploidy is frequently seen in cancers, but not in healthy cells, lies in the observation I alluded to last. Trisomy of chromosome 5 increased invasion and migration of HCT116 cells *in vitro* and metastasis *in vivo* compared with wildtype and HCT116 cells harbouring other trisomies (Vasudevan et al., 2020). These data suggest that different trisomies impact cellular physiology differently despite the consistently observed fitness penalty observed in trisomic cells. Furthermore, DLD1 cells, which are also otherwise near-diploid colorectal cancer cells, harbouring trisomies have been shown to overcome the trisomy-associated fitness penalty under nonstandard culture conditions such as hypoxia or in the absence of serum (Rutledge et al., 2016).

Taken together, constitutional aneuploidy is detrimental to cellular and organismal health for reasons that I will describe below. However, under conditions of selective pressure certain aneuploidies can confer a fitness advantage. The recurring patterns of aneuploidy, such as the previously mentioned idiosyncratic gain of chromosome 13 in colorectal cancer or the loss and gain of chromosomes 7 and 10, respectively, in glioblastoma multiforme, support the notion that specific numerical chromosome imbalances are selected for during tumourigenesis. The reasons for this cancer type-specific aneuploidy profile selection are subject of intense study and both, the selection of tumour suppressors and oncogenes on lost and gained chromosomes, respectively, as well as underlying gene expression patterns of the normal tissue, have been suggested as causes (Auslander et al., 2019; Sack et al., 2018).

1.3.5: Aneuploidy as a consequence of chromosomal instability in cancer

Aneuploidy is the consequence of one or multiple chromosome mis-segregation events during mitosis. In cancer, there is a clear distinction between aneuploidy and CIN. Importantly, it is possible that cancer cells with highly aneuploid genomes do not display CIN, likewise, it is conceivable that near-euploid cells mis-segregate chromosomes regularly but aneuploid karyotypes never emerge (Bakhoum et al., 2018; Drost et al., 2015). While CIN does not necessarily manifest at all stages of cancer development, it may have occurred transiently generating an aneuploid cancer genome. The causes of CIN have been reviewed in detail by Bastians (2015), therefore, I will

provide a concise overview of the dysfunctional processes preceding cell division and during mitosis itself that cause chromosome segregation errors.

The most intuitive causes of chromosome segregation errors are observed during the process of chromosome segregation itself. The weakening of SAC integrity by complete or partial deletion of SAC components has been shown to result in CIN. Loss of one allele of *MAD2L1* in HCT116 cells results in pervasive chromosome segregation defects (Michel et al., 2001). These observations are consistent with data obtained from mice conditionally deficient for *Bub1*, another SAC gene, where depletion of *Bub1* in MEFs led to highly aberrant mitoses (Perera et al., 2007). Multiple mouse models fully or partially deficient for SAC genes have been generated since and have reproducibly shown that deregulation of the SAC robustly perturbs faithful chromosome segregation, the most up to date account on these models was recently given by Vasudevan et al. (2021). Despite the overwhelming evidence that SAC perturbations cause CIN and thus aneuploidy, mutations in SAC genes are rarely observed in cancers sequenced as part of TCGA. Likewise, functional studies in chromosomally unstable colorectal cancer cells provide evidence to reject the notion of SAC deficiency in cancer cells (Tighe et al., 2001).

Incorrect attachments of microtubules to kinetochores have also been shown to cause CIN. In this particular context, its causes are threefold as follows (Bastians, 2015). First and foremost, erroneous attachments of microtubules to kinetochores prior to anaphase onset result in segregation defects. Normally, each sister chromatid should be attached to microtubules emanating from one spindle pole only (amphitely; Fig. 1.5A-B). However, abnormal attachments are also observed especially since microtubule-kinetochore attachments are thought to occur in a stochastic manner. Under a condition known as monotely, only one sister chromatid is attached to a spindle pole whereas under syntely both sister chromatids are attached to the same spindle pole by microtubules. Lastly, merotely describes a situation where one sister chromatid is attached correctly and the other is attached to both spindle poles at anaphase onset. Merotely is most frequently observed in cells that harbour supernumerary centrosomes as a result of transient multipolar spindle formation which increases the number of microtubule attachments to kinetochores. Ultimately, multipolar spindles undergo centrosome clustering forming a pseudo-bipolar spindle while chromatids remain attached to one or more poles (Ganem et al., 2009; Silkworth et al., 2009). Second, microtubule-kinetochore attachment instability has been identified as a source of chromosome segregation defects. Genetic disruption of the mitotic kinesin CENP-E results in a decreased number of microtubule-kinetochore attachments and

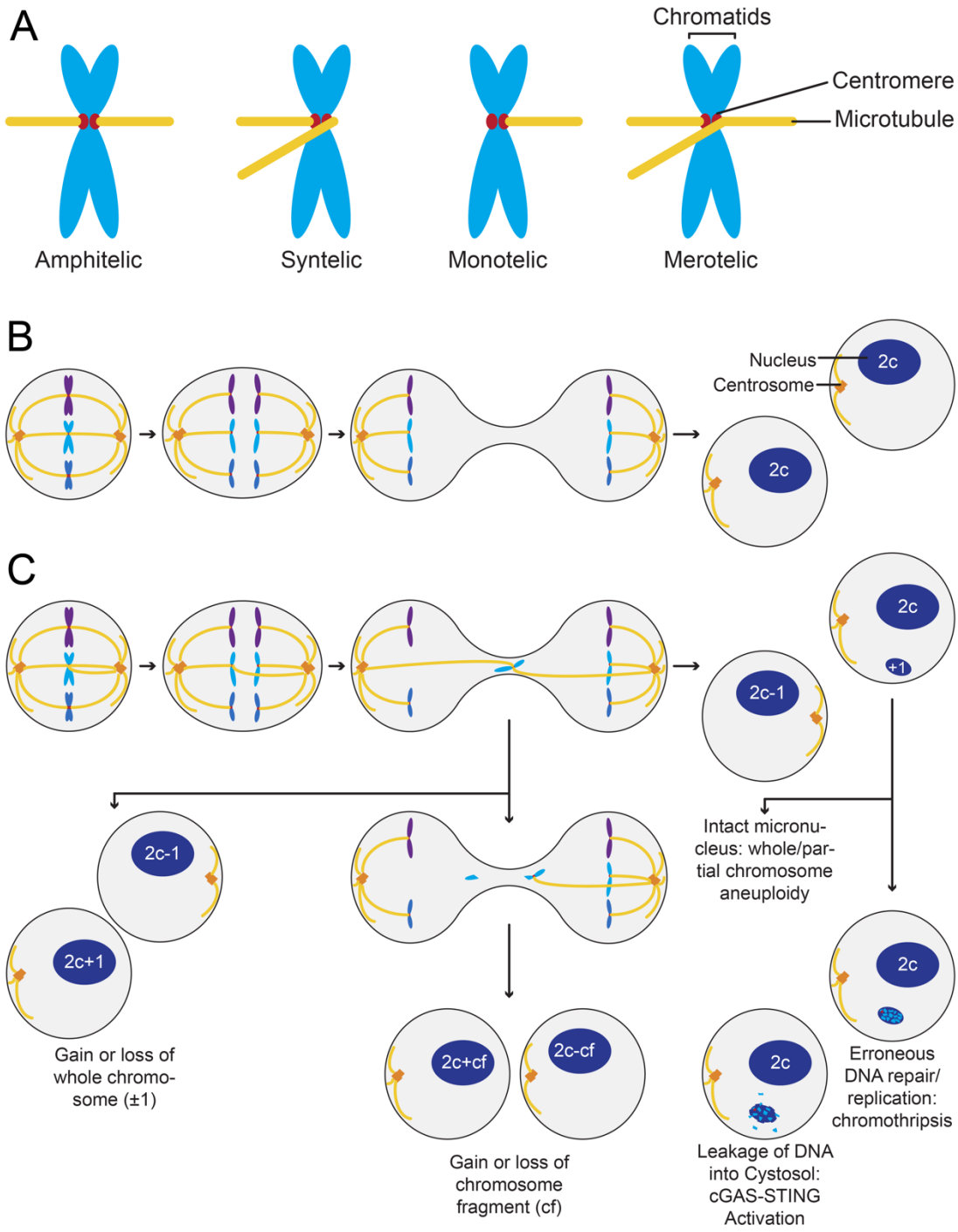

Figure 1.5: Erroneous attachments of chromosomes and consequences of chromosome mis-segregation
A Correct and incorrect attachments of microtubules to kinetochores of chromosomes in metaphase. Figure inspired by Bastians (2015). **B** Faithful chromosome segregation resulting in two diploid (2c) daughter cells. **C** Depiction of chromosome mis-segregation of a merotelically attached chromosome and four potential outcomes resulting in a single chromosome aneuploidy, segmental aneuploidy, the generation of a micronucleus which can lead to chromothripsis or innate immune signalling upon leakage of DNA into the cytosol.

in some cases a complete absence, which prevents chromosomes from being moved to the metaphase plate and equal distribution of chromosomes to daughter cells (Putkey et al., 2002). Third, aberrant microtubule assembly rates lead to chromosome segregation errors by inducing transient defects in spindle geometry that precipitate chromosome mis-segregation (Ertych et al., 2014).

Lastly, defects in sister chromatid cohesion can also contribute to CIN. During and after DNA replication sister chromatids are held together by cohesion which is resolved during the early stages of mitosis, however, if this process fails sister chromatids will not be separated resulting in incorrect DNA distribution in daughter cells (Bastians, 2015). This concludes the causes of CIN directly linked to chromosome segregation in mitosis.

Defects preceding mitosis that have been shown to cause CIN are DNA replication stress and altered transcriptional programmes controlling mitosis that are activated towards the end of interphase. DNA replication stress was observed in chromosomally unstable colorectal cancer cells and replicated pharmacologically in chromosomally HCT116 cells which displayed elevated segregation errors as a result (Burrell et al., 2013). Faithful chromosome segregation is, in part, controlled by the timely expression of mitotic genes such as *CCNB1*, *PLK1* and *CENPF* which are controlled by the transcription factor FOXM1. Indeed, loss of FOXM1 in MEFs leads to mitotic defects (Laoukili et al., 2005).

These observations clearly demonstrate that in addition to mitotic deregulation, alterations in interphase processes can also lead to CIN.

1.3.6: Consequences of chromosomal instability other than aneuploidy

Aneuploidy has been defined as whole chromosome or chromosome arm deviations from a multiple of the haploid genome (Ben-David and Amon, 2020). Therefore, I have focused on CIN as a cause of aneuploidy, however, mis-segregation of chromosomes can also lead to other numerical imbalances and structural genomic changes (Bakhoum and Cantley, 2018). Moreover, chromosomes are physical entities of DNA which, under the right circumstances, can be recognized by pattern recognition molecules in cells.

Structural changes such as unbalanced translocations, chromothripsis and extrachromosomal DNA fragments are regularly observed in human tumours and cell lines derived from solid tumours. Chromosome mis-segregation that damages the mis-segregated chromosome or results in the formation of a micronucleus can result in severe

damage to the DNA (Fig. 1.5C) (Janssen et al., 2011). Especially DNA encapsulated in a micronucleus cannot be repaired adequately leading to the shattering of the chromosome and non-faithful ligation of the fragments; the resulting genomic aberration is referred to as chromothripsis (Zhang et al., 2015). Initially, the DNA is fragmented in the micronucleus as a result of impaired transport of proteins required to maintain genome integrity across the micronucleus membrane (Liu et al., 2018). Over the course of the following cell cycles, the DNA in the micronucleus fails to replicate and, if the micronucleus disassembles, spills into the cytoplasm during mitosis and is distributed across the two daughter cells. Following this scenario derivative chromosomes of the initially mis-segregated chromosome can be observed (Ly et al., 2017). Longer term expansion of cells that have undergone chromosome shattering in a micronucleus after mis-segregation has further revealed that non-inherited fragments can be detected as genomic deletions and that fragments can be incorporated incorrectly on other chromosomes (Ly et al., 2019). Lastly, selection pressures can drive the selection of specific loci that amplify either extrachromosomally or by forming homogenously staining regions which are chromosomal loci of multiple copies of the same gene; both of these are detected as focal amplifications in cancer genomes (Shoshani et al., 2020). Collectively, these data exemplify that chromosome segregation errors not only lead to aneuploidy but can also result in more complex genomic aberrations.

Lastly, chromosomes are physical entities made up of DNA and usually confined to the nucleus or in some instances after chromosome mis-segregation to micronuclei. Upon breakage of micronuclei, chromosomal DNA has been shown to be detected by the pattern recognition molecule cyclic GMP-AMP synthase (cGAS) which produces cyclic GMP-AMP (cGAMP), a potent activator of the protein Stimulator of Interferon Genes (STING) (Bakhoum et al., 2018; Harding et al., 2017; Mackenzie et al., 2017). The detection of mis-segregated chromosomes as cytosolic double-stranded DNA by cGAS results in inflammatory signalling in the absence of interferon type I induction in cancer cells (Bakhoum et al., 2018).

Thus, chromosome mis-segregation does not only lead to aneuploidy but can also result in complex genomic rearrangements and the activation of cytosolic sensing of double-stranded DNA and subsequent inflammatory signalling.

1.3.7: Consequences of aneuploidy

The constitutional imbalance of genetic material, such as an aneuploid chromosome, needs to be distinguished from the immediate cellular response following a

chromosome mis-segregation event. Therefore, I will first summarize the immediate consequences of a chromosome segregation error that causes acute aneuploidy and then allude to consequences of constitutional aneuploidy.

In normal cells, mechanisms are in place that suppress further proliferation after a chromosome has been mis-segregated or if mitotic duration has exceeded a certain amount of time, this mechanism was termed the mitotic timer (Lambrus et al., 2016). The mitotic timer safeguards diploidy immediately after mitosis is completed and dependent on a signalling cascade that culminates in p53 and p21 activation via USP28 and TP53BP1 (Lambrus et al., 2016). An additional mechanism that suppresses aneuploidy in the immediate setting is governed by p38α which ultimately leads to apoptosis downstream (Simoes-Sousa et al., 2018). Lastly, as described in the previous section for cancer cells, chromosome mis-segregation can also lead to inflammatory signalling when cytosolic DNA is detected by cGAS after micronuclei rupture. However, the response in non-transformed cells differs from what is observed in cancer cells. In non-transformed cells, type I interferon is upregulated as expected in response to cGAS-STING activation (Harding et al., 2017; Mackenzie et al., 2017).

The consequences of constitutional aneuploidy, which I mentioned briefly in *1.3.4: The aneuploidy paradox*, are an increase of gene expression from the aneuploid chromosome, proteotoxic stress, altered metabolism and ultimately a decrease in cellular and organismal fitness. Gene expression has been shown to follow gene dosage in a number of studies using DLD-1 and HCT116 cells harbouring trisomies, MEFs harbouring trisomies and haploid yeast harbouring disomies. Indeed, the findings consistently show that on the mRNA expression level, gene expression is proportional to gene copy number, i.e., chromosome-wide gene expression scales with chromosome dosage (Torres et al., 2007; Upender et al., 2004; Williams et al., 2008). However, the linear increase in RNA expression has been found to be decreased on the protein level where up to 27% of proteins were found to be reduced to normal expression levels observed in euploid cells (Stingele et al., 2012). Upon identification that constitutive aneuploidy leads to increased gene expression, it was shown in the same study that aneuploidy led to downregulated DNA replication and repair as well as mRNA processing and transcription gene sets. Gene sets representing lipid and membrane biogenesis, endoplasmic reticulum, Golgi vesicles and lysosome function, mitochondrial respiratory and carbohydrate metabolism in contrast were upregulated in aneuploid cells. Due to the lysosomes' involvement in autophagy the authors functionally validated their proteomics observation and showed that autophagy is activated in aneuploid cells. The activation of autophagy in aneuploid cells has also been shown to

be an immediate consequence of chromosome mis-segregation and is a result of proteotoxic stress, another chronic cellular stress observed in aneuploid cells (Oromendia et al., 2012; Santaguida et al., 2015). Lastly, a unifying observation made in yeast as well as human aneuploid cells is an increase in cell cycle duration mostly observed in G1 and S (Beach et al., 2017; Stingele et al., 2012; Torres et al., 2007).

In summary, multiple complementary mechanisms are in place in non-transformed cells to prevent the proliferation of aneuploid progeny. Furthermore, cells with constitutive aneuploidy are impaired as a result of increased protein expression from the aneuploid chromosome which leads to proteotoxic stress. Lastly, the additional genetic material in aneuploid cells leads to G1 and S delays during the cell cycle. In summary, the collective impact of these consequences results in a reduction in proliferative potential of aneuploid cells.

1.3.8: Direct and indirect means to assess chromosomal instability

The study of CIN relies on multiple complementary approaches and measurements. In this section, I will introduce direct and indirect means for the assessment of CIN.

Since CIN manifests in mitosis, the most direct way to assess perturbations in chromosome segregation fidelity is to study mitotic cells. Live-cell, fluorescence microscopy that allows the visualization of DNA, e.g., by fluorescently tagging histone variant H2B, or immunofluorescence microscopy of fixed cells allows the assessment of chromosomes that lag behind the bulk of chromosomes of during anaphase; they are commonly referred to as lagging chromosomes or laggards (Nelson et al., 2020; Tamura et al., 2020). These methods also allow for the identification of other mitotic defects such as chromatin bridges and polar chromosomes which are DNA structures that stretch between the two chromosomes masses and chromosomes that failed to congress to the metaphase plate, respectively. Another commonly used way to estimate CIN is to quantify micronuclei formation. Chromosome mis-segregation frequently results in the formation of micronuclei in daughter cells which makes micronucleus quantitation a useful surrogate marker for CIN though this assay is less direct compared with assays performed on live cells or fixed, mitotic cells. A high frequency of lagging chromosomes, chromatin bridges, polar chromosomes and micronuclei indicates on-going CIN.

In addition to these direct assays, CIN can be inferred in a number of indirect ways by measuring DNA copy number changes which I will described below. The principle of inferring CIN indirectly, however, is the same independent of the employed assay. In normal human cells the expectation is that close to 46 chromosomes can be

detected, two of each autosome and either two X chromosomes or one each of chromosome X and Y. Note, that some cancer cell lines are highly aneuploid thus their baseline might be different from 46. A high number of cells with a chromosome complement that deviates from the modal chromosome count determined as the baseline for the cell line of interest would thus indicate CIN. Importantly, in addition to the quantitative aspect, qualitative assessment can also provide clues about on-going CIN. It is conceivable that a population is made up of two or more clones which are karyotypically stable yet differ in chromosome number.

The simplest, most indirect and highest in throughput method to determine ploidy is the analysis of DNA content by flow cytometry. However, flow cytometry only provides a low resolution picture of ploidy and direct comparisons with other cell lines or appropriate controls in the case of CIN-inducing treatment are recommended (Foijer et al., 2014). An increase in resolution is achieved by visualizing and enumerating chromosomes of dividing cells. Metaphase spreads of chromosomes are obtained by pharmacologically arresting cells in prometaphase and subsequently preparing slides for analysis. This approach offers much higher resolution than flow cytometry. Building on metaphase spreads, molecular cytogenetic methods, such as multiplex-fluorescence *in situ* hybridization (M-FISH) and spectral karyotyping (SKY), can provide qualitative insight in addition to quantitative data as chromosomes can be distinguished and structural aberrations identified more easily (Schrock et al., 1996; Speicher et al., 1996). Expanding on the enumeration of chromosomes, fluorescence *in situ* hybridization (FISH) of centromeres or gene loci eliminates the requirement for the preparation of mitotic cells thus allowing for an increase in throughput. Using FISH, hundreds of cells can be hybridized to test for numerical deviations of the selected centromere and gene loci. Sequential hybridization of the same cells with multiple different centromere and gene probes by multi-colour interphase fluorescence *in situ* hybridization (miFISH) can provide a more detailed picture of copy number changes (Heselmeyer-Haddad et al., 2012). Another metaphase-independent manner to detect copy number changes in single cells is single-cell shallow-depth whole genome sequencing (scWGS) (Bakker et al., 2016). This methodology provides a genome-wide picture of copy number changes at the highest resolution yet lowest throughout in comparison to the other methods described.

The direct and indirect methods to assess CIN have thus far focused on proliferating cells in culture. Some of these assays can also be employed on archived or fresh patient samples. For instance, lagging chromosomes can be detected in histopathological specimens prepared as part of routine diagnostics (Zaki et al., 2014).

Furthermore, miFISH was initially established on formalin fixed, paraffin embedded patient samples (Heselmeyer-Haddad et al., 2012). Such datasets, however, are limited in number and not readily available for many different cancer types like the TCGA cohort. To infer CIN from TCGA samples, Taylor et al. (2018) developed an *aneuploidy score* which determined for each individual tumour if a chromosome arm is lost, gained or unaltered from the baseline ploidy. This way, tumours with few chromosome arm alternations are considered chromosomally stable and those with many chromosome arm alterations are considered chromosomally unstable.

This illustrates multiple different ways to assess CIN in dividing cells and archived samples either directly or indirectly by cell biological or molecular cytogenetic means, respectively. Ultimately, orthogonal approaches that overcome each other's shortcomings are most commonly employed to maximize confidence.

1.4: The genetic drivers of high-grade serous ovarian cancer

The genetic mutations driving HGSOC have been introduced in section *1.2.2: Genomics of high-grade serous ovarian cancer*, however, a more detailed account of the implicated genes' canonical roles in tumour suppression and oncogenesis is required for a better understanding of the disease and selection of genes for this thesis' work. Therefore, I will introduce three key genes and discuss CIN specifically in the context of tumour promotion and HGSOC.

1.4.1: Ubiquitous *TP53* mutations

Mutations in *TP53* are observed in up to one third of human cancers (Fig. 1.6A) and in HGSOC specifically *TP53* mutations are ubiquitous and already detected in precursor lesions (Ahmed et al., 2010; Kuhn et al., 2012; Labidi-Galy et al., 2017; TCGA, 2011; Vang et al., 2016). As such, HGSOC is the only tumour entity with ubiquitous *TP53* mutations. Moreover, mutations in *TP53* accumulate with age as they were shown to increase in prevalence in women with and without ovarian cancer when cells isolated by uterine lavage were subjected to NGS (Salk et al., 2019). These data of somatic mutations surveyed across different cancer types illustrate the role and importance of p53, the protein *TP53* codes for, in tumour suppression. Furthermore, germline mutations in *TP53* cause the cancer predisposition syndrome Li-Fraumeni (OMIM: 151623), which confers a lifetime cancer risk of 93% and 68% in women and men by the age of 50, respectively.

Due to its importance for cancer biology, p53 is one of the most widely studied proteins; a simple National Library of Medicine search for "p53" yields more than 100,000

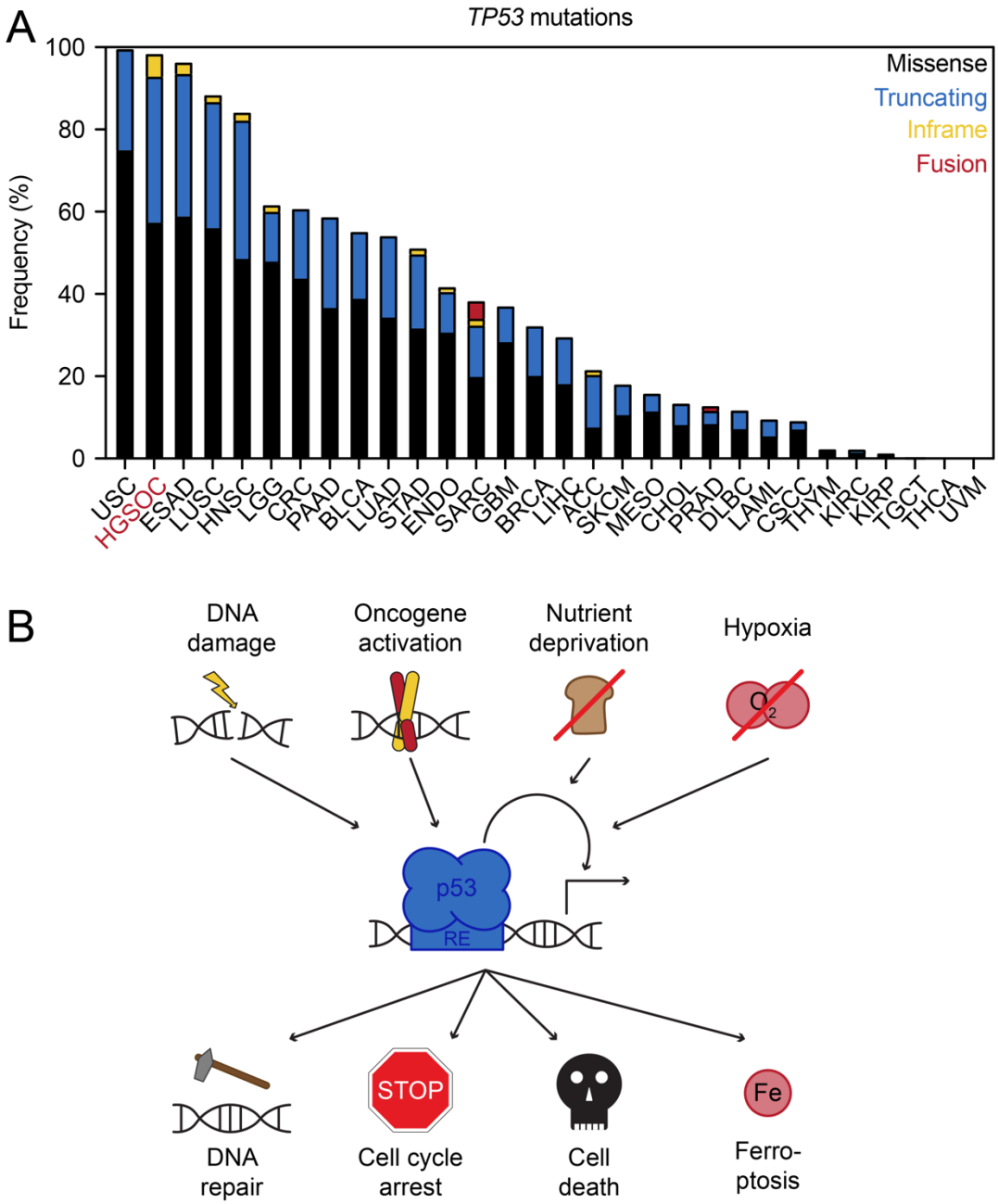

Figure 1.6: *TP53* mutations in human cancers and p53's role in tumour suppression
A Frequency of mutations in *TP53* across 30 cancer types analysed by TCGA. Colour depicts kind of mutation. Data was accessed and analysed using cBioPortal. **B** Schematic of p53 signalling in tumour suppression indicating causes of p53 activation and downstream effects. Figure inspired by Boutelle & Attardi (2021).

UCS - Uterine carcinosarcoma, HGSOC - High-grade serous ovarian cancer, ESAD - Oesophageal adenocarcinoma, LUSC - Lung squamous cell carcinoma, HNSC - Head and neck squamous cell carcinoma, LGG - Low-grade glioma, CRC - Colorectal carcinoma, PAAD - Pancreatic adenocarcinoma, BLCA - Bladder urothelial carcinoma, LUAD - Lung adenocarcinoma, STAD - Stomach adenocarcinoma, ENDO - Endometrial carcinoma, SARC - Sarcoma, GBM - Glioblastoma multiforme, BRCA - Brest invasive carcinoma, LIHC - Liver hepatocelluar carcinoma, ACC - Adrenocortical carcinoma, SKCM - Skin cutaneous melanoma, MESO - Mesothelioma, CHOL - Cholangiocarcinoma, PRAD - Prostate adenocarcinoma, DLBC - Diffuce large B-cell lymphoma, LAML - Acute myeloid leukaemia, CSCC - Cervical squamous cell carcinoma, THYM - Thymoma, KIRC - Kidney renal clear cell carcinoma, KIRP - Kidney renal papillary cell carcinoma, TGCT - Testicular germ cell tumour, THCA - Thyroid carcinoma, UVM - Uveal melanoma.

results. At first, p53 was identified as an interactor of the simian virus 40 large T antigen (SV40 TAg) and thus proposed to be an oncogene aiding viral transformation of cells (Lane and Levine, 2010). Mounting evidence in the 1980s following that discovery suggested that p53 was an oncogene as the ectopic expression of isolated *TP53* cDNA clones cooperated with other oncogenes in transformation assays. These findings were later traced to the ectopic expression of mutated *TP53* cDNAs (Lane and Levine, 2010). Mutations in *TP53* were also discovered in human cancer cell lines and human cancers further suggestion that, in fact, wildtype *TP53* encoded a tumour suppressive protein. Lastly, functional validation of the mouse homologue of *TP53*, *Trp53*, as a tumour suppressor by developing a knockout mouse showed a definitive link between the absence of p53 and tumour incidence. Homozygous *Trp53*-null mice developed mostly malignant lymphoma, but also sarcoma, within 18 weeks of life (Donehower et al., 1992).

The p53 protein is a transcription factor which binds to DNA in a sequence specific manner as a tetramer (Boutelle and Attardi, 2021). Under physiological conditions, p53 levels are low. An auto-regulatory feedback loop between p53 and MDM2 controls p53 levels as *MDM2* is a canonical target gene which in turn encodes the E3 ubiquitin ligase MDM2. In the absence of p53-activating stresses, *MDM2* transcription is being induced and in turn p53 is ubiquitinated and degraded. Activation of p53 occurs following a number of cellular stresses (Fig. 1.6B). Upon activation, p53 binds its target genes in a DNA sequence-dependent manner at p53 response elements (RE) and recruits the transcription machinery. For these purposes, the p53 protein is contains two transcriptional activation domains and a sequence-specific DNA binding domain, respectively (Boutelle and Attardi, 2021). In this manner, p53 can induce a number of downstream genes that directly or indirectly influence cell physiology.

An important role in preventing GI has been attributed to p53 and earned it the alias *guardian of the genome* (Lane, 1992). Indeed, analyses of tumour sequencing data from studies such as TCGA have shown that mutations in *TP53* correlate consistently and most highly with aneuploid tumour genomes (Ciriello et al., 2013; Taylor et al., 2018). So, how does p53 ensure diploidy? As introduced previously, p53 is activated in response to a number of pathways and initiates corresponding downstream responses. Most pertinent to diploidy control, however, was the separation of some of these functions. In a mouse model of p53 separation of function, a apoptosis-deficient mutant ensures chromosomal stability, however, in an apoptosis-proficient, cell cycle arrest-deficient mutant CIN was observed. The requirement for p53's cell cycle arrest function was further illustrated by deletion of p53's canonical cell cycle arrest

transcriptional target *Cdkn1a* in the apoptosis-deficient mutant which also resulted in CIN (Barboza et al., 2006). These data illustrate that p53 ensures diploidy in a manner dependent on its ability to induce cell cycle arrest.

1.4.2: Homologous recombination deficiency in *BRCA1/2*-mutated cases

The breast cancer susceptibility genes *BRCA1* and *BRCA2* were first identified in breast and ovarian cancer families (Futreal et al., 1994; Wooster et al., 1995). Their description was closely followed by mapping *BRCA1* and *BRCA2* to chromosome arms 17q and 13q, respectively (Miki et al., 1994; Wooster et al., 1994). Clinically, the estimated absolute risk of breast cancer in women aged 40 years with germline truncation mutations in *BRCA1* and *BRCA2* is around 10% and 5%, respectively. This risk increases with age to a maximum of around 55% and 45% in *BRCA1* and *BRCA2* mutation carriers at age 80 years, respectively (Breast Cancer Association et al., 2021). In HGSOC, the majority of mutations in *BRCA1/2* are protein truncating germline mutations and *BRCA1* was found to be mutated more frequently than *BRCA2* in the TCGA cohort (12% vs 11%) (TCGA, 2011). Functionally, BRCA1/2 are involved in homologous recombination (HR), alternatively referred to as homology-directed repair, thus their wildtype role is to maintain genomic stability (Chen et al., 2018). Indeed, loss of wildtype Brca1/2 proteins in MEFs results in increased GI including CIN and centrosome amplification, which due to the reported increase in ploidy might result from WGD (Tutt et al., 1999; Xu et al., 1999). Furthermore, a role in controlling microtubule assembly via Aurora kinase A signalling has been attributed to BRCA1 thus crediting it with a role in mitosis (Ertych et al., 2016; Stolz et al., 2010).

Loss of BRCA1/2 function leads to HRD (Chen et al., 2018). Up to half of all HGSOC cases are thought to be HRD brought on by either *BRCA1/2* mutation, *BRCA1* promoter methylation or mutations in other HR controlling genes such as *PALB2*, *RAD51C*, *RAD51D* or *ATM* (Chen et al., 2018; Wang et al., 2017). HR is an important – understood to be the most accurate – pathway for the repair of DNA double-strand breaks. The other pathways utilized to repair DNA double-strand breaks are nonhomologous end joining, microhomology-mediated end joining and single strand annealing (Chen et al., 2018). Repair pathway choice is cell cycle stage dependent, during G1, in the absence of a repair template, nonhomologous end joining is favoured over HR.

BRCA1 and BRCA2 canonically function in HR. First, upon detection of a DNA double-strand break in the presence of a repair template, typically a sister chromatid during S or G2, BRCA1 promotes 5'-3' DNA end resection in an incompletely understood manner. End resection exposes a stretch of single-strand DNA that is coated by RPA.

Second, BRCA1 interacts with PALB2 through its coiled-coil domain to facilitate BRCA2-mediated RPA displacement. Third, BRCA2 directly interacts with RAD51 to displace RPA. Lastly, the RAD51-coated DNA strands can invade the homologous strand and DNA repair can be completed (Chen et al., 2018). In the absence of functional BRCA1/2 protein, the efficiency with which single-strand DNA is coated with RAD51 is suppressed and as such RAD51 focus formation has been established as a surrogate marker for BRCA1/2 function (Callen et al., 2020). Additional roles for BRCA1/2 have been identified in the protection from environmental and endogenous aldehydes as well as of reversed DNA replication forks. Replication fork reversal is observed when the replication machinery encounters a single strand break or nucleotides have been depleted (Chen et al., 2018). Similar to their roles in HR, BRCA1/2 facilitate the loading of RAD51 onto single-stranded DNA.

The loss of BRCA1/2 function and consequential HRD leaves a genomic scar which was first identified as mutational signature 3 (Nik-Zainal et al., 2012). This signature is defined by a wide distribution of base substitutions as well as insertions and deletions spanning fewer than 50 base-pairs. Strikingly, the prevalence of this signature was found to be highest in ovarian adenocarcinoma out of 32 cancer types (Alexandrov et al., 2020).

Lastly, loss of BRCA1/2 function renders cells more reliant on alternative, potentially more error-prone, DNA repair pathways, which likely explains the aforementioned genomic scar. However, HRD also leaves BRCA1/2-deficient cells vulnerable to the inhibition of poly(ADP)-ribose-polymerase (PARP) proteins (Bryant et al., 2005; Farmer et al., 2005). This synthetically lethal relationship between BRCA1/2-deficiency and PARP inhibition arises as at least one of the two proteins is required for cell viability. Maintenance therapy with a PARP inhibitor (PARPi) for BRCA1/2-mutant ovarian cancer patients lowered the risks of progression and death by 70% compared with patients receiving a placebo (Moore et al., 2018). Despite this clinical success for BRCA1/2 mutation carriers, the targeted nature of PARPi presents an evolutionary bottleneck. Indeed, resistance to PARPi is frequently observed and several mechanisms have been identified such as secondary, reversion mutations in *BRCA1/2* and mutations in *RAD51* and its paralogs *RAD51C/D* (Chen et al., 2018). Interestingly, mutations in exon 11 of BRCA1 have been shown to cause a diminished PARPi response in comparison to other BRCA1 mutations. This is a consequence of partial exon 11 skipping that results in an incompletely functional BRCA1-isoform (Wang et al., 2016).

In summary, BRCA1/2 play important roles in maintaining genomic integrity, suppressing tumourigenesis and as synthetically lethal targets for therapeutic intervention.

1.4.3: The amplification and overexpression of *MYC*

The *MYC* oncogene was first discovered in chicken retroviruses and remained subject of intensive study since (Baluapuri et al., 2020). In HGSOC, MYC is the most frequently amplified and overexpressed oncogene (TCGA, 2011). In fact, HGSOC displays the highest frequency of *MYC* amplifications and fourth highest frequency of gains of the chromosome arm it maps to (8q) across a number of solid and haematological malignancies (Fig. 1.7) (Zeng et al., 2018). Its importance for cancer biology has long been established yet tissue-specific roles remain to be determined.

MYC is a basic helix-loop-helix zipper transcription factor and member of a gene family which also includes its paralogs *MYCN* and *MYCL* (Dang, 2012). All three paralogs are oncogenic when overexpressed, however, their expression itself is restrained in a tissue- and tumour entity-specific manner. *MYCL* overexpression is confined to small cell lung cancer and *MYCN* overexpression is observed in tumours of neuronal lineage such as glioma and neuroblastoma (Baluapuri et al., 2020; Dang, 2012). Thus, the focus of this introduction will be on *MYC*.

In its function as transcription factor, MYC controls the cell cycle, biogenesis and apoptosis to name a few biological processes as examples. MYC binds DNA in a sequence-specific and -unspecific manner as a heterodimer formed with MAX and three models of MYC- controlled gene expression have been suggested as reviewed by Baluapuri et al. (2020). First, MYC binds specific target genes that it either activates or represses. Second, MYC acts as a global amplifier of transcription in a sequence agnostic manner. Third, gene expression regulated by MYC is determined by its binding affinity to a target. High-affinity target genes are expressed at physiological levels and will not be amplified as MYC levels increase while low-affinity targets are only present at low levels, if at all, under physiological MYC levels and increase in expression dependent on MYC levels. A definitive determination of the exact processes, however, remains difficult to achieve due to the number of different cell types and models used for the elucidation of the aforementioned models (Baluapuri et al., 2020).

MYC's oncogenic role is undisputed, e.g., in an *in vivo* model of promyelocytic leukaemia the *Myc* locus is selected for through a gain of chromosome 15, where it maps to in the mouse genome. Ectopic expression of *Myc* from a transgene on a different chromosome alleviates the selection of chromosome 15 (Jones et al., 2010). Furthermore, sustained expression of *MYC* is required for tumour growth in a xenograft

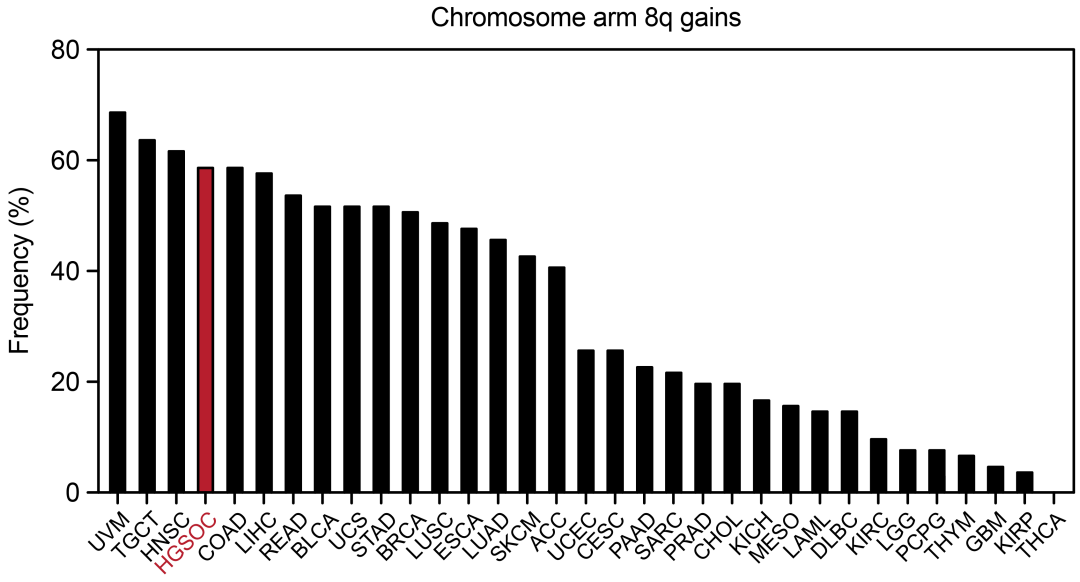

Figure 1.7: Pan-cancer assessment of chromosome 8q

Frequency of chromosome 8 gains across the cohort of cancers analysed as part of TCGA. Chromosome arm aneuploidy is based on the analysis performed by Taylor et. (2018).

UVM - Uveal melanoma, TGCT - Testicular germ cell tumour, HGSOC - High-grade serous ovarian cancer, COAD - Colon adenocarcinoma, LIHC - Liver hepatocelluar carcinoma, READ - Rectum adenocarcinoma, BLCA - Bladder urothelial carcinoma, UCS - Uterine carcinosarcoma, STAD - Stomach adenocarcinoma, BRCA - Brest invasive carcinoma, LUSC - Lung squamous cell carcinoma, ESCA - Oesophageal carcinoma, LUAD - Lung adenocarcinoma, SKCM - Skin cutaneous melanoma, ACC - Adrenocortical carcinoma, UCEC - Uterine corpus endometrial carcinoma, CESC - Cervical squamous cell carcinoma and endocervical adenocarcinoma, PAAD - Pancreatic adenocarcinoma, SARC - Sarcoma, PRAD - Prostate adenocarcinoma, CHOL - Cholangiocarcinoma, KICH - Kidney chromophobe, MESO - Mesothelioma, LAML - Acute myeloid leukaemia, DLBC - Diffuse large B-cell lymphoma, KIRC - Kidney renal clear cell carcinoma, LGG - Low-grade glioma, PCPG - Pheochtomocytoma and paraganglioma, THYM - Thymoma, GBM - Glioblastoma multiforme, KIRP - Kidney renal papillary cell carcinoma, THCA - Thyroid carcinoma.

model of breast cancer transformation (Lourenco et al., 2019). Functionally, as a globally acting transcription factor, MYC regulates a number of the *hallmarks of cancer*. In sum, however, *MYC* overexpression facilitates autonomous cell growth by increasing cellular metabolism and inducing a transcriptional network of cell cycle promoters and supressing cell cycle inhibitors (Baluapuri et al., 2020). Indeed, MYC drives biogenesis beyond the restriction point at which cells are committed to replicate their DNA. Following the restriction point, MYC derepresses E2F in turn initiating the transcription of DNA replication factors and S-phase (Dang, 2013). Importantly, MYC also represses the expression of cell cycle inhibitors like p21 which inhibits CDK2 and cycle E further aiding the release of E2F and promoting S-phase entry. After S-phase is complete and prior to entry into mitosis, mitotic proteins need to have accumulated which are transcribed by FOXM1, also a MYC target (Baluapuri et al., 2020). Lastly, a role for MYC in ensuring proper mitotic spindle geometry has recently been revealed though the exact mechanism remains to be determined (Littler et al., 2019; Rohrberg et al., 2020). In both studies, the number of MYC-overexpressing cells harbouring micronuclei following mitosis was increased.

Thus, MYC steers tumourigenesis by promoting cell cycle progression and biogenesis which, as a by-product, precipitates another *hallmark of cancer*, CIN.

1.4.4: Chromosomal instability

As introduced in *1.3: Chromosomal Instability and aneuploidy*, CIN is the fuel for the selection of genomic aberrations that result in oncogene amplification and tumour suppressor gene loss. Clinically, CIN is associated with intratumour genetic heterogeneity, drug resistance, a propensity for metastasis and, likely as a result of the aforementioned, poor prognosis (Bakhoum and Cantley, 2018; Sansregret et al., 2018).

Next to mutations in *TP53*, copy number changes as a result of CIN are the second most prominent characteristic of HGSOC. Frequently lost tumour suppressor genes are *RB1* and *PTEN* while *KRAS*, *CCNE1* and *MYC* are the most frequently gained and amplified oncogenes (Cerami et al., 2012; Gao et al., 2013; TCGA, 2011). In fact, computational analyses showed that HGSOC is one of the most chromosomally unstable tumour entities analysed as part of TCGA (Ciriello et al., 2013; Shukla et al., 2020; Taylor et al., 2018). Strikingly, on-going CIN is already detected in pre-cursor lesions of HGSOC (Salvador et al., 2008). Cell biological studies corroborating these observations will be introduced in *1.6: Studies of chromosomal instability in high-grade serous ovarian cancer*.

HGSOC presents pre-dominantly as stage 3 or 4 disease with metastatic lesions outside the pelvis and potentially beyond (Torre et al., 2018). While HGSOC patients respond well to chemotherapy initially, recurrence and therapy resistance are frequent (Kurman and Shih Ie, 2016). Thus, HGSOC demonstrates the molecular, cell biological and clinical characteristics that are associated with CIN.

1.5: Approaches to study high-grade serous ovarian cancer

Cancer research depends heavily on the combined use of GEMMs, cancer cell lines, xenografts and increasingly also on patient-derived models such as patient-derived xenografts (PDXs), organoids and *ex vivo* cell lines. For many tissues of cancer origin, normal, immortalized and non-transformed cell lines have also been developed. In this chapter, I will introduce the commonly utilized model systems in HGSOC research specifically to illustrate potential model systems for this work prior to outlining my choice in *1.7: Rationale and Aims*.

1.5.1: Genetically engineered mouse models

GEMMs are a cornerstone of cancer research as they can be used to validate putative tumour suppressor genes and oncogenes, drug targets, therapy efficacy and the impact of the stroma in a controlled manner *in vivo* (Kersten et al., 2017). Classically, GEMMs are bred with a combination of transgenic alleles, many of which are flanked by loxP sites. Expression of the Cre-recombinase under a tissue-, lineage- or developmental stage-specific promoter results in the excision of loxP-flanked sequences (Kersten et al., 2017). This recombination technology has been used to delete entire exons of genes resulting in loss of function, but also to express mutated genes either ectopically or from the endogenous locus (Dankort et al., 2007; Xu et al., 1999).

To study epithelial cancers, many different GEMMs have been developed (House et al., 2014). Mice are usually bred to generate desired genotypes, often including loxP-flanked *Trp53* (*Trp53*$^{fl/fl}$). Initially, mice of desired genotypes would then undergo surgery to inject adenoviral particles expressing the Cre-recombinase (Adeno-Cre) into the ovarian bursa, a membrane structure containing the distal end of the oviduct and the ovary (Zhang et al., 2013). Indeed, this approach results in ovarian tumourigenesis in *Trp53*$^{fl/fl}$;*Rb1*$^{fl/fl}$ mice (Flesken-Nikitin et al., 2003). Alternatively, ovaries from transgenic mice were explanted, cultured *in vitro* and transduced with Adeno-Cre and ectopic oncogene overexpression constructs (Orsulic et al., 2002; Xing and Orsulic, 2006). In this setting, *in vitro* expanded cells are subsequently implanted into recipient mice to test tumourigenicity. A combined approach of tissue-specific promoter driven

oncogene expression and Adeno-Cre delivery to perturb tumour suppressor genes has also been described. This combination of Cre-mediated loss of p53 and Brca1/2 function in the presence of the SV40 TAg oncogene expressed under the control of an epithelial specific promoter, Keratin 18, led to the development of ovarian cancer (Szabova et al., 2012). Collectively, these models have illustrated that specific combinations of perturbations in commonly mutated genes can yield ovarian tumours similar to human HGSOC. However, since Adeno-Cre is not directed at a specific cell type in the ovarian bursa, it can infect many different epithelial cells in the ovary and some parts of the oviduct thus making the origin of cancers difficult to discern (Morin and Weeraratna, 2016).

Two independent GEMMs have been described in *1.2.3: Cellular origin of high-grade serous ovarian cancer* already that overcome the aforementioned limitation of uncertain cell-of-origin. Briefly, in both models the expression of the Cre-recombinase is driven by an oviduct-specific promoter, either *Pax8* or *Ovgp1*. Perets et al. (2013) described the *Pax8*-dependent Cre-expression model which tested tumourigenesis from the oviduct secretory epithelium after *in vivo* mutagenesis of mutant *Trp53*, *Brca1/2* and *Pten* alleles in a tissue-specific and tetracycline-dependent manner. In the *Ovgp1*-dependent model, *Trp53*, *Brca1*, and *Rb1*, or *Nf1* or *Rb1* and *Nf1* alleles were mutated *in vivo* after tamoxifen administration to activate Cre^{ERT2} (Sherman-Baust et al., 2014; Zhai et al., 2017). The tetracycline-dependence in the *Pax8* model and tamoxifen-dependence of Cre^{ERT2} adds an additional layer of temporal control in the oviduct secretory epithelium based model of HGSOC genesis.

In summary, GEMMs have been and continue to be of great utility to test putative HGSOC driver genes *in vivo*, however, the limitations of Adeno-Cre infection mentioned above as well as the time-consuming and resource-intensive generation of transgenic mice are substantial limitations for their use.

1.5.2: Human and mouse cancer cell lines

In comparison to the mouse models introduced in the previous section, human and mouse cancer cell lines are facile and resourceful *in vitro* models of cancer. Cancer cell lines are also another cornerstone of cancer research (Mirabelli et al., 2019).

In ovarian cancer research, the most commonly used cell lines are SK-OV-3, A2780, OVCAR-3, IGROV-1, CAOV-3, 59M and OVCAR-8 as determined by literature research (Barnes et al., 2020). However, as the authors allude to, only three of these seven cell lines were determined to be highly likely of HGSOC origin (OVCAR-3, CAOV-3 and 59M) in a comparative study using the TCGA HGSOC dataset as a

reference for the genetic makeup of ovarian cancer cell lines (Barnes et al., 2020; Domcke et al., 2013). In contrast, the authors also show that seven other cell lines that were found to be highly likely of HGSOC origin by Domcke et al. (2013) account for less than 1% of the search results (KURAMOCHI, OVSAHO, SNU-119, COV362, OVCAR-4, COV318 and JHOS-4) (Barnes et al., 2020). These data raise concerns, because HGSOC is the commonest and deadliest ovarian cancer subtype yet studies on ovarian cancer seem to underuse HGSOC cell lines. Despite the absence of clinical data from the patient of cell line origin and the imbalance of usage, there is no shortage of *bona fide* HGSOC cell lines. Many of the cell lines determined to be highly likely or possibly of HGSOC origin harbour the characteristic mutations in *TP53* or *BRCA1/2* and amplifications of oncogenes such as *MYC* and *CCNE1*. Indeed, careful selection of HGSOC cell lines has led to insightful discoveries on the interplay between mechanisms of CIN and drug response (Tamura et al., 2020).

Additional cancer cell line models have been derived from mouse tissues. One commonly used mouse ovarian cancer cell line is ID8. Similar to the discordance of ovarian cancer cell lines with HGSOC genomics, ID8 cells were found to be devoid of HGSOC-characterizing mutations such as *Trp53*, *Brca1/2*, *Nf1* and *Rb1* mutations (Walton et al., 2016). Using CRISPR/Cas9 technology – which I will introduce in more detail in *1.5.7: CRISPR/Cas9 use in high-grade serous ovarian cancer models* – *Trp53*, *Brca1/2*, *Nf1* and *Pten* mutations were engineered thus generating ID8 subclones more representative of human HGSOC genetics (Walton et al., 2016; Walton et al., 2017). Additionally, *Trp53*-mutant mouse oviduct-derived fallopian tube carcinoma cells (OvidT 497, $Dicer^{-/-}$;$Pten^{-/-}$) were generated (Walton et al., 2017). Furthermore, ovarian cancer cell lines have been derived by explanting tumours that developed in transgenic mice. UKP10 cells were derived from a $Trp53^{fl/fl}$/$Kras^{G12D}$ double-transgenic ovarian tumour which was initiated by intra-bursal injection of Adeno-Cre (Scarlett et al., 2012). Similarly, tumours developed in mice expressing SV40 TAg under the Keratin 18 promoter's control and injected intra-bursally with Adeno-Cre to excise $Trp53^{fl/fl}$ and $Brca1^{fl/fl}$ were used to generate *in vitro* mouse ovarian cancer models (Szabova et al., 2014). This collection of mouse ovarian cancer cell lines reflects the genetic make-up of human HGSOC and to an extent the fallopian tube origin. Their utility will be discussed in more detail in *1.5.6: Allograft and Xenograft Models*.

1.5.3: Human *ex vivo* cancer cultures

As demonstrated in the previous section, a number of human and mouse ovarian cancer cell lines are available for the study of HGSOC. However, all of these cell lines

have been described more than two decades ago thus likely requiring extensive passaging to maintain stocks (Barnes et al., 2020). Most of these cancer cell lines also lack clinical annotation which limits their prognostic value in the pre-clinical setting. To complement the currently used *in vitro* cancer models, the National Cancer Institute (NCI) has initiated the Patient-Derived Models Repository (PDMR). Its aims are to overcome the limited number of models for some of the most aggressive and rarest cancer types, but also to increase the number of well-annotated models for the community. Sequential sampling aims to establish matched pre- and post-treatment samples and the unified molecular characterization of donated samples will allow for direct comparison between different samples of the same cancer type.

The HGSOC community has pioneered the development of novel, patient-derived model systems. The generation of the Ovarian Carcinoma Modified Ince medium (OCMI) has enabled the generation of primary ovarian tumour-derived *ex vivo* cultures from solid tumour and ascitic fluid samples (Ince et al., 2015; Nelson et al., 2020). The *ex vivo* cultures from both of these studies are clinically annotated, i.e., it is known whether donating patients have received therapy and whether the disease progressed. In addition, molecular genetic features have been shown to be consistent between the tumour of origin and the *ex vivo* culture. The exclusion of a potential *culture shock* means that these cells are the closest model system to a patient tumour available as they reflect heterogeneity in origin and genetic composition. Of note, attempts to maintain the same culture's cells in different media failed on most occasions, however, perhaps more importantly, led to selective pressures on the karyotypic composition of the culture that differed from the primary tumour (Ince et al., 2015).

The generation of additional HGSOC models thus overcomes some of the limitations of the available cell lines, such as the absence of definitive clinical annotation and treatment history, at the expense of the requirements for a specialized media and for access to human tumour samples.

1.5.4: Human and mouse organoids

In addition to the classic cancer cell line models which are grown in large quantities on tissue culture plastics in two dimensions, NCI's PDMR initiative has also announced the generation of complementary patient-derived cancer organoids. Organoids of normal tissue and cancer origin, in contrast to traditional cell lines, are grown in three dimensions in an artificial extracellular matrix (Matrigel) using a highly specialized growth medium that contains several growth stimulants such as R-spondin-1 and epidermal growth factor (EGF) and inhibitors of anti-growth molecules bone

morphogenic protein (BMP; noggin), transforming growth factor-β (TGFβ) and p38 (Tuveson and Clevers, 2019). This approach has, up to this point in time, led to the generation of human cancer organoid models of colorectal, breast, liver, gastric, bladder and lung cancer (Tuveson and Clevers, 2019). In addition, two independent collections of human ovarian cancer-derived organoids have also been described recently (Hoffmann et al., 2020; Kopper et al., 2019). These organoid models, in a similar manner to the *ex vivo* cultures described by Ince et al. (2015) and Nelson et al. (2020), faithfully recapitulate the genetic makeup of the primary tumours and can be cultured for multiple generations *ex vivo*. Likewise, their utility for drug screening and the generation of PDXs was described (Kopper et al., 2019).

The generation of patient-derived cancer organoids was preceded by experiments studying growth factor dependencies in mouse tissues and in a similar manner to these pioneering studies, normal fallopian tube-derived organoids had been described prior to ovarian cancer-derived organoids (Tuveson and Clevers, 2019). Studying the dependence of paracrine signalling for tissue homeostasis, a fallopian tube-derived organoid model system was described that allows long-term expansion of fallopian tube epithelial cells from adult stem cells (Kessler et al., 2015). As these cells are expanded *in vitro*, they retain differentiation capacity and form organoids that contain ciliated and non-ciliated, secretory epithelial cells. Additional fallopian tube-derived, normal organoids were described by Kopper et al. (2019), however, the normal organoids from this study were generated by mutating *TP53* using CRISPR/Cas9 prior to propagation. Lastly, fallopian tube-derived organoids have also been used to study growth factor dependence following suppression of the tumour suppressor genes *TP53*, *PTEN* and *RB1* mediated by RNA interference (RNAi) (Hoffmann et al., 2020).

A key advantage of patient-derived models, either cell lines or organoids, is that they represent the genetic heterogeneity of the human patient population as well as the genetic heterogeneity of human cancers (Tuveson and Clevers, 2019). In contrast, this notion makes it difficult to draw conclusions about specific genetic changes alone or in combination with multiple genetic perturbations as cancer genomes are complex. Therefore, organoids of mouse oviduct and ovarian surface origin have been engineered using either Cre-loxP or CRISPR/Cas9 technologies (Lohmussaar et al., 2020; Zhang et al., 2019). The study utilizing the Cre-loxP system generated transgenic mice by breeding and subsequently isolating stem cells from oviducts and ovaries prior to induction of Cre-recombinase by tetracycline. The Cre-recombinase was controlled in combination by tetracycline addition and the oviduct-specific promoter of *Pax8* and the epithelial adult stem cell promoter of *Lgr5* in the ovary. The organoids

described in this particular study express SV40 TAg and R172H-mutant Trp53 (Zhang et al., 2019). The other study, in contrast, employed CRISPR/Cas9-mediated gene editing and generated normal organoids from the oviducts and ovaries of Cas9-expressing mice prior to mutagenizing *Trp53*, *Brca1* and *Nf1* or *Pten* sequentially. Thus single-, double- and two different triple-mutant organoid lines of oviduct and ovary origin were made (Lohmussaar et al., 2020). Subsequently, more sophisticated mouse oviduct-derived organoids were developed which are all based on *Trp53*-deficient starting material either from *Trp53*$^{-/-}$ or *Trp53*$^{fl/fl}$ mice, whose organoids were subjected to ectopic Cre expression (Iyer et al., 2021; Zhang et al., 2021). Mutations in *Brca1* were introduced to model HRD driven disease either by breeding Trp53-deficient mice with *Brca1*$^{-/-}$ or *Brca1*$^{fl/fl}$ mice. Furthermore, mutations in other tumour suppressor genes such as *Pten* or *Nf1* were introduced using CRISPR/Cas9 and overexpression of oncogenes was achieved by ectopic expression of *Myc*, *Brd4*, *Smarca4*, G12V-mutant *Kras*, *Ccne1* and *Akt2*.

In conclusion, the organoid systems described in this section recapitulate many aspects of human HGSOC and satisfy the need for clinically well-annotated human model systems that reflect inter- and intrapatient genetic heterogeneity. In combination their utility lies in studying drug responses in isolation or in combination with commonly used therapeutics *in vitro* and *in vivo*, however, matched normal and tumour samples remain lacking.

1.5.5: Human immortalized fallopian tube cell lines

Prior to the *in vivo* works experimentally confirming a fallopian tube origin of HGSOC, human fallopian tube-derived cell lines had already been used to study the oncogenic requirements for transformation of human fallopian tube cells.

In these systems, cells were obtained from the distal fallopian tube where the non-ciliated, epithelial, secretory cell type is found and cultured *in vitro*. To achieve immortalization, the p53/RB1 pathways were inhibited either by expression of the SV40 TAg oncoprotein or knockdown of p53 in combination with the expression of human telomerase (*hTERT*) (Karst and Drapkin, 2012; Karst et al., 2011). Additional expression of oncogenes such as *CCNE1*, *KRAS*, *HRAS*, *YAP* or *MYC* and combinations thereof mimicked the genomic aberrations observed in HGSOC and led to malignant transformation (Hua et al., 2016; Karst et al., 2014; Karst et al., 2011). Independently, simultaneous transduction of fallopian tube cells with retroviral particles for the ectopic expression of dominant negative p53, *hTERT*, *MYC*, G12V-mutant *HRAS* and a *BRCA1*-suppression construct, revealed that multiple of these oncogenic,

ectopically expressed genes are required for sustained growth and ultimately transformation of cells (Jazaeri et al., 2011). These studies provided functional evidence supporting the notion that the fallopian tube, non-ciliated, secretory epithelium can give rise to HGSOC in humans. However, the two cell lines described above are limited in their utility, because the immortalization step requires suppression of p53.

This particular limitation was overcome in two other studies. Nakamura et al. (2018) achieved immortalization by ectopic overexpression of cyclin D1, R24C-mutant CDK4 and *hTERT*. In contrast to these triple-transgenic and the p53-suppressed cell lines mentioned above, FNE1 and FNE2 cells were immortalized using *hTERT* alone (Merritt et al., 2013). The successful immortalization in the absence of p53-suppression or promoters of cell cycle progression is due to the modified medium composition which is the same as the previously mentioned OCMI with the exception of reduced serum concentration.

Despite different modes of immortalization, the fallopian tube-derived, immortalized cell lines share that all of them are a cell population originally derived from PAX8 positive, non-ciliated, secretory epithelial cells. These cell lines are a facile model system that does not require access to primary tissues samples or GEMMs. A potential limitation of some of these cell lines is the requirement for a specialized culture media, however, additional requirements such as extracellular matrix are not given.

1.5.6: Allograft and xenograft models

As I alluded to GEMMs being a cornerstone of cancer research, mouse and human cancer cell lines that are readily transplantable in immune-proficient and -deficient mice are an important complimentary *in vivo* system. These transplantable models are expanded in vitro and can be implanted into mice in a variety of ways. For drug efficacy studies, tumour cell lines are most frequently implanted subcutaneously for facile tumour measurements using a calliper. To model HGSOC *in vivo*, however, two additional tumour cell delivery modes are employed: intraperitoneal and intrabursal inoculation (Hernandez et al., 2016). Both of these modes can be considered orthotopic, however, the injection of cells into the ovarian bursa is more restrictive as cells do not disseminate as readily in the peritoneal cavity as they would after intraperitoneal inoculation.

In addition to drug efficacy studies, tumourigenicity assays of novel, potentially transformed cell lines are performed by inoculation of mice with the cells of interest. The aforementioned, transgenic organoids were determined to be tumourigenic by implantation of cells into mice subcutaneously or intrabursally (Iyer et al., 2021;

Lohmussaar et al., 2020; Zhang et al., 2019; Zhang et al., 2021). Similarly, the ID8 and OvidT 497 cells, which were CRISPR/Cas9-engineered to better reflect the genomic aberration profile of HGSOC, were also subjected to tumourigenicity and drug efficacy studies (Walton et al., 2016; Walton et al., 2017). Strikingly, in both cases *Trp53* mutations led to a decrease in survival of mice inoculated with p53-deficient cells compared with control cells.

Moreover, the fallopian tube-derived immortalized and transformed cell lines mentioned above were also subjected to tumour formation assays by intraperitoneal and subcutaneous injection of cells into immune-deficient mice (Jazaeri et al., 2011; Karst et al., 2011; Merritt et al., 2013; Nakamura et al., 2018). Patient-derived organoids have also been shown to form tumours *in vivo* upon intrabursal inoculation (Kopper et al., 2019). Importantly, these organoid-derived xenograft tumours retain pathological features of their tumour of origin.

Lastly, PDXs are additional models that bridge the gap between patient-derived organoids as well as cell lines and *in vivo* models. These model systems, much like patient-derived *in vitro* systems, reflect the genetic inter- and intrapatient heterogeneity and are an indispensable tool in drug efficacy studies as the treatment histories of PDXs are typically known. For HGSOC a limited number of PDXs is available based on a variety of implantation modes and immune-deficient mouse strains used. Implantation of tumour cells after dissociation and depletion of immune cells into the mammary fat pad has been shown to yield tumour models that largely reflect the original tumour and its response to therapeutic intervention (Cybulska et al., 2018). Alternatively, intraperitoneal implantation of ascites samples from patients has also been described as a route to obtain PDXs that are congruent with their primary tumour (Liu et al., 2017).

Thus, human and mouse implantation models of cancer are useful to test therapeutic vulnerabilities and tumourigenic potential of genome-edited cells. While allograft and xenograft models are less resource intensive than GEMMs, their use remains less resourceful than experiments performed *in vitro*.

1.5.7: CRISPR/Cas9 use in high-grade serous ovarian cancer models

CRISPR (clustered regularly interspaced short palindromic repeats)/Cas9 (CRISPR-associated protein 9) technology has been developed on the basis of a prokaryotic immune defence mechanism (Adli, 2018). After its detailed study as well as description following successful generation of DNA double-strand breaks and mutations in a human cell line transfected with CRISPR/Cas9 constructs, it was quickly adopted for

eukaryotic gene-editing (Cong et al., 2013). Its superiority over previously described gene-editing tools, e.g., meganucleases, zinc finger nucleases and TALENs, lies in its versatility. Mutating a specific locus using CRISPR/Cas9 only involves the identification of a suitable target sequence; for the most commonly used SpCas9 protein (of *Streptococcus pyogenes* origin), this requires an NGG motif followed by 20 base-pairs. This motif and the 20 base-pair sequence together form the site-specific part of a synthetic RNA which guides Cas9 to its target, this RNA is known as single guide RNA (gRNA) (Adli, 2018). Since the description of gene-editing in human cells by Cong et al. (2013), a plethora of CRISPR/Cas9 tools and reagents has become available commercially and publicly. Many of these reagents are available as bacterial plasmids, lenti-, retro- or adenoviruses and Cas9/gRNA ribonucleoprotein complexes that are assembled *in vitro* and subsequently transfected into cells.

CRISPR/Cas9 has been employed extensively in cancer research and beyond. In sections *1.5.2: Human and mouse cancer cell lines* and *1.5.4: Human and mouse organoids*, I have already alluded to the generation of improved human and mouse HGSOC cancer models. Indeed, the use of CRISPR/Cas9 has enabled the generation of cell lines and organoids that, as a result of gene-editing, reflect the genetic landscape of human HGSOC better. The introduced mutations, specifically in *Trp53* and *Brca1*/2, were subsequently validated using pharmacological approaches. Loss of Brca1/2 has been established as synthetically lethal in combination with the inhibition of PARP proteins and as expected the newly generated Brca1/2-deficient ID8 models are PARPi sensitive (Bryant et al., 2005; Farmer et al., 2005; Walton et al., 2016; Walton et al., 2017). Similarly, the negative regulator of p53, MDM2, can be inhibited pharmacologically using Nutlin-3 which results in the abrogation of p53-degredation thus stabilizing p53 levels (Vassilev et al., 2004). Upon *Trp53*-mutagenesis in ID8 and OvidT 497 cell lines, survival in the presence of Nutlin-3 was increased compared with control cells (Walton et al., 2016; Walton et al., 2017). This synthetic viable relationship of p53-deficient cells in the presence of Nutlin-3 is also employed for the expansion of normal and BRCA1-deficient fallopian tube-derived organoids following CRISPR/Cas9-mediated mutagenesis of *TP53* (Kopper et al., 2019). Furthermore, gene-editing by CRISPR/Cas9 has also been employed to study oncogene dependency in HGSOC. As mentioned previously HGSOC displays the highest frequency of *MYC* amplifications, thus making MYC an attractive therapeutic target which was validated by mutagenizing *MYC* using CRISPR/Cas9 to show that a decrease in MYC protein levels correlates with growth suppression (Zeng et al., 2018).

In conclusion, CRISPR/Cas9-mediated gene editing is a well-established and widely used tool for the improvement of existing human and mouse models, the generation of novel patient-derived models and the validation of oncogene dependency in HGSOC.

1.6: Studies of chromosomal instability in high-grade serous ovarian cancer

As first introduced in *1.1: Overview* and alluded to in subsequent sections, HGSOC is one of the most chromosomally unstable cancer entities based on *in silico* analyses of cancer genomes (Ciriello et al., 2013; Shukla et al., 2020; Taylor et al., 2018). Yet, despite the pertinence of CIN for HGSOC, studies of chromosome segregation fidelity in HGSOC GEMMs, cell lines and organoids are limited.

Only recently, it was shown that chromosome mis-segregation events occur in HGSOC *ex vivo* cultures at frequencies higher than would have been expected from previous studies using alternative model systems (Nelson et al., 2020). Using live-cell fluorescence imaging of patient-derived cell lines, a number of mitotic aberrations was observed in cells grown in two as well as in three dimensions. These mitotic aberrations were also shown to manifest on the genomic level as whole chromosome and chromosome arm aneuploidies by shallow whole genome sequencing of single cells (scWGS). Additionally, in some cases, structural rearrangements and focal amplifications of genomic regions were observed. Taken together these data provide functional evidence backing up the *in silico* analyses of HGSOC samples and illustrate the extensive karyotypic diversity observed as a consequence of CIN in HGSOC. From a mechanistic point of view, the causes underlying CIN in HGSOC have also recently been investigated in a number of *bona fide* HGSOC cell lines. First, it was shown that HGSOC cell lines display evidence of both DNA replication stress and abnormal microtubule assembly rates which are two well-established causes of CIN (Tamura et al., 2020). Second, it was illustrated that a better understanding of CIN in HGSOC has important implications for therapeutic interventions. HGSOC cell lines displaying high microtubule assembly rates were less sensitive to the standard of care chemotherapeutic paclitaxel. This clearly demonstrates that a better understanding of on-going cell biological processes in cancer cells has the potential to impact outcomes for patients.

Together with the computational works, the above-mentioned studies have laid the foundation for a better understanding of CIN in HGSOC. The number of available models and molecular cell biology tools, such as CRISPR/Cas9, should facilitate more detailed investigations into the causes of CIN in HGSOC specifically.

1.7: Rationale and aims

As alluded to in the previous sections, multiple causes of CIN have been described in insightful studies using colorectal cancer cell lines, RPE-1 cells and most recently also HGSOC cell lines. However, our understanding of CIN, the absence of mutations in genes controlling mitosis and DNA replication and the impact of HGSOC-defining mutations on chromosomal stability in fallopian tube-derived cells remains limited. Important, emerging evidence suggests that tissue specificity in chromosome segregation needs to be taken into consideration as organoids generated from colon and small intestine cells of the same transgenic mouse mis-segregate chromosomes at different rates (Hoevenaar et al., 2020). Similarly, a study dissecting p53 signalling in mice revealed differing p53 responses across tissues following irradiation (Stewart-Ornstein et al., 2021). Indeed, a better understanding of p53's role in normal fallopian tube cells has been set out as a critically important aspect of study for the HGSOC community (Bowtell et al., 2015). So, to further our understanding of CIN, p53 and BRCA1 perturbations as well as MYC amplification and overexpression in HGSOC genesis in a physiologically relevant setting, I decided to use a non-transformed model as a starting point to minimize the potential contribution of other genetic aberrations. Therefore, I set out to:

(i) Determine if FNE1 cells are a suitable baseline model.
(ii) Generate novel model systems reflecting the HRD-dependent arm of HGSOC genesis.
(iii) Assess CIN in novel model systems using orthogonal approaches.
(iv) Delineate phenotypic changes upon introduction of genetic modifications.
(v) Assess the tumourigenic potential of the novel models *in vivo*.

Despite the ubiquitous presence of *TP53* mutations in HGSOC samples, genetically defined, matched p53-proficient and -deficient models are currently lacking. Likewise, models to determine BRCA1's role in HRD-driven HGSOC genesis are scarce. Due to the potential tissue specificity alluded to above, a panel of isogenic cell lines filling that gap has the potential to uncover previously unappreciated dysregulation of cellular physiology upon p53- and BRCA1-loss as well as MYC overexpression in a setting relevant to HGSOC.

While RPE-1 cells have been shown to display an increase in aneuploidy after p53-suppression or knockout, potential causative mechanisms remained elusive (Kok et al., 2020; Soto et al., 2017). Thus, the work done as part of this thesis has the potential to provide novel insight into the cellular processes controlling diploidy in p53- and BRCA1-proficient cells in the absence of MYC activation. Moreover, potential

discoveries can have important implications beyond HGSOC as *TP53* mutations and CIN are both increased in metastatic compared with primary tumours (Priestley et al., 2019; Shukla et al., 2020).

The generation of genetically well characterized model cell lines that are amenable to CRISPR/Cas9-mediated genome engineering will be of utility for further studies. Novel genes implicated in HGSOC or mechanisms pertinent to it could thus be probed easily. Many studies rely on the use of mice for *in vivo* validation of potential drug candidates or the assessment of metastatic potential, therefore, evaluating the newly generated subclones' tumourigenic potential might provide additional, transplantable xenograft models.

Lastly, direct comparison between normal and mutagenized subclones might reveal therapeutic targets for HGSOC. As such, genes that are exclusively highly expressed in, for instance, mutant cells could be targeted sparing normal cells. Therefore, the transcriptomics dataset generated as part of this thesis might ultimately be of utility for drug discovery purposes capitalizing on fundamental cell biological research for patient benefit.

Chapter 2: Materials and Methods

2.1: Cell biology

2.1.1: Cell culture

FNE1 cells were obtained from Dr Tan A. Ince and cultured in WIT-Fo (FOMI) at 5% O_2 and 5% CO_2 in a humidified environment at 37°C as described previously (Merritt et al., 2013). Briefly, FOMI is a specialised media formulation established for the culture of FNE1 cells and was prepared in-house; it was supplemented with 1% foetal bovine serum (FBS; Thermo Fisher Scientific, MA) and 100 U mL^{-1} penicillin and 100 U mL^{-1} streptomycin (both from Thermo Fisher Scientific, MA). AAV293T cells were obtained from American type culture collection (Agilent Technologies, CA) and cultured in Dulbecco's modified eagle media (DMEM; Thermo Fisher Scientific, MA). OVCAR8 cells were a kind gift from Dr Christina Annunziata and were cultured in Roswell Park Memorial Institute 1640 media (RPMI; Thermo Fisher Scientific, MA). DMEM and RPMI were supplemented with 10% FBS and 100 U mL^{-1} penicillin and 100 U mL^{-1} streptomycin and cells were cultured at atmospheric O_2 and 5% CO_2 in a humidified environment at 37°C. All cell lines were authenticated by short tandem repeat (STR) profiling using the Powerplex 21 System (Promega, WI) and regularly tested negative for Mycoplasma either by inhouse polymerase chain reaction (PCR; both performed by CRUK Manchester Institute Molecular Biology Core Facility) or the MycoAlert™ Mycoplasma Detection Kit (Lonza, Switzerland; performed by Animal Molecular Diagnostics Laboratory at NCI Frederick). Cells were sub-cultured when near-confluent by washing with 1X phosphate-buffered saline (PBS), incubating with 0.05% trypsin (both from Thermo Fisher Scientific, MA) for up to one minute and quenching with 10% FBS in DMEM. FNE1 cells were seeded at a density of at least 10^4 cells cm^{-2} growth area and maintained in Primaria™ T25 or T75 cell culture flasks (Corning, NY).

2.1.2: Drug treatments

Nutlin-3, GSK923295 (CENP-Ei) and Olaparib were dissolved in dimethyl sulfoxide (DMSO). Cisplatin was dissolved in 0.9% sodium chloride (Sigma Aldrich, MO). Colcemid and tetracycline were dissolved in water. All drugs were diluted in growth media prior to commencing experiments. Source, stock and working concentrations are in indicated in Table 2.1.

Drug	Source	Stock	Final
CENP-Ei	Bennett et al. (2015)	10 mM	250 nM, unless stated otherwise
Cisplatin	Sigma Aldrich, MO	10 mM	10 µM
Colcemid	Roche, Switzerland	10 µg mL^{-1}	100 ng mL^{-1}
Nutlin-3	Sigma Aldrich, MO	10 mM	10 µM
Olaparib	Selleckchem, TX	10 mM	As stated
Tetracycline	Sigma Aldrich, MO	1 mg mL^{-1}	15 µg mL^{-1}, unless stated otherwise

Table 2.1: Drugs used in tissue culture experiments.

Component	Quantity	Source
Lentivirus of interest	375 ng	This work
psPAX2	500 ng	Gift from Dr Didier Trono via Addgene
pMD2.G	125 ng	
2M $CaCl_2$	30 µL	Part of transfection kit
2X HBS	30 µL	
10% FBS (HyClone) DMEM	400 µL	

Table 2.2: Transfection media for the generation of lentiviral supernatant.

2.1.3: Lentivirus production

All lentiviruses were produced by co-transfection of AAV293T cells with recombinant DNA using the ProFection Mammalian Transfection System (Promega, WI) according to manufacturer instructions. Briefly, AAV293T cells were seeded into a 24 well microtiter plate (Corning, NY) at a concentration of 5 x 10^4 cells $well^{-1}$ on day 1. On day 3, growth medium was replaced one hour prior to transfection. Transfection medium (Table 2.2) containing lentivirus of interest and lentiviral packaging plasmid recombinant DNA was made up in 1M $CaCl_2$ in HEPES-buffered saline (HBS), mixed vigorously and incubated at room temperature for 20 minutes. Subsequently, fresh DMEM supplemented with 10% FBS (specifically HyClone™ FBS; Cytiva, MA) but omitting penicillin and streptomycin was added and growth media was replaced with 450 µL transfection media. On day 4, transfection media was removed, cells were washed

thrice with DMEM supplemented with 10% FBS and harvesting media (DMEM supplemented with 30% regular FBS) was added. Lentivirus was harvested in supernatant on days 5 and 6, 48 hours and 60 hours after initial transfection, respectively. Supernatant containing lentivirus was centrifuged, sterilised with a 0.45 µm syringe-driven filter and frozen for storage at -80°C.

2.1.4: Lentiviral transduction

All lentiviral transductions of FNE1 cells were performed in the same manner using lentiviruses either available commercially, in the laboratory or generated as part of this work (details in "Molecular Biology", Table 2.3).

Lentivirus	Source
Edit-R Inducible Lentiviral Cas9 Particles	GE Healthcare Dharmacon, CO
lentiGuide g*BRCA1* exon 10 1 Neo	This thesis
lentiGuide g*BRCA1* exon 10 2 Neo	This thesis
lentiGuide g*BRCA1* exon 10 3 Neo	This thesis
lentiGuide g*BRCA1* exon 10 4 Neo	This thesis
lentiGuide g*BRCA1* exon 2 Neo	This thesis
lentiGuide g*BRCA1* exon 3 Neo	This thesis
lentiGuide g*TP53* Puro	Generated by Dr Paul Minshall
pLenti CMV Hygro *MYC*	This thesis
pLenti CMV Hyrgo DEST	Campeau et al. (2009)
pLVX mCherry-H2B Puro	Generated by Dr Anthony Tighe

Table 2.3: All lentiviruses used for the generation and analysis of FNE1 subclones and their source.

On day 1, 6 x 10^4 cells $well^{-1}$ were seeded into Primaria™ 24 well microtiter plates (Corning, NY) and left to adhere overnight. On day 2, transduction media was prepared by combining commercially available lentiviral particles, aiming for a multiplicity of infection of 0.3, 0.5 and 0.7, or increasing amounts of in-house produced lentivirus containing supernatant (12.5%, 25%, 50%, 100%) with standard FOMI media. Polybrene (Sigma Aldrich, MO) was added to transduction media at a final concentration of 4 µg mL^{-1}. Transduction media (1 mL) was added to each well and microtiter

plates were subsequently centrifuged at 300 rounds minute^{-1} (RPM) at 30°C for 2.5 hours. For each condition at least two wells were transduced with lentivirus and two wells were exposed to DMEM supplemented with 10% FBS and 4 µg mL^{-1} polybrene only as "mock transduction" which later served as negative control for antibiotic selection of transduced cells. Lastly, on day 3, transduced cells were passaged using PBS, 0.05% trypsin and DMEM supplemented with 10% FBS as described before and seeded into two wells of a Primaria™ 6 well microtiter plate (Corning, NY). Once cells adhered to the growth surface, circa six hours after seeding, selection antibiotic was added. Cells were then expanded as confluence was reached. Details about the generation of lentiviral recombinant DNA are described in *2.4: Molecular biology* and details about the generation of clonal and polyclonal FNE1 subclones are described in the following section.

2.1.5: Generation of CRISPR/Cas9 mutagenized FNE1 subclones

Target gene (exon)	gRNA sequence (5' – 3')	Source
TP53 (2)	AATGTTTCCTGACTCAGAGG	Simoes-Sousa et al. (2018)
BRCA1 (2)	AAATCTTAGAGTGTCCCATC	This thesis
BRCA1 (3)	TGCTAGTCTGGAGTTGATCA	
BRCA1 (10)	GTTTCAGATGATGAAGAAAG	
BRCA1 (10)	AGATGATGAAGAAAGAGGAA	
BRCA1 (10)	GATGATGAAGAAAGAGGAAC	
BRCA1 (10)	TGAAGAAAGAGGAACGGGCT	

Table 2.4: gRNAs used for CRISPR/Cas9 gene editing and their sources.

Cas9 expressing FNE1 cells (FNE1 TO Cas9) were generated by transduction with Edit-R Inducible Lentiviral Cas9 particles followed by selection with blasticidin S (Melford Laboratories, UK) at 8 µg mL^{-1} until all control cells were eliminated under the same selection conditions. Cas9 expression was assessed by titrating tetracycline and measuring Cas9 protein expression by immunoblot (more detail in "Biochemistry"). Ultimately, Cas9 was induced using 15 µg mL^{-1} in subsequent experiments.

To mutate *TP53*, FNE1 TO Cas9 cells were transduced with lentiGuide g*TP53* Puro (the backbone was a kind gift from Dr. Feng Zhang (Sanjana et al., 2014)) containing a gRNA targeting *TP53* (g*TP53*; Table 2.4) and selected with puromycin (Sigma

Aldrich, MO) at 0.7 µg mL^{-1}. As before puromycin selection was continued until all control cells were eliminated. Once selection was complete, Cas9 was induced for five days and cells were then either single cell cloned by limiting dilution or selected for a further five days with Nutlin-3 and then single cell cloned by limiting dilution. Initially, cells were seeded into Primaria™ 96-well microtiter (Corning, NY) plates by limiting dilution and as cells became confluent expanded to Primaria™ 24-well microtiter then Primaria™ 6-well microtiter plates and ultimately into Primaria™ T25 and T75 tissue culture flasks. Putative p53-deficient clones were screened for the absence of full-length p53 by immunoblot as described in *2.3: Biochemistry*.

To mutate *BRCA1*, P1 cells were taken forward. P1 cells were transduced simultaneously with six different lentiGuide g*BRCA1* Neo lentiviruses each containing a unique gRNA targeting *BRCA1* (Table 2.4). After neomycin (Sigma Aldrich, MO) selection at 0.8 mg mL^{-1}, Cas9 was induced as before and cells were single cell cloned by limiting dilution and expanded as described above. All screening of clones was performed by immunoblotting for the absence of full-length BRCA1.

Functional deficiency of p53 and BRCA1 was confirmed by exploiting the known synthetic viable and synthetic lethal relationships with Nutlin-3 and Olaparib treatment in putative clones, respectively. Details about live cell imaging employed for functional validation of p53-deficiency are outlined in *2.2: Microscopy* and experiments using viability measurements in response to Olaparib are described in *2.1.8: Colony formation and viability assays*.

Mutations in *TP53* and *BRCA1* were assessed in the RNA sequencing dataset using Integrative Genomics Viewer (IGV, Version 2.8.0 (Robinson et al., 2011)) and annotated according to standard practices (Ogino et al., 2007). *BRCA1* mutations in PB1 and PB2 cells were also confirmed by Sanger sequencing as detailed in *2.4: Molecular biology*.

2.1.6: Generation of *MYC*-overexpressing FNE1 subclones

MYC-overexpressing and cognate “empty vector” (EV) control cells were generated by transduction of P1, P2, P3, PB1, PB2 and PB3 cells with pLenti CMV Hygro DEST (a kind gift from Drs. Eric Campeau and Paul Kaufman (Campeau et al., 2009)) or pLenti CMV Hygro MYC lentiviruses and selection with hygromycin B (Sigma Aldrich, MO) at 25 µg ml^{-1} maintaining a polyclonal cell population. Immunoblotting and RNAseq were employed to confirm functionality of *MYC* overexpression as detailed in *2.3: Biochemistry* and *2.4: Molecular biology*, respectively.

2.1.7: Generation of mCherry-H2B expressing FNE1 subclones

FNE1, P1 and P3 cells were additionally transduced as before with the pLVX mCherry-H2B Puro lentivirus to generate cells expressing mCherry-tagged histone H2B to enable more precise cell number measurements by live cell microscopy (details below). However, only FNE1 cells could be selected with puromycin as P1 and P3 cells harboured lentiGuide g*TP53* Puro rendering those resistant to puromycin, thus, P1 and P3 cells were enriched by fluorescence activated cell sorting (FACS) and expanded. Briefly, cells were harvested by trypsinisation as described previously and kept on wet ice in PBS supplemented with 0.1% of bovine serum albumin (BSA; Sigma Aldrich, MO). Sorting was performed on a BD FACSAria™ Fusion Cell Sorter (BD Biosciences, CA) using untransduced FNE1 cells as negative control. Dead cells and cell debris were excluded based on forward and side scatters. Negative gating of untransduced FNE1 cells allowed for the selection of mCherry-H2B positive cells. Cells were subsequently maintained as a polyclonal population and prior to experimentation confirmed to express mCherry-H2B by flow cytometry of live cells. These analyses were performed on the Attune NxT Flow Cytometer (Thermo Fisher Scientific, MA) comparing the fraction of mCherry positive cells with mCherry negative. Again, FNE1 cells served as a negative control.

2.1.8: Colony formation and viability assays

For colony formation assays, 2 x 10^3 cells were seeded into Primaria™ 6 well microtiter plates and left to adhere overnight. Treatments commenced the next day with CENP-Ei (Table 2.1) and were continued for twelve days. Drugs were washed out at indicated timepoints and media was replenished every three to four days. After the assay concluded, cells were washed once with PBS and fixed with 1% paraformaldehyde (Biotium, CA) in PBS for ten minutes. Cells were then stained with crystal violet solution (0.05% weight/volume; Sigma Aldrich, MO) for 20 minutes. Stained microtiter plates were washed with water until clear and allowed to air-dry. For viability assays, 100 cells were seeded into Primaria™ 96 well microtiter plates. Olaparib was added immediately prior to cells adhering to the growth surface. Media containing Olaparib was replenished every three days and the assay concluded after seven days.

Since FNE1 cells do not form colonies but grow as a cell lawn, colony formation was quantified by extraction of crystal violet using 10% acetic acid (volume/volume). After extraction of crystal violet, absorbance was measured at 595 nm on a SpectraMax M2 (Molecular Devices, CA) operated using SoftMax® Pro software (Molecular Devices, CA). Viability was reported as fraction of DMSO treated cells.

Viability after Olaparib treatment was measured by adding 30 µL of CellTiter-Blue (Promega, NY) reagent to wells on the final day. Fluorescence (excitation 555 nm, emission 585 nm) was measured on a SpectraMax M2 plate reader as above and viability was reported as a fraction of DMSO treated cells.

2.1.9: DNA content measurements by flow cytometry

Cells were seeded at ≥10^4 cells cm^{-2} growth area in either Primaria™ T25 or T75 tissue culture flasks, treated when experimentally required, but otherwise maintained and harvested as normal. After harvesting, cells were washed once with PBS containing 1% BSA (weight/volume; henceforth PBS-B), fixed in 70% ethanol in PBS and stored at -20°C for at least one night. Prior to staining, cells were washed thrice with PBS-B, counted and stained in 500 µL staining solution 10^{-6} cells. Staining solution was either PBS containing 40 µg mL^{-1} propidium iodide (Sigma Aldrich, MO) and 50 µg mL^{-1} RNase H (Thermo Fisher Scientific, MA) or 1 µg mL^{-1} 4',6-diamidino-2-phenylindole (DAPI; Sigma Aldrich, MO). Analyses of DNA content were either performed using FlowJo™ 10 (BD Biosciences, CA) or ModFit LT™ (Verity, ME) software.

2.2: Microscopy

2.2.1: Immunofluorescence

3 x 10^4 cells were seeded onto collagen coated 19 mm coverslips (VWR International, PA) and allowed to adhere overnight. Following treatment, if applicable, cells were washed with PBS twice and fixed using 1% Paraformaldehyde in PBS for five minutes. After fixation, coverslips were washed thrice with PBS, quenched with glycine diluted in PBS for five minutes and permeabilized with 0.1% Triton-X-100 in PBS (PBS-T). The primary antibody against p53 (mouse, clone DO-1, Santa Cruz, CA) was diluted 1:500 in PBS-T and staining was performed for 30 minutes. After two washes with PBS-T, staining with the secondary antibody against mouse (goat, polyclonal Cy5-conjugated, Jackson ImmunoResearch Laboratories Inc., PA) diluted at 1:500 in PBS-T was performed for 30 minutes. Cells were then stained with either DAPI or Hoechst (both at 1 µg mL^{-1}; both from Sigma Aldrich, MO) after two washes with PBS-T for two minutes to visualize DNA. All procedures were performed at room temperature unless indicated otherwise. Coverslips were washed twice with PBS-T, left to air-dry and mounted onto microscopy slides (90% glycerol, 20 mM Tris, pH 9.2). Microtiter plates were washed twice with PBS-T and left to air-dry, too. Slides were stored at -20°C and microtiter plates at room temperature prior to image acquisition.

Slides were imaged on an Axioskop2 (Zeiss Inc., Germany) microscope fitted with a CoolSNAP HQ camera (Photometrics, AZ) operated by MetaMorph (Molecular Devices, CA) software and image analysis was performed with Photoshop® CC 2015 (Adobe Systems Inc., CA).

2.2.2: Fluorescence *in situ* hybridization

Cells were harvested by trypsinisation, quenched with media as described and centrifuged to obtain a pellet. The pellet was dispersed carefully with hypotonic buffer (0.075M KCl) in which cells were incubated for 30 minutes at 37°C. Afterwards, cells were fixed and washed thrice with methanol/acetic acid (3:1) being spun between washes and stored at -20°C. Prior to dropping cells onto slides, cells were washed thrice with methanol/acetic acid and dropping of slides was done under environmentally controlled humidity. Slides were aged at 37°C for at least ten days and used within 21 days.

For the hybridisation of the first panel, slides were pre-treated in an acid bath (0.1 M HCl) with pepsin for one to five minutes, subsequently washed thrice in PBS, dehydrated in an ethanol series for five minutes each (70%, 90%, 100%) and air-dried. Once dried, denaturation of DNA was performed with 70% deionized formamide/2X saline-sodium citrate (SSC) solution at 73°C under a 24 mm x 60 mm coverslip (VWR International, PA) on a ThermoBrite system (Abbott Molecular Inc., IL). Slides were incubated for up to 30 seconds and then dehydrated in an ice-cold ethanol series for three minutes each (70%, 90%, 100%) and airdried.

Colour	Panel 1		Panel 2		Panel 3		Panel 4	
Aqua	*MYC*	1.5 µL	*ZNF217*	2 µL	*CCNE1*	2 µL	*CDKN2A*	2 µL
Far red	*DBC2*	1.5 µL	*PIK3CA*	2 µL	*CCP10*	0.5 µL	*HER2*	2 µL
Gold	*KRAS*	1 µL	*TP53*	1 µL	*SMAD4*	1 µL	*NF2*	1 µL
Green	*RB1*	1 µL	*NF1*	1.5 µL	*CCND1*	1 µL	*CDH1*	1.5 µL
Red	*COX2*	1 µL	*CCNB1*	1.5 µL	*FBXW7*	1 µL	*PTEN*	1.5 µL

Table 2.5: Assembly of fluorescently labelled DNA probes for miFISH experiments.

Custom DNA probes were obtained from Cytotest (MD) and assembled into four panels in indicated quantities (Table 2.5) to enumerate 19 gene loci and one centromere on 16 chromosomes. Panel mixes containing five different probes were made up in 10-20 µL and stored at -20°C, before each use the panel mix was denatured at 73°C

for five minutes and pre-annealed at 37°C for one hour under shaking at 350 RPM. Once panel mixes were pre-annealed, 2 µL were added to the denatured slides, covered with a 13 mm coverslip (VWR International, PA), which was fixed in place with rubber cement (MP Biomedicals™ Fixogum, OH), and incubated in a humid hybridization chamber at 37°C overnight. The next day, the rubber cement and coverslip were removed carefully and the slide washed twice in 2X SSC and once in PBS for two minutes each. Then, cells were stained in 5 µg mL^{-1} DAPI in PBS for one minute, washed thrice in 2X SSC for two minutes each and dehydrated in an ethanol series (70%, 90%, 100%) for two minutes each and airdried. A 24 mm x 60 mm coverslip was mounted using Vectashield® Antifade Mounting Medium (Vector Laboratories Inc., CA).

For hybridisations of subsequent panels, probes were denatured the same way as described above, but slides were treated differently. The large coverslip and mounting media were removed gently in 2X SSC and slides were washed thrice in 2X SCC for two minutes each. Then DNA was denatured in 70% deionized formamide / 2X SSC at 80°C for ten seconds, immediately dehydrated in an ice-cold ethanol series (70%, 90%, 100%) and air-dried. Once dry, pre-annealed probes were added and the slide treated as described before for the first panel's hybridisation.

Images were acquired on an automated microscope system consisting of a BX63 microscope equipped with a 40X oil immersion objective (both Olympus, Japan), custom optical filters (Chroma, VT) and a motorized stage BioView (Israel). The custom image acquisition and analysis system was from BioView (Israel).

2.2.3: Live cell imaging

5 x 10^3 or 3 x 10^4 cells were seeded either into Primaria™ 96 or 24 well microtiter plates, respectively, and left to adhere overnight. Drugs were added at indicated concentrations the following day and plates were moved onto an IncuCyte® ZOOM time-lapse microscope operated by IncuCyte® ZOOM custom software (both from Essen BioScience, Germany) and housed in a low oxygen (5% O_2, 5% CO_2) incubator. Filming commenced immediately and images were acquired every ten minutes for cell fate profiling experiments or every one to four hours for proliferation experiments for a duration of up to four days. Images were analysed with IncuCyte® ZOOM custom software and Excel.

2.3: Biochemistry

2.3.1: SDS-Page

Component	Resolving			Stacking
	8%	10%	12%	
Deionized H_2O	7.1 mL	6.1 mL	5.1 mL	5.7 mL
1.5M Tris (pH 8.8)	3.75 mL			0 mL
0.5M Tris (pH 6.8)	0 mL			2.5 mL
Acrylamide (30%)	4 mL	5 mL	6 mL	1.7 mL
SDS (10%, volume/volume)	150 µL			100 µL
APS (10%, volume/volume)	150 µL			100 µL
TEMED	15 µL			10 µL

Table 2.6: Composition of acrylamide gels for SDS-PAGE.

Prior to loading onto gels, cells were lysed in sample buffer (0.35 M Tris pH 6.8, 0.1 g ml^{-1} sodium dodecyl sulphate (SDS), 93 mg ml^{-1} dithiothreitol, 30% glycerol, 50 mg ml^{-1} bromophenol blue) and boiled for five minutes. To resolve and subsequently blot for Cas9 8% acrylamide gels were used, for p53 and MYC 10% acrylamide gels and for p21 and BCL-XL 12% acrylamide gels were used (Table 2.6). To resolve BRCA1, a NuPAGE™ 3-8% Tris-Acetate gradient gel (Thermo Fisher Scientific, MA) was used. Acrylamide gels were run in 1X running buffer (25 mM Tris, 200 mM of glycine, 0.1% (weight/volume) SDS) and gradient gels were run in NuPAGE™ Tris-Acetate SDS running buffer (Thermo Fisher Scientific, MA). Acrylamide gels were initially run at 80 V for 40 minutes and then at 120 V for another 2 hours whereas gradient gels were run at 120 V for 2 hours. All gels were run on a Hoefer™ SE260 small format electrophoresis system (Hoefer, MA). Precision Plus Protein™ Dual Colour Standard (BioRad Laboratories, CA) was used to control for molecular weight.

2.3.2: Immunoblotting

Resolved protein was electroblotted by wet transfer onto methanol-activated Immobilion-P membranes (Millipore, MA) in 1X transfer buffer (25 mM Tris, 190 mM glycine, 0.1% SDS (wight/volume), 20% methanol) at 50 V for one hour using a Mini-PROTEAN® Tetra System (BioRad Laboratories, CA). Membranes were blocked in

5% milk (Marvel, UK) dissolved in TBS-T (50 mM Tris pH 7.6, 150 mM NaCl, 0.1% Tween-20) for 30 minutes. Subsequently, membranes were incubated with primary antibodies at indicated concentrations (Table 2.7) overnight at 4°C. Membranes were then washed thrice with TBS-T for ten minutes prior to incubation with secondary antibodies for 2 hours. Secondary antibodies were horseradish-peroxidase-conjugated and also diluted in 5% milk. Prior to detection, membranes were washed thrice in TBS-T. Detection was performed using EZ-ECL Chemiluminescence Substrate (Biological Industries, CT) or Luminata™ Forte Western HRP Substrate (Millipore, MA). Membranes were imaged after detection on a Biospectrum 500 (UVP) imaging system operated using VisionWorks LS (Labortechnik, Germany) software. Images were analysed and annotated with Photoshop® CC 2015 (Adobe Systems Inc., CA).

Target	Host	Clone	Source	Dilution
Primary antibodies				
BCL-XL	Rabbit	Polyclonal	Cell Signaling, MA	1:1,000
BRCA1	Mouse	MS110	Millipore, MA	1:100
Cas9	Mouse	7A9	Millipore, MA	1:1,000
MYC	Rabbit	Y69	Abcam	1:3,500
p21	Mouse	F-5	Santa Cruz, CA	1:100
p53	Mouse	DO-1	Santa Cruz, CA	1:1,000
TAO1	Sheep	Polyclonal	Westhorpe et al. (2010)	1:1,500
Secondary antibodies				
Mouse	Goat	Polyclonal	Thermo Fisher Scientific, MA	1:2,000
Rabbit	Goat			
Sheep	Rabbit			

Table 2.7: Primary and secondary antibodies used for immunoblotting.

2.4: Molecular biology

2.4.1: Restriction digest

DNA was digested with indicated restriction enzymes typically for at least one hour at 37°C for analytical restriction digests to confirm plasmid identity or successful cloning. For cloning reactions, restriction digests were performed overnight at 37°C. Reactions were set up as outlined in Table 2.8.

	Analytical	**Cloning**
Recombinant DNA	1 µL	1 µg
Restriction enzyme(s)	0.1 µL each	0.5 µL each
10X Reaction buffer	1 µL	5 µL
Deionized H_2O	7.9 µL	Up to 50 µL

Table 2.8: Composition of restriction digests for analytical and cloning purposes.

2.4.2: Gel electrophoresis

Two kinds of gel electrophoresis were performed; one for analytical purposes which used regular agarose and one for cloning purposes which used Microsieve LM agarose (both from Meridian Bioscience, OH). Either agarose was dissolved at an appropriate concentration to resolve DNA fragments of interest in TBE buffer (88 mM Tris, 88 nM Boric acid, 2 mM EDTA, pH 8.2). Samples were loaded onto agarose gels with 5X loading dye (50% glycerol, 10% bromophenol blue, 10% xylene blue) and gels run in TBE buffer at varying voltages and durations as appropriate for fragment size on Bio-Rad Minisub® CELL GT (Bio-Rad, CA). To visualize DNA, gels were stained with ethidium bromide (Sigma Aldrich, MO), washed thrice with water and exposed to UV light.

2.4.3: In-gel ligation

To ligate fragments of interest following digestion and isolation from agarose gels, agarose slices were melted at 70°C for 10 minutes with intermittent mixing. In a total volume of 8 µL the digested vector and insert were combined at a ratio of 7:1 adding 1 µL 10X T4 ligation buffer (New England BioLabs Inc., MA). The mixture was moved onto wet ice and 1 µL T4 ligase (400 units; New England Biolabs Inc., MA) was added. After 2 hours of incubation at room temperature the reaction was stopped by adding 40 µL of deionized water and incubating the mixture at 70°C for 10 minutes with

intermittent mixing. This ligation product was used for transformation of competent bacteria.

lentiGuide	NeoR
ACGCGTTAAGTCGACAATCAACC	CCATTTCAGGTGTCGTGACGTACGGCCAC-CATGATTGAACAAGATGGATTGCAC
GGTGGCCGTACGTCACGAC	ATCCAGAGGTTGATTGTCGACTTAAC-GCGTTCAGAAGAACTCGTCAAGAAGGC

Table 2.9: Oligonucleotides used for PCR-amplification of indicated fragments for Gibson Assembly-based generation of lentiGuide Neo. Primers are displayed 5' -> 3', grey indicates forward and white reverse primers.

	lentiGuide	NeoR
Template DNA	15 ng	1 ug
5X Reaction buffer	20 µL	20 µL
dNTPs	200 µM	200 µM
Forward primer	500 nM	500 nM
Reverse primer	500 nM	500 nM
Q5 DNA polymerase	1 µL	1 µL
Deionized H_2O	Up to 100 µL	Up to 100 µL

Table 2.10: PCR mixture for indicated fragment amplification.

	lentiGuide			NeoR		
	Temperature	Time	Cycles	Temperature	Time	Cycles
Melt	98 °C	30 s	1	98 °C	30 s	1
Re-melt	98 °C	10 s	25	98 °C	10 s	25
Anneal	49.9 °C	30 s		69 °C	30 s	
Extend	72 °C	30 s		72 °C	6 mins 20 s	
Final extension	72 °C	2 mins	1	72 °C	2 mins	1
Hold	4 °C	∞	1	4 °C	∞	1

Table 2.11: PCR conditions for the amplification of indicated fragments.

2.4.4: Transformation of competent bacteria

All recombinant vectors were grown in XL1-Blue chemically competent bacteria. Bacteria were stored at -80°C and upon removal thawed on wet ice. Once thawed, 50 µL of bacteria were added to 10 µL chilled ligation mixture (see previous section) and incubated on wet ice for 20 minutes. Afterwards, the bacteria were heat-shocked at 42°C for 1.5 minutes and returned to wet ice. Sterilized glass beads were utilized to spread 50 µL of bacteria onto pre-warmed Luria-Bertani (LB) agar plates with carbenicillin (100 µg mL^{-1}). Glass beads were removed, plates inverted and incubated overnight at 37°C. The next day, colonies were picked and expanded in 3 mL overnight cultures in LB broth (Invitrogen, CA) with ampicillin (25 µg mL^{-1}) incubated at 37°C with shaking. DNA was extracted from overnight cultures using the QIAprep Spin Miniprep kit (Qiagen, Germany) according to manufacturer instructions.

2.4.5: Cloning of lentiGuide Neo to target *BRCA1*

Gibson Assembly was utilized to create lentiGuide Neo. lentiGuide Puro was amplified by PCR omitting the puromycin resistance cassette (Tables 2.9-2.11). Separately, the neomycin resistance cassette (NeoR) was amplified by standard PCR from pLXV MYC-mCherry Neo (Tables 2.9-2.11). After amplification, PCR products were resolved by gel electrophoresis on regular agarose to confirm successful amplification and on Microsieve LM Agarose for Gibson Assembly reaction as described above. DNA fragments were excised with a scalpel under UV light and DNA was eluted from excised agarose blocks using the QIAquick PCR Purification Kit (Qiagen, Germany) according to manufacturer instructions. DNA concentration after elution was measured on a NanoDrop™ One/OneC Microvolume UV-Vis Spectrophotometer (Thermo Fisher Scientific, MA). Finally, fragments were assembled into lentiGuide Neo using Gibson Assembly® Master Mix (New England BioLabs Inc., MA) according to manufacturer instructions (Table 2.12). The reaction was performed at 50°C for 15 minutes. Subsequently, competent cells were transformed and expanded as described above. Upon extraction of putative lentiGuide Neo plasmid DNA, two restriction digests using HindIII and SalI as well as PvuII alone (all from New England BioLabs Inc., MA) confirmed successful generation of the desired lentiviral plasmid with a success rate of 91.6%.

gRNAs targeting *BRCA1* were introduced into lentiGuide Neo by ligating the annealed forward and reverse oligonucleotides into BsmBI digested lentiGuide Neo. The restriction digest was performed overnight using BsmBI and subsequent gel electrophoresis using Microsieve LM Agarose of digested lentiGuide Neo was performed as

described previously. Oligonucleotides containing the gRNA sequences were annealed using an Applied Biosystems PCR Thermal Cycler (Thermo Fisher Scientific, MA; Table 2.13). After a 30-minute incubation at 37°C, the samples were heated to 95°C for 5 minutes and then rapidly cooled to 25°C at a rate of 5°C minute^{-1} (Sanjana et al., 2014). Subsequent in-gel ligation and transformation were performed as described above. Following successful culture of bacteria and plasmid DNA isolation, vectors were validated by Sanger sequencing as described below.

lentiGuide	0.02 pmols (21 ng)
NeoR	0.04 pmols (124.7 ng)
Gibson Assembly® Master Mix	10 µL
Deionized H_2O	Up to 20 µL

Table 2.12: Gibson Assembly reaction to generate lentiGuide Neo.

lentiGuide g*BRCA1* exon 2 Neo	CACCGAAATCTTAGAGTGTCCCATC
	AAACGATGGGACACTCTAAGATT
lentiGuide g*BRCA1* exon 3 Neo	CACCGTGCTAGTCTGGAGTTGATCA
	AAACTGATCAACTCCAGACTAGCAC
lentiGuide g*BRCA1* exon 10 1 Neo	CACCGGTTTCAGATGATGAAGAAAG
	AAACCTTTCTTCATCATCTGAAACC
lentiGuide g*BRCA1* exon 10 2 Neo	CACCGAGATGATGAAGAAAGAGGAA
	AAACTTCCTCTTTCTTCATCATCT
lentiGuide g*BRCA1* exon 10 3 Neo	CACCGGATGATGAAGAAAGAGGAAC
	AAACGTTCCTCTTTCTTCATCATCC
lentiGuide g*BRCA1* exon 10 4 Neo	CACCGTGAAGAAAGAGGAACGGGCT
	AAACAGCCCGTTCCTCTTTCTTCAC

Table 2.13: Oligonucleotides constituting the gRNAs targeting *BRCA1*. Primers are displayed 5' -> 3', white indicates forward and grey reverse primers.

2.4.6: Cloning of pLenti CMV MYC Hygro

MYC cDNA was amplified from pcDNA5 FRT/TO CR MYC by PCR to generate a BglII and a SalI restriction site using primers and PCR conditions outlined in Tables 2.14-2.15 (Littler et al., 2019). Subsequently, the MYC PCR fragment was digested as described above using BglII and SalI (both from New England BioLabs Inc., MA). The destination vector, pLenti CMV Hygro DEST, was digested with restriction enzymes SalI and BamHI (both from New England BioLabs Inc., MA) as described above. Successful digestion of recombinant DNA was confirmed by analytical gel electrophoresis and then DNA fragments were resolved on Microsieve LM Agarose for the ligation re-

action. Ultimately, the digested *MYC* PCR product was ligated as described above into the digested pLenti CMV Hygro DEST creating pLenti CMV MYC DEST.

MYC	CACAGATCTCAGATCCCGAGGTCCGACAGC
	CACGTCGACTTACGCACAAGAGTTCCGTAGCTG

Table 2.14: Oligonucleotides used to amplify MYC cDNA by PCR. Primers are displayed 5' -> 3', white indicates forward and grey reverse primers.

PCR mixture		**PCR cycles**			
Template DNA	1 µg	Step	Temperature	Time	Cycles
5X reaction buffer	20 µL	Melt	98 °C	30 s	1
dNTPs	200 µM	Re-melt	98 °C	10 s	25
Forward primer	500 nM	Anneal	70 °C	30 s	
Reverse primer	500 nM	Extend	72 °C	40 s	
Q5 DNA polymerase	1 µL	Final extension	72 °C	2 mins	1
Deionized H_2O	Up to 100 µL	Hold	4 °C	∞	1

Table 2.15: PCR composition and cycle conditions for the amplification of *MYC* cDNA.

PCR mixture		**PCR cycles**			
Template DNA	10 ng	Step	Temperature	Time	Cycles
REDTaq® ReadyMix™ PCR Reaction Mix	25 µL	Melt	94 °C	30 s	1
		Re-melt	94 °C	1 min	25
Forward primer	500 nM	Anneal	55 °C	2 mins	
Reverse primer	500 nM	Extend	72 °C	3 mins	
Deionized H_2O	Up to 50 µL	Final extension	72 °C	2 mins	1
		Hold	4 °C	∞	1

Table 2.16: PCR conditions employed for the identification of g*BRCA1* used in *TP53/BRCA1* double-mutant FNE1 subclones and to subsequently amplify the genomic region adjacent to the g*BRCA1* target site.

2.4.7: Identification of gRNAs in *TP53/BRCA1* double-mutant FNE1 subclones

Genomic DNA was extracted from P1, PB1 and PB2 cells using the PureLink™ Genomic DNA Mini Kit (Thermo Fisher Scientific, MA) according to manufacturer instructions. Since P1 cells had been transduced with six different lentiGuide g*BRCA1* Neo lentiviruses simultaneously prior to single-cell cloning, the causative gRNA could be determined based on which one of the six lentiviruses had integrated into the genome. Thus, PCR was performed according to Table 16 using the forward primers used to generate the g*BRCA1* inserts (described in Table 2.11) as forward primer and the 3' sequencing primer as reverse primer (previously described 5' ATTGTGGATGAATACTGCC 3' by Sanjana Nat Methods & Science). Since lentiGuide g*TP53* Puro was expected to be detectable in P1 cells, a reaction using the corresponding oligonucleotide as forward primer was performed as positive control (5' CACCGAATGTTTCCTGACTCAGAGG 3', courtesy of Dr Paul Minshall).

2.4.8: Sanger sequencing

The Sanger sequencing itself was performed on an ABI 3130xl 16 Capillary Array Sequencer (Applied Biosystems, CA) by the Molecular Biology Core Facility at the Cancer Research UK Manchester Institute. All sequencing reactions contained 15 pmol sequencing primer, 300 ng DNA of interest and were made up to a total volume of 12 µL using deionized water. Individual sample preparation was performed as described below.

lentiGuide g*BRCA1* Neo: After cloning, the presence of gRNAs was confirmed by Sanger sequencing using the 3' sequencing primer described (5' ATTGTGGATGAATACTGCC 3' (Sanjana et al., 2014; Shalem et al., 2014)).

***BRCA1* locus:** Once the g*BRCA1* was identified the genomic region adjacent to the g*BRCA1*'s target site was amplified from genomic DNA extracted from P1, PB1 and PB2 cells by PCR using primers designed to generate XhoI and NotI restriction sites (Tables 2.16-2.17). PCR amplified fragments and pBlueScript II SK- (Agilent Genomics, CA) were digested overnight using XhoI and NotI (both from New England BioLabs Inc., MA) as described above. Gel electrophoresis-based separation of DNA fragments was performed using regular agarose to confirm successful amplification and digestion and using Microsieve LM agarose to isolate DNA fragments for ligation. DNA fragments of interest were excised from agarose gel under UV light, in-gel ligation and transformation were performed as described above. Bacterial colonies were expanded and plasmid DNA extracted from up to six overnight cultures as described

above. Ultimately, the same forward primers used for the amplification of the genomic region were utilized for the Sanger sequencing reaction (Table 2.17).

BRCA1 exon 3	CACCTCGAGATGGAGCTTAAAGATGAGATGTG
	CACGCGGCCGCTGGGAGGCTGAGGTAGAAGAATC
BRCA1 exon 10	CAC CTCGAGTTGGCAAAGGCATCTCAGGAAC
	CACGCGGCCGCCCTTGCTTTGGGACACCTGGAT

Table 2.17: Oligonucleotides used for PCR amplification of the indicated genomic region and Sanger sequencing of the cloned product. Primers are displayed 5' -> 3', white indicates forward and grey reverse primers.

Note, sections 2.4.9, 2.4.10 and 2.5 are the same as in Bronder et al., 2021, see Appendix 1.

2.4.9: RNA sequencing

RNA was extracted from logarithmically growing cells *in situ* using the RNeasy Plus Mini kit (Qiagen, Germany) according to manufacturer instructions. RNA integrity and quality were assessed using a 2200 TapeStation (Agilent Technologies, CA; performed by the CCR Genomics Core, Bethesda, MD). Libraries were prepared using TruSeq® Stranded mRNA Library Prep (Illumina, CA), pooled and paired end sequenced on NovaSeq™ 6,000 system (Illumina, CA) using an SP flow cell according to manufacturer instructions (Sequencing Facility at NCI Frederick, MD). Samples returned 37 to 51 million pass filter reads with more than 91% of bases above the quality score of Q30.

2.4.10: Shallow-depth whole genome sequencing

Single cell shallow depth whole genome sequencing was performed on single cells sorted for a 2c (P1) or 4c (PB3, PBE3, PBM3) genome content (PB2, PBE2 and PBM2, 12 cells from each population were sorted) as described previously (Bakker et al., 2016; Nelson et al., 2020; van den Bos et al., 2016).

2.5: Bioinformatics

2.5.1: RNA sequencing

For RNA sequencing, sample reads were processed using the CCBR Pipeliner utility (https://github.com/CCBR/Pipeliner). Briefly, reads were trimmed for adapters and low-quality bases using Cutadapt (version 1.18) (http://gensoft.pasteur.fr/docs/cutadapt/1.18)

before alignment to the human reference genome (hg38/Dec. 2013/GRCh38) from the UCSC browser and the transcripts annotated using STAR v2.4.2a in 2-pass mode (Dobin et al., 2013; Martin, 2011). Expression levels were quantified using RSEM (version 1.3.0) (Li and Dewey, 2011) with GENCODE annotation version 30 (Harrow et al., 2012). The same approach was used for mouse model data downloaded from Gene Expression Omnibus (GEO, accession number GSE125016), with alignment to the mouse reference genome (mm10).

Raw read counts (expected counts from RSEM) were imported to the NIH Integrated Data Analysis Platform for downstream analysis. Low count genes (counts-per-million (CPM) < 0.5), ≥ three samples were filtered prior to the analysis. Counts were normalized to library size as CPM and the voom algorithm (Law et al., 2014) from the Limma R package (version 3.40.6) (Smyth, 2004) was used for quantile normalization. Batch correction was performed prior to analysis using the ComBat function in the sva package (Johnson et al., 2007). Differentially expressed genes (DEG) using Limma and pre-ranked gene set enrichment analysis (GSEA) were computed between each genotype using the molecular signatures database (Liberzon et al., 2011; Subramanian et al., 2005). And gene set variation analysis (GSVA) was performed using the GSVA package (Hanzelmann et al., 2013). Genes or gene sets with an adjusted p-value ≤ 0.05 were considered statistically significant. Preparation of heatmaps was performed in R Studio (Subramanian et al., 2005).

2.5.2: Shallow-depth whole genome sequencing

Analysis of copy number changes based on scWGS was executed according to previous reports (Bakker et al., 2016; Nelson et al., 2020; van den Bos et al., 2016).

2.6: Mouse work

2.6.1: Husbandry and implantation of cells

All mouse work was performed in accordance with the MB-045 protocol approved by the institutional animal care and use committee (IACUC) at NCI (Bethesda, MD). Athymic nude, female mice were purchased from Jackson Laboratories (ME) at age 5 weeks and housed in groups of five in a pathogen free environment on a 12 hour day-night cycle with access to flash-autoclaved chow and water *ad libitum*.

In preparation for injection, subconfluent cells were harvested normally and washed twice in complete media. 10^6 cells were injected intraperitoneally in 200 µl of

appropriate media. Five 6-8-week-old mice were injected per group and weighed twice weekly afterwards with a maximum follow-up of one year.

Mice were euthanized by cervical dislocation when moribund in accordance with the animal study protocol or when the one-year follow-up was reached. Humane criteria for euthanasia were as follows: rapid weight loss, debilitating diarrhoea, hunched posture, laboured breathing, lethargy, persistent recumbence, jaundice anaemia, significantly abnormal neurological signs, bleeding from any orifice, self-induced trauma, impaired mobility, distended abdomen, or inability obtain food or water.

2.6.2: miFISH analysis of harvested tumours and ascites

Ascites and tumours were collected from mice at necropsy and immediately processed. Cells were separated from ascitic fluid by centrifugation at 1,200 RPM for five minutes and washed with PBS. If red blood cells were present a lysis step was performed using red blood cell lysis buffer (155 mM NH_4Cl, 10 mM $KHCO_3$, 100 nM EDTA, pH 7.3) for five minutes at 37°C. In contrast, tumours were first minced mechanically using scalpels and digested with 0.05% trypsin for one hour at 37°C. The reaction was quenched with DMEM containing 10% FBS and cells were separated by centrifugation at 1,200 RPM. Again, if red blood cells were present lysis was performed as described above. Upon successful isolation, cells were swelled with hypotonic buffer, fixed with methanol/acetic acid, dropped onto glass slides, aged and ultimately hybridized in the same manner as described in *2.2.2: Fluorescence in situ hybridization*.

2.6.3: Immunohistochemistry

Tumour samples were harvested at necropsy of mice and fixed in formalin overnight. Subsequently, fixed samples were stored for no more than one week in 70% ethanol and shipped to the Molecular Histopathology Laboratory at NCI, Frederick, MD, where the following immunohistochemistry staining were performed:

Human mitochondria staining was performed on BondRX autostainer (Leica Biosystems, IL). Following antigen retrieval with citrate buffer (Bond Epitope Retrieval Solution 1; Leica Biosystems, IL), sections were incubated for one hour with a biotin-conjugated anti-human mitochondria antibody (mouse, clone MTC02, Abcam, MA) diluted 1:50. Staining was completed with the Bond Intense R Detection Kit (Leica Biosystems, IL).

Green fluorescence protein (GFP) staining was performed manually. Following pretreatment with proteinase K (DAKO, CA) for five minutes at room temperature,

sections were blocked with normal goat serum and then incubated overnight at 4°C with an anti-GFP antibody (rabbit, polyclonal, Abcam, CA) diluted 1:4,000. Staining was completed with biotinylated goat anti-rabbit IgG, ABC Elite and DAB (all from Vector Laboratories Inc., CA). Isotype control antibodies were used in place of the primary antibodies for negative controls. Lastly, images were acquired at 20X using an Aperio AT2 scanner (Leica Biosystems, IL) to create whole slide digital images.

2.7: Statistics

Prism 9 (GraphPad, CA) and R Studio (R Project for Statistical Computing) were used to generate graphs and heatmaps, respectively. In Prism, statistical analyses of significance were determined using Brown-Forsythe and Welsh ANOVA to detect differences in enrichment scores between samples. R packages Complex Heatmaps, AneuFinder and Enhanced Volcano were utilised to make heatmaps and volcano plots. Differentially expressed genes were determined in NIDAP using the Benjamini-Hochberg algorithm.

Chapter 3: Characterization and genetic engineering of FNE1 cells

3.1: Overview

As alluded to in *1.5: Approaches to study high-grade serous ovarian cancer*, a number of model systems are available to study HGSOC *in vitro* and *in vivo*. Aims (i) and (ii) outlined in *1.7: Rationale and aims* were to validate FNE1 cells as a model system and subsequently model the mutations typically observed in the HRD-driven group of HGSOC. These aims effectively ruled out all established HGSOC cell lines as they are invariably *TP53* mutant and ectopic expression of p53 in otherwise p53-deficient cancer cells has been shown to result in growth suppression (Baker et al., 1990). In addition, a number of non-transformed fallopian tube-derived models which either relied on CRISPR/Cas9-mutagenesis of *TP53* (human organoids) or suppression of p53 by RNAi, the expression of SV40 TAg or the expression of a dominant negative isoform of p53 were also ruled out. Likewise, the mouse oviduct-derived organoids are all underpinned by mutations in *Trp53*.

Therefore, I chose the FNE1 cell line for the purpose of this study, because it was immortalized using *hTERT* alone in the absence of other genetic manipulation which might act upon the p53 pathway (Merritt et al., 2013). Another clear advantage of the FNE1 cells is that they are grown in 2D under physiologically relevant O_2 conditions (5% O_2 concentration versus the traditionally employed atmospheric concentration) which makes them a facile and inexpensive, physiologically relevant model system for many of the experiments I am presenting in this thesis. Nonetheless, the possibility that aberrations in the p53 pathway have arisen spontaneously in the process of immortalization cannot be excluded, thus FNE1 cells were first subjected to rigorous characterization probing p53 pathway proficiency and genomic stability.

In this chapter, I will address aim (i), the initial characterization of FNE1 cells with regard to p53 pathway proficiency and genomic stability using cell biological and molecular cytogenetics tools. Once a robust p53 response and a stable karyotype were shown in FNE1 cells, I proceeded with aim (ii), to generate a genetically and functionally well characterized panel of CRISPR/Cas9-edited *TP53* single-, *TP53/BRCA1* or *TP53/MYC* double- and *TP53/BRCA1/MYC* triple-mutant FNE1 subclones.

3.2: FNE1 cells are near-diploid and p53-proficient

Key features of HGSOC are *TP53* mutations and CIN, which I plan to introduce and study. Thus, only the use of a p53-proficient, near-diploid and chromosomally stable model system as baseline will be informative to my aims.

In order to obtain a karyotype of FNE1 cells, as one was not published at the time this project started, single-cell shallow depth whole genome sequencing (scWGS) was performed (Bakker et al., 2016). Sequencing and bioinformatics analyses of FNE1 cells revealed a near-diploid karyotype with two segmental monosomies and one whole chromosome monosomy (Fig. 3.1A). The affected chromosome arms were 9p and 15p as well as chromosome X. In addition to the partial and whole chromosome monosomies, scWGS did not show any evidence of substantial cell to cell karyotypic variation indicative of CIN. Despite its utility of detecting copy number changes with high confidence, scWGS does not detect structural genomic changes. Therefore, conventional cytogenetic karyotyping employing spectral karyotyping (SKY) was performed as an orthogonal method to scWGS (Padilla-Nash et al., 2006; Schrock et al., 1996). Indeed, SKY revealed a previously unappreciated, unbalanced translocation between chromosome arms 9p and 15q in addition to the known monosomy of chromosome X (Fig 3.1B). These findings corroborate the scWGS data, are consistent with a recently reported karyotype of FNE1 cells by Tamura et al. (2020) and also indicate that FNE1 cells have a functional SAC as the SKY procedure relies on a prometaphase arrest induced by colcemid treatment.

Furthermore, I probed p53 function to establish if p53 pathway proficiency had been perturbed spontaneously during the immortalization of FNE1 cells. I first tested if p53 would be stabilized in response to pharmacological inhibition of its negative regulator MDM2 by Nutlin-3 (Vassilev et al., 2004). After eight hours of treatment, I observed penetrant, nuclear p53 protein expression in Nutlin-3 treated compared with DMSO treated FNE1 cells by immunofluorescence microscopy (Fig. 3.1C). These data suggest that p53 is stabilized upon inhibition of its negative regulator and able to enter the nucleus to fulfil its function as transcriptional activator. However, this does not confirm p53 functionality which I addressed by immunoblotting and measuring the induction of p53's canonical transcriptional target p21 (encoded by *CDKN1A*; Fig. 3.1D). Indeed, I confirmed the immunofluorescence-based observation that p53 is stabilized in response to Nutlin-3 over time and additionally confirmed its function by showing that p21 levels increase in a manner similar to p53 over time. Using Nutlin-3 to inhibit MDM2 enabled me to probe p53 functionality in response to the direct inhibition of its negative regulator, however, this is not reflective of physiological stresses. Thus, I treated FNE1 cells with cisplatin to induce DNA crosslinks which lead to DNA damage and subsequently measured p53 expression by immunoblotting. As expected, I observed the stabilization of p53 over time upon treatment with cisplatin (Fig. 3.1D).

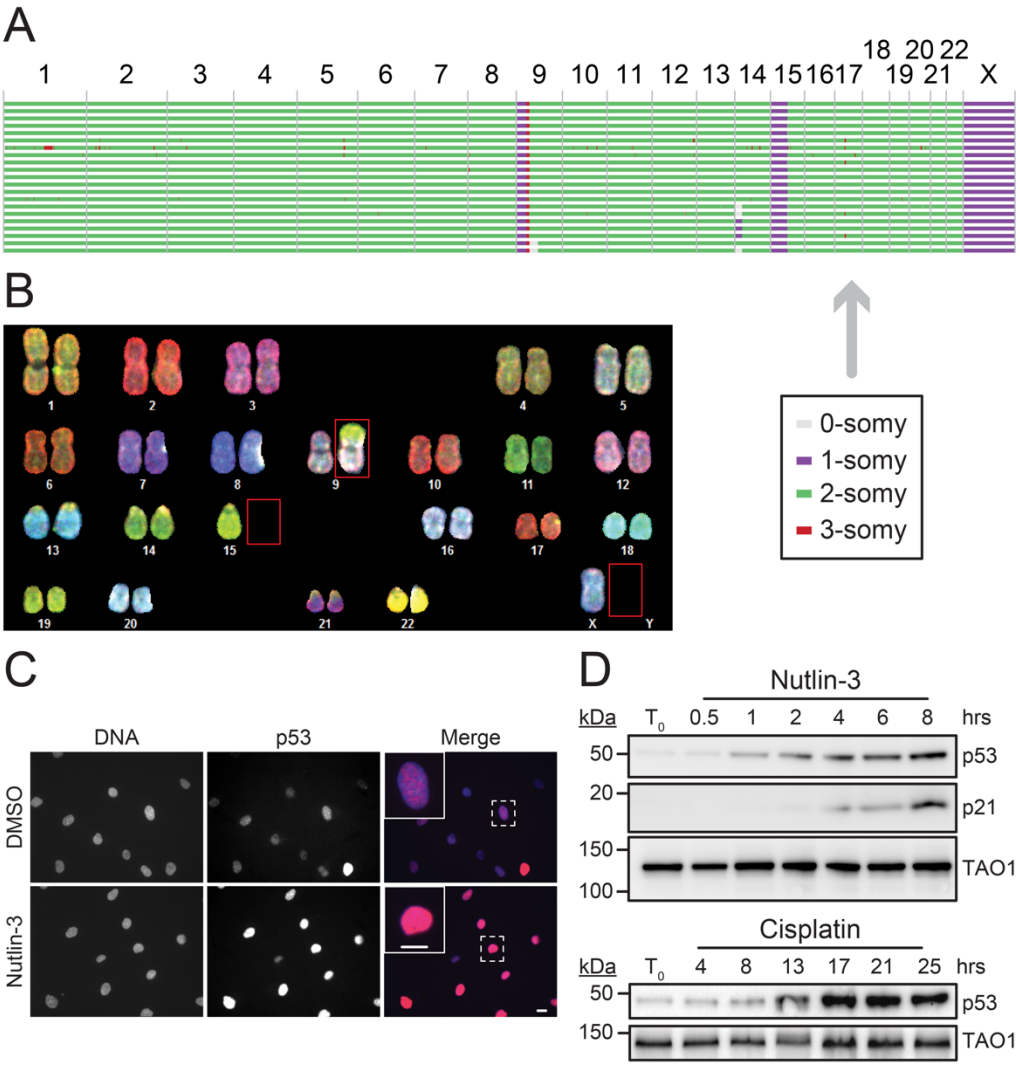

Figure 3.1: FNE1 cells are near-diploid and mount a robust p53 response
A Single-cell whole genome sequencing of FNE1 cells. Each row represents a single cell and each column represents the indicated chromosome. The colour indicates the detected copy number. **B** Representative image of spectral karyotype of an FNE1 cell. Note the absence of chromosomes 15 and X and the unbalanced translocation between chromosome arms 9p and 15q as highlighted by the red boxes. **C** Representative images of DMSO and Nutlin-3 treated FNE1 cells stained for p53 and DAPI. Scale bar indicates 5nm. **D** p53 and p21 expression measured by immunoblotting in response to Nutlin-3 or cisplatin treatment over time. TAO1 serves as loading control.

Taken together, FNE1 cells are an informative model system for my study as they are near-diploid, chromosomally stable and p53 proficient.

3.3: CRISPR/Cas9-mediated *TP53* mutagenesis

The use of CRISPR/Cas9 for genetic manipulation is an established method and FNE1 cells have been shown to be infectable with retroviruses (Merritt et al., 2013). Many CRISPR/Cas9 constructs rely on transient transfection of cells, however, preliminary data from my colleague Dr Olivia Sloss showed poor efficiency of transient transfection in FNE1 cells. Based on these observations and the infectability of FNE1 cells with retroviruses, I surmised that using lentiviral constructs in FNE1 cells would be the right avenue to pursue. Additionally, many CRISPR/Cas9 constructs are readily available as lentiviruses. Pertinent to this aspect, CRISPR/Cas9 has been associated with off-target effects ranging from off-target mutations at nucleotide sequences similar to the target to large insertions and deletions especially in cancer cell lines with basal levels of genomic instability (Rayner et al., 2019). Therefore, a commercially available, lentiviral and tetracycline-inducible Cas9 construct was chosen with the view to minimize its expression to mitigate potential consequences of off-target effects. In the first step of my mutagenesis approach (Fig. 3.2A), FNE1 cells were made amenable to CRISPR/Cas9 genome editing by generating a polyclonal, blasticidin S-resistant FNE1 cell line expressing Cas9 under tetracycline control (FNE1 TO Cas9; Fig. 3.2B). As expected, these cells remained near-diploid even when maintained in blasticidin S as confirmed by SKY (Fig. 3.2C).

As outlined in *1.2.2: Genomics of high-grade serous ovarian cancer*, *TP53* mutations occur early and are ubiquitous in HGSOC thus I first aimed to generate p53-deficient subclones of FNE1 cells (Fig. 3.2A). I chose a previously published gRNA to target *TP53* (Simoes-Sousa et al., 2018). This gRNA was cloned into the widely used lentiviral backbone lentiGuide Puro (Sanjana et al., 2014). I then transduced the newly established FNE1 TO Cas9 cells with lentiGuide Puro g*TP53* and selected for transduced cells with puromycin. I induced Cas9 expression with 15 µg ml^{-1} tetracycline for a period of four days and then aimed to evaluate if my experimental approach had reduced p53 levels as expected. In the first instance, I assessed p53 protein expression on a population level in the absence or presence of Nutlin-3 in FNE1 and FNE1 TO Cas9 g*TP53* cells by immunoblotting (Fig. 3.3A). Indeed, p53 levels were reduced in FNE1 TO Cas9 g*TP53* compared with FNE1 cells, however, the inconsistent loading did not allow for a definitive conclusion. Therefore, I investigated nuclear p53 levels in the same cell populations in the presence or absence of Nutlin-3 by

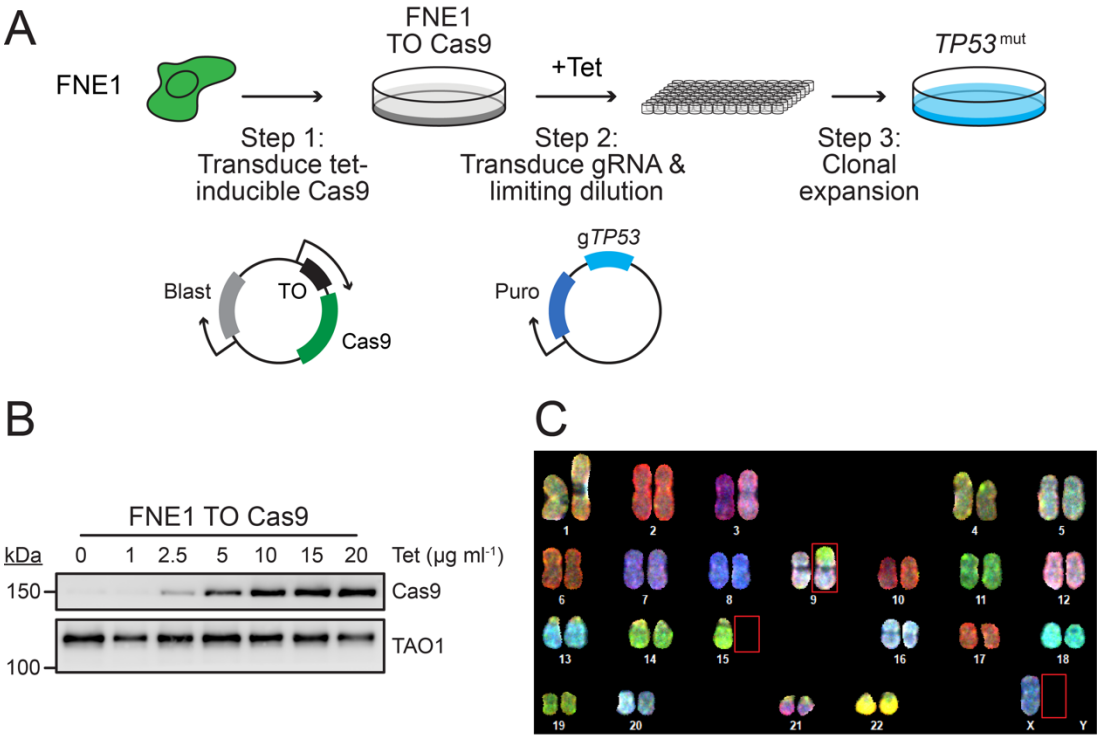

Figure 3.2: Experimental approach and generation of Cas9-expressing FNE1 cells
A Experimental approach schematic outlining the steps taken in this chapter to first generate FNE1 cells that express Cas9 under tetracycline control and subsequently generate single cell-derived *TP53*-mutant FNE1 subclones. **B** Tetracycline concentration-dependent expression of Cas9 in FNE1 cells measured by immunoblotting after 24 hours of exposure. TAO1 serves as loading control. **C** Representative image of SKY-based karyotyping of FNE1 TO Cas9 cells. Red boxes indicate aberrations observed in FNE1 cells.

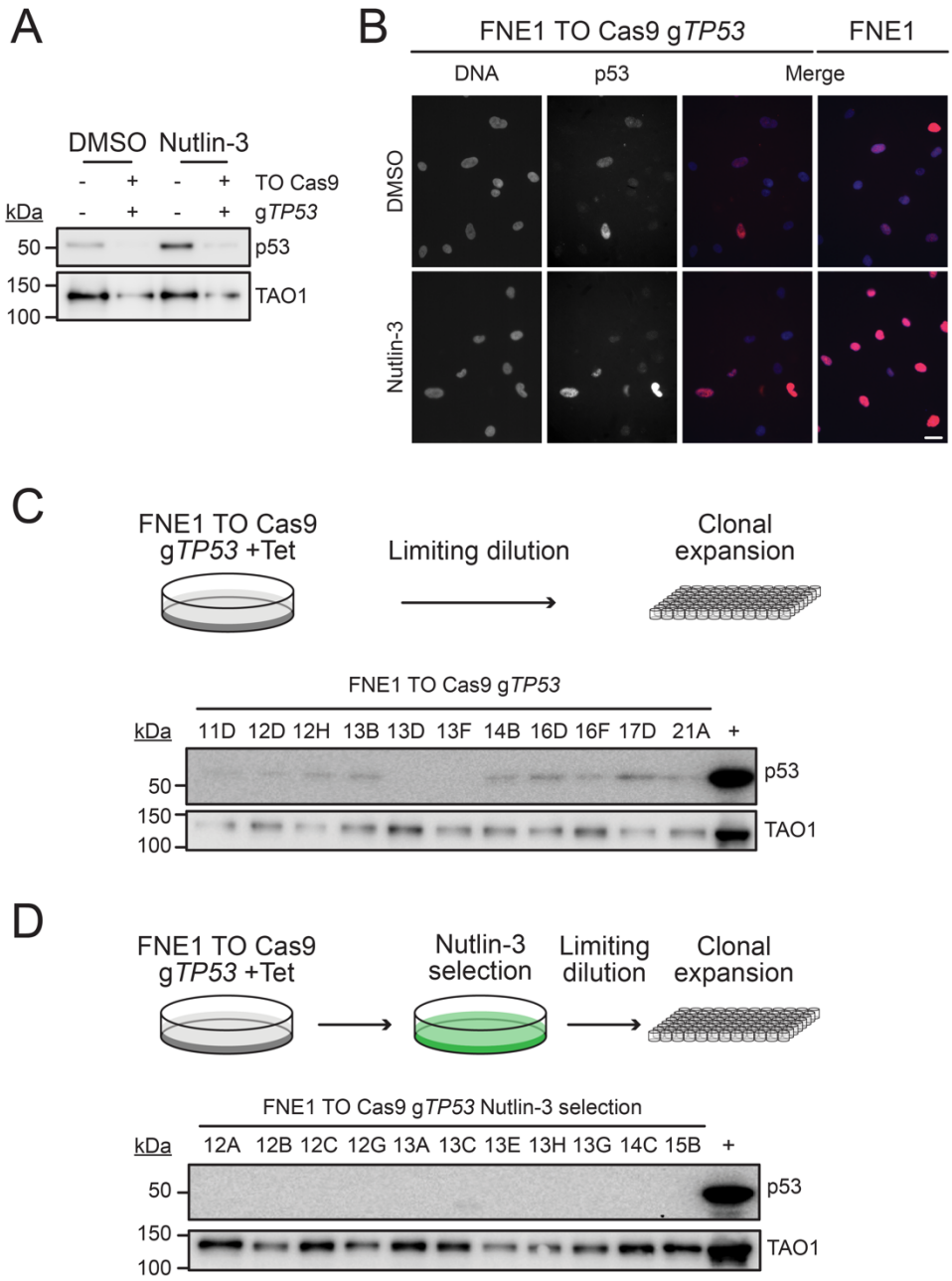

Figure 3.3: Generation of FNE1 subclones deficient for full-length p53
A Population wide p53 protein expression in FNE1 and polyclonal FNE1 TO Cas9 cells transduced with a guide RNA targeting TP53 (g*TP53*) after treatment with DMSO or Nutlin-3. **B** Nuclear p53 protein expression in single cells assayed by immunofluorescence microscopy in FNE1 and polyclonal FNE1 TO Cas9 sgTP53 cells. Scale bar equals 10nm. Note, FNE1 merge images are replicated from Fig. 3.1. **C** Schematic and immunoblot of FNE1 single cell-derived subclones after limiting dilution and expansion screening for the absence of full-length p53 protein. **D** Schematic and immunoblot of FNE1 single cell-derived subclones after intermittent Nulin-3 selection and limiting dilution and expansion screening for the absence of full-length p53 protein. TAO1 serves as loading control in C and D.

immunofluorescence microscopy next (Fig. 3.3B). In the absence of Nutlin-3, p53 staining was consistent between FNE1 TO Cas9 g*TP53* and FNE1 cells, in both cases, nuclear p53 expression is an exception, not the rule. In contrast, Nutlin-3 treatment led to robust nuclear p53 expression in FNE1 cells, but not in FNE1 TO Cas9 g*TP53* cells where a number of nuclei remained p53-negative. Taken together, these two experiments gave me the confidence that I was able to generate p53-deficient cells by sequentially transducing FNE1 cells with Cas9-expression and g*TP53* lentiviruses. At this point, I pursued two strategies to generate isogenic p53-deficient FNE1 subclones. The first strategy was to perform limiting dilution immediately after the four days of Cas9-induction to generate isogenic p53-deficient, single cell-derived FNE1 subclones, which showed an efficiency of 18.18% as determined by immunoblotting for full-length p53 expression (Fig. 3.3C). The second strategy was to perform an interim Nutlin-3 selection after the Cas9-induction to enrich for p53-deficient cells prior to limiting dilution, which showed an efficiency of 100% (Fig. 3.3D). I screened a total of 22 FNE1 subclones which were designated with the plate number and well of origin for screening purposes, but henceforth will be referred to as P1 (13D), P2 (13F) and P3 (12C; Table 3.1 at the end of this chapter summarizes all FNE1 subclones generated).

Finally, I characterized the newly generated p53-deficient FNE1 subclones functionally and with respect to the underlying mutation on the nucleotide level. For functional characterization, I once again employed Nutlin-3 and could show that one p53-proficient FNE1 (WT) subclone derived from the CRISPR procedure retained p53 expression upon Nutlin-3 exposure whereas P1 cells failed to express p53 in response to Nutlin-3 treatment (Fig. 3.4A). Furthermore, I evaluated the proliferative potential of FNE1 cells and p53-deficient subclones by live cell microscopy measuring population doublings as a proxy of proliferation. As expected, FNE1 cells proliferated unrestrained under control conditions but failed to proliferate in the presence of Nutlin-3 (Fig. 3.4B). In contrast, p53-deficient P1 and P3 cells proliferated in the absence and presence of Nutlin-3 albeit to a lesser extent in the presence of Nutlin-3. Lastly, I took advantage of the RNA sequencing data (more detail to follow in *Chapter 5: Transcriptomic analysis of mutant FNE1 subclones*) I generated to identify the genetic basis of p53-deficiency in P1, P2 and P3 cells. Manual inspection of RNA sequencing reads of *TP53* exon 2, where g*TP53* was predicted to and had been shown to induce mutations (Simoes-Sousa et al., 2018), revealed that all p53-deficient but not wildtype FNE1 subclones showed deletions. These deletions resulted in a frameshift of the

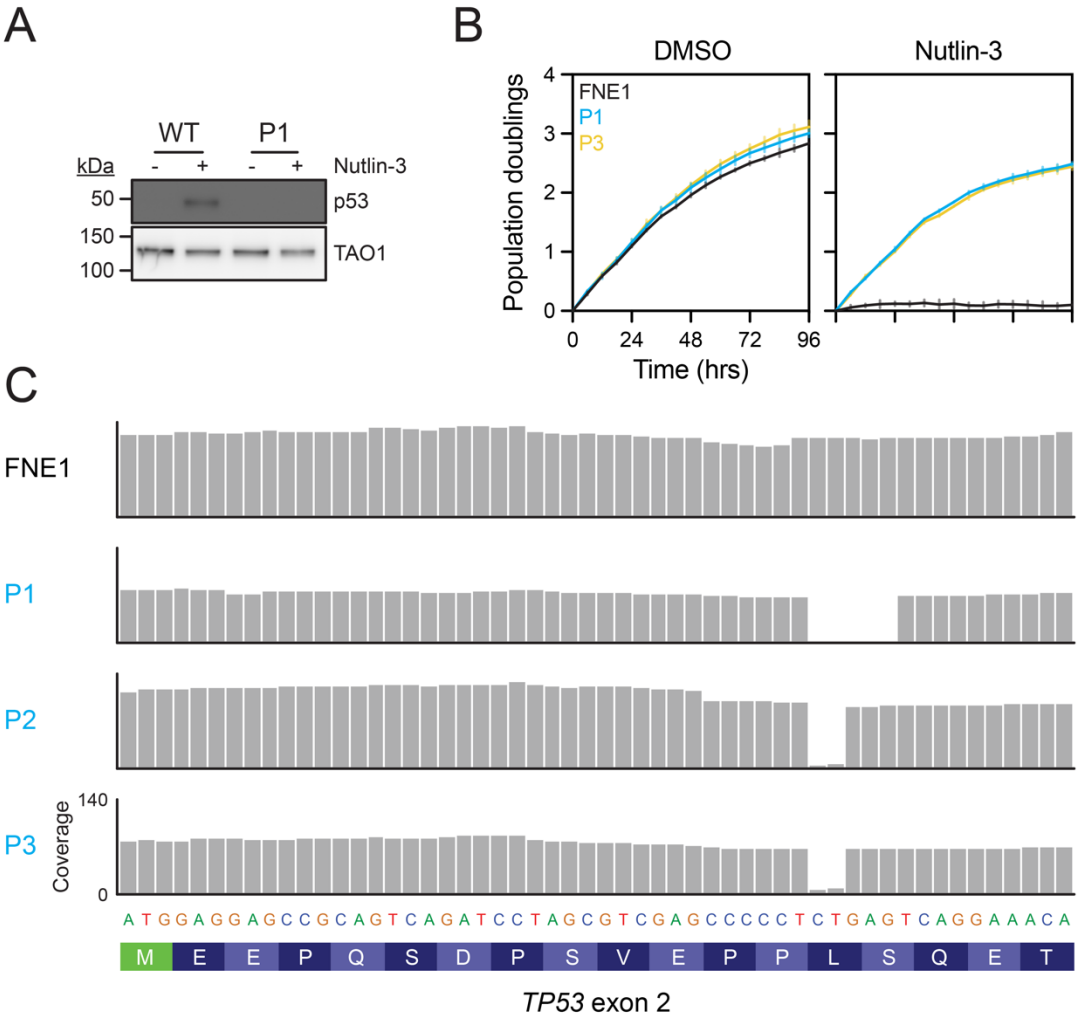

TP53 exon 2

Figure 3.4: Functional and RNA sequence characterization of p53-deficient FNE1 subclones

A Representative immunoblot of two FNE1 subclones derived after limiting dilution and treated with either DMSO or Nutlin-3 which I considered p53-proficient, hence wildtype (WT), and p53-deficient, P1. TAO1 serves as loading control. **B** Functional assessment of proliferation in the presence of DMSO or Nutlin-3 of FNE1, P1 and P3 cells transduced with an mCherry-tagged histone H2B lentivirus to measure red object counts. Population doubling was calculated by dividing red object counts by the red object count at timepoint 0 and log2 transformation. **C** Analysis of the nucleotide sequences in FNE1, P1, P2 and P3 cells in exon 2 of the TP53 locus based on the RNA sequencing data (more detail in chapter 5). RNA sequencing coverage was visualised in integrative genomics viewer.

open reading frame and a premature termination codon (PTC) downstream hence providing the genetic foundation of p53-deficiency (Fig. 3.4C, Table 3.1).

In conclusion, I generated FNE1 TO Cas9 cells and then employed these to establish three genetically and functionally p53-deficient FNE1 subclones.

3.4: CRISPR/Cas9-mediated *BRCA1* mutagenesis

Next, I decided to mutagenize *BRCA1* as it is the second most commonly mutated gene in HGSOC and all *BRCA1*-mutant cases of HGSOC fall into the HRD classification (Wang et al., 2017). Due to the immortalized nature of FNE1 cells there was no reason to suggest that FNE1 cells are BRCA1/2-deficient, indeed recent findings showed FNE1 cells to be HR proficient (Tamura et al., 2020).

First, I confirmed that Cas9 expression was retained in P1 and P3 cells in response to the previously established concentration of tetracycline. Indeed, Cas9 was induced in response to exposure of P1 and P3 cells to 15 µg ml^{-1} of tetracycline (Fig. 3.5A). Importantly, Cas9 was not detected in untreated cells which adds confidence to my approach mitigating off-target effects by using an inducible system. Induction of Cas9 was higher in P1 than in P3 cells thus for the subsequent *BRCA1* mutagenesis P1 cells were selected as the parental background. Due to the genomic size of the *BRCA1* gene and the absence of established guides at the time, I chose an approach using multiple gRNAs for simultaneous lentiviral transduction prior to limiting dilution and clonal expansion (Fig. 3.5B). I designed six gRNAs, one gRNA targeting exons 2 and 3 each and four gRNAs targeting exon 11 (Fig. 3.5C). Screening of successfully mutagenized subclones was performed by immunoblotting for the absence of full-length BRCA1 protein. Of 26 screened subclones, I failed to detect full-length BRCA1 protein in four thus yielding a CRISPR/Cas9 success rate of 15.4% (Fig. 3.5D). *TP53/BRCA1* double-mutant (PB) subclones 17, 23 and 26 were selected for further analysis and designated PB1, PB2 and PB3, respectively (Table 3.1).

To validate the knockout of *BRCA1* genetically, PB subclones were first screened for gRNA integration by PCR using primers with the gRNA sequence and a primer designed to confirm gRNA integration during cloning of the gRNA construct. This approach would yield a fragment (200 base-pairs in size) amplifiable from genomic DNA extracted from the subclones of interest. In P1 cells, the PCR using the g*TP53* sequence as a primer yielded a band of the expected size, however, no bands using g*BRCA1* sequences were detected, thus this approach does not generate off-target fragments (Fig. 3.6A). Yet, because of this, the use of the g*TP53* sequence emerged as valuable positive control. Utilizing this approach, I could confirm that *BRCA1*

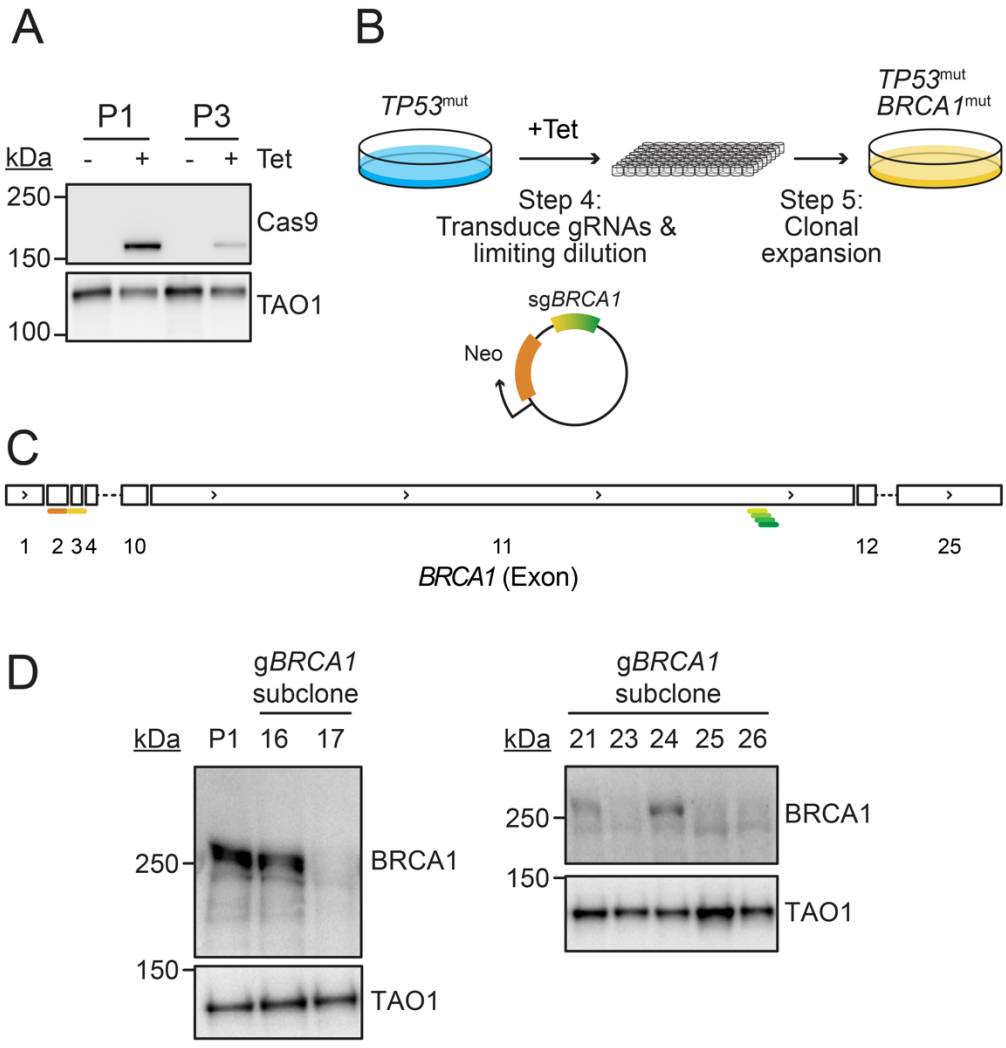

Figure 3.5: Experimental strategy and generation of *TP53/BRCA1* double-mutant FNE1 subclones

A Validation of Cas9 protein expression in P1 and P3 cells transduced with gBRCA1 lentivirus after exposure to 15 µg ml^{-1} of tetracycline (Tet) for 24 hours. **B** Schematic depicting the experimental strategy to generate *TP53/BRCA1* double-mutant FNE1 subclones. **C** Schematic of the *BRCA1* locus indicating the locations of six gRNAs used for CRISPR/Cas9-mediated knockout of BRCA1. **D** Representative immunoblots screening for the absence of full-length BRCA1 protein after derivation of clonal CRISPR/Cas9-edited subclones. TAO1 serves as loading control.

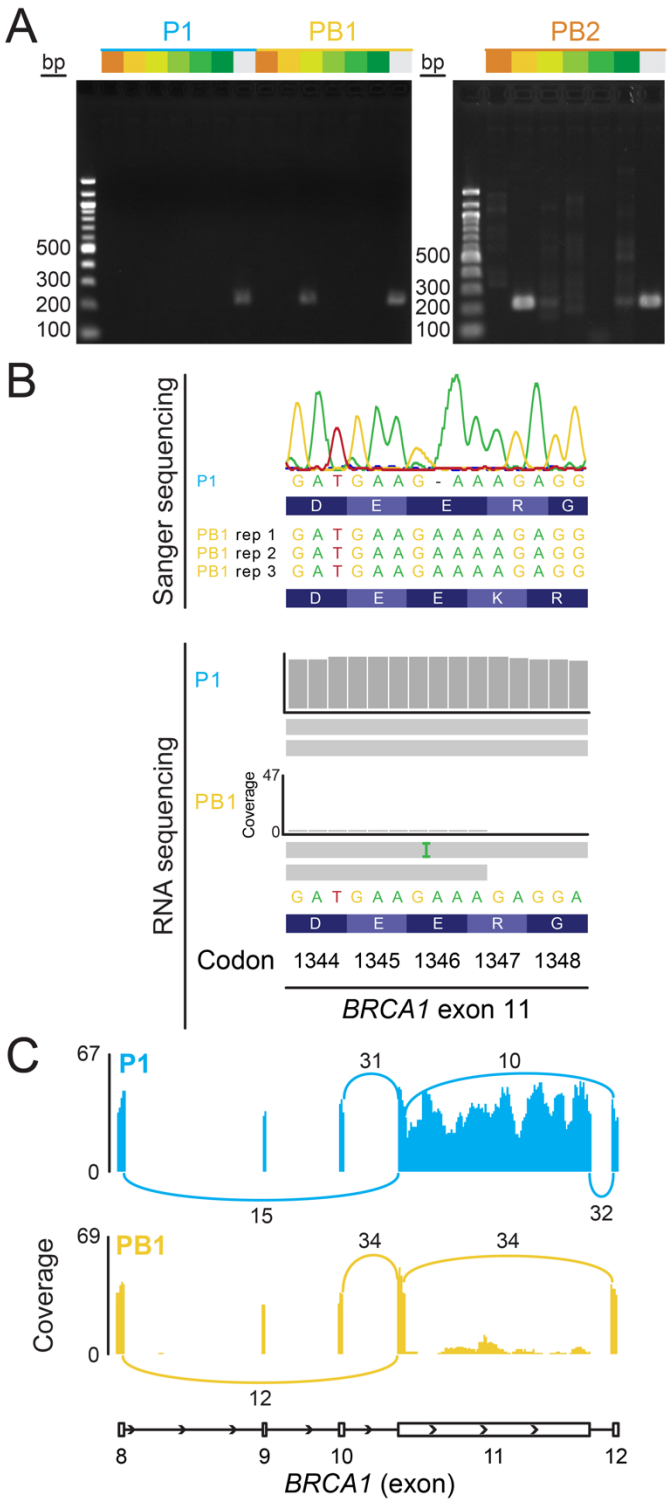

Figure 3.6: DNA and RNA sequencing reveal *BRCA1* exon 11 mutation and alternative splicing in PB1

A PCR-based analysis of CRISPR/Cas9 g*BRCA1* used to obtain *TP53/BRCA1* FNE1 subclones. Genomic DNA from indicated subclones was analysed for integration of six g*BRCA1* and g*TP53* as a control. The colours and grey indicate individual g*BRCA1* and g*TP53*, respectively. **B** DNA Sanger and RNA sequencing reveal the insertion of an adenine at codon 1,346 in PB1 resulting in a frameshift. P1 was included as parental control. In RNA sequencing data, two representative reads are shown for P1 whereas all detected reads are shown for PB1. The green vertical bar represents the adenine insertion. **C** Representative sashimi plots of *BRCA1* exon 11 alternative splicing in PB1 versus P1 reveals the absence of detectable reads mapping 3' terminally of exon 11 and 5' terminally of exon 12 in PB1.

mutagenesis occurred using guides designed to target exon 11 and 3 in PB1 and PB2 subclones, respectively. Second, once the genomic region of mutagenesis was narrowed down by identification of the associated g*BRCA1*, analysis of the genomic DNA sequence and RNA sequence was used to determine the underlying mutations. Sanger sequencing of PB1 genomic DNA revealed an adenine insertion in codon 1,346 in exon 11 which results in a frameshift of the open reading frame ultimately leading to a PTC (Fig. 3.6B). An attempt to validate this observation in the RNA sequencing data was only partially successful and instead revealed that sequencing coverage of exon 11 in PB1 was diminished compared with sequencing coverage of the same region in P1 cells. In total 47 reads were detected in P1 cells in comparison to only two in PB1, one of which confirmed the adenine insertion while the other did not. Note, however, that this second read's coverage terminated three nucleotides downstream of the adenine insertion. The diminished coverage of exon 11 was not specific to the mutation in question, in fact this reduction in coverage spans nearly all of exon 11 in PB1 cells. Alternative splicing is known to occur between various exons of BRCA1 and indeed ten reads spanning a 5' terminal region of exon 11 and 5' terminal region of exon 12 are detected in P1 cells (Fig. 3.6C). In addition, coverage of exon 11 in P1 cells remains consistent across the whole exon. In contrast, coverage of exon 11 in PB1 cells is only detectable at low levels and the number of reads spanning the 5' terminal region of exon 11 and 5' terminal region of exon 12 is three times higher in comparison to P1 cells. Similarly, 32 reads span exon 11 3' terminally and exon 12 5' terminally in P1 cells while reads spanning this region in PB1 cells are undetectable. These data are indicative of increased alternative splicing occurring in PB1 cells compared with P1 cells. Sanger sequencing of PB2 genomic DNA revealed an adenine insertion in codon 31 in *BRCA1* exon 3 (Fig. 3.7A). Again, I aimed to validate the Sanger sequencing data in the RNA sequencing data. In contrast to the observation of reduced coverage of the genomic region near the CRISPR/Cas9 mutation in PB1 cells, coverage of exon 3 remained consistent in P1, PB2 and PB3 cells. Indeed, all PB2 reads mapping to the genomic region of interest of *BRCA1* exon 3 showed the expected adenine insertion (Fig. 3.7A). Having validated the *BRCA1* mutations utilizing two orthogonal sequencing approaches in PB1 and PB2 cells, I next scanned *BRCA1* RNA sequencing reads in PB3 and determined that the same *BRCA1* exon 3 mutation was present in PB2 and PB3 (Fig. 3.7A, Table 3.1).

Mutations in *BRCA1* have been shown to be synthetically lethal with the inhibition of PARP proteins (Farmer et al., 2005). This relationship thus presented the potential to functionally validate *BRCA1* loss in the putative *TP53/BRCA1* double-mutant

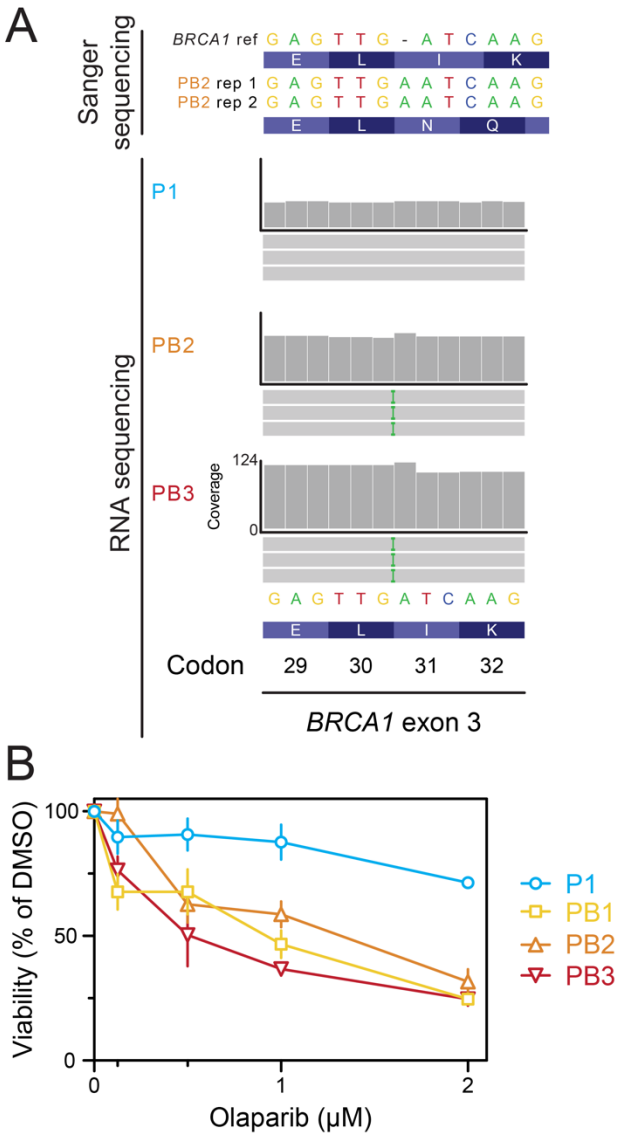

Figure 3.7: Mutations in BRCA1 exon 3 and 11 render *TP53/BRCA1* double-mutant FNE1 subclones sensitive to the PARP inhibitor Olaparib

A DNA Sanger and RNA sequencing reveal the insertion of an adenine at codon 31 in *BRCA1* exon 3 in PB2 and PB3. P1 was included in the RNA sequencing as control while the *BRCA1* reference (ref) sequence was used for Sanger sequencing. Three representative reads are included in the RNA sequencing data where the green vertical bar indicates the adenine insertion. **B** CellTiter-Blue® viability measurements of P1 and PB1-3 cells treated with escalating concentrations of the PARP inhibitor Olaparib for a period of seven days. Viability was normalized to DMSO treated cells. Error bars indicate standard deviation from three technical replicates.

subclones in a manner similar to the synthetically viable relationship observed in *TP53* single-mutant subclones with Nutlin-3. Therefore, P1, PB1, PB2 and PB3 cells were treated with an inhibitor of PARP, Olaparib, in an end-point assay to measure viability. In P1 control cells, viability remained largely unaffected in response to increasing concentrations of Olaparib as expected (Fig. 3.7B). In PB1, PB2 and PB3 cells, however, a concentration-dependent reduction in viability was observed which validates functional BRCA1-deficiency. This therefore demonstrated that I generated three genetically and functionally *TP53/BRCA1* double-mutant FNE1 subclones.

3.5: Generation of *MYC*-overexpressing mutant FNE1 subclones

Once I established *TP53* single-mutant and *TP53/BRCA1* double-mutant FNE1 subclones, I set out to ectopically overexpress the oncogene *MYC* as it is the most frequently amplified oncogene in HGSOC (Zeng et al., 2018). I chose to use a CRISPR/Cas9-resistant cDNA generated in the laboratory which would allow me to directly compare endogenous with ectopic *MYC* transcript levels in my downstream RNA sequencing experiments (Littler et al., 2019).

First and foremost, I generated a hygromycin-resistance conferring lentivirus to overexpress *MYC* driven by the human cytomegalovirus promoter. The cDNA used contained three synonymous mutations already and after generation of the lentivirus an additional fourth synonymous mutation was identified. Subsequently, I transduced P and PB subclones with either the control lentivirus (empty vector - EV) or the *MYC*-overexpressing lentivirus (Fig. 3.8A). Taking advantage of the RNA sequencing data, I next visualized the sequencing reads at the *MYC* locus and quantified the number of reads with the wildtype (endogenous) or mutant (ectopic) nucleotide at four locations (Fig. 3.8B). In P1M, P2M, P3M and PB1M endogenous *MYC* read counts were comparable and ectopic *MYC* reads exceeded endogenous *MYC* reads at least two-fold (Fig. 3.8C, Table 3.1). In contrast, in PB2M and PB3M endogenous *MYC* read counts were increased in comparison with the other samples. In PB2M, ectopic *MYC* reads were reduced at three sites compared with endogenous *MYC* reads, however at codon 181 ectopic *MYC* reads exceeded endogenous *MYC* reads. While ectopically expressed *MYC* reads were detected in PB3M at all four sites, endogenous *MYC* reads were detected at higher levels at each of them. As expected, MYC was also increased on the protein level in P1 cells transduced with the *MYC*-overexpressing lentivirus compared with empty vector lentivirus transduced cells (Fig. 3.8D). The decrease in BCL-XL abundance further suggests that ectopically expressed MYC is functional.

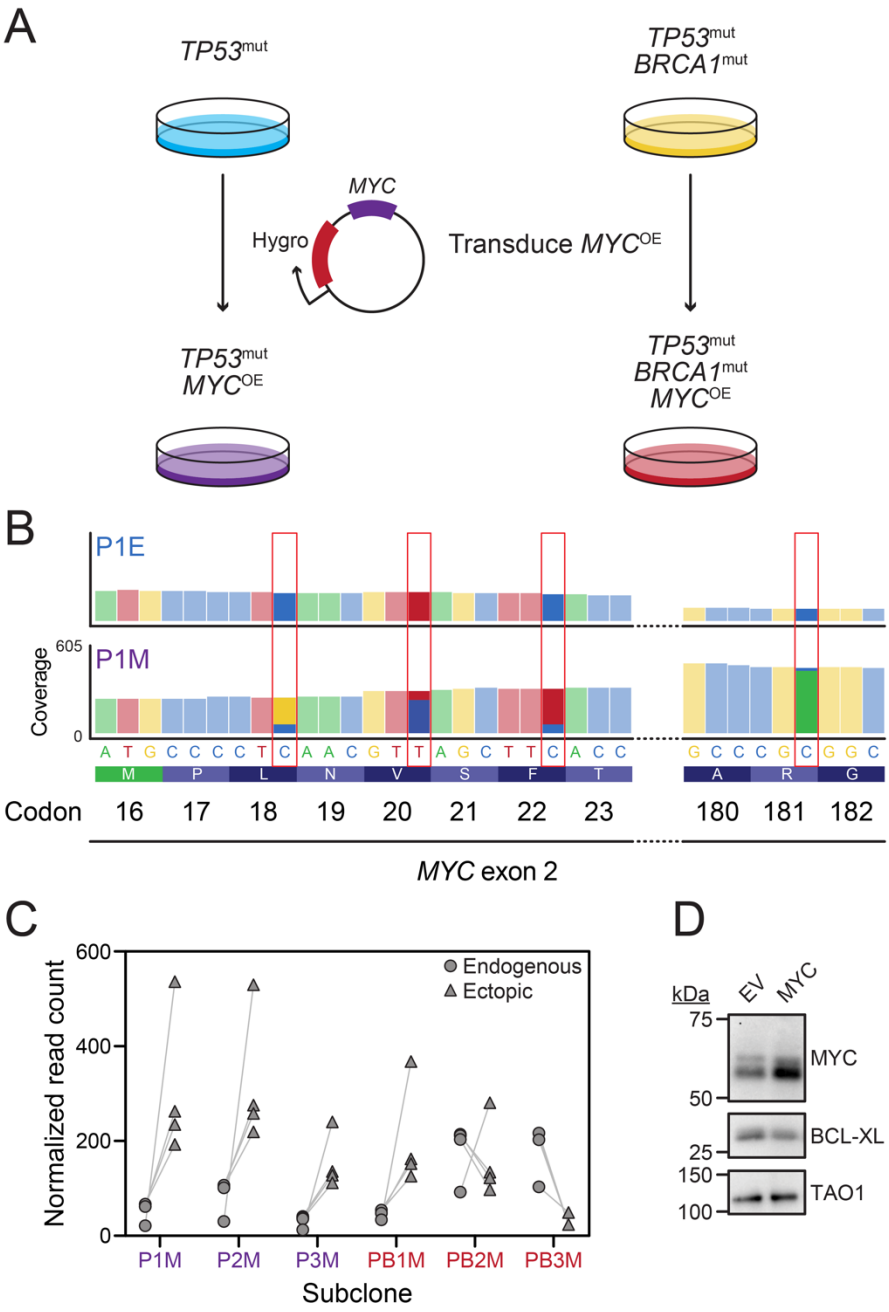

Figure 3.8: Ectopic overexpression of *MYC* in *TP53* single- and *TP53/BRCA1* double-mutant FNE1 subclones

A Schematic depicting the experimental approach of ectopic *MYC* overexpression (*MYC*^{OE}) in mutant FNE1 subclones by lentiviral transduction. **B** RNA sequencing coverage of *MYC* exon 2 in P1E and P1M cells starting at the translational start site indicated in green, codon 16. Red boxes indicate the nucleotides deviating from the wildtype sequence to control for ectopic *MYC* expression on the transcript level. **C** Quantitation of ectopically expressed *MYC* at the four mutant sites in six FNE1 subclones which were transduced with the *MYC*^{OE} lentivirus. Note, P1M was sequenced in triplicate thus the data presented here are the mean of three replicates. Raw read counts were normalized to uniquely mapped reads. **D** MYC and BCL-XL protein expression measured by immunoblot in P1 cells transduced with either an empty vector (EV) or MYC overexpression lentivirus. TAO1 serves as loading control.

To further validate MYC function in transduced subclones, I turned to the RNA sequencing data set. MYC is a well-established pleiotropic amplifier of transcription thus measuring an increase of differentially expressed genes would allow me to confirm its function (Lin et al., 2012; Nie et al., 2020; Nie et al., 2012). Therefore, I compared the number of differentially expressed genes in P vs FNE1 and PM vs FNE1 cells. When contrasting P vs FNE1 samples, 868 and 828 genes were found to be significantly differentially down- and upregulated, respectively (Fig. 3.9A). In comparison, in the contrast PM vs FNE1 2,533 and 3,266 genes were significantly down- and upregulated, respectively. Indeed, *MYC* itself was one of the most significantly upregulated genes in the PM vs FNE1 contrast. These analyses provide mounting evidence that ectopically expressed *MYC* is biologically active. In order to assess specifically if canonical *MYC* target genes were deregulated as expected gene set enrichment analysis (GSEA) of genes ranked by t-statistics after the analysis of differentially expressed genes was performed (Subramanian et al., 2005). Canonical *MYC* target genes have been summarized in two gene sets of the Hallmark gene set collection which were utilized for this analysis. Indeed, MYC target V1 and V2 gene sets are significantly positively enriched in PM vs P samples (Fig. 3.9B,C).

Taken together these data demonstrate that I have generated six *bona fide* *TP53/MYC* double-mutant and *TP53/BRCA1/MYC* triple-mutant FNE1 subclones.

3.6: Summary and discussion

In this chapter, I presented the generation of 18 novel *TP53* single-, *TP53/BRCA1* or *TP53/MYC* double- and *TP53/BRCA1/MYC* triple-mutant FNE1 subclones (Table 3.1). In addition to the initial screening by immunoblotting, all mutant subclones were subjected to genetic analyses of the CRISPR/Cas9-induced mutation by both Sanger sequencing and RNA sequencing. Furthermore, functional assays were employed to confirm p53- and BRCA1-deficiency capitalizing on well-established synthetic viable and synthetic lethal relationships with Nutlin-3 and Olaparib, respectively (Farmer et al., 2005; Vassilev et al., 2004). With regards to MYC-overexpression, RNA sequencing provided functional evidence of biologically active MYC due to its role in amplifying gene expression (Lin et al., 2012; Nie et al., 2020; Nie et al., 2012). This panel of genetically and functionally defined mutant FNE1 subclones is the first of its kind to the best of my knowledge and allowed me to investigate the consequences of the introduced mutations on hallmarks of CIN and thus address aim (iii), which will be presented in the next chapter.

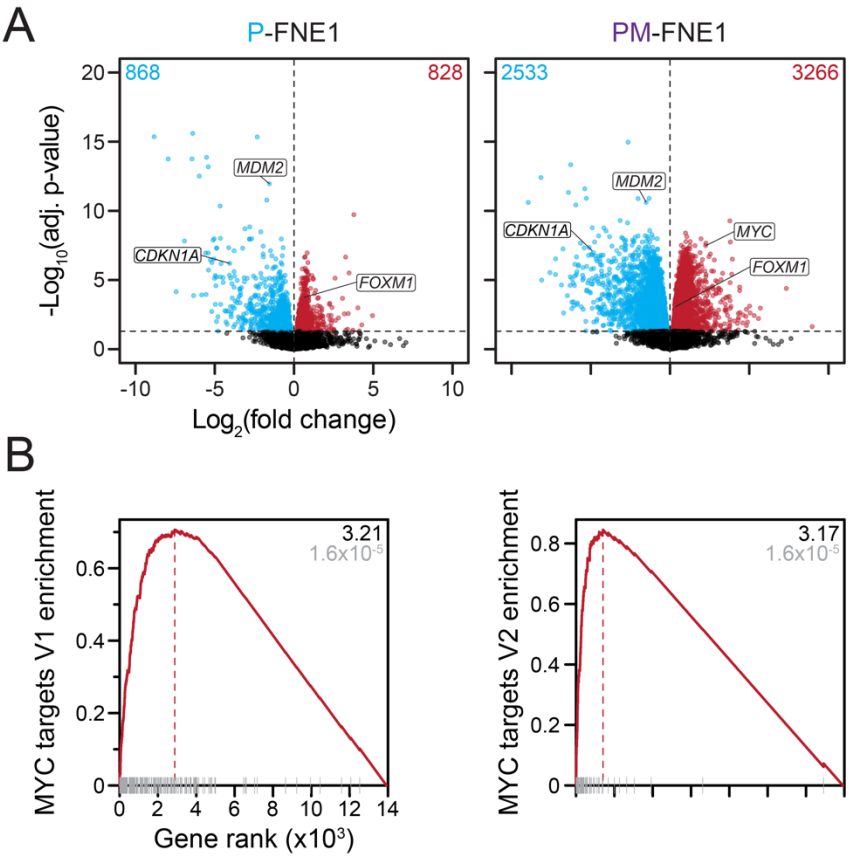

Figure 3.9: RNA sequencing shows ectopic MYC is functional
A Volcano plots of differentially expressed genes comparing *TP53*^{mut} (P) and *TP53*^{mut}/*MYC*^{OE} (PM) cells with FNE1 cells. Black indicates that genes do not reach significance of an adjusted (adj.) p-value ≤ 0.05, red and blue dots and numbers indicate genes that are significantly positively and negatively enriched, respectively. Canonical p53 targets *MDM2*, *CDKN1A* and *FOXM1* as well as *MYC* are highlighted exemplarily if significantly defferentially expressed. **B** shows gene set enrichment plots of the Hallmark MYC targets V1 and V2 gene sets in PM-P contrast, revealing enrichment of MYC targets in *MYC*^{OE} samples. Black and grey fonts are the normalised enrichment score and adj. p-value, respectively. Vertical grey bars reflect ranked genes contained in the gene sets.

As the generation of these subclones was founded on the p53-proficient, genomically stable FNE1 cells, which are a suitable model for the tissue of HGSOC origin, it is important to appreciate that the reliance on only one cell line is a limitation, because the conclusions drawn might not apply to all fallopian tube-derived cells. Thus, only analytical and contextual integration with observations made in other, independent model systems will allow more definitive conclusions about the biological deductions made based on this panel of mutant FNE1 subclones. This limitation will, in part, be addressed in *5.4: Cell cycle deregulation is also observed in mutant mouse oviduct organoids*. Additional, future work using alternative model systems such as human fallopian tube-derived organoids that do not depend on *TP53* mutagenesis will complement the presented panel (Kessler et al., 2015). This model system was ruled out as these organoids are comprised of both ciliated and non-ciliated, secretory fallopian tube epithelial cells. However, this particular aspect also provides an interesting opportunity to study if *TP53*-mutagensis impacts differentiation and organoid composition, an aspect that was not yet looked at in the mouse oviduct organoids (Iyer et al., 2021; Lohmussaar et al., 2020; Zhang et al., 2019; Zhang et al., 2021).

Cell line	*TP53*			*BRCA1*					*MYC*		
	Nucleotide sequence	Protein sequence	Full length protein expression	Nucleotide sequence	Protein sequence	Full length protein expression	HRP/D	PARPi	RNA[§] 4 sites End	RNA[§] 4 sites Ect	RNA[§] CPM
FNE1	WT	WT	Pres	WT	WT	Pres*	HRP[†]		149	0	6.11
P1	r.40_44delCTGAG	p.Leu14Serfs*12	Abs	WT	WT	Pres	HRP	Res	127	0	6.06
P1E									133	0	6.16
P1M									54	307	8.37
P2	r.40_41delCT	p.Leu14Glufs*13	Abs	WT	WT	Pres*	HRP[‡]		176	0	6.26
P2E									119	0	6.05
P2M									85	321	8.42
P3	r.40_41delCT	p.Leu14Glufs*13	Abs	WT	WT	Pres*	HRP[‡]		123	0	6.46
P3E									167	0	6.35
P3M									32	154	8.33
PB1	r.40_44delCTGAG	p.Leu14Serfs*12	Abs	c.4038_4039insA	p.Glu1346Glufs*10	Abs	HRD	Sen	120	0	6.32
PB1E									174	0	6.39
PB1M									47	202	8.02
PB2	r.40_44delCTGAG	p.Leu14Serfs*12	Abs	c.90_91insA	p.Ile31Asnfs*10	Abs	HRD	Sen	143	0	6.53
PB2E									157	0	6.23
PB2M									180	159	7.53
PB3	r.40_44delCTGAG	p.Leu14Serfs*12	Abs	r.90_91insA	p.Ile31Asnfs*10	Abs	HRD	Sen	308	0	7.17
PB3E									396	0	7.13
PB3M									184	30	7.25

Table 3.1: Geno- and phenotype summary of mutant FNE1 subclones

Mutations and expression of full length protein in individual cell lines are indicated. Pres - present; Abs - absent; WT - wildtype; HRP - Homologous recombination proficiency; HRD - Homologous recombination deficiency; Res - resistant; Sen - sensitive; End - endogenous; Ect - ectopic. CPM - Log_2-transformed, counts per million. *BRCA1 protein expression was not assessed, however, there is no indication of *BRCA1* mutations. [†]HRP of FNE1 cells was shown by Tamura et al. (2020). [‡]HRP was not formally tested, however, there is no indication of BRCA1 mutations. [§]Normalized RNA expression was quantified at four sites with synonymous mutations to calculate a mean across all four sites. Where samples were sequenced in triplicate (FNE1, P1/E/M) the mean of all samples was generated.

Chapter 4: Assessing chromosomal instability in mutant FNE1 subclones

4.1: Overview

The role of p53 in protecting diploidy in humans and other mammals has been studied intensively. Indeed, data to support and refute a role of p53 in diploidy maintenance have been reported. Initial studies using p53-proficient and -deficient HCT116 cells had suggested that p53 was not required to maintain diploidy (Bunz et al., 2002). Rather p53-loss led to a modest increase in tetraploidy. Similar observations were made using the same cell lines, however, pharmacological perturbation of mitosis revealed a role for p53 in suppressing the growth of emerging aneuploid cells (Thompson and Compton, 2010). In contrast, analyses of cancer genomics data showed that tumours harbouring *TP53* mutations are more aneuploid and chromosomally unstable than tumours harbouring wildtype *TP53* (Davoli et al., 2017; Shukla et al., 2020; Taylor et al., 2018; Zack et al., 2013). Indeed, more recent studies utilizing RPE-1 cells have shown that p53-suppression by RNAi or CRISPR/Cas9 mutagenesis leads to increases of non-clonal chromosomal gains and losses (Kok et al., 2020; Soto et al., 2017). These observations merit further investigation of the interplay between p53-loss and CIN in a physiological relevant setting.

It is widely accepted that HGSOC is one of the most chromosomally unstable tumour entities (Ciriello et al., 2013; Shukla et al., 2020; Taylor et al., 2018). Indeed, is has been shown that HGSOC patients' cells cultured *ex vivo* displayed profound mitotic heterogeneity and an in-depth analysis of hundreds of live cells undergoing mitosis from ten patients revealed that some cells exceed 6 hours from nuclear envelope breakdown to anaphase onset (Nelson et al., 2020). However, studying the role of p53 in ploidy maintenance and CIN in HGSOC directly has previously been hindered by the unavailability of matched p53-proficient and -deficient model systems which I have overcome by generating p53-deficient subclones of the otherwise p53-proficient FNE1 cells. Similarly, the role of BRCA1 and MYC in ploidy control in HGSOC has not been studied in detail.

In this chapter, I am presenting data from experiments performed to probe ploidy maintenance in the mutant FNE1 subclones I described in *Chapter 3: Characterization and genetic engineering of FNE1 cells*. These data were collected to address aim (iii) set out in *1.7: Rationale and aims*. Thus, I utilized three orthogonal approaches

that assess aneuploidy to make inferences about the presence or absence of ongoing CIN in wildtype and mutant FNE1 cells.

4.2: Whole genome doubling occurs in *TP53*, *BRCA1* exon 3 double-mutant FNE1 subclones

As a first step, I utilized two complementary approaches with different sensitivities of detecting aneuploidy and throughput. Flow cytometry is the ideal methodology to obtain a low-resolution picture of ploidy changes in a large number of cells based on the analysis of DNA content. In contrast to the high throughput that flow cytometry enables, multiplex interphase Fluorescence *in situ* Hybridization (miFISH) allows for the detection of specific gene-level copy number changes in single cells (Heselmeyer-Haddad et al., 2012).

Therefore, I first assessed the DNA content of *TP53* single and *TP53*/*BRCA1* double-mutant cells either in the presence of an empty vector control or *MYC* overexpression construct by flow cytometry. I observed that P1E and P1M cell seemed largely diploid (2c) as evidence by sharp G1 and G2 peaks reflective of cells with a 2c genome and those which have gone through S-phase having replicated their genome; cells with a replicated genome are now reminiscent of tetraploid (4c) cells (4c; Fig. 4.1). The *TP53*/*BRCA1* double-mutant samples displayed heterogeneity with respect to their ploidy. PB1E and PB1M cells, like P1E/M cells, both seemed largely diploid with a characteristic 4c peak of replicated cells in either G2 or mitosis. In contrast to P1E, P1M, PB1E and PB1M cells, the other two *TP53*/*BRCA1* double-mutant subclones showed increases in ploidy. In PB2E/M cells, I observed two cycling populations, one 2c and one 4c as evidenced by an 8c peak which reflects replicated 4c cells. In PB3E/M cells, I only observed 4c and 8c peaks, but no 2c peak, indicating that this subclone has undergone a WGD event which resulted in the manifestation of a 4c population that outcompeted any remaining 2c cells.

In order to increase the sensitivity in aneuploidy detection, I turned to miFISH, which is most powerful when determining copy numbers of cancer type-specific genes as it is limited by the number of targets. In this case, I aimed to assemble four panels that each contained five DNA FISH probes targeting at least one centromere and 19 gene loci totalling 20 targets. To determine which centromere and loci would be most suitable for the miFISH analysis, I turned to a publicly available dataset of copy number changes in HGSOC (Taylor et al., 2018). In their study, Taylor et al. (2018) computed arm level gains and losses for 552 HGSOCs analysed as part of the Cancer Genome Atlas Research Network as integers where -1, 0 and 1 designate loss, no change or

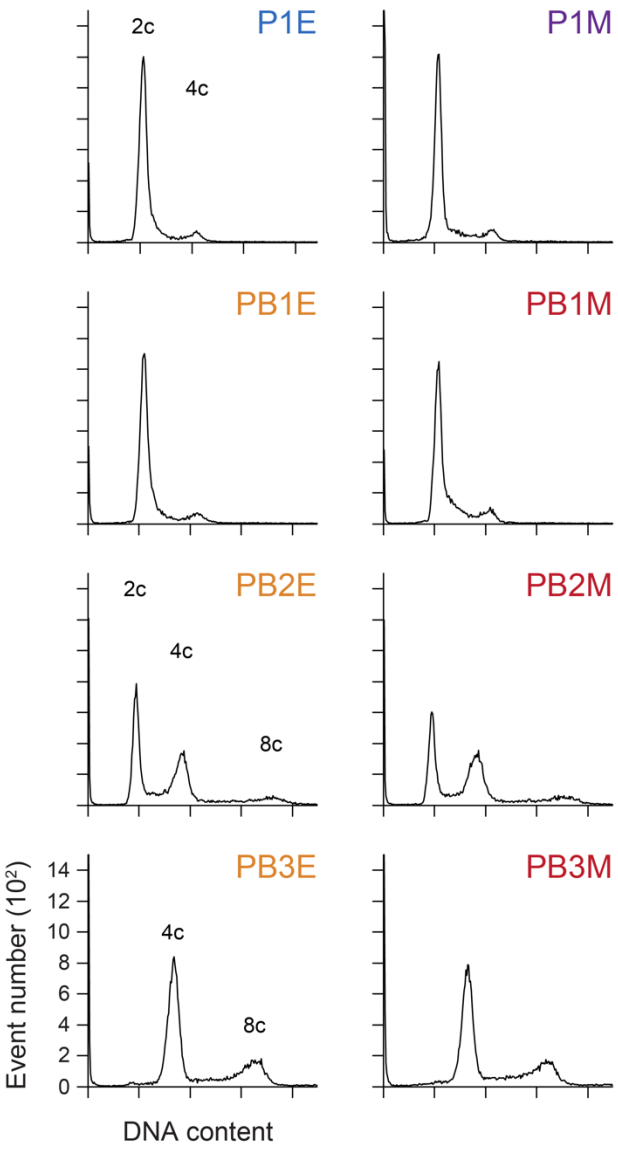

Figure 4.1: DNA content analysis suggests whole genome doubling in *TP53* and *BRCA1* exon 3 double-mutant FNE1 subclones
DNA content was measured by flowcytometric analysis of DAPI stained cells. Ungated samples are shown where 2c, 4c and 8c indicate a diploid, tetraploid and octoploid DNA content of at least 10,000 single cells.

gain of a given chromosome arm, respectively. I utilized these data to inform my decision making by evaluating how frequently chromosome arms were gained or lost (Fig. 4.2A). The reanalysis of these data revealed that several chromosome arms were altered at a frequency higher than 50%. Chromosome arms 3q, 8q and 20q were gained in more than 50% of cases while the following chromosome arms were lost in more than 50% of cases 4q, 5q, 6q, 8p, 9q, 13q, 15q, 16q, 17p, 17q, 18q and 22q. Of note, chromosome arms that were frequently lost were rarely gained and vice versa. Based on this analysis, the selected miFISH probes cover centromere 10 and 18 chromosome arms including twelve of the 15 chromosome arms were subject to copy number changes in at least 50% of cases (Fig. 4.2B). Once I established the four panels, I sequentially hybridized, stripped and rehybridized (after each individual panel) the parental FNE1 and the most aberrant, PB2M and PB3M, subclones to enumerate copy number changes in single cells (Fig. 4.2C).

The analysis of FNE1 cells showed that 93 of 100 cells analysed had two signals for 19 of the 20 loci (Fig. 4.3A). The *CDKN2A* locus was the only deviation from the signal pattern consistently displaying only one signal which is in agreement with the described loss of a segment of chromosome 9 where *CDKN2A* maps (described previously in Fig. 3.1). Of the remaining 7 cells, which deviated from the two-signal pattern, 4 cells displayed only one signal of the following genes *PIK3CA*, *FBXW7*, *CCNB1* and *MYC*. In one cell, I detected three *PTEN* signals and two other cells harboured multiple deviations. One cell showed three *FBXW7* signals and one *SMAD4* signal whereas another cell had three signals of the following genes: *DBC2*, *MYC*, *CCND1* and *ZNF217*. In contrast to FNE1 cells, PB2M and PB3M cells are not as homogenous. In the 2c population of PB2M, I observed only one signal for *COX2*, *CDKN2A* (as expected from observations made in FNE1 cells) and *RB1* (Fig. 4.3B). This reduction in signal counts is clonal as it is observed in the vast majority of cells analysed and maintained in the 4c population of cells where it is detected as two signals, a result of its doubling (Fig. 4.3C). Further, miFISH allowed me to definitively determine that 85% of the PB2M population are 2c and 15% of the population are 4c. In contrast to all other cell lines analysed by either flow cytometry or miFISH, PB3M is the only mutant subclone where no 2c population of cells was detected either by flow cytometry or miFISH. In PB3M cells, like 4c PB2M cells, I detected four signals for most loci with the following exceptions: *COX2*, *FBXW7*, *CDKN2A* (as expected from observations made in FNE1 and 4c PB2M cells) and *CDH1* mostly displayed two signals (Fig. 4.4A). Most interestingly in PB3M, the three probes mapping to chromosome 17, i.e., *TP53* (17p), *NF1* and *HER2* (both 17q) show a discrepancy; in many cells the signal

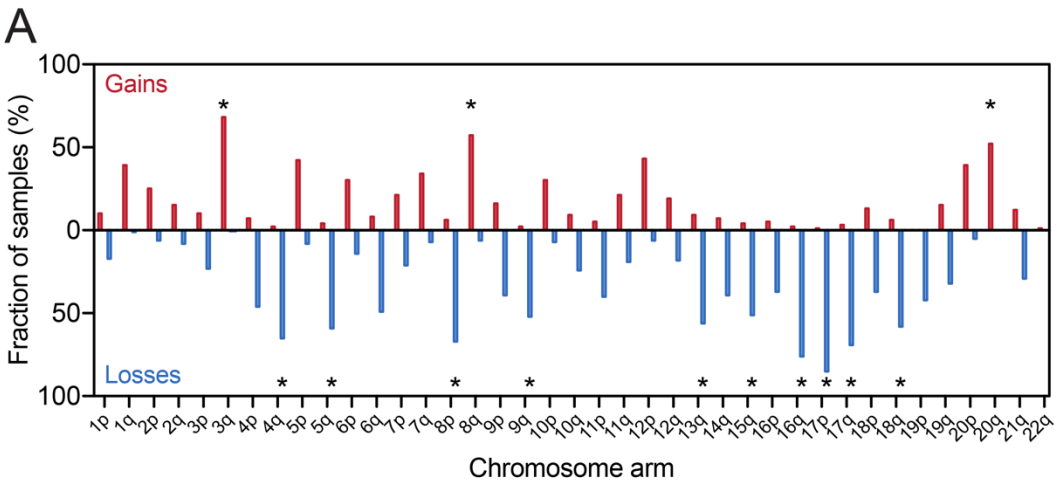

B

Color	Panel 1	Panel 2	Panel 3	Panel 4
	COX2 (1q31.1)	*CCNB1* (5q13.2)	*FBXW7* (4q31.3)	*PTEN* (10q23.31)
	RB1 (13q14.2)	*NF1* (17q11.2)	*CCND1* (11q13.3)	*CDH1* (16q22.1)
	KRAS (12p12.1)	*TP53* (17p13.1)	*SMAD4* (18q21.2)	*NF2* (22q12.2)
	DBC2 (8p21.3)	*PIK3CA* (3q26.32)	CCP10	*HER2* (17q12)
	MYC (8q24.21)	*ZNF217* (20q13.2)	*CCNE1* (19q12)	*CDKN2A* (9p21.3)

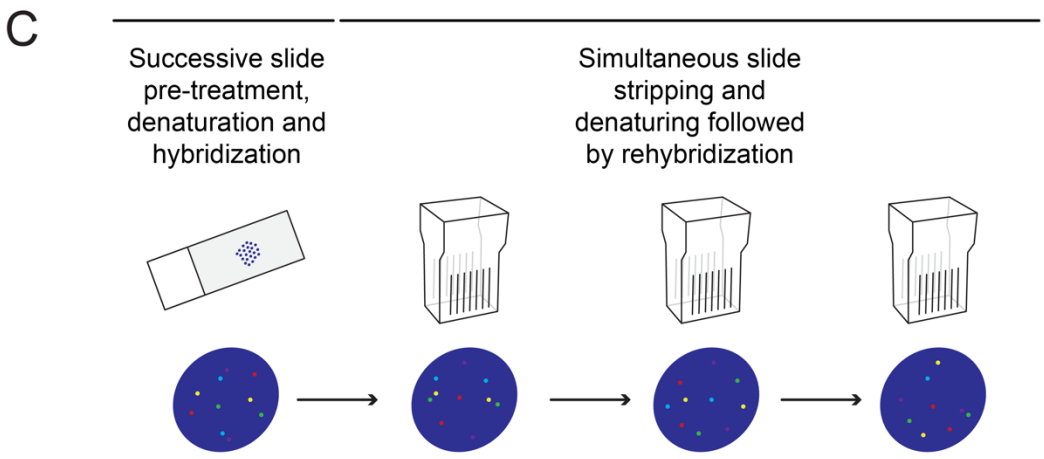

Figure 4.2: Selection of high-grade serous ovarian cancer-specific gene probes and miFISH schematic

A Reanalysis of chromosome arm copy number gains (red) and losses (blue) in 522 HGSOC samples based on publicly available data from Taylor et al. (2018). Asterisks denote chromosome arms altered in more than 50% of samples. Note, unaltered samples were omitted, hence the sum of gains and losses does not add up to 100%. **B** Summary of colour and panel allocation of one centromere and 19 gene probes used for the analysis of copy number changes in mutant FNE1 subclones. Chromosomal location is indicated in parenthesis. **C** Schematic of miFISH methodology depicting initial pre-treatment, denaturation and hybridization of slides which is followed by imaging. Rehybridization is preceded by a one-step stripping and denaturing procedure in coplin jars, followed by imaging and repeated twice totalling four panels.

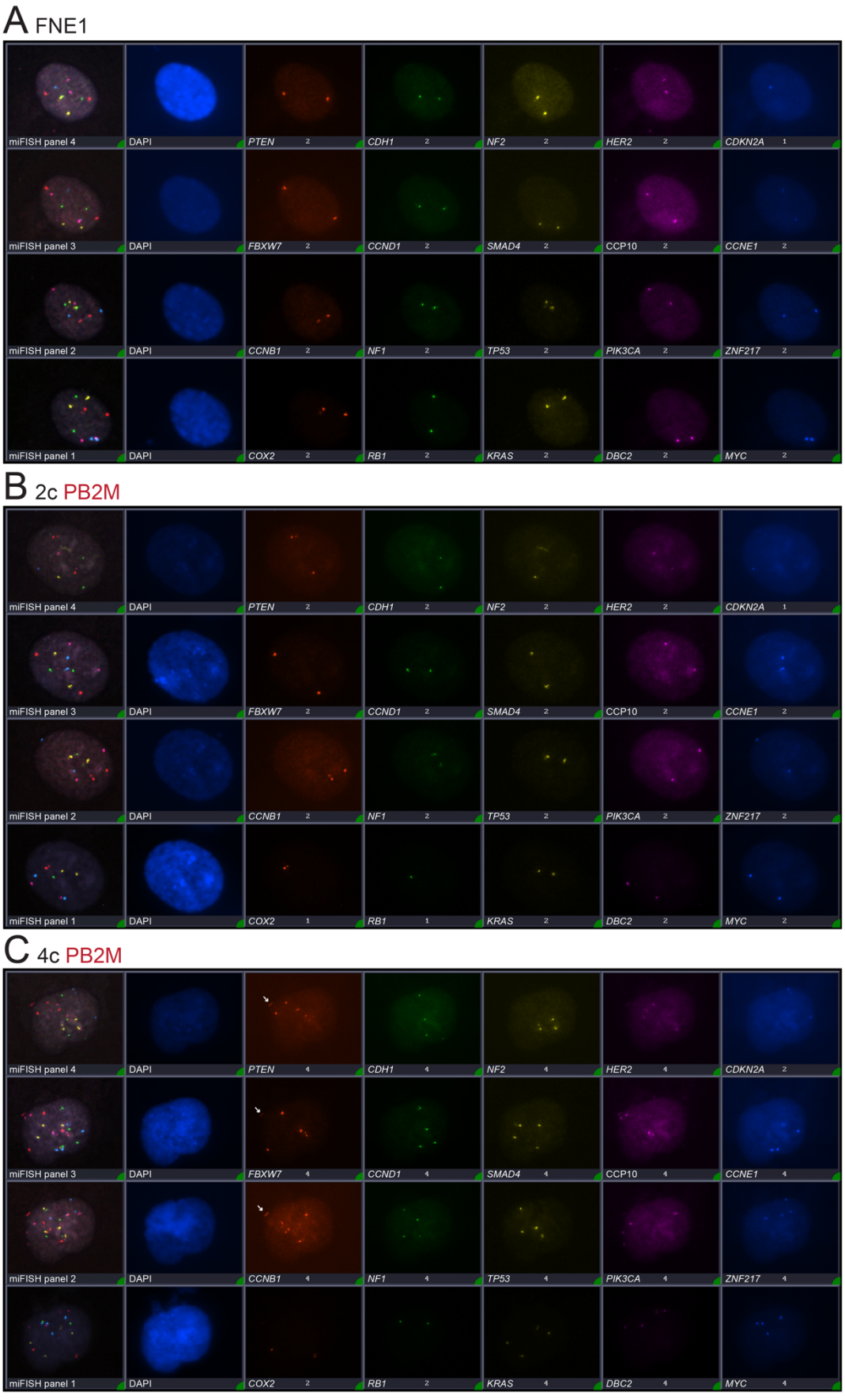

Figure 4.3: Representative images of FNE1, diploid as well as tetraploid PB2M cells
A, **B** and **C** show representative miFISH images of FNE1, diploid PB2M and tetraploid PB2M cells. Arrow denotes a hybridization artifact.

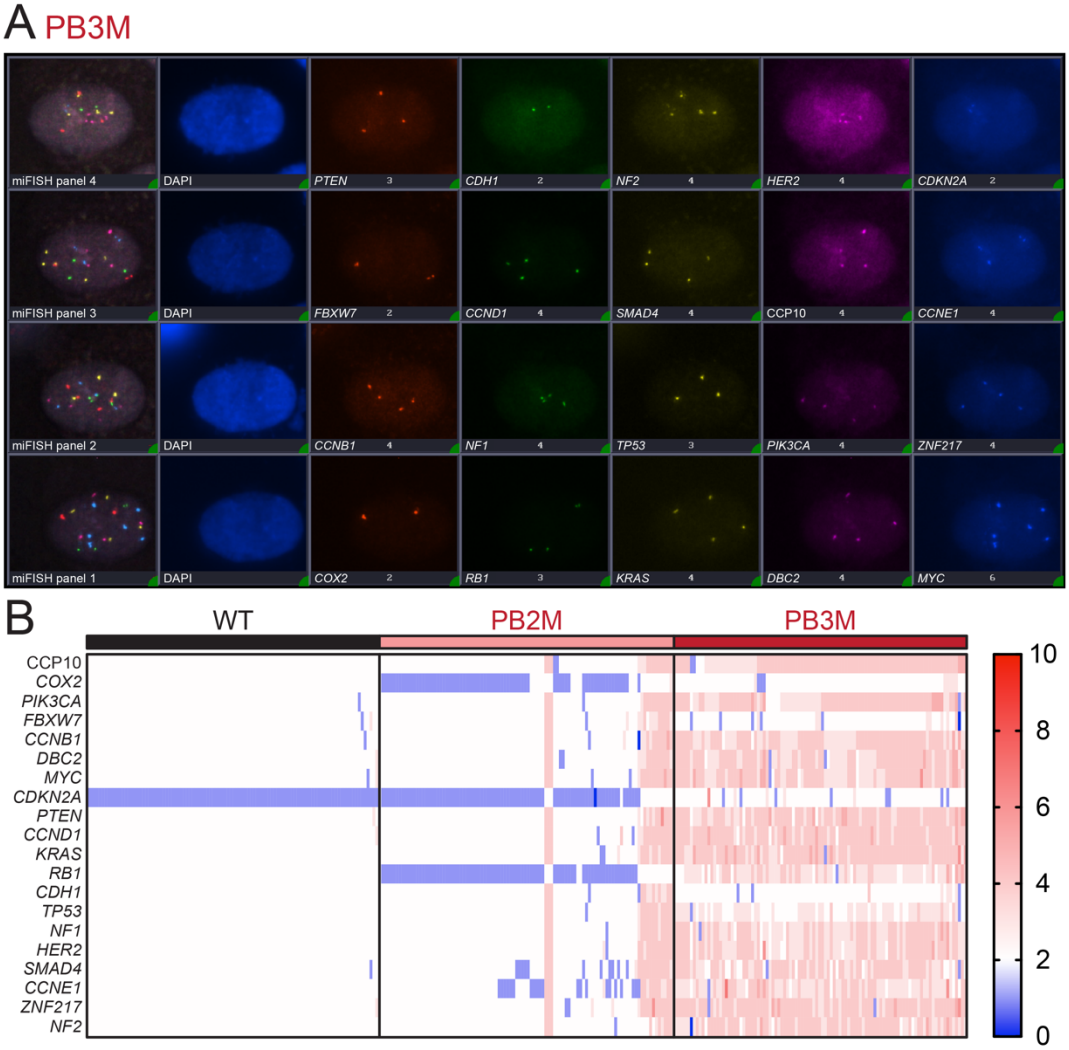

Figure 4.4: miFISH corroborates flow cytometric DNA ploidy measurements
A Exemplar miFISH image of a PB3M cells with six copies of MYC. **B** Quantitation of miFISH signals observed in 100 FNE1, PB2M and PB3M cells. Centromere and gene loci are plotted as rows and each column represents a single cell. The colour indicates the copy number at which the respective centromere or gene locus was detected. White indicates diploidy whereas blue and red indicate loss and gain from a diploid baseline, respectively.

count of *TP53* is reduced by exactly one count compared with *NF1* and *HER2* (Fig. 4.4B). Overall, PB3M is the most unstable of the three samples I assessed using miFISH as evidence by the fact that no two cells display the same signal pattern.

I conclude that upon mutation of *BRCA1* in exon 3 tetraploidy emerged in PB2E/M and PB3E/M although only PB2E/M cells remained heterogenous by maintaining a 2c and 4c population.

4.3: Low level aneuploidy is already observed upon *TP53* mutagenesis

Flow cytometry and miFISH yielded valuable insight into the emergence of aneuploidy and CIN across a number of mutant subclones, however, to analyse aneuploidy in more mutant subclones genome-wide, I turned to single cell shallow-depth whole genome sequencing.

I chose to perform the analysis on subclones which were in parental relationships. Therefore, the scWGS analysis was carried out on FNE1, P1, PB2/E/M and PB3/E/M cells which included subclones that were not transduced with a lentivirus, transduced with an empty vector lentivirus or transduced with the *MYC*-overexpressing lentivirus. Consistent with the validation of the FNE1's karyotype in *3.2: FNE1 cells are near-diploid and p53-proficient*, the additional scWGS analysis showed that FNE1 cells harbour disomies across the genome with the following exceptions: segmental monosomies of chromosome arms 9p and 15p as well as the X chromosome (Fig. 4.5). Interestingly, one FNE1 cell from the second scWGS experiment harboured a tetraploid karyotype at baseline with additional segmental and whole chromosome losses, e.g., this cell only had three copies of chromosome 13 and only one copy of the X chromosome, however, this cell represents an exception since the majority of cells are diploid. In contrast, P1 cells showed additional, non-clonal segmental and whole chromosome monosomies and trisomies across the entire genome and two cells showed the same tetrasomy of chromosome arm 11q (Fig. 4.5). In fact, only two of the 35 sequenced FNE1 cells displayed partial or whole chromosome aneuploidies compared with ten of 18 P1 cells. While FNE1 and P1 cells have a diploid baseline with minimal and moderate deviation from the modal copy number profile, respectively, PB2/E/M and PB3/E/M cells show more deviation and heterogeneity.

Since the presence of PB2/E/M cells with two different ploidies is known from the previous analyses, I decided to sequence equal numbers of 2c and 4c PB2/E/M cells. Thus, the equal number of 2c and 4c PB2/E/M cells in this analysis might suggest an over-representation of 4c cells which is not reflecting the cell population as a whole. As expected from the miFISH data (Fig. 4.4B), PB2/E/M and PB3/E/M cells were

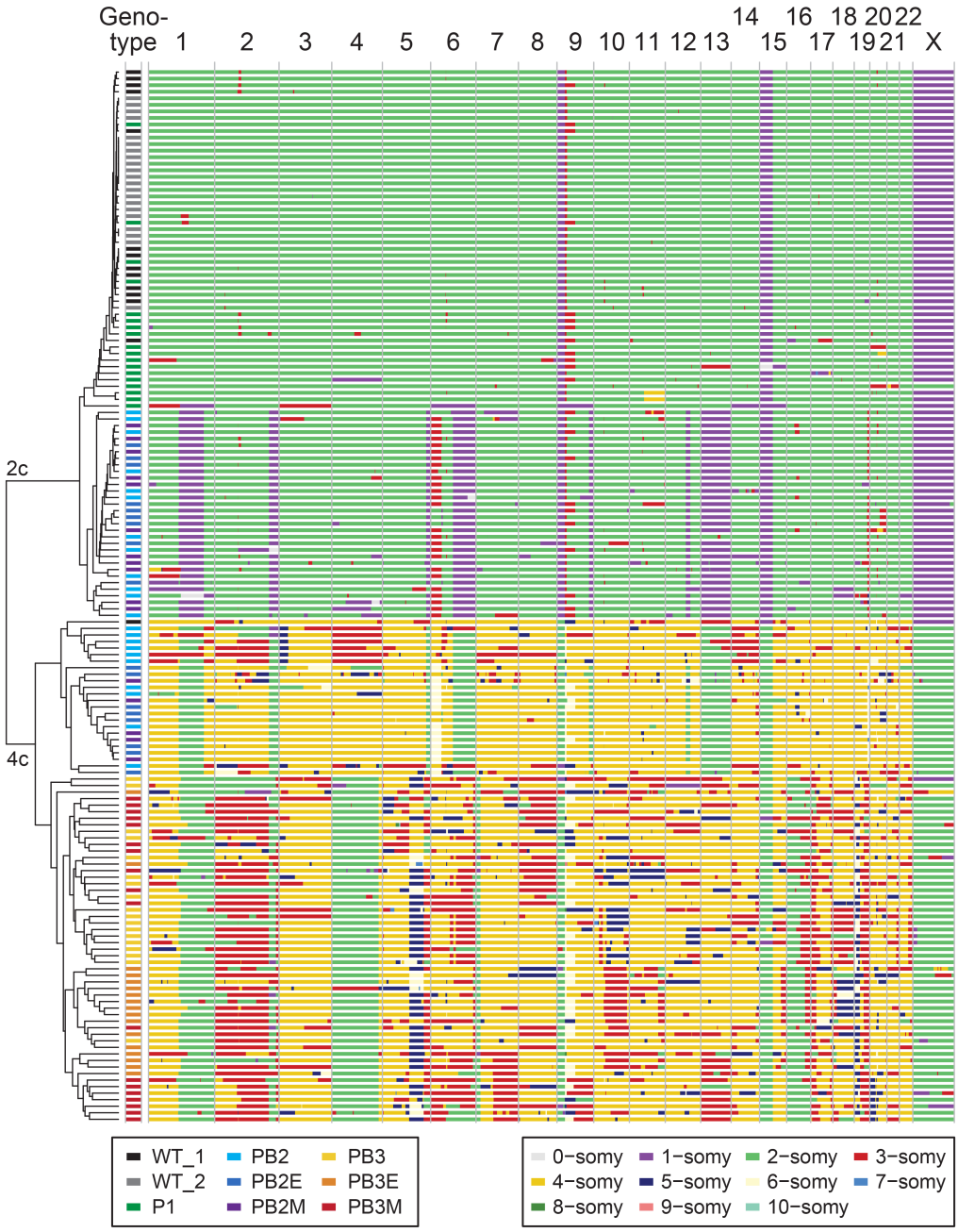

Figure 4.5: Single-cell whole genome sequencing reveals aneuploidy and chromosomal instability in mutant FNE1 subclones
Individual cells and chromosomes are plotted horizontally as rows and vertically as columns, respectively. The first column on the left indicates the genotype of the corresponding cell by colour and is associated with the left-hand box. The colour of the other horizontal bars reflects the detected copy number at the respective chromosomal location and is associated with the right-hand box.

found to be monosomic and disomic for chromosome arm 1q (*COX2*) in the diploid and tetraploid populations, respectively (Fig. 4.5). This commonality is intriguing, however, upon closer inspection PB3/E/M cells have lost the entirety of chromosome arm 1q whereas in PB2/E/M cells, the region closer to the telomeric end of chromosome arm 1q is disomic and tetrasomic in the diploid and tetraploid cells, respectively. In addition to this shared copy number change of chromosome 1q, PB/E/M2 and PB/E/M3 cells also share an aberration towards the telomeric end of chromosome arm 2q. Similar to 1q, PB2/E/M cells were found to have a monosomic and disomic segment near the telomere of chromosome 2q in the 2c and 4c cells, respectively, while the remainder of the chromosome did not deviate from the ploidy in most of the cells. In contrast, in PB3/E/M cells the baseline of chromosome 2 is not tetrasomic, but trisomic and the loss near the telomere of chromosome arm 2q is segmental with the region closest to the telomere being trisomic, i.e., at modal ploidy of that chromosome arm.

Beyond these commonalities, PB2/E/M were also found to have an aberration of chromosome 6 which had previously remained undetected as chromosome 6 was not probed by miFISH. In the 2c cells, the short arm 6p is trisomic while the long arm 6q is monosomic, intriguingly the centromeric region remains disomic. This aberration is reflected in the 4c cells by a two-fold increase in dosage. An expected result is the monosomy and disomy of chromosome 13 in the 2c and 4c PB2/E/M cells, respectively. *RB1* maps to chromosome 13 and was already found to be present in one or two copies using miFISH. In a manner similar to PB2/E/M cells, I observed expected and unexpected copy number changes in PB3/E/M cells. The expected results are the disomies of chromosomes 4 and 16 where *FBXW7* and *CDH1* map, respectively. Similarly, I noted the reduction in signal counts between chromosome arms 17p (*TP53*) and 17q (*NF1* and *HER2*) by one in the scWGS data. Unexpected findings in PB3/E/M include some cells harbouring penta- and hexasomies of chromosome arm 5q. Furthermore, tri- and pentasomies of chromosome 10 were observed. Overall, in PB3/E/M cells losses are quite striking, in particular those observed on chromosome 2 where only very few tetrasomies are detected. These data, despite the shared features observed on chromosomes 1 and 2 between PB2/E/M and PB3/E/M cells suggest that WGD occurred independently.

In addition to this qualitative description, quantitative analysis of the data by unsupervised hierarchical clustering separates the cells at multiple nodes. First and foremost, the cells are separated into a 2c and 4c cluster (Fig. 4.5). Within the 2c cluster in turn, WT and P1 cells form a cluster defined by disomies with the occasional deviation and

PB2E/M cells form a cluster defined by mostly disomies and the described clonal monosomies. Of note, the WT and P1 cells are mostly distinct from one another and the cophenetic distance between P1 cells is larger than it is between WT cells even from the two different sequencing runs. This increase in cophenetic distance between cells is also observed in the 2c PB2E/M cells. Within the 4c cluster, cells are separated by subclone and the cophenetic distance between cells is larger than it was in the 2c cluster. Interestingly, the clustering analysis does not separate PB2E/M or PB3E/M cells into parental, empty vector lentivirus transduced or *MYC*-overexpressing lentivirus transduced cells.

Ultimately, the scWGS data was used to calculate aneuploidy, heterogeneity and structural scores (Fig. 4.6). Each one of these scores reflects the extent of deviation from an assumed diploid baseline, the deviation from one cell to another and the number of changes (oscillation) in copy number per megabase, respectively. In a manner similar to the unsupervised hierarchical clustering, the scoring of FNE1s and mutant subclones separated them into 2c and 4c clusters. FNE1 and P1 cells were found to be similar to one another, however, the one near-tetraploid FNE1 cell impacted the score in a way that would suggest FNE1 cells are more aberrant than P1 cells (Fig. 4.6). The exclusion of this single cell, however, confirms that quantitatively these cells are not dramatically different. PB2E/M cells are structurally more aberrant than FNE1 and P1 cells but score similarly in terms of aneuploidy. In contrast, all 4c cells increase in aneuploidy, heterogeneity and structural scores. Interestingly, PB2E and PB2M cells show slightly higher aneuploidy and structural scores than PB2 cells which might be confounded at least for PB2M by fewer successfully sequenced and analysed cells. In contrast, the heterogeneity score of PB2 is higher than in PB2E and PB2M cells. The PB3E/M cells score similar with regards to all three scores where the structural score is moderately higher in PB3 and PB3E cells.

In conclusion, scWGS corroborates flow cytometric and miFISH data, but in addition provides a picture of the whole genome which uncovered additional karyotypic changes that were previously undetectable by miFISH.

4.4: *TP53* loss of function permits tolerance of CENP-E inhibition

Since I already observed low levels of CIN without additional perturbations in P1 cells, I decided to perturb mitosis pharmacologically using an inhibitor of the mitotic kinesin CENP-E using the small molecule inhibitor GSK923295 (henceforth CENP-Ei). This way, I could achieve both, a similarly increased mitotic duration as observed in *ex vivo* patient cells and an increase in chromosome mis-segregation.

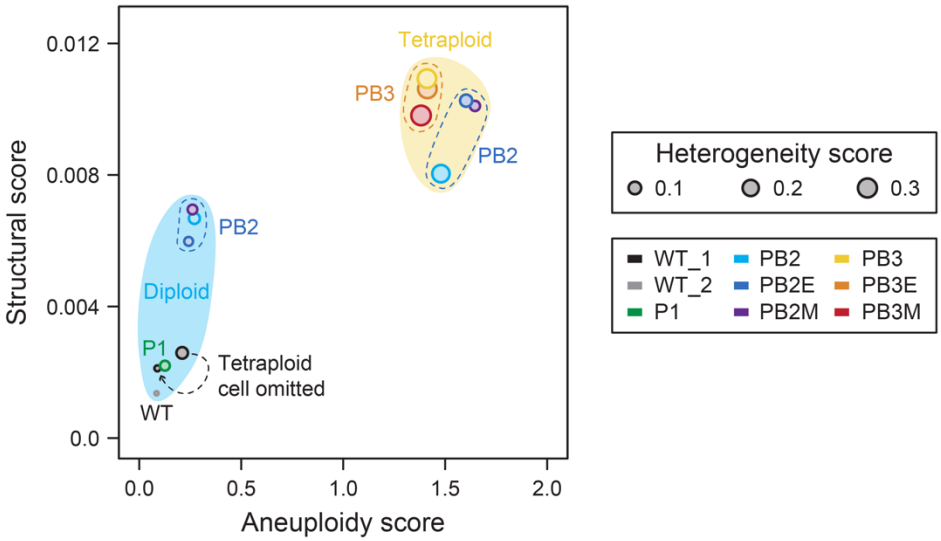

Figure 4.6: PB2/E/M and PB3/E/M subclones display elevated structural changes and cell to cell heterogeneity
Aneuploidy, heterogeneity and structural scores were computed based the single-cell whole genome sequencing data presented in the previous figure and plotted to obtain a picture of differences and similarities between FNE1 and mutant cells. The colour and the size of the individual bubble correspond to genotype and the heterogeneity score, respectively.

First, I determined an operating concentration of the CENP-Ei using live-cell microscopy measuring confluence over time to infer cellular proliferation. I performed a two-fold titration of CENP-Ei between 0.03 µM and 2 µM as well as vehicle treatment. Due to the number of technical replicates and cell lines used, I performed this initial experiment in a 96-well microtiter plate, however, noticed upon analysis that FNE1 cells which served as control did not proliferate as well as P1 cells did, even under vehicle-treated conditions (Fig. 4.7A). An independent experiment confirmed this observation which ultimately led me to switch to a 24-well microtiter plate (Fig. 4.7B). I also decided, based on the data from the experiments using P1 cells and a previous report also using the CENP-Ei, to proceed with an operating concentration of 250 nM (Fig. 4.7A,B) (Littler et al., 2019).

Indeed, the change from a 96-well to a 24-well microtiter plate alleviated the suppression in proliferation in FNE1 cells under control conditions which meant that the observed phenotype could be attributed to the inhibition of CENP-E directly excluding the possibility of a synthetic, combination effect. Under control conditions, FNE1 and P1 cells proliferated at a comparable rate as indicated by a consistent increase in confluence over the first 48 hours of filming (Fig. 4.8A,B). From that timepoint onward, both cell lines plateaued, although P1 cells ceased proliferation 12 hours later than FNE1 cells at higher confluence. In contrast, CENP-Ei treated cells displayed a very different pattern of proliferation. In both cases, during the first 24 hours of filming, confluence did not increase at all. After that, FNE1 cells steeply increased in number as reflected by a rapid increase in confluence and plateaued after 48 hours. In contrast, P1 cells showed a less dramatic increase in confluence and plateaued after 36 hours after which confluence rose a second time. Ultimately, after 96 hours both cell lines were similarly confluent and, in both cases, less confluent than control cells. Assessing the number of mitotic cells revealed that CENP-Ei treated FNE1 and P1 cells arrested increasingly in mitosis for 20 hours prior to the increase in confluence (Fig. 4.8C). Over time, fewer mitotic FNE1 cells were observed, in contrast, an increase in mitotic P1 cells was observed again after 36 hours. This suggests that FNE1 cells divide only once in the presence of CENP-Ei, however, P1 cells divide at least twice under the same conditions.

I next tested if this proliferative advantage of P1 over FNE1 cells also held true long-term. For that purpose, I performed colony formation assays treating FNE1 and P1 cells for 24, 48 and 72 hours with vehicle or CENP-Ei. I washed out CENP-Ei at indicated timepoints and allowed the cells to grow for up to 11 days. Colony formation was suppressed in FNE1 cells to levels below 20% of vehicle treated cells after 24

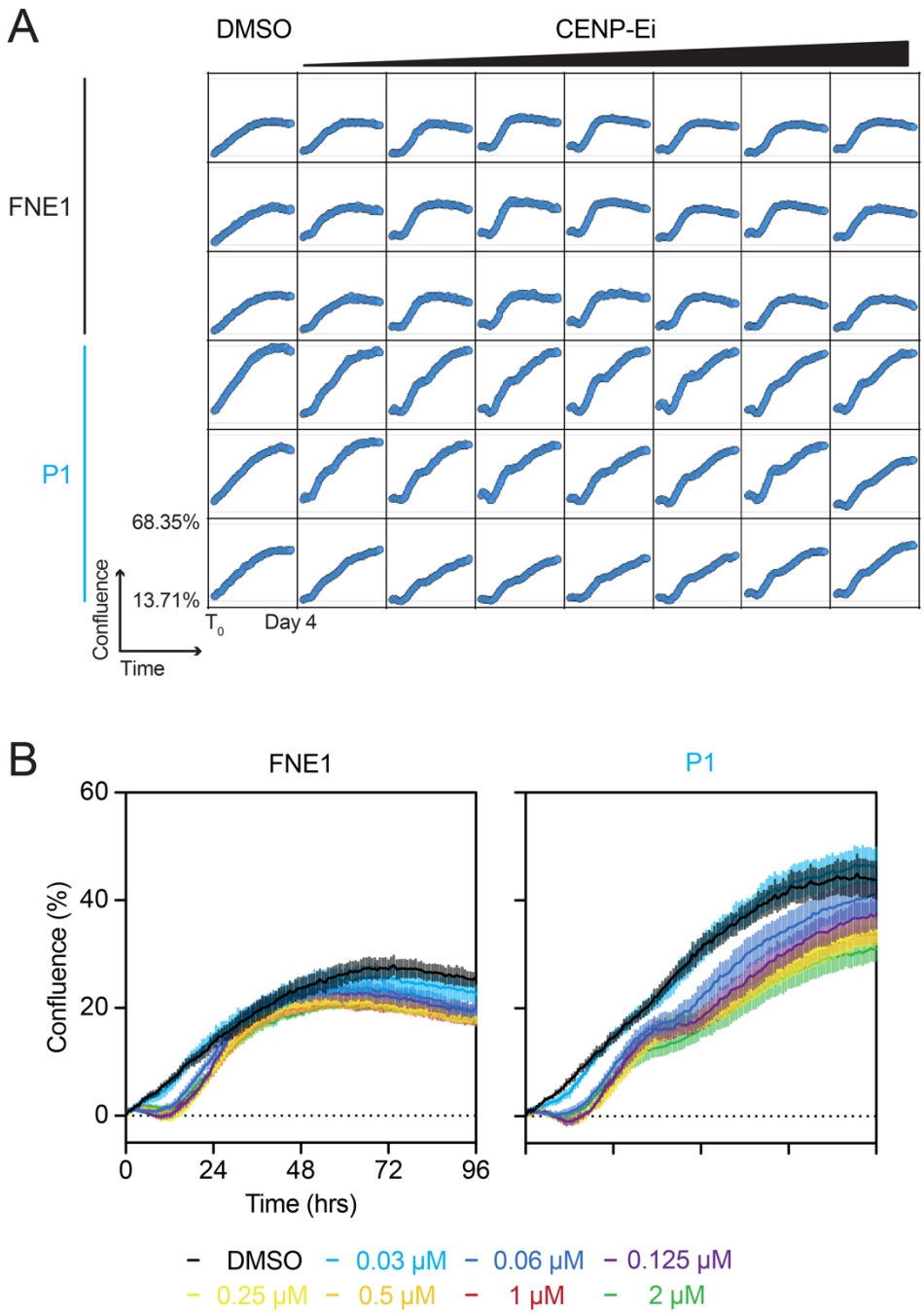

Figure 4.7: A pharmacological approach to increase mitotic duration and chromosome mis-segregation using CENP-Ei
A Representative titration matrix from one independent experiment measuring raw confluence of FNE1 and P1 cells treated with DMSO and increasing concentrations of CENP-Ei. **B** Normalized, mean confluence measurements of FNE1 and P1 cells treated with DMSO and increasing concentrations of CENP-Ei. Normalization was performed by subtraction of T_0 measurement. Data are from two independent experiments and three technical replicates each. Error bars represent standard error of the mean.

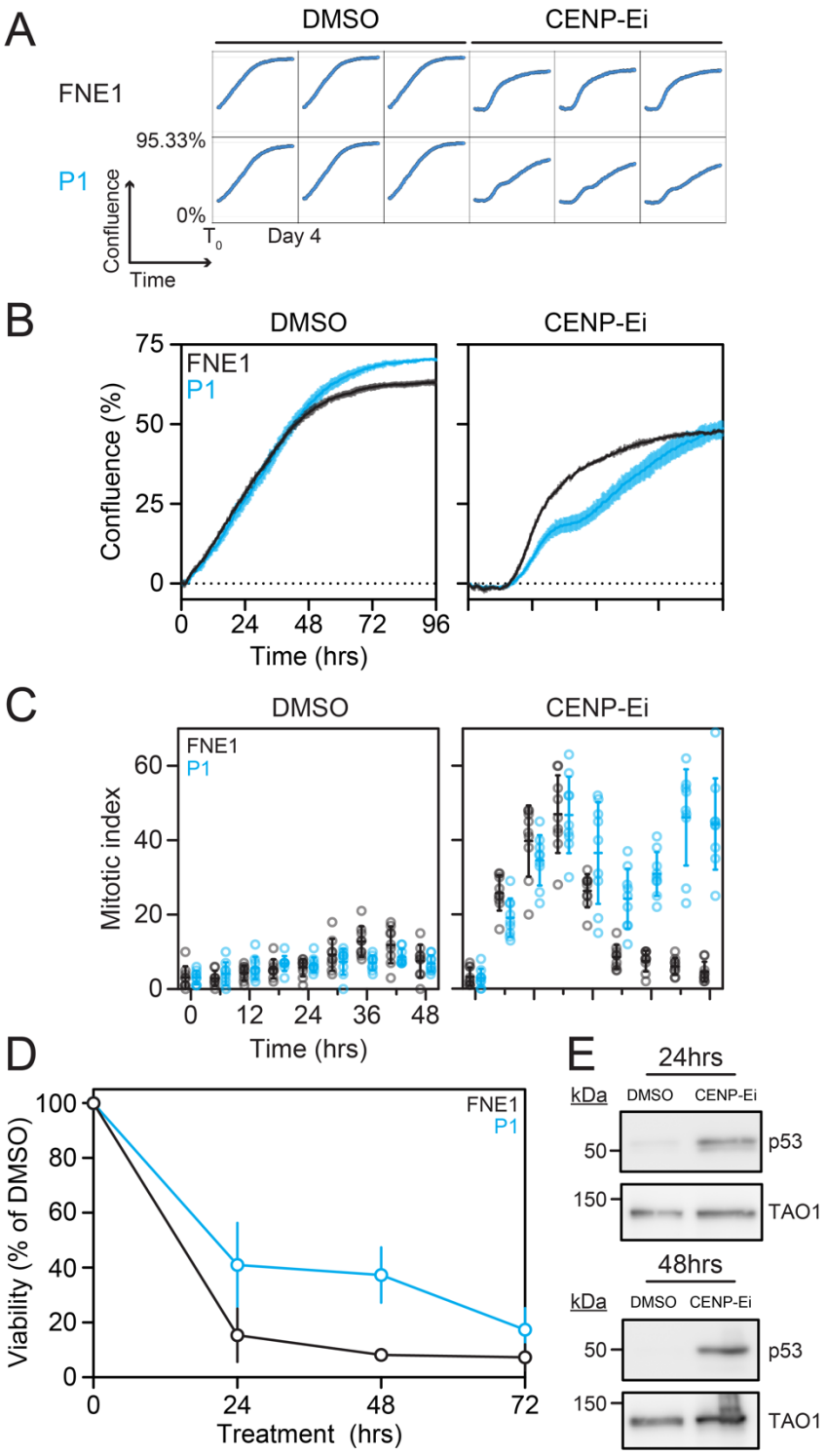

Figure 4.8: CENP-Ei suppresses proliferation in FNE1 but not P1 cells
A Raw confluence titration matrix of FNE1 and P1 cells treated with DMSO or CENP-Ei. **B** Normalized, mean confluence measurements from three technical replicates presented in A. Data was normalized to T_0 by subtraction. Error bars represent standard error of mean. **C** The number of mitotic cells was determined in three fields of view in three wells and plotted as mitotic index. Mean and standard deviation are represented as bar and error bars. **D** Crystal violet-based, normalized viability was measured by colony formation. Cells were treated with DMSO or CENP-Ei for the indicated amount of time after which the drug was washed out. Error bars represent standard deviation. **E** p53 protein expression was measured in FNE1 cells by immunoblotting following 24 or 48 hours of treatment with either DMSO or CENP-Ei. All CENP-Ei treatments were at 250 nM.

hours and even further at later timepoints (Fig. 4.8D). In P1 cells viability was also suppressed, however, to a lesser extent than in FNE1 cells. P1 cells retained around 40% viability of vehicle treated cells, but ultimately at the 72 hour washout viability suppression was similar in P1 to FNE1 cells. As a potential cause for this suppression in FNE1 cells, I investigated p53 expression by immunoblotting. Indeed, p53 expression was elevated in CENP-Ei treated cells after 24 and 48 hours in comparison to vehicle treated cells (Fig 4.8E).

p53 has been shown to limit proliferation of cells that have undergone lengthy mitoses and/or a chromosome mis-segregation event. Since CENP-E inhibition can result in both and I already observed elevated p53 expression upon treatment, I decided to examine post-mitotic cell fate in DMSO and CENP-Ei treated FNE1 and P1 cells by live cell microscopy. I again seeded cells into a 24 well microtiter plate and this time captured images of the proliferating cells every 10 minutes. This way I could follow individual daughter cells after their mother had divided. Cellular behaviour was consistent with previous experiments in response to DMSO or CENP-Ei which gave me confidence that the analysis of cell fates would further my understanding (Fig. 4.9A). Under control conditions, both FNE1 and P1 cells divided frequently and up to three mitoses could be observed readily within 72 hours of analysis (Fig. 4.9B). In contrast, under CENP-Ei conditions mitotic duration was increased in both FNE1 and P1 cells. Strikingly, the majority of FNE1 daughters I followed did not divide again, i.e., FNE1 cells underwent one prolonged mitosis and then remained in interphase. Only two exceptions of this behaviour were observed. In contrast, P1 cells regularly entered a second, also prolonged, mitosis. These observations are consistent with the increase in mitotic P1 cells after 36 hours which was not observed in FNE1 cells (Fig. 4.8C).

To further dissect the interphase arrest phenotype observed in CENP-Ei treated FNE1 cells, I assessed the cell cycle distribution in FNE1 and p53-deficient P1 and P3 cells by flow cytometry. Once again, I treated cells with DMSO or CENP-Ei for 24, 48 and 72 hours and harvested them for analysis of DNA content. Using standard flow cytometric gating strategies (Fig. 4.10A), I was able to determine the distribution of cells in the cell cycle. As expected, and independent of the timepoint, the cell cycle profiles under control conditions showed similar numbers of cells in G1, S and G2-phases (Fig. 4.10B,C). However, treatment with CENP-Ei resulted in a dramatic increase in the number of cells in G1 across all cell lines. Strikingly, the fraction of cells in G1 remained above 80% in FNE1 cells after 24, 48 and 72 hours of CENP-Ei treatment but below 60% in P1 and P3 cells. In addition, the fraction of FNE1 cells in S-phase decreased with the duration of CENP-Ei treatment. As FNE1 cells grew to

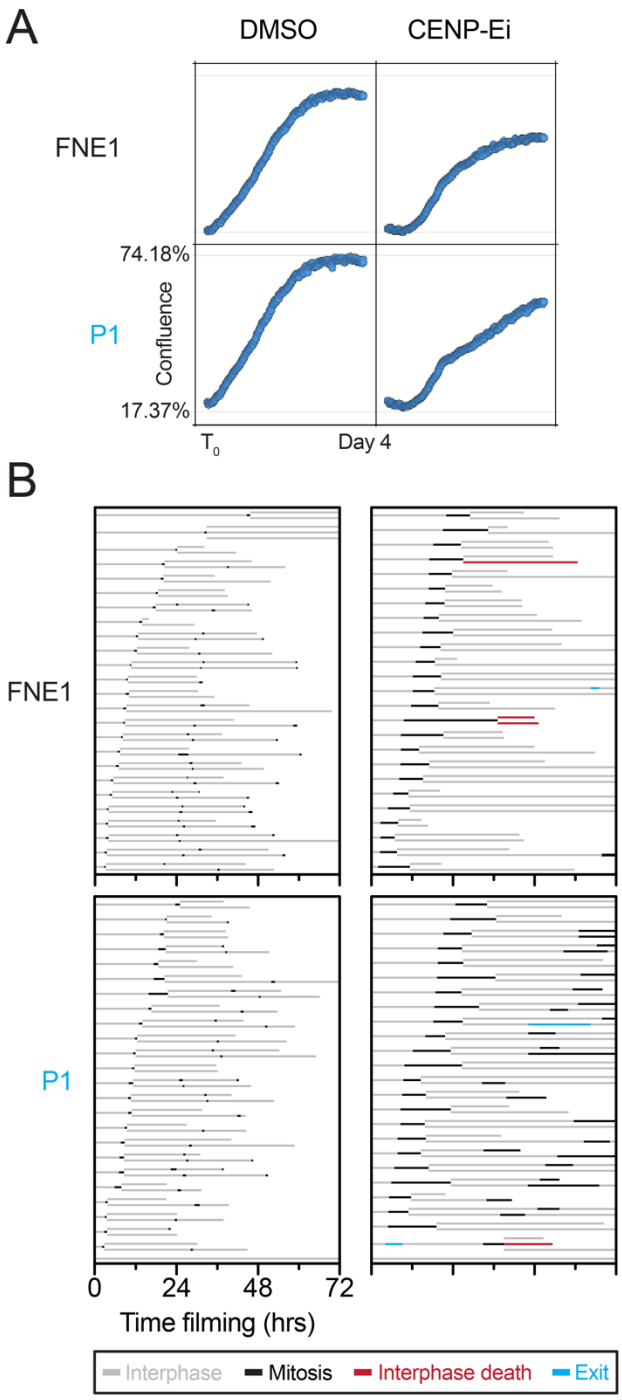

Figure 4.9: FNE1 cells arrest in interphase following division in the presence of CENP-Ei
A Raw confluence titration matrix of FNE1 and P1 cells treated with DMSO or CENP-Ei. **B** Cell fate profiling of DMSO or CENP-Ei treated FNE1 and P1 cells by live cell microscopy. 25 cells were tracked through at least one mitosis and their daughters were followed to determine post-mitotic fate. Where possible one daughters' daughter was followed-up to a third mitotic event. The legend below indicates the nature of cell fate. All CENP-Ei treatments were at 250 nM.

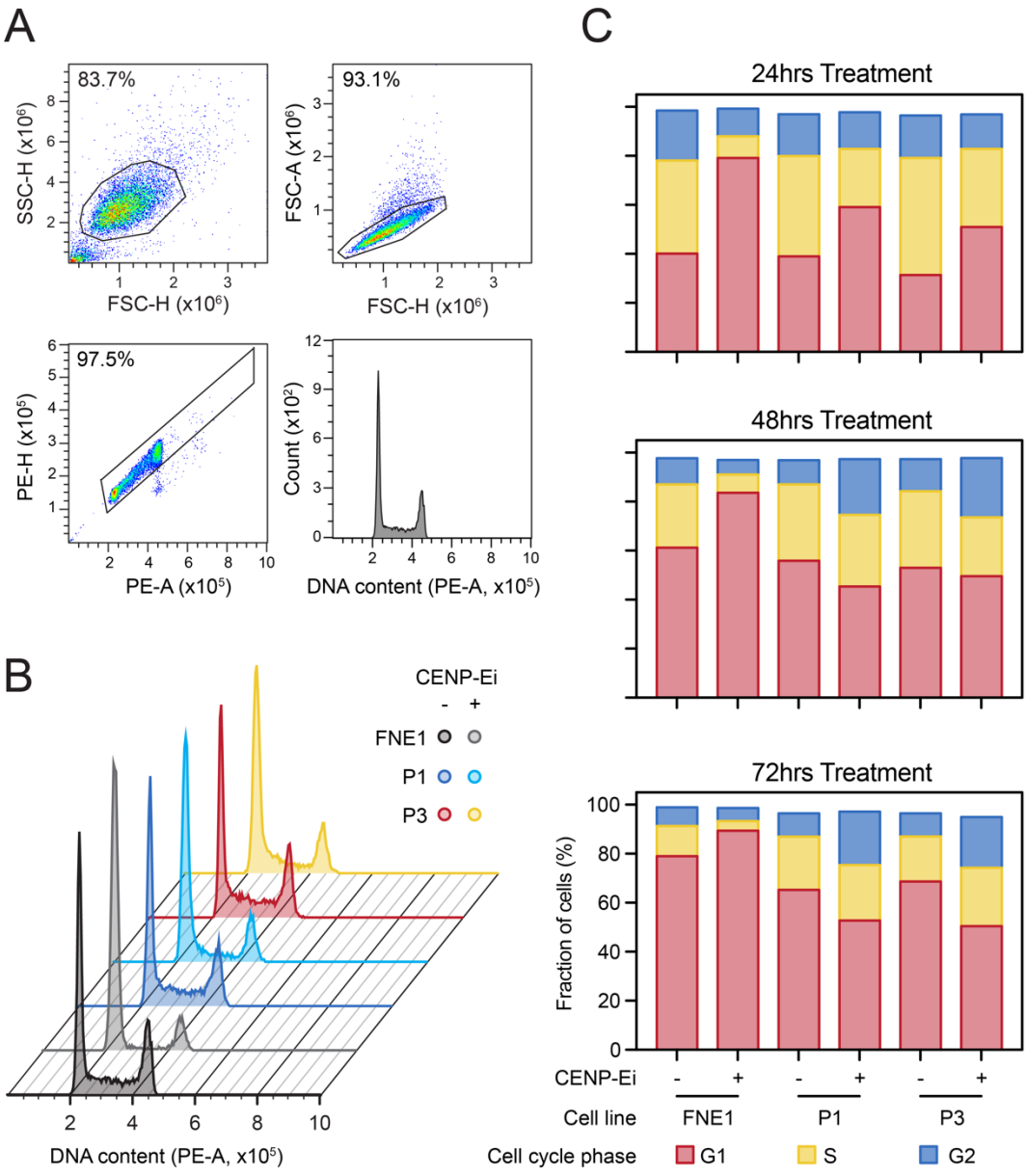

Figure 4.10: FNE1 cells arrest in G1 following division in the presence of CENP-Ei
A Gating strategy to obtain high-quality DNA content profiles for the analysis of cell cycle distribution using the pragmatic Watson model in FlowJo. Morphology discrimination is followed by a two-step doublet-discrimination yielding a high-quality DNA content profile. Exemplarily shown FNE1 cells under control conditions after 24 hours. Percentage indicates fraction of events contained within gate. **B** DNA content profiles of FNE1, P1 and P3 cells treated for 24 hours with either DMSO or CENP-Ei. **C** Quantification of DMSO and CENP-Ei treated FNE1, P1 and P3 cells over time. At least 10,000 cells were acquired on the second doublet-discrimination gate yielding more than 9,000 cells for analysis in each sample.

confluence over the treatment period, the fraction of G1 cells increased in the vehicle treated groups, too, however, not to the same extent as CENP-Ei treated groups. Taken together, these data and the cell fate profiling of FNE1 and P1 cells suggest that p53-proficient cells arrest in G1 following prolonged mitosis.

4.5: Summary and discussion

In this chapter I investigated (i) if the mutant FNE1 subclones displayed aneuploidy and on-going CIN and (ii) if pharmacologically exacerbated CIN was tolerated in *TP53*^{mut} FNE1 cells.

Combining three orthogonal approached to query the ploidy of wildtype and mutant FNE1 cells, I was able to show that P1 cells harboured more segmental or whole chromosome aneuploidies than FNE1 cells and that WGD occurred independently in two of the three PB lineages. My findings in P1 cells are consistent with reports showing non-clonal aneuploidies in p53-suppressed or CRISPR/Cas9-engineered *TP53*$^{-/-}$ *hTERT*-immortalized RPE-1 cells, but in contrast to observations made in p53-proficient and -deficient HCT116 cells which remain near-diploid in the absence of p53 (Bunz et al., 2002; Kok et al., 2020; Soto et al., 2017). It is important, however, to consider the aspect of physiological relevance. FNE1 cells represent the tissue of origin of HGSOC and are grown at 5% O_2, thought to more accurately reflect *in vivo* physiology, instead of atmospheric levels typically employed for routine cell culture. Indeed, evidence from a *Kras*-dependent MEF transformation model suggests that p53-deficiency leads to pleiotropic changes in cellular processes, including ploidy maintenance, under physiological levels of O_2 (Valente et al., 2020). A potential contribution of *hTERT*-overexpression to the emergence of aneuploidy after p53-loss can also not be ruled out since RPE-1 cells, the closest cell line model to FNE1 cells used in similar studies, were immortalized in the same manner.

The findings in PB2/E/M and PB3/E/M cells are unexpected since *BRCA1* mutations have not been reported to correlate with WGD (Bielski et al., 2018). However, WGD is considered a mechanism that protects cells from otherwise detrimental genome dosage imbalances (Bielski et al., 2018; Holland and Cleveland, 2012; Torres et al., 2007). While the observation of WGD was unexpected in PB2E/M and PB3E/M cells, the emergence of aneuploidy upon *BRCA1* mutation was not. In fact, genomic analyses of BRCA1/2-deficient tumours have suggested frequent loss of heterozygosity events which is consistent with the emergence of monosomies in PB2/E/M and disomies in PB3/E/M cells (Macintyre et al., 2018). Furthermore, BRCA1-deficient GEMMs as well as MEFs have been found to be aneuploid showing features of

perturbed cell cycle progression (Weaver et al., 2002; Xu et al., 1999). In contrast, PB1E/M cells showed no evidence of aneuploidy by flowcytometry thus I did not include them in the miFISH analysis. As described and discussed in the previous chapter, the potential retention of some HR proficiency as a result of *BRCA1* exon 11 splicing might protect PB1E/M cells from aneuploidy.

Lastly, in this chapter I tested FNE1 and P1 cells' tolerance to CENP-Ei. p53-deficiency has been firmly established as a tolerance mechanism of (i) aneuploidy (Thompson and Compton, 2010) and (ii) prolonged mitosis (Lambrus et al., 2016). I have shown that the vast majority of FNE1 cells divided only once in the presence of CENP-Ei and subsequently arrested in G1 potentially through a p53-dependent mechanism as p53 was stabilized upon CENP-Ei treatment. Despite a fitness cost in comparison to untreated cells, P1 cells divided multiple times in the presence of CENP-Ei. Other pathways that ensure genomic integrity and diploidy might be unaffected by p53-deficiency and thus remain functional providing a potential explanation why p53-loss only partially alleviates the proliferative defect observed upon CENP-Ei treatment. Aneuploidy-associated stresses such as proteotoxicity, metabolic stress, autophagy and an increase in DNA damage might signal in manner independent of p53 to suppress proliferation.

In summary, I conclude that p53-loss not only initiates CIN in HGSOC, but also contributes to CIN and aneuploidy tolerance. Furthermore, additional mutations in *BRCA1* can exacerbate aneuploidy and CIN. The role of MYC in ploidy maintenance could only be addressed partially in *BRCA1*-mutant backgrounds. Thus, I addressed aim (iii) in this chapter and to put forward potential mechanisms underpinning these observations. To address aim (iv), I performed an RNA sequencing experiment described in the following chapter.

Chapter 5: Transcriptomic analysis of mutant FNE1 subclones

5.1: Overview

Having observed CIN in some of the sequentially mutated FNE1 subclones by flow cytometry, scWGS and miFISH, I addressed aim (iv), to investigate potential mechanisms underpinning this observation, next. Several potential monogenic causes of CIN have been described previously, as alluded to in *1.3: Chromosomal instability and aneuploidy*. However, mutations in genes directly involved in chromosome segregation and DNA replication, with the exception of *BRCA1/2*, are rarely observed in HGSOC. In contrast, transcriptional alterations of specific genes have been found to disrupt mitosis and cause CIN (Bastians, 2015). Therefore, to explore the possibility that deregulation of genes involved in DNA replication and mitosis contribute to the observed karyotypic changes, I performed RNA sequencing.

RNA sequencing is a widely used and accepted, experimentally resourceful and genome-wide approach (making it unbiased) to study changes that manifest on the RNA expression level, which in turn suggest changes in cellular phenotypes. Thus, it is the ideal methodology to approach aim (iv) to better understand potential causes of CIN in the mutant FNE1 subclones in an unbiased manner. Alternative technological approaches such as gene expression microarrays and proteomics were ruled out due to limitations in sensitivity and the requirement for more laborious sample preparation, respectively. Furthermore, alternative experimental approaches, e.g., RNAi suppression or CRISPR/Cas9 suppression or activation screens are not only limited by the readout assay, which would have to be selected carefully, but are also more labour intensive. Thus, RNA sequencing was the most suitable option to address aim (iv). In addition, many analytical tools are available for RNA sequencing to investigate if groups of genes, rather than individual genes, have been deregulated. This utility has already been illustrated in the functional characterization of *TP53/BRCA1* double-mutant and the *MYC*-overexpressing FNE1 subclones (see *3.4: CRISPR/Cas9-mediated BRCA1 mutagenesis* and *3.5: Generation of MYC-overexpressing mutant FNE1 subclones*).

5.2: Transcriptomic analysis separates wildtype from mutant FNE1 cells

As a first step in the analysis, I aimed to determine if transcriptomic changes as a consequence of sequential mutagenesis would allow for discrimination of parental FNE1 cells and mutant subclones. Thus, principal component analysis (PCA), an unbiased dimensionality reduction methodology, was employed. The PCA revealed four

distinct clusters that in part correspond to the genotypes of samples contained within (Fig. 5.1). Cluster 1, FNE1, is comprised of the three parental FNE1 samples. Cluster 2, P, contains P and PE samples as well as PB1 and PB1E, likely a consequence of the potentially partly functional splice variant detected in this subclone described in *3.4: CRISPR/Cas9-mediated BRCA1 mutagenesis*. Cluster 3, PB, contains all PB2 and PB3 samples. Ultimately, cluster 4, PM, is comprised of all PM samples as well as PB1M in the same manner that the P cluster contains PB1 and PB1E. The distinct separation of parental FNE1 samples and subclones in this analysis reveals a substantial impact of the sequentially introduced genetic manipulations on the transcriptome.

Next, to discern differences in genes grouped together based on their cellular function, the Hallmark collection of gene sets was employed to perform gene set variation analysis (GSVA) (Hanzelmann et al., 2013). This way, gene sets that are positively or negatively enriched in some, but not other, samples could be identified and statistically probed to determine if the enrichment is significant. First, however, the enrichment score calculated for each of the 50 Hallmark gene sets for each sample was used for unsupervised hierarchical clustering which yielded a picture remarkably similar to the PCA (Fig. 5.2). Parental FNE1 samples fell in a clade by themselves, P and PE samples formed multiple clades close to one another that again included PB1 and PB1E. Notably, the cophenetic distance between the three FNE1 samples is very small in contrast to an increased cophenetic distance between P and PE samples. In line with the previous observations and similarly to the PCA, PB2 and PB3 samples fell within clades next to one another, however, PB3 was more closely related to the fourth PCA cluster, consisting of the PM samples, than to the PB2 clade. PB1M, as before, clustered among the PM samples.

In the same manner that samples were clustered, gene sets were also subjected to unsupervised hierarchical clustering. The clustering of gene sets essentially revealed two clades that were further divided into additional clades; however, the overarching trend observed in these clades is more striking. The first clade contains eleven gene sets, five of which are related to the cell cycle such as MYC targets V1 and V2, E2F targets, G2M checkpoint and DNA repair. The arrangement of the heatmap itself reflects the stepwise introduction of mutations, indeed an increasingly positive enrichment score of the gene sets in that clade is observed as additional genetic manipulations were introduced. In other words, the enrichment score for all eleven gene sets in the first clade was negative in FNE1 samples, remained negative in P and PE samples (albeit to a lesser extent), was mostly positive in PB2 and PB3 and highly positive in PM samples. The second clade contains the remaining 39 gene sets. Ten

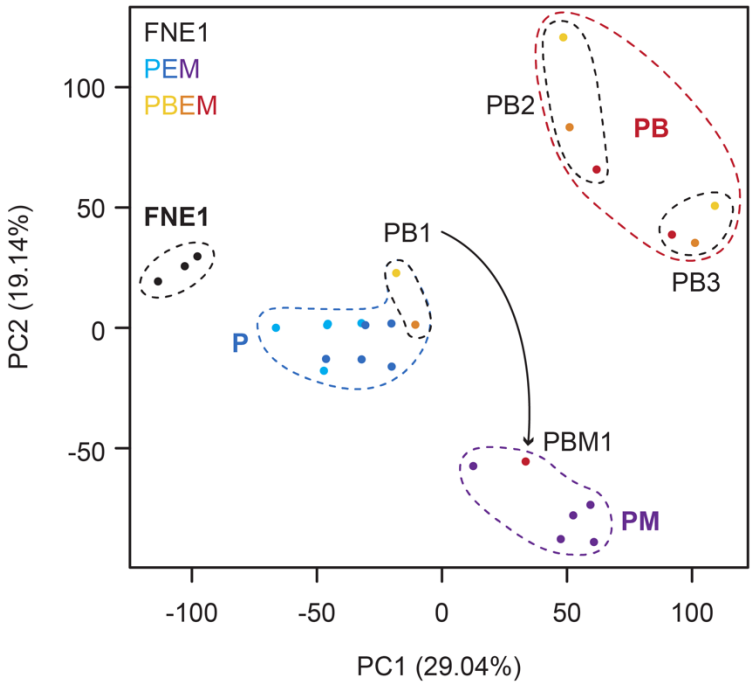

Figure 5.1: Dimensionality reduction separates parental FNE1 and mutant subclones
Principle component analysis (PCA) of 27 samples included in the RNA sequencing analysis shows separation into four distinct clusters. Colours indicate sample genotype. Principle components (PC) one and two are indicated on the axes with variance shown in parentheses.

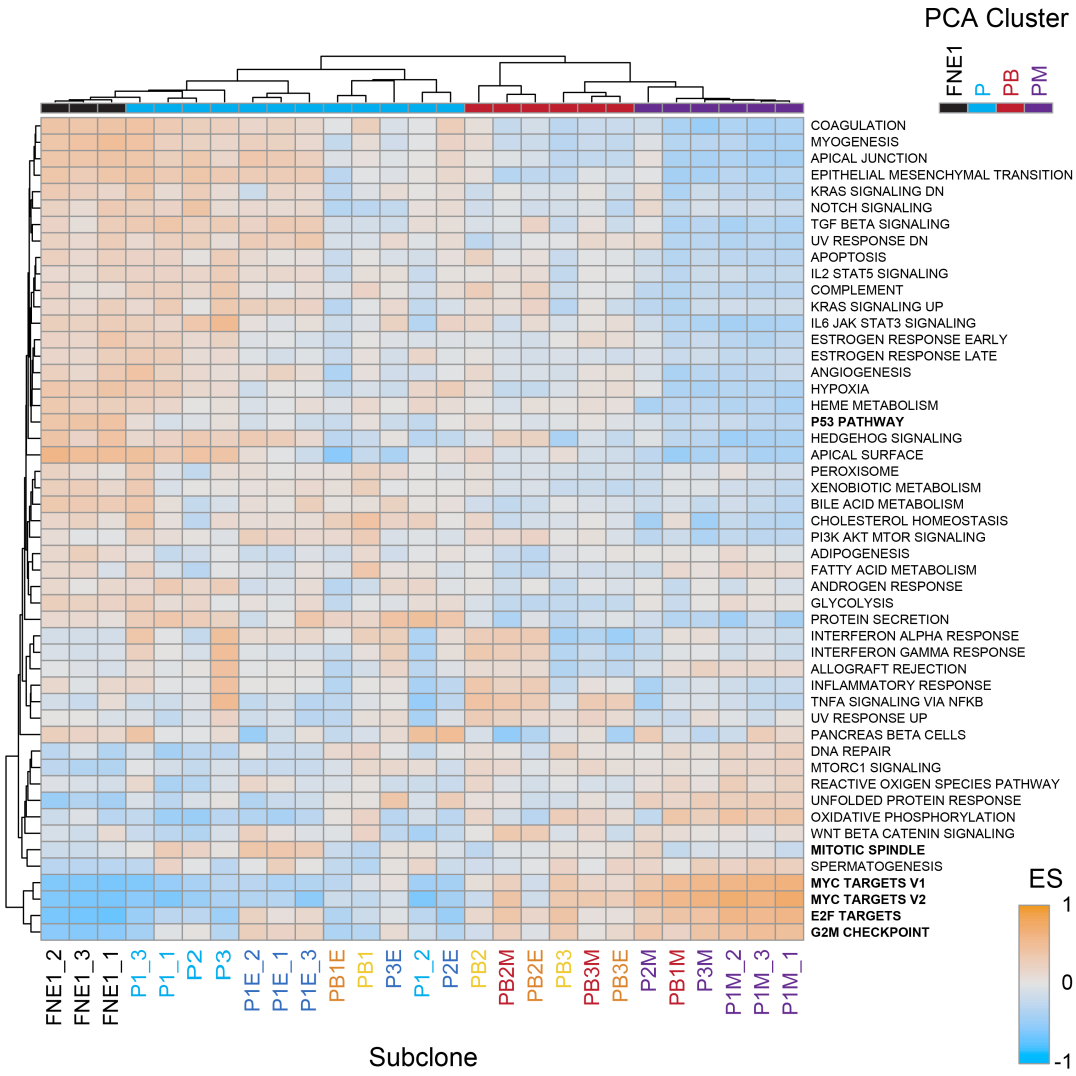

Figure 5.2: Gene set variation analysis reveals Hallmark gene sets discriminating parental FNE1 from mutant subclones

Gene set variation analysis and subsequent unsupervised hierarchical clustering were performed on the Hallmark collection of gene sets across all 27 samples. Subclones are distributed along horizontal and gene sets along the vertical axes. The samples' font colour corresponds to genotype as seen in Fig. 5.1 while the PCA cluster is indicated in black (FNE1), cyan (P), red (PB) and purple (PM) above the heatmap. Blue and orange colours reflect negative and positive enrichment, respectively.

of these display heterogenous enrichment scores that are inconsistent across all samples and do not display a specific pattern. In contrast, the remaining 29 gene sets display an opposite trend to what I observed in the first clade of gene sets. These 29 gene sets are highly positively enriched in FNE1 samples, positively enriched in P and PE samples (albeit to a lesser extent) and mostly negatively enriched in PB2/E/M, PB3/E/M and PM samples. In this group several gene sets display an interesting enrichment pattern. The p53 pathway gene set is, as expected, strongly positively enriched in the FNE1 samples which are the only p53-proficient samples in this analysis. In all remaining samples, the enrichment score is reduced and mostly negative. Another interesting pattern is that the mitotic spindle gene set seems to be positively enriched in P and PE samples, but not others. In addition, enrichment scores of the TNFα signalling and UV response up gene sets are negative in most samples with exception of PB2/E/M and PB3/E/M samples which display positive enrichment scores. The interferon alpha and gamma response gene sets also display heterogenous enrichment scores across all samples, but when looking at PB2/E/M and PB3/E/M samples only, these two gene sets display positive enrichment in PB2/E/M samples but intriguingly negative enrichment scores in PB3/E/M samples.

Thus, PCA and GSVA reveal features that discriminate parental FNE1 samples from mutant subclones and subclones from one another. In addition, the GSVA provides clues of cellular transcription programmes that are altered after mutagenesis which will be explored in the following section.

5.3: Cell cycle gene sets are highly positively enriched in mutant subclones

To simplify the GSVA-based clustering analysis, I pooled the enrichment scores from all samples according to the PCA clustering. This summarized data was then again subjected to unsupervised hierarchical clustering which led to similar clade formation separating FNE1 subclones and gene sets as observed previously (Fig. 5.3A). The overall pattern of the gene set distribution was also maintained; 41 gene sets displayed a pattern of decrease in enrichment from highly positive in FNE1 to highly negative in PM, instead of 39. Likewise, in the opposite direction nine instead of eleven gene sets were highly negatively enriched in FNE1 and highly positively enriched in PM.

As expected, the p53 pathway and MYC targets V1 and V2 gene sets were some of the most positively and negatively enriched gene sets in FNE1, respectively, and consequently most negatively and positively enriched in PM. Indeed, the p53 pathway gene set was significantly negatively enriched in all three groups compared with the

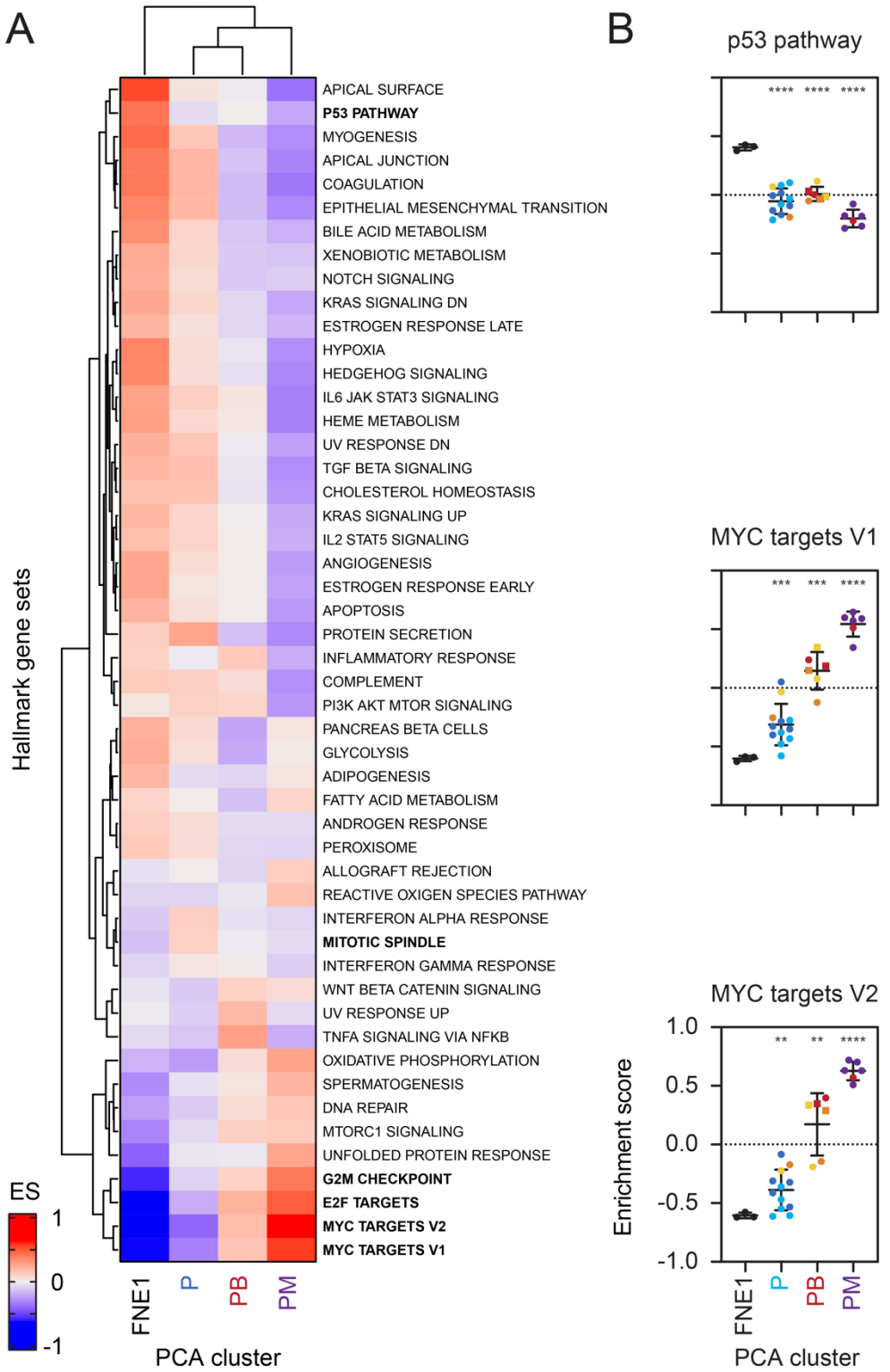

Figure 5.3: Sequential mutagenesis of FNE1 cells deregulates key tumour suppressive and oncogenic gene sets

A Summary heatmap of enrichment scores generated by gene set variation analysis (GSVA) of indicated Hallmark collection gene sets. Samples were grouped according to PCA clusters. Bold font indicates gene sets of interest. Blue and red colour reflects negative and positive enrichment scores, respectively. **B** Three exemplar gene sets' enrichment scores shown for PCA cluster groups. Colour of bubbles indicates genotype as seen in PCA. Squares reflect samples from the PB3 lineage. *p ≤ 0.05, **p ≤ 0.01, ***p ≤ 0.001, ****p ≤ 0.0001
FNE1 = 3 samples, P = 12 samples, PB = 6 samples, PM = 6 samples.

FNE1 group (Fig. 5.3B). Similarly, the MYC targets V1 and V2 gene sets were significantly positively enriched in all three groups compared with FNE1. However, much like the mean enrichment score of each group, the significance level was not the same. While negative enrichment of the p53 pathway seemed binary, the positive enrichment of MYC targets V1 and V2 appeared dynamic, i.e., the mean enrichment score in P remained negative despite being significantly different from FNE1. The mean enrichment score for these two gene sets was only positive in the PB and PM groups. As expected, the PM group displays the highest mean enrichment score of MYC targets V1 and V2 consistent with my observations during the validation of these subclones and the fact that *MYC* is ectopically overexpressed (see also *3.5: Generation of MYC-overexpressing mutant FNE1 subclones*). Interestingly, the samples in the PB group seem to display heterogenous enrichment scores. PB3/E/M samples have an enrichment score of MYC targets V1 and V2 greater than the mean whereas that only holds true for PB2M and not PB2 or PB2E. Nonetheless, these samples still have an enrichment score greater than the mean of the P group. Taken together, this further supports that PB3 has increased MYC levels independent of ectopic MYC expression and that PB2 subclones may have upregulated MYC target genes independently of MYC as its overexpression clearly has a functional consequence.

Beyond these anticipated changes, I already described differential enrichment of cell cycle related gene sets in the previous section which remain highly negatively enriched in FNE1 and highly positively enriched in PM upon summarizing of samples into the PCA groups. Indeed, statistical analyses of enrichment scores in the four groups revealed significant differences between FNE1 and the other three groups in the E2F targets and G2M checkpoint gene sets (Fig. 5.4A). The magnitude of the effect scales with the number of genetic perturbations similarly to what I described for the MYC targets V1 and V2 gene sets. In both cases, the mean enrichment score of FNE1 and P was negative although less negative in P than in FNE1. In contrast, both PB and PM groups display a positive mean enrichment score with PM displaying the highest mean in both E2F targets and G2M checkpoint gene sets. Lastly, the mitotic spindle gene set displays a different picture to the previously described gene sets. The mean enrichment score remains negative in FNE1, PB and PM groups, however, it is positive and significantly different from FNE1 in the P group.

In addition to cell cycle deregulation, I wanted to test if DNA replication genes specifically were also differentially enriched upon sequential mutagenesis, however, the Hallmark collection of gene sets does not include a DNA replication gene set. Therefore, the DNA replication gene sets from the Kyoto Encyclopedia of Genes and

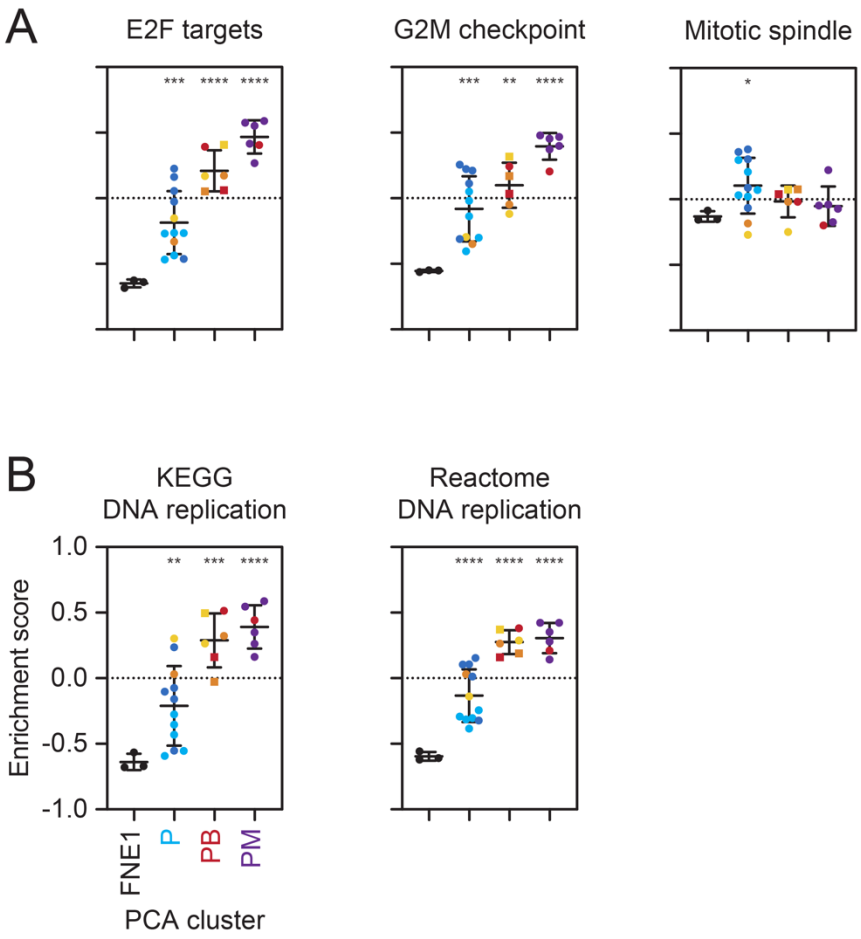

Figure 5.4: Oncogenic gene sets are enriched upon loss of p53
A Enrichment scores of three oncogenic gene sets from the Hallmark collection are shown for samples according to PCA clusters. **B** Enrichment of DNA replication gene sets from the KEGG and Reactome collections are shown for samples according to PCA clusters.
Colour of bubbles indicates genotype as seen in PCA. Squares reflect samples from the PB3 lineage. *p ≤ 0.05, **p ≤ 0.01, ***p ≤ 0.001, ****p ≤ 0.0001, FNE1 = 3 samples, P = 12 samples, PB = 6 samples, PM = 6 samples.

Genomes (KEGG) and the Reactome collection were employed for this purpose. Indeed, in gene sets from both collections, the mean enrichment score was significantly increased in all subclones compared with FNE1 (Fig. 5.4B). The pattern of said increase is similar to what I observed in the Hallmark E2F targets and G2M checkpoint gene sets, i.e., the mean enrichment score is negative in FNE1 and negative yet increased in P and positive in PB and PM.

Taken together, these data indicate that the transcriptome of the mutant subclones is significantly rewired upon introduction of genetic manipulations. Specifically, genes involved in cell cycle regulation and DNA replication have been shown to be affected significantly.

5.4: Cell cycle deregulation is also observed in mutant mouse oviduct organoids

In order to validate my observations in an independent system, I turned to publicly available data from a GEMM of oviduct-derived HGSOC and interrogated it in a manner that would allow comparison with the parental FNE1 cells and mutant subclones. Zhang et al. (2019) described the generation of wildtype and mutant oviduct organoids to query the tissue of origin of HGSOC in mice. For the purpose of this section, however, I will focus on the RNA sequencing data gathered from wildtype and mutant oviduct organoids which were designed to express mutant *Trp53* (specifically, hemizygous *Trp53*^{R172H} as the other allele was deleted in a Cre-dependent manner) and the oncoprotein SV40 TAg which inhibits Rb1.

Dimensionality reduction by PCA showed separation of wildtype and mutant organoid samples which is the first indication of consistency with my observation in the human samples (Fig. 5.5). However, to make more specific comparisons between the human and mouse data, analysis of differentially expressed genes was performed contrasting mutant to wildtype mouse organoids and P to FNE1 samples followed by gene ranking based on t-statistic to ultimately enable GSEA (Subramanian et al., 2005). This way, enrichment of specific gene sets for each contrast was determined. In line with the previously described GSVA the p53 pathway gene set was found to show a negative normalized enrichment score (NES) and the Mitotic spindle gene set showed a positive NES in the P versus FNE1 contrast (Fig. 5.6A). Similarly, the analysis of the publicly available mouse data contrasting mutant with wildtype organoids confirmed the observations made by Zhang et al. (2019); the G2M checkpoint and Mitotic spindle gene sets were positively enriched in mutant organoids (Fig. 5.6B).

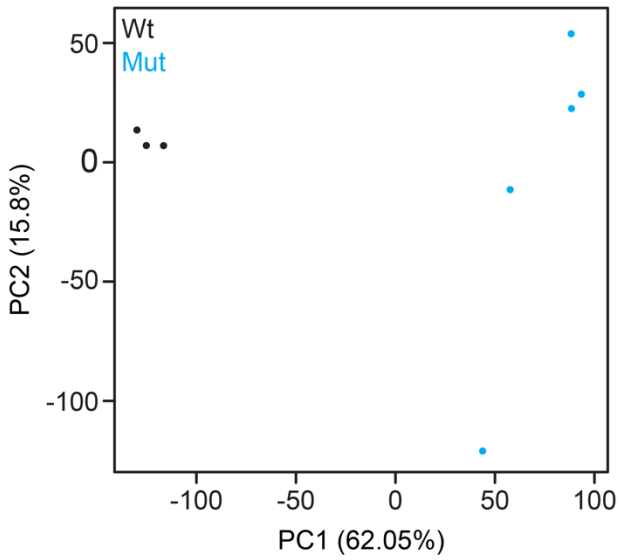

Figure 5.5: Dimensionality reduction separates wildtype from mutant oviduct organoids
Principle component analysis (PCA) of eight samples included in the RNA sequencing analysis shows separation of samples along the x-axis. Colours indicate sample genotype. Principle components (PC) one and two are indicated on the axes with variance shown in parentheses.

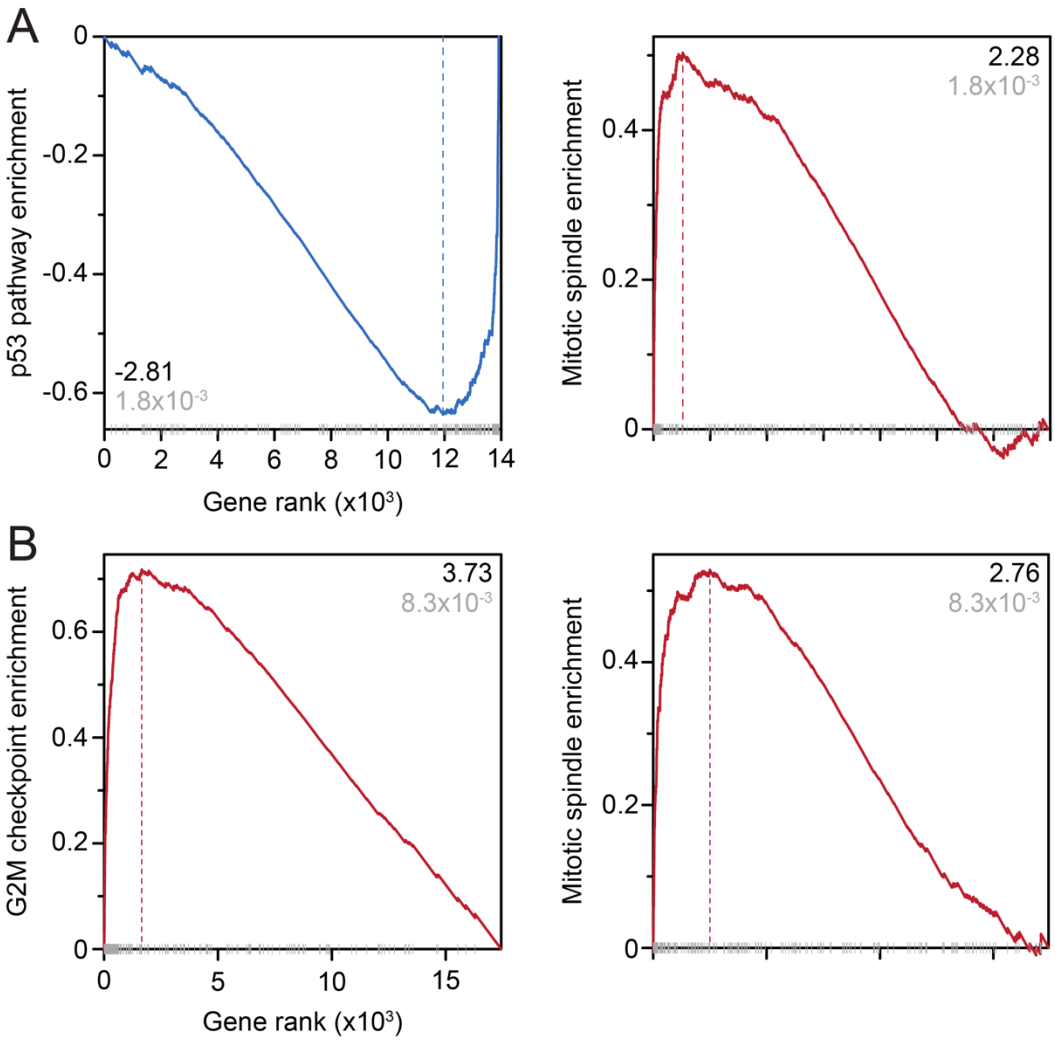

Figure 5.6: Gene set enrichment analysis confirms previous findings
A, **B** Gene set enrichment plots of indicated gene sets from the Hallmark collection contrasting p53-deficient with wildtype FNE1 cells and mutant with wildtype mouse organoids, respectively. Black font indicates the normalised enrichment score and grey font the adjusted p-value. Vertical bars along the x-axis indicate genes ranked as part of the gene set.

These observations provide evidence of the data's validity and thus the utility of the chosen approach.

Finally, to visualize the correlation of all 50 gene sets in the Hallmark collection, the NES of all gene sets in the human data was plotted against the NES of all gene sets in the mouse data (Fig. 5.7). The NES is inconsistent for 24 gene sets, i.e., positively enriched in mouse, but not human, data and vice versa or reached significance in one contrast, but not the other. However, 26 gene sets were consistently positively or negatively enriched in both datasets. Six gene sets, which were significantly, positively enriched in both mouse and human datasets, stood out: MYC targets V1 and V2, Mitotic spindle, E2F targets, G2M checkpoint and mTORC1 signalling.

The fact that the three cell cycle related gene sets were significantly, positively enriched in both datasets in addition to my previous observation of their progressive enrichment in the GSVA led me to investigate if discrimination of samples was possible based solely on genes' expression from these three gene sets. Therefore, I performed a z-score transformation followed by unsupervised hierarchical clustering of both mouse and human data. Indeed, wildtype and mutant mouse organoid samples were separated based on the expression of 478 genes from the E2F, G2M and mitotic spindle gene sets (Fig. 5.8A). Similarly, in the human data, wildtype FNE1 samples formed their own clade completely separate from the 24 mutant subclones (Fig. 5.8B). Within the clade of mutant subclones, P samples formed a clade that included PB1 and PB1E. PM samples formed a third clade that included PB1M. Lastly, the fourth clade included all PB2/E/M and PB3/E/M samples. This clustering analysis revealed a striking similarity to the sample-wise clustering based on GSVA's enrichment scores.

In conclusion, cell cycle deregulation observed in mouse organoids that harbour mutant p53 and an additional perturbation of Rb1 are similarly reflected in FNE1 subclones that are only deficient for p53.

5.5: Summary and discussion

Overall, these data suggest that transcriptional rewiring of the cell cycle is a prominent outcome of the sequential induction of genetic perturbations of *TP53* and *BRCA1* as well as the ectopic overexpression of *MYC*. Indeed, I found enrichment of several gene sets consistent with the genetic background of the samples in which the enrichment was observed, e.g., the p53 pathway gene set was exclusively positively enriched in p53-proficient FNE1 samples or the MYC targets V1 and V2 were most positively enriched in PM samples. Furthermore, when P samples were contrasted with FNE1 samples for GSEA the p53 pathway gene set was consistently negatively

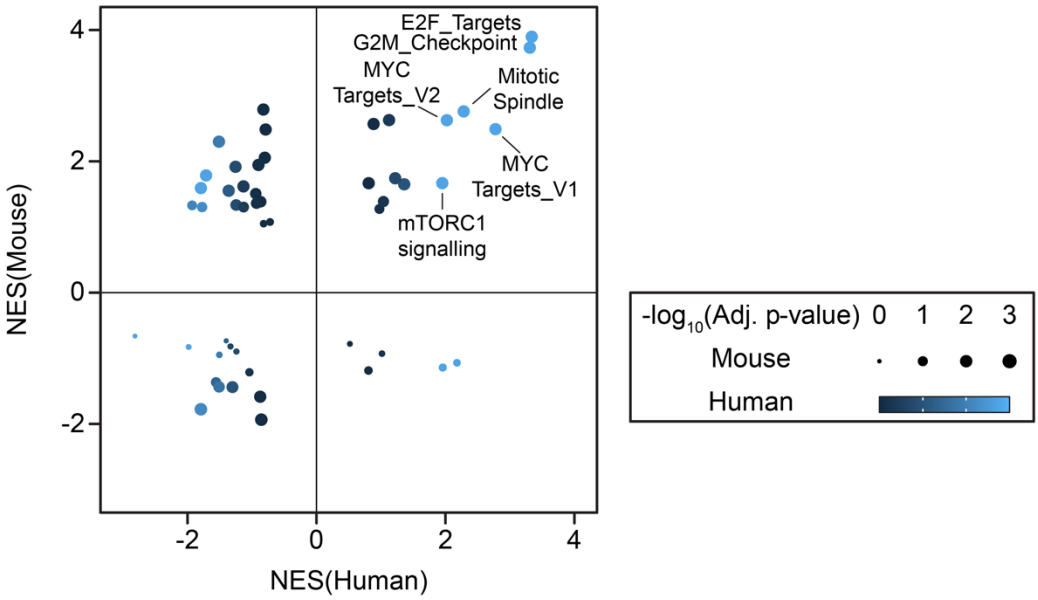

Figure 5.7: Correlation analysis between human and mouse data independently confirms upregulation of oncogenic gene sets
The correlation of gene set enrichment scores between human P and FNE1 samples and mutant and wildtype mouse organoids is shown by plotting the normalized enrichment scores (NES) of human and mouse data on the x- and y-axes, respectively. The colour and size of the bubble reflect the adjusted p-value of the individual gene set's NES in the human and mouse data, respectively.

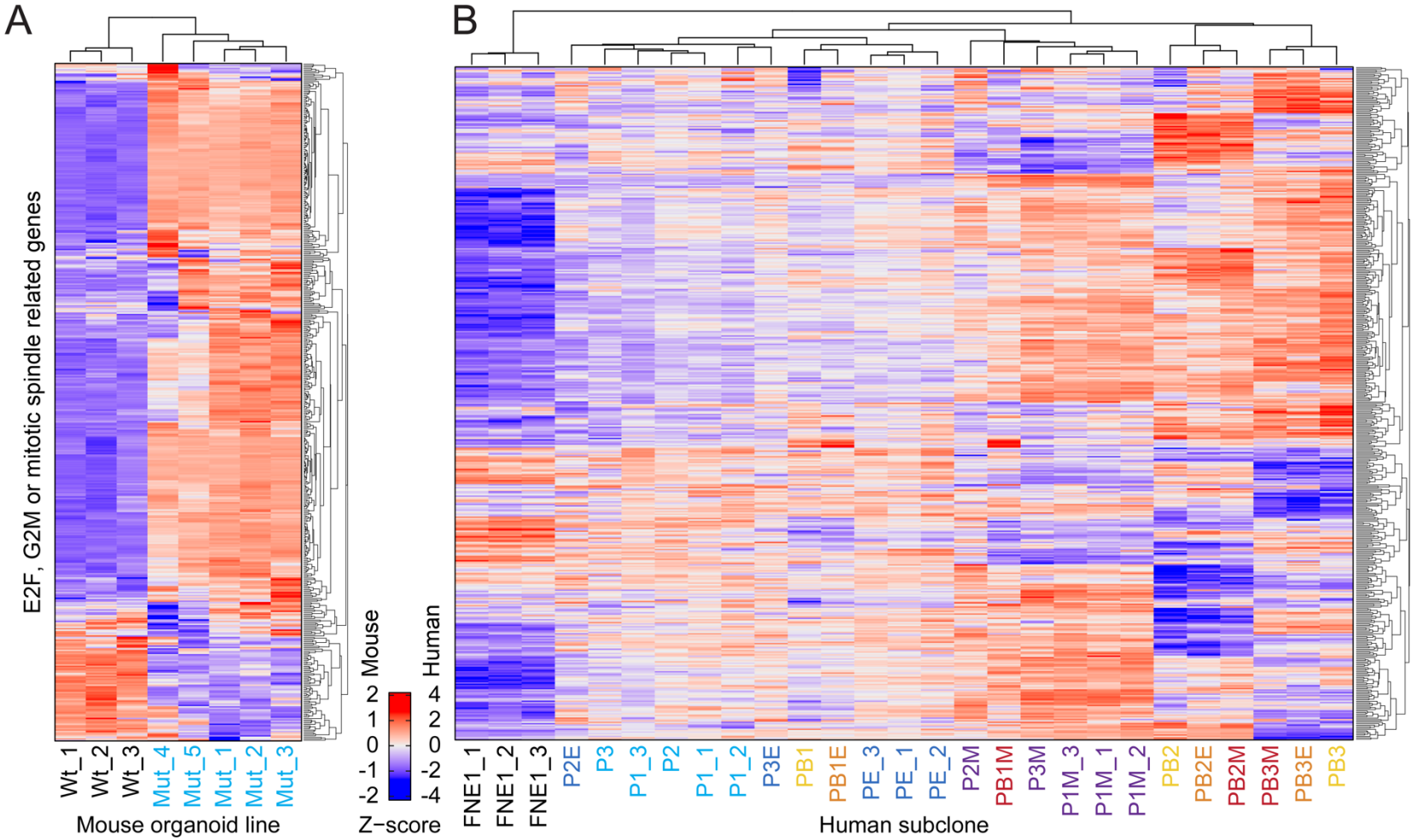

Figure 5.8: A union of cell cycle and mitosis related genes separates wildtype from mutant samples
A, **B** Unsupervised hierarchical clustering of mouse and human samples based on a union of genes from the Hallmark E2F targets, G2M checkpoint and mitotic spindle gene sets. Red and blue colour indicates positive and negative z-scores, respectively.

enriched. In addition, enrichment scores of the TNFα signalling and UV response up gene sets were only found to be positively enriched in PB2/E/M and PB3/E/M cells. Indeed, BRCA2-deficient cells have previously been shown to upregulate genes from the TNFα signalling gene set (Heijink et al., 2019). These observations contribute to the validity of the generated data as "control" gene sets, such as the p53 pathway and MYC targets V1 and V2, display expected patterns consistent with genotypes of samples and the literature.

The significant deregulation of E2F targets, G2M checkpoint, Mitotic spindle and DNA replication gene sets suggests that multiple pathways contributing to chromosomal stability are transcriptionally rewired. To exclude the possibility that these observations are limited to the mutant FNE1 subclones, I interrogated a publicly available dataset from a complementary model system, mouse oviduct organoids. This analysis independently confirmed the findings described in mutant FNE1 subclones that the aforementioned cell cycle gene sets are significant positively enriched upon perturbation of p53 signalling and potentially drive CIN.

Indeed, several transcriptional signatures reflecting CIN have been described in the literature. In essence, these signatures are gene sets comprised of genes that are overrepresented in chromosomally unstable samples in comparison to chromosomally stable samples; the CIN25 and CIN70 gene sets were the first of their kind (Carter et al., 2006). Subsequent reanalyses of these signatures, however, showed that rather than reflecting CIN they are a correlate for proliferation. Thus, alternative gene sets were developed, namely HET70 and HET5 represent genetic heterogeneity in cancer samples (Sheltzer, 2013). More recently, CA20 was developed which is a gene set that correlates with centrosome amplification, a driver of CIN (de Almeida et al., 2019). Thus, these data illustrate that conclusions about CIN can be made effectively based on RNA sequencing. Moreover, these additional analytical tools could prove valuable in the analysis of CIN by RNA sequencing in mutant FNE1 subclones.

Nonetheless, it is important to appreciate that the data and observations presented in this chapter are only an inference of cellular phenotypes in the absence of direct, experimental assessments of these processes. It has been shown previously that the overexpression of DNA replication factors, namely TIMELESS and CLASPIN, on the RNA and protein levels reflects adaptation to on-going DNA replication stress and correlates with increased expression of DNA damage markers such as phosphorylated CHEK1 and H2AX (Bianco et al., 2019). Thus, immunoblot experiments measuring expression levels of these proteins would provide additional, more functional evidence of DNA replication stress. The same holds true for DNA fibre assays.

Regarding analyses of cell cycle deregulation, flowcytometric analysis of the distribution of cells in G1, S, G2 and M phases of the cell cycle would provide functional evidence of deviation from the wildtype cell cycle.

Chapter 6: Probing tumourigenicity of mutant FNE1 subclones

6.1: Overview

An important aspect in the generation of the mutant FNE1 subclones was the generation of novel genetically defined model cell lines. Thus, I set out exploring their tumourigenic potential *in vivo* as aim (v). Further, the analysis of engrafted cells and tissues could yield valuable insight into HGSOC biology. Indeed, xenografts of human cancer cell lines and PDX models are a cornerstone of cancer research. To model HGSOC *in vivo*, three different routes of cell inoculation are commonly used. First, subcutaneous, heterotopic inoculation in the flank of mice allows for facile tumour implantation and measurements, which is useful for drug treatment assays. Second, intrabursal implantation of ovarian cancer cells mimics human tissue tropism most closely and is the most resource intensive method. Third, intraperitoneal implantation of cells is the most facile and resourceful route. Therefore, I chose to inoculate FNE1 cells and mutant subclones intraperitoneally as that route represents a near-orthotopic environment and is less resource intensive and laborious than intrabursal inoculation.

In the absence of an established workflow for intraperitoneal tumour implantation and subsequent tissue harvesting, I performed an initial study using OVCAR8 cells. These cells were reported to possibly be of HGSOC origin by Domcke et al. (2013), however, a more recent transcriptomic analysis has suggested their origin as low-grade serous ovarian cancer (Barnes et al., 2020). Despite their ambiguous origin, OVCAR8 cells are the ideal choice to set up a workflow as they were reported to engraft readily intraperitoneally and subcutaneously in nude mice (Hernandez et al., 2016). Building on this study, I could establish a robust experimental procedure to allow not only the assessment of tumorigenic potential but also downstream analyses of engrafted cells by miFISH.

6.2: Validation of an intraperitoneal carcinomatosis model using OVCAR8 cells

Inoculation of nude mice with OVCAR8 cells, five intraperitoneally and five subcutaneously, led to reliable tumour formation over the course of 91 days. Body weight was measured and used as a primary reference to infer well-being as successful engraftment resulted in the formation of ascites and typically rapid weight changes in mice inoculated intraperitoneally (Fig. 6.1A). Mice inoculated with cells subcutaneously were utilized as a control as this route of inoculation allows for facile tumour

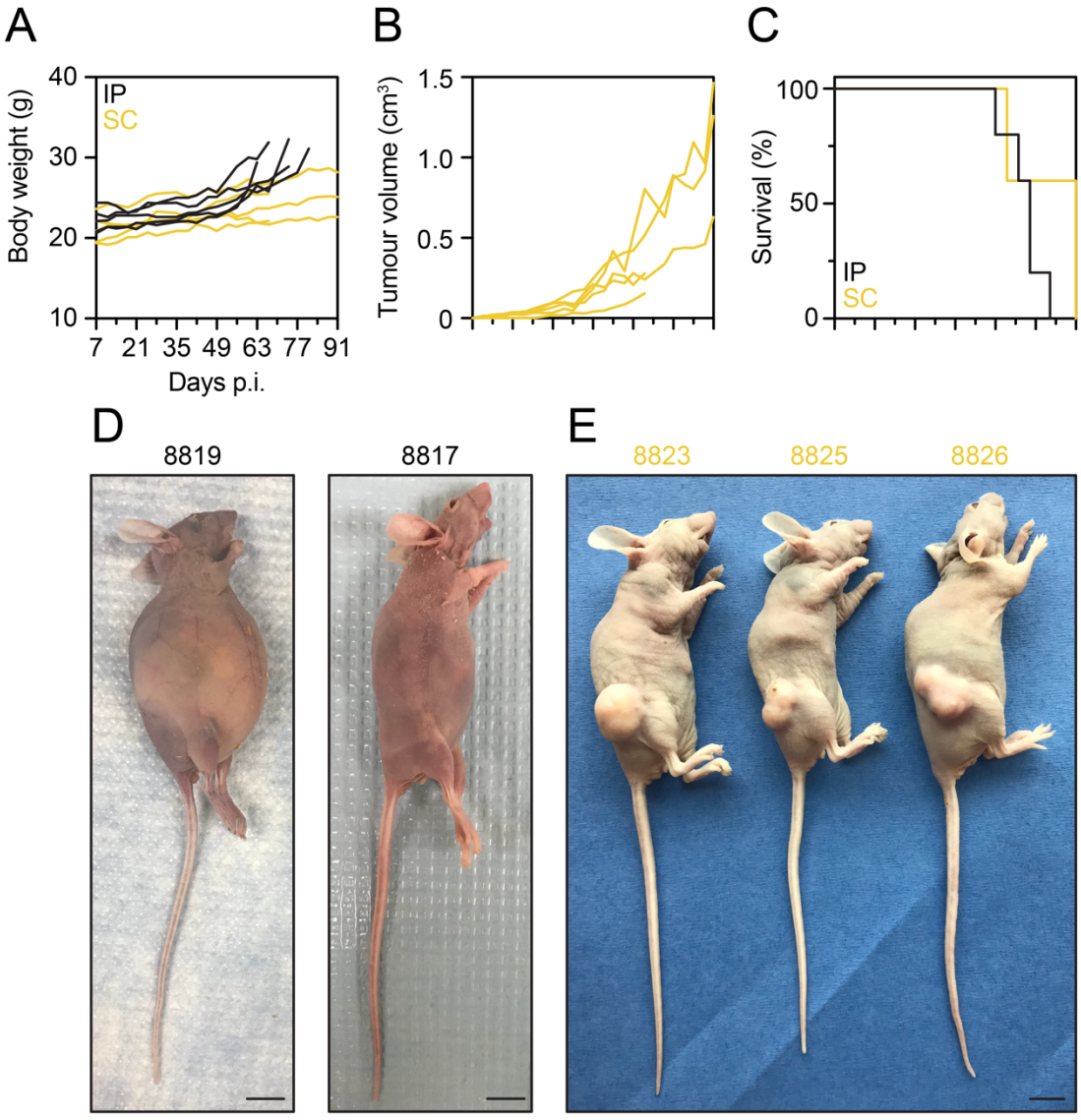

Figure 6.1: OVCAR8 cells engraft reproducibly in nude mice
A Measurements of body weight of individual mice inoculated with cells intraperitoneally (IP) or subcutaneously (SC). **B** Individual measurements of tumour volume of the five mice inoculated with cells subcutaneously. **C** Survival of mice implanted with cells IP or SC. **D**, **E** Representative images of two and three mice inoculated with cells IP and SC, respectively.
C-E, scale bars reflect 1 cm. Five mice were used per group and all measurements were taken twice weekly over a period of 91 days post inoculation (p.i.).

measurements using a calliper. Indeed, successful tumour formation was observed after 35 days which was followed by a rapid growth phase (Fig. 6.1B). Ultimately, all mice reached humane euthanasia endpoints within 91 days of inoculation (Fig. 6.1C). Intraperitoneally injected mice frequently developed abdominal distention as a result of the accumulation of ascites, however, weight loss and tissue wasting was also observed in one mouse which had accumulated ascites (Fig. 6.1D). Subcutaneous tumours also developed reliably after inoculation, however, none of the mice reached the tumour volume endpoint as the tumours would frequently ulcerate, which is another euthanasia criterium (Fig. 6.1E).

Having observed robust tumour formation, I developed a workflow for the downstream analysis of tissues and cells from xenografts by miFISH next. Ascitic fluid and solid tumour tissues were harvested during mouse necropsies and prepared for miFISH using enzymatic digestion, red blood cell lysis and standard cell swelling as is done for routine miFISH. Therefore, I hybridized OVCAR8 cells grown regularly in tissue culture and two samples from ascites and one from a digested tumour. Cultured OVCAR8 cells hybridized as expected and displayed a largely diploid signal pattern with the exception of three *RB1* and six *MYC* signals (Fig. 6.2A). Similarly, cells derived from xenografted tissue also hybridized, however, I noticed the presence of small nuclei that did not hybridize (Fig. 6.2B-C). The consistently small size of these nuclei and complete absence of detectable signals led me to surmise that these cells are of murine origin likely reflecting inflammatory cells.

In conclusion, I developed a suitable protocol to probe tumourigenicity by intraperitoneal inoculation of cells which has been validated using OVCAR8 cells. Additionally, capitalizing on the availability of ample tissue I was able to develop a workflow that would allow for downstream miFISH analysis of engrafted cells isolated from either solid tumour masses or ascites.

6.3: Neither FNE1 cells nor triple-mutant subclones form tumours in nude mice

Having established a workflow for intraperitoneal inoculation of cells in nude mice and tissue harvesting, I probed the tumourigenicity of FNE1 cells and the three triple-mutant subclones, PB1M, PB2M and PB3M, inoculating five mice per cell line. Over the course of the one-year follow-up period most mice gained weight as expected during aging, however, sudden weight loss was observed occasionally (Fig. 6.3A). During this follow-up, the majority of mice reached humane euthanasia endpoints of various causes. However, there was no temporal distinction between groups reaching said

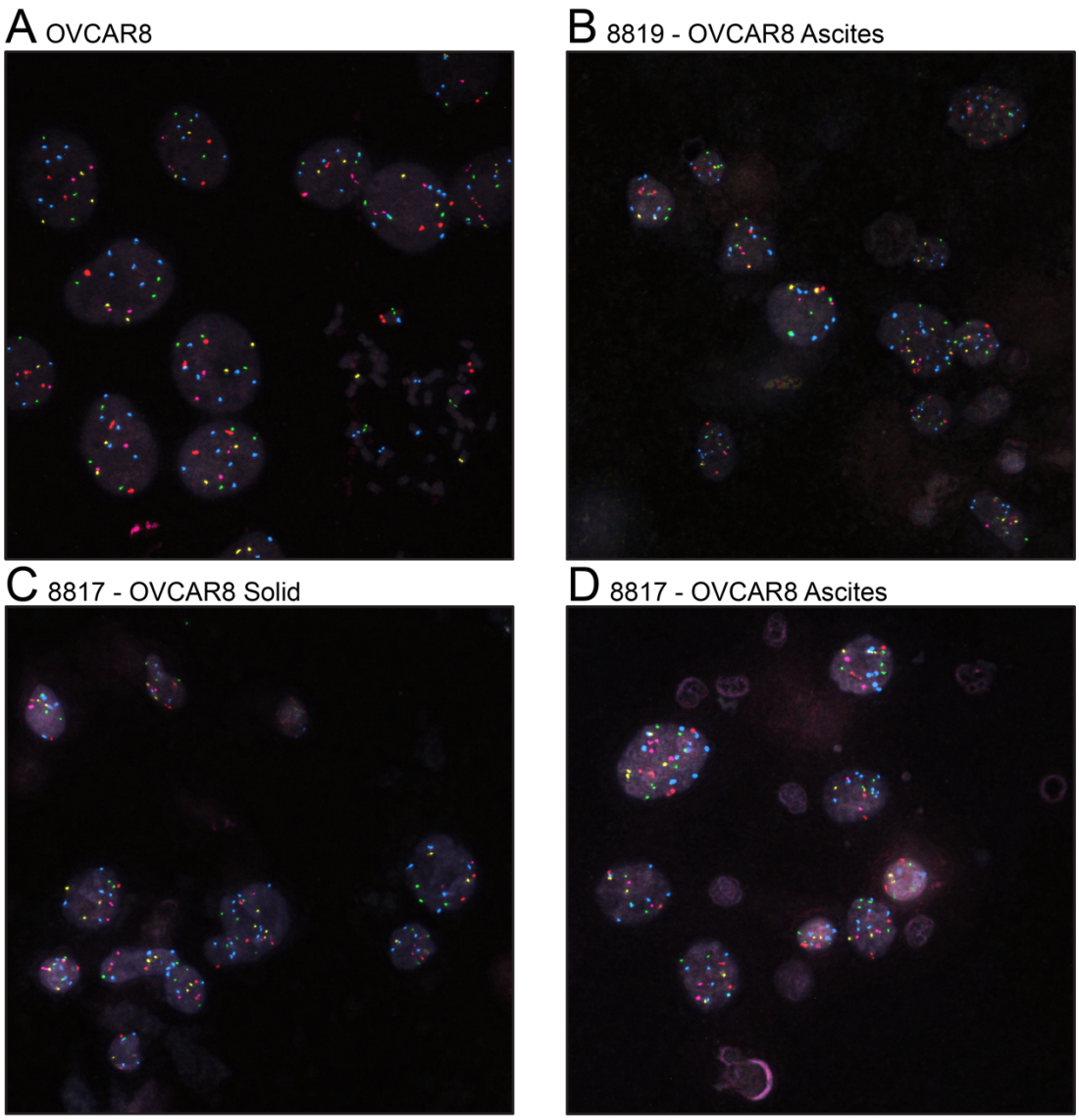

Figure 6.2: Xenografted tissue can be subjected to miFISH
A-D Cells of indicated origin were hybridized with the first miFISH panel and overview images extracted. The DNA probes' colours correspond to the following loci: aqua - *MYC*, far red - *DBC2*, gold - *KRAS*, green - *RB1*, red - *COX2*.

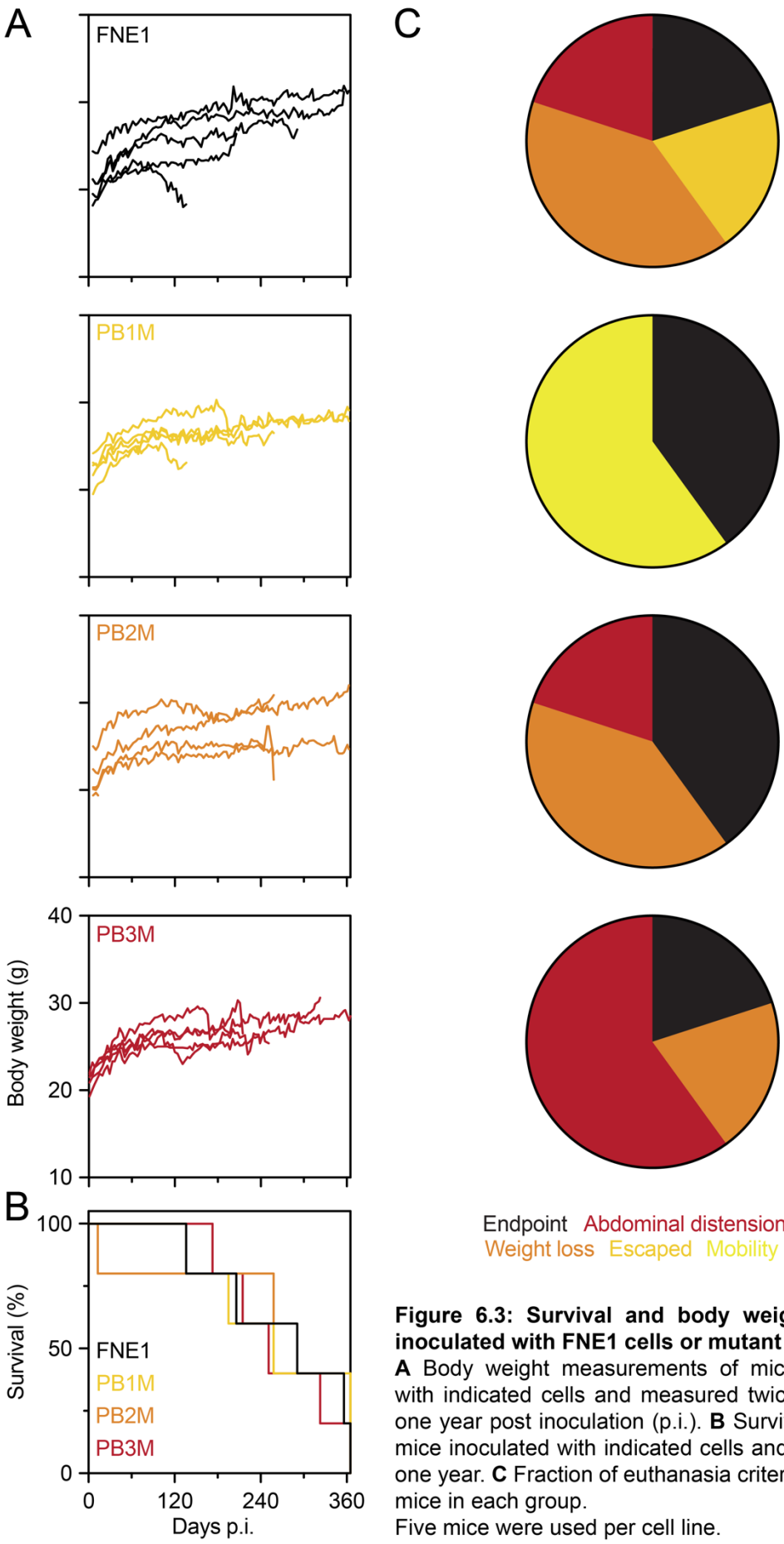

Figure 6.3: Survival and body weight of mice inoculated with FNE1 cells or mutant subclones
A Body weight measurements of mice inoculated with indicated cells and measured twice weekly for one year post inoculation (p.i.). **B** Survival curves of mice inoculated with indicated cells and followed for one year. **C** Fraction of euthanasia criteria utilized for mice in each group.
Five mice were used per cell line.

endpoints (Fig. 6.3B). Mice were euthanized for a variety of reasons including sudden weight loss, loss of mobility, abdominal distension and reaching the one-year follow-up timepoint (Fig. 6.3C). Across the four groups, weight loss, abdominal distension and reaching the one-year endpoint occurred at similar frequency. Three mice were euthanized due to a loss of mobility and one mouse escaped during rehousing. Upon necropsy and macroscopic evaluation of tissues, I noticed that two of the five mice euthanized due to abdominal distension presented with hepatosplenomegaly and one with splenomegaly. The other two mice harboured tumours, one had been injected with FNE1 cells and the other with PB1M cells. These data raised suspicion as FNE1 cells do not harbour any oncogenic aberrations that I could detect and, in general, tumour formation was only observed in two of 20 mice (10%). To learn more about these tumours I submitted them for histopathological analysis. Interestingly, this analysis revealed a homogenous, monomorphic infiltration of cells with little to no cytoplasm suggesting a lymphoma rather than an FNE1-derived tumour (Fig. 6.4A). Additional immunohistochemical staining for GFP, which is expressed by FNE1 cells, and human mitochondrial antigens was performed. Staining of both tumours failed to detect GFP or human mitochondrial antigens thus ruling out human and instead supporting murine origin of these tumours (Fig. 6.4B-C).

Taken together, I demonstrated that FNE1 cells and triple-mutant subclones fail to form tumours in nude mice over a follow-up period of one year after inoculation. Instead, I observed that nude mice succumbed due to other tumour-unrelated causes such as hepatosplenomegaly and tumours of murine origin.

6.4: Summary and discussion

Here, I have demonstrated the utility of a newly established workflow aimed at modelling peritoneal carcinomatosis and subsequently analysing fresh tissue utilizing OVCAR8 cells, which have previously been shown to reliably induce both tumour formation in the abdominal cavity and ascites (Hernandez et al., 2016). Indeed, I was able to reproduce these previous findings and further illustrate the feasibility of harvesting and processing these tissues for downstream analysis by miFISH.

This workflow was set up with the intention of addressing aim (v), probing tumourigenicity of FNE1 cells as control and the three triple-mutant subclones. However, none of the mice from this study showed evidence of engraftment of FNE1 cells or mutant subclones. Mice from all groups were euthanized at similar timepoints throughout follow-up and the two tumours that developed did not express markers suggestive of human origin. To determine a murine lymphocytic origin of the two

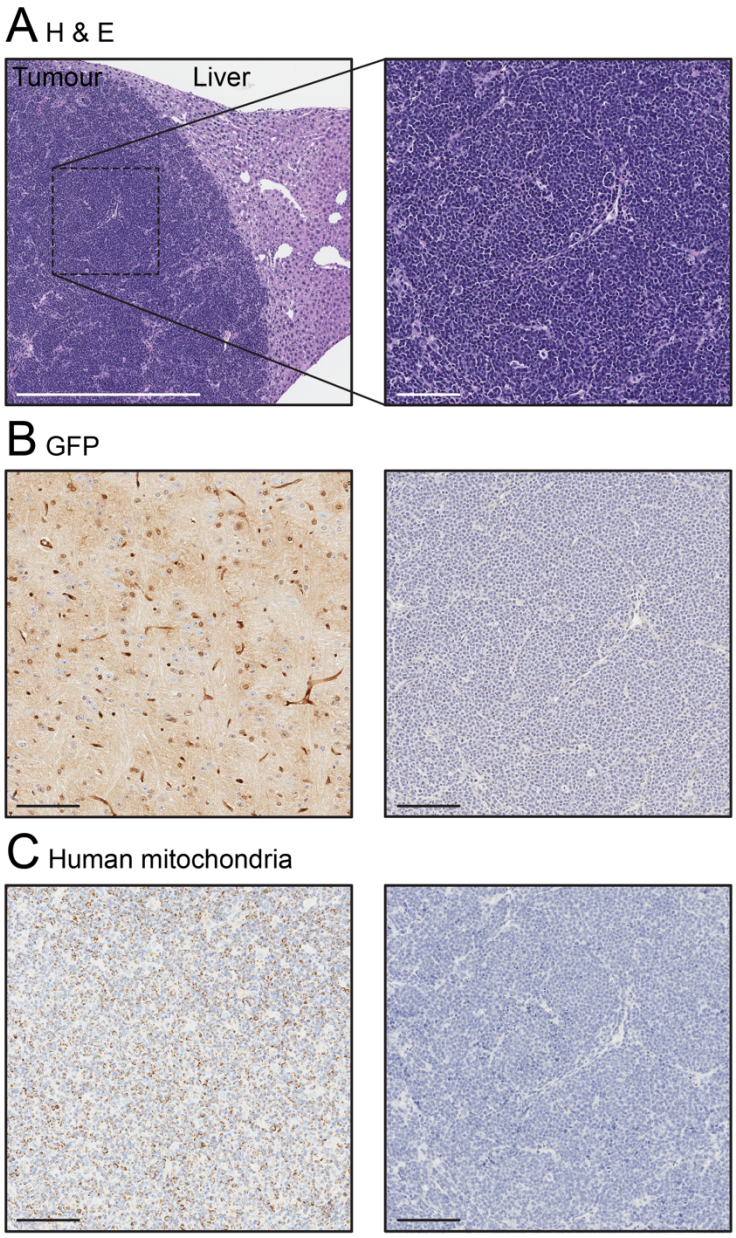

Figure 6.4: Harvested FNE1-derived tumours do not express GFP or human mitochondrial antigens
A Representative image of a liver nodule harvested from a mouse injected with PB1M cells and stained with haematoxylin and eosin (H & E). **B** & **C** Sectioned liver nodule stained for GFP and human mitochondria, respectively. Left-hand panels were included as positive control.
Scale bar in left panel of A 1 mm and elsewhere 100 μm.

tumours I observed, staining of a pan-lymphocyte marker such as CD45 would be required. Since athymic nude mice are largely T-cell-deficient staining for CD19 would provide more conclusive evidence suggesting a B-cell lymphoma. Nonetheless, the data shows that neither FNE1 cells nor the three triple-mutant subclones display tumourigenic potential.

These findings are at odds with previous observations made by Merritt et al. (2013) in whose study transformed FNE1 cells were tumourigenic in athymic nude mice. An important difference between the approach of the aforementioned study and this work is the implantation of FNE1 cells. First, I implanted cells intraperitoneally in media whereas Merritt et al. (2013) implanted cells in media mixed with Matrigel (an extracellular matrix replacement). Second, in the aforementioned study mice were injected at three sites, i.e., two subcutaneous sites and one intraperitoneal, in contrast, I inoculated mice only intraperitoneally.

In addition to the difference in implantation strategy the transformed FNE1 cells were retrovirally transduced to express the SV40 TAg oncoprotein and oncogenic, mutant *HRAS* ectopically (Merritt et al., 2013). Since SV40 TAg is known to perturb not only p53 but also RB1 function its ectopic expression combined with mutant *HRAS* might impact the oncogenic potential of cells differently than genetic p53/BRCA1-deficiency with *MYC* overexpression modelled in the subclones described as part of this work. Similarly, fallopian tube-derived cells ectopically expressing a dominant negative isoform of p53, mutant *KRAS* and *MYC* also displayed tumourigenic potential in athymic nude mice, however, a ten-fold higher number of cells was inoculated (Nakamura et al., 2018). Lastly, additional fallopian tube-derived cell lines that were transformed using various combinations of SV40 TAg, RNAi-mediated suppression of p53, *MYC* and mutant *KRAS* also formed tumours *in vivo*. However, in these experiments severely combined immunodeficient (SCID) and non-obese diabetic SCID gamma (NSG) mice, which are not only T-cell-deficient but also lack B-cells and some innate immune cells, were used. Besides the use of more severely immunocompromised mice, the number of cells was also increased by ten- and twenty-fold (Jazaeri et al., 2011; Karst et al., 2011).

Several of these studies point to exploitable directions that could improve engraftment of mutant FNE1 subclones. First, inoculating cells in media mixed with extracellular matrix could improve engraftment efficiency. Second, an increased number of inoculated cells either with or without extracellular matrix might also improve engraftment. Third, the use of more severely immunocompromised mice such as SCID or NSG mice in combination with the aforementioned improvements could lead to better

engraftment. Lastly, the change of the injection site to intrabursal inoculation of cells would provide an even more orthotopic environment for the cells. This change could also be combined with the use of extracellular matrix and SCID or NSG mice to maximize engraftment potential.

In conclusion, however, mutant FNE1 subclones do not display tumour formation capacity in the athymic nude mouse intraperitoneal implantation assay employed. However, technical differences between this and other studies as well as the potentially different impact of oncogenic aberrations introduced into cells might account for the absence of tumourigenic potential.

Chapter 7: General discussion

HGSOC has been consistently found to be one of the most chromosomally unstable cancer entities in pan-cancer studies (Ciriello et al., 2013; Davoli et al., 2017; Taylor et al., 2018). In light of the poor survival of HGSOC patients and the association of CIN with metastasis, poor survival and drug resistance, it is imperative to better understand CIN in HGSOC (Bakhoum et al., 2018; Jamal-Hanjani et al., 2017; Lee et al., 2011). Indeed, a better understanding of both, CIN and the impact of the ubiquitous, truncal mutations in *TP53*, in HGSOC has been outlined as a central question for the field (Bowtell et al., 2015).

The study of CIN has largely relied on colorectal cancer cell lines derived from tumours with either microsatellite instability (MIN) or CIN. The utility of these cell lines lies in the fact that MIN cancer cells have near-diploid karyotypes with few cytogenetic abnormalities compared with CIN cells that in contrast do not display MIN (Knutsen et al., 2010). These observations have recently been corroborated in an analysis of TCGA, pan-cancer genomics data that showed mutual exclusivity of MIN and aneuploidy, the most prominent consequence of CIN (Auslander et al., 2020). In addition, p53-proficient and -deficient RPE-1 cells are also widely used to study the impact of perturbed chromosome segregation fidelity in a non-transformed cell type (Kok et al., 2020; Santaguida et al., 2017; Santaguida et al., 2015; Soto et al., 2017). However, it is important to appreciate that perturbations of the tightly controlled and highly conserved cell division process display a certain degree of tissue specificity. Recently, it was shown in organoids generated from either the colon or the small intestine of mice with identical genetic perturbations in the adenomatous polyposis coli gene (*Apc*) and *Ttk* that chromosomes mis-segregated at different frequencies in organoids derived from the colon and small intestine (Hoevenaar et al., 2020). These observations lend weight to studying chromosome segregation fidelity in a tissue context.

Many causes of CIN have been described and multiple GEMMs showed a causal link between the disruption or overexpression of SAC genes and mitotic aberrations (Bastians, 2015; Vasudevan et al., 2021). In contrast to these observations, reoccurring mutations in genes involved in mitosis are rarely observed in human cancers. However, deregulation of processes involving these genes have been shown to cause CIN, such as mal-attachments of kinetochores to spindle microtubules, microtubule assembly rates and centrosome amplification (Ertych et al., 2014; Ganem et al., 2009; Thompson and Compton, 2011). Thus far, the only monogenetic link between CIN consequential aneuploidy pan-cancer and in breast cancer specifically has

been found to be mutations in *TP53* (Ciriello et al., 2013; Davoli et al., 2017; Pfister et al., 2018; Taylor et al., 2018; Zack et al., 2013). As alluded to above, *TP53* is also ubiquitously mutated in HGSOC. This precipitates the question how mutations in *TP53* drive CIN.

Therefore, I set out to address the urgent questions of (i) *TP53* mutations specifically and HRD mediated by *TP53/BRCA1* mutations more broadly as a cause of CIN in HGSOC and (ii) their impact on otherwise healthy fallopian tube cells as they represent the tissue of origin of HGSOC. Additionally, HGSOC is a devastating disease with an important clinical need. Many classically used cell lines for the study of HGSOC proved no utility for this study as they ubiquitously harboured *TP53* mutations, in line with the disease of origin (Barnes et al., 2020). Moreover, most fallopian tube non-ciliated secretory epithelial cell-derived, immortalized and yet non-transformed cell lines rely on the suppression of p53 either directly or indirectly (Jazaeri et al., 2011; Karst and Drapkin, 2012; Karst et al., 2011). Organoids derived from fallopian tube tissue have also been described and rely on the culture of stem cells in a growth factor rich environment which also allows for the growth of ciliated epithelial cells thus potentially confounding efforts to study the secretory non-ciliated cell type specifically (Kessler et al., 2015). Alike to the fallopian tube-derived cell lines relying on p53-suppression, an independently conceived organoid system other than the aforementioned one depends on the genetic perturbation of *TP53* and selection of p53-deficient *normal* organoids (Kopper et al., 2019). Taken together, this left me with two fallopian tube-derived cell lines that fulfilled the criteria of being of non-ciliated secretory epithelial origin and presumably p53-proficient. Of these two systems, one was immortalized using ectopic expression of cyclin D1, R24C mutant CDK4 and *hTERT* and the other relied on the ectopic expression of *hTERT* and the maintenance of cells in a specialized media formulation (Merritt et al., 2013; Nakamura et al., 2018). Thus, FNE1 cells exclusively expressing *hTERT* ectopically were chosen to mitigate the potential contribution of other genetic alterations. Of note, Nakamura et al. (2018) only described their cell line two years after this project was started.

7.1: Sequential mutagenesis generates novel fallopian tube-derived models

The rapid uptake of CRISPR/Cas9 technology coupled with the development of various reagents for its use has led to novel biological insights previously unappreciable or difficult to probe due to the requirement of laborious, alternative techniques (Adli, 2018). While CRISPR/Cas9 has been utilized to perform genome-wide activation and perturbation screens, it has also been widely adopted to perturb a single gene in

isolation or multiple genes in combination either simultaneously or sequentially (Adli, 2018). In fact, an early application of CRISPR/Cas9 was the development of sequentially mutagenized colon organoids (Drost et al., 2015). This illustrates the utility of CRISPR/Cas9-mediated gene editing to generate novel model systems to study specific aspects of cell biology.

Despite its wide applicability and utility, CRISPR/Cas9 technology has been scrutinized extensively highlighting several drawbacks that require appropriate controls. Indeed, sequence similarity between the target locus and alternative target sequences can lead to off-target mutations and thus unintended gene disruption. Furthermore, mutations have also been found to not only result in sequence changes, but also in larger scale insertions and deletions; particularly telomeric regions have been found vulnerable (Kosicki et al., 2018; Przewrocka et al., 2020). Lastly, the selection of cell lines used for mutagenesis also plays an important role as underlying GI and thus cellular heterogeneity can result in clonal selection effects being studied rather than genotype-dependent effects (Giuliano et al., 2019; Rayner et al., 2019).

In my approach to sequentially mutagenize the *TP53* and *BRCA1* loci I therefore chose an inducible Cas9 construct to minimize unintended endonuclease activity. Furthermore, I found that FNE1 cells are genomically stable which decreases the potential of selection effects from the expansion of cell line subclones. The choice to use only one gRNA to target *TP53* was based on previously reported data showing that the particular gRNA sequence generated p53-deficient cells most efficiently (Simoes-Sousa et al., 2018). Additional work using complementary gRNAs reported in the literature with similar efficiencies to corroborate the findings in cells generated using this g*TP53* sequence would add further support to the findings presented here. The use of additional gRNAs is recommended to rule out effects due to mutations in functionally important regions of the gene of interest (Giuliano et al., 2019). Nonetheless, the rigorous characterization of the mutant subclones using molecular and cellular biological tools in addition to firmly established pharmacological means validated the mutant phenotypes corresponding to their genotype and is well accepted in cancer research (Ischenko et al., 2021).

In sum, I have firmly shown the utility of not only FNE1 TO Cas9 cells but also p53-deficient subclone P1 to add on additional genetic perturbations to study the loss of tumour suppressor genes in the context of HGSOC.

7.2: p53-loss initiates CIN

As alluded to above, mutations in *TP53* have consistently been found to correlate with aneuploidy, a primary consequence of CIN, in human cancers (Ciriello et al., 2013; Davoli et al., 2017; Pfister et al., 2018; Taylor et al., 2018; Zack et al., 2013). Furthermore, *TP53* mutations are also enriched in metastatic cancers reflecting the most aggressive disease stage (Priestley et al., 2019). Likewise, CIN increases with disease stage across tumour entities and CIN levels are higher in metastatic than in primary tumours (Priestley et al., 2019; Shukla et al., 2020). In addition to the correlations between *TP53* mutations, CIN and tumour aggressiveness, *TP53* mutations and CIN have also been found to be enriched in hypoxic tumours (Bhandari et al., 2020). Taken together, these observations overwhelmingly suggest a causative relationship between *TP53* mutations, CIN and tumour growth and progression.

Intriguingly, early studies using the MIN colorectal cancer cell line HCT116, which have since been independently confirmed, have led to the understanding that p53-loss permits the proliferation of aneuploid cells but does not cause aneuploidy *per se* (Bunz et al., 2002; Simoes-Sousa et al., 2018; Thompson and Compton, 2010). More recent findings in p53-suppressed or *TP53* CRISPR/Cas9 knockout RPE-1 or 184-*hTERT* mammary epithelial cells have called the aforementioned concept into question by showing an increase in whole or segmental chromosomal aneuploidies in p53-deficient cells compared with wildtype controls (Kok et al., 2020; Salehi et al., 2020; Soto et al., 2017). These recent data correspond to observations made in human cancers, however, do not elucidate a causative mechanism. The data I presented in this thesis also suggests a causal role for p53 in controlling euploidy as I could show that more than half of sequenced P1 cells harboured aneuploidies compared with less than 5% of sequenced wildtype FNE1 cells.

Importantly, many *in vitro* model systems are maintained at atmospheric oxygen levels including the most frequently used cell lines and organoids. In contrast, FNE1 cells are maintained at 5% oxygen which is considered to reflect normoxia more closely. In fact, direct comparison of p53-deficient and -proficient MEFs transformed with *E1a*;*Hras*^{G12V} also maintained under normoxic conditions has shown that multiple cellular processes including the maintenance of genomic stability were deregulated (Valente et al., 2020). These observations led the authors to conclude that the pleotropic effects of p53-loss may have been masked in previous studies due to the maintenance of cells under atmospheric oxygen. Indeed, trisomic DLD-1 cells, another MIN displaying, otherwise near-diploid colorectal cancer cell line, have been shown to overcome a fitness deficit compared with control, disomic cells under non-

standard growth conditions such as hypoxia (Rutledge et al., 2016). Therefore, by using FNE1 cells in a normoxic environment I was able to show that p53-deficiency leads to CIN in a more physiologically relevant setting than previous studies.

7.3: BRCA1-loss results in exacerbated aneuploidy and tetraploidy

The second most commonly mutated gene in HGSOC is *BRCA1* (TCGA, 2011). *BRCA1* was first discovered as a susceptibility locus of breast cancer and mutations in *BRCA1* have since been shown to increase the risk of breast, ovarian, prostate and pancreatic cancer in carriers (Futreal et al., 1994). In breast cancer specifically, *BRCA1* germline mutations confer the highest risk of disease onset (Breast Cancer Association et al., 2021). GEMMs were generated to confirm a role of *BRCA1* disruption in cancer development and to dissect potential mechanisms underpinning *BRCA1*-driven tumourigenesis. Indeed, Cre-recombinase-mediated disruption of *Brca1* results in mammary tumour formation with long latency that could be accelerated in a p53-perturbed background (Xu et al., 1999a). In fact, tumours from mice engineered to only harbour the *Brca1* disruption were found to be *Trp53* mutant. An analysis of human, *BRCA1*-associated breast cancers also showed that all *BRCA1* mutated cases were also *TP53* mutated (Holstege et al., 2009). These findings were recently confirmed in ovarian carcinomas where mutations in *TP53* and *BRCA1* were found to co-occur (Ghezelayagh et al., 2020).

Functionally, BRCA1 has been implicated in a number of cellular processes controlling genomic integrity. Its canonical function, however, lies in HR which occurs once S-phase has been entered and DNA has been replicated to serve as template (Chen et al., 2018). Further to its role in the DNA damage response, *BRCA1* has also been implicated in controlling chromosome segregation fidelity. Indeed, suppression of *BRCA1* by RNAi in HCT116 cells results in chromosome mis-segregation and is linked directly to suppressing microtubule assembly rates which at increased levels leads to CIN (Ertych et al., 2014; Ertych et al., 2016; Stolz et al., 2010). Thus, BRCA1's role in controlling genomic stability is at least two-fold.

Unsurprisingly therefore, studies of Brca1-deficient MEFs revealed impaired G2- to M-phase transition (Xu et al., 1999b). In the same study, SKY analysis showed structural abnormalities in chromosome spreads from Brca1-deficient MEFs. Mammary tumours recovered from Brca1-deficient mice have also been found to be aneuploid with recurring patterns of chromosomal gains and losses similar to those observed in human breast cancers (Weaver et al., 2002). Correspondingly to these data, the knockout of *BRCA1* in FNE1 cells led to aneuploid karyotypes with frequent additional

gains and losses deviating from the mode thus indicating on-going CIN. Strikingly, I also observed that in BRCA1-deficient subclones PB2/E/M and PB3/E/M tetraploid cells emerged likely as a result of WGD events. The fraction of tetraploid cells in PB2M was determined to be around 10%, in contrast, all PB3/E/M cells analysed were tetraploid. Importantly, the near-diploid population of PB2/E/M cells displayed multiple whole or arm-level losses of chromosomes, which followed dosage in the tetraploid population. In a similar manner, multiple chromosomes displayed whole or partial two-fold reductions from the expected four copies in PB3.

Despite WGD being a frequently observed event in advanced cancers – up to 38% of HGSOC from the TCGA cohort have been classified as having undergone a WGD event – *BRCA1* mutations are not associated with WGD (Bielski et al., 2018). In contrast to these observations, data from Brca1-deficient MEFs and mammary tumours showed that Brca1-deficient cells display features of having undergone a WGD event. MEFs deficient for Brca1 are not only frequently aneuploidy, but also harbour supernumerary centrosomes (Xu et al., 1999b). Mouse mammary tumours with *Brca1* mutations were also found to be aneuploid, harbouring supernumerary centrosomes and frequently showed two-fold ploidy increases consistent with WGD events (Weaver et al., 2002). Mechanistically, centrosome amplification can be driven by overexpression of genes responsible for physiological centrosome duplication during S-phase, e.g., *PLK4*, however, more importantly in this context it is also observed as a consequence of WGD (Holland et al., 2012). Indeed, tetraploid subclones of the MIN, near-diploid colorectal cancer cell line RKO have been reported to harbour supernumerary centrosomes more frequently than the near-diploid control cells (Wangsa et al., 2018). Thus, taking together these data from MEFs, mouse tumours and RKO cells, the observation of WGD events in PB2/E/M and PB3/E/M cells is not entirely unexpected.

Furthermore, WGD itself has been proposed as an aneuploidy tolerance mechanism (Holland and Cleveland, 2012). Observations made in yeast have shown that the introduction of disomies decreased cellular fitness in otherwise haploid cells while WGD of haploid yeast cells did not result in the same fitness reduction (Torres et al., 2007). Similarly, in diploid yeast cells with engineered trisomies the fitness defect was less severe than an engineered disomy in haploid yeast cells. An *in silico* analysis of human lung cancers combined with evolutionary modelling has additionally proposed that WGD events buffer negative selection of mutations in haploid regions of cancer genomes (Lopez et al., 2020). Thus, I suggest that during the expansion of the PB3/E/M lineage, cells harbouring a detrimental monosomy spontaneously underwent WGD (becoming tetraploid) gaining a relative fitness advantage outcompeting

their diploid counterparts. This could potentially have been a monosomy that is now present as a disomy in PB3/E/M cells, but not observed as such in PB2/E/M cells. In contrast, PB2/E/M retain diploid cells in their population suggesting that the monosomies observed are compatible with cellular viability. Interestingly, data presented in a study using trisomic and matched euploid DLD-1 cells has revealed a role for a gene, namely *SPG20*, mapping to the trisomic chromosome 13 whose increase in dosage resulted in a cytokinesis failure phenotype and thus WGD providing a mechanism by which aneuploidy directly results in WGD potentially alleviating aneuploidy-induced stress (Nicholson et al., 2015).

While the observation of WGD in PB2/E/M and PB3/E/M cells may not be entirely unexpected, data from pan-cancer analyses did not suggest an association of BRCA1 with WGD. The potential mechanisms of the WGD events in PB2 and PB3 cells remain to be explored, however, data from previous studies lead me to speculate that: (i) the dosage imbalance of genes mapping to the monosomic chromosomes might have resulted in a significant reduction of one or multiple genes required for faithful chromosome segregation during mitosis or cytokinesis thus precipitating WGD and (ii) WGD alleviates negative selection pressures on PB2 and PB3 cells that would otherwise accumulate detrimental mutations on the monosomic chromosomes.

7.4: Ectopic MYC does not affect ploidy in BRCA1-deficient background

The pleiotropic transcription factor MYC has long been recognized as an oncogene. In human solid tumours *MYC* is frequently gained on the DNA copy number level which results in a dosage-dependent increase of expression while in haematological malignancies translocations involving *MYC* result in constitutive activation. The target loci for *MYC* translocations in human haematological malignancies are typically those required for cell type specific gene expression, e.g., in T-cell acute lymphoblastic leukaemia the T-cell receptor locus is frequently rearranged with *MYC* while in Burkitt's lymphoma the immunoglobulin encoding loci are affected (Boxer and Dang, 2001). These observations from human cancers have been confirmed functionally in GEMMs as tumours from mice predisposed to tumour development were found to be trisomic for mouse chromosome 15 where *Myc* maps (Jones et al., 2010). Tumours in mice expressing *Myc* ectopically following random integration of the transgene into the mouse genome were no longer found to be trisomic for mouse chromosome 15. In line with these observations that MYC promotes tumourigenesis in a dosage-dependent manner, mutations in *MYC* are rarely observed.

In HGSOC specifically, MYC has been identified as a therapeutic vulnerability as it has been found to be amplified in more than 40% of cases in which its amplification directly correlates with increased mRNA expression (Zeng et al., 2018). Therefore, I chose to overexpress *MYC* ectopically in the single- and double-mutant FNE1 subclones. On a functional level, as indicated above, MYC acts as a transcriptional amplifier of several cellular processes, an observation I confirmed (Lin et al., 2012; Nie et al., 2020; Nie et al., 2012).

With respect to a role of MYC in mitosis, observations have shown that RKO cells expressing physiological and high levels of MYC spent more time in mitosis than *MYC*$^{-/-}$ RKO cells (Littler et al., 2019). Furthermore, spindle size was altered by MYC-overexpression, i.e., cells with high levels of MYC had increased spindle width and reduced spindle length compared with MYC-deficient cells. Upon pharmacologic perturbation of mitosis, cell death and the number of cells with micronuclei following mitosis increased uniformly independent of perturbation. Similar findings were described using non-transformed, *hTERT* immortalized RPE-1 cells that ectopically express *MYC* (Rohrberg et al., 2020). In the latter case, the authors also found that cells overexpressing *MYC* spent more time in mitosis, a larger fraction of cells displayed mis-aligned chromosomes in metaphase, lagging chromosomes in anaphase and ultimately micronuclei after completion of mitosis (note, this observation is at odds with what was observed in RKO cells). These phenotypes were then corroborated in cancer cell lines with high MYC expression by RNAi-mediated knockdown which suppressed the aforementioned phenotypes in treated cells (MYC-reduced) compared with control cells. Ultimately, both reports show that multiple genes involved in mitosis are deregulated in MYC overexpressing cells and that their individual knockdown or pharmacological inhibition results in cell death.

Unlike these reports, I did not observe an increase in CIN in PB2M or PB3M cells compared with PB2/E or PB3/E cells, respectively. An important difference between the studies described above and this one is the modality employed to study CIN. Both, Littler et al. (2019) and Rohrberg et al. (2020), studied CIN directly by monitoring mitosis by live-cell imaging and looking for micronuclei in interphase cells after mitosis was completed. In contrast, I used an indirect method, scWGS, on a limited number of cells, thus my observations might be underestimating CIN in comparison to the aforementioned reports. The most critical difference, however, is that RKO and RPE-1 cells have a near-diploid karyotype and are chromosomally stable to begin with whereas PB2/E and PB3/E cells display a certain degree of CIN in the absence of *MYC*-overexpression and PB3/E cells were also found to have upregulated *MYC*

spontaneously. As I did not investigate the karyotype of any PM subclones, it remains conceivable that ectopic overexpression of *MYC* in otherwise near-diploid cells, such as P1 cells, would result in increased CIN. As done in this thesis, a combination of scWGS and miFISH or direct studies of chromosome segregation fidelity could be employed to answer this question.

7.5: Transcriptional deregulation of the cell cycle is a potential cause of CIN

To decipher potential causes of CIN in the sequentially mutagenized FNE1 subclones, I chose to perform RNA sequencing as it allows for transcriptome-wide analyses of alterations in a manner independent of a readout assay. As outlined in the previous section, gene expression profiling has an illustrated utility for the identification of causative gene deregulation. However, it is important to appreciate that this approach would likely identify multiple potential causative genes. As such, Rohrberg et al. (2020) selected three candidate genes at first and narrowed those down to study *TPX2* in more detail. The importance of understanding multiple genome integrity controlling mechanisms at the same time was recently in illustrated in HGSOC cell lines (Tamura et al., 2020). Specifically, the authors found that five HGSOC cell lines displayed increased microtubule assembly rates compared with FNE1 cells. Likewise, all HGSOC cell lines displayed a reduction in DNA replication speed, the primary indicator of replication stress, compared with FNE1 cells. Taken together, and in light of the also reported increased number of chromosome segregation errors in HGSOC cancer cells in comparison to FNE1 cells, multiple mechanisms are deregulated in HGSOC to cause CIN, yet the underlying reasons for this deregulation remained undetermined.

In comparison to FNE1 cells, all mutant subclones displayed enrichment of gene sets comprising genes involved in the cell cycle (G2M checkpoint and E2F targets) and DNA replication. In addition, samples in the P cluster also displayed an enrichment of the Mitotic spindle gene set, intriguingly however, the samples from other clusters did not display the same enrichment. While these data are only indirect evidence of functional activation of these pathways, spontaneous upregulation of DNA replication factors has recently been described as a consequence of oncogene-induced replication stress (Bianco et al., 2019). Furthermore, tumour aneuploidy has been shown to correlate with positive enrichment of the E2F targets, G2M checkpoint, Mitotic spindle, MYC targets and Spermatogenesis gene sets in a pan-cancer analysis of TCGA tumour samples (Taylor et al., 2018). Thus, measurements of cell cycle regulators

and DNA replication factors on the mRNA expression levels are a reliable surrogate to determine if cells are experiencing cell cycle alterations and DNA replication stress.

My findings, therefore, are consistent with observations made *in vivo* and suggest a causative role for cell cycle and DNA replication upregulation in CIN. The latter having been established as a *bona fide* cause of CIN in colorectal cancer and HGSOC (Burrell et al., 2013; Tamura et al., 2020). While functional evidence from FNE1 cells confirming the RNA sequencing data is lacking, it has been shown in p53-suppressed human osteosarcoma (U2OS) cells and p53-deficient HCT116 cells, MEFs and murine thymocytes that all undergo replication stress compared with p53-proficient control cells (Klusmann et al., 2016; Yeo et al., 2016). Further experiments probing DNA replication dynamics and cell cycle distribution by DNA fibre assays and flowcytometric evaluation of DNA content, respectively, would provide valuable functional insight to the mRNA expression based observations.

Based on my observations and the evidence from previous reports, I propose that the collective deregulation of multiple processes involved in ploidy and genome maintenance leads to CIN. Due to p53's function as a transcriptional activator of cell cycle repressors, its absence leads to derepression of cell cycle and DNA replication drivers across the genome. A simplified example is p53's canonical transcriptional target *CDKN1A* which encodes the CDK inhibitor p21 and is differentially downregulated in P samples versus FNE1 samples. It is conceivable that with decreased abundance of p21 one of its targets, e.g., CCNE1, is uninhibited which results in accelerated RB1 hyperphosphorylation and thus E2F release. Ultimately, the E2F release drives S-phase. Additionally, an absence of p53 could result in cell cycle progression in the presence of DNA damage as it is the primary signalling target for DNA damage response kinases CHEK1/2. In addition to *CDKN1A*, other genes such as the transcriptional regulator of mitotic genes *FOXM1*, have been found to be differentially upregulated in P cells versus FNE1 cells. *FOXM1* was first identified as a controller of mitosis in knockout MEFs and was later shown to be repressed by p53, thus *FOXM1* upregulation in a manner dependent on p53-loss likely contributes to CIN observed in mutant subclones (Barsotti and Prives, 2009; Laoukili et al., 2005). Indeed, *FOXM1* and five downstream targets have been proposed as drivers of CIN in HGSOC specifically, namely, *CDC25B*, *BIRC5*, *AURKA*, *CCNB1* and *PLK1* (TCGA, 2011). Functionally, *FOXM1* overexpression has been shown to result in increased CIN in *Xenopus* embryos injected with human mRNA, however, the effect depended on co-injection of *FOXM1* mRNA with *E2F1* and *MYBL2* mRNAs (Pfister et al., 2018).

Since I have not performed rescue experiments by re-expressing p53 ectopically, because previous studies have shown that ectopic p53 expression suppresses growth dramatically in *TP53*-mutant cells, alternative rescue experiments might provide insight into the causes of CIN in p53-deficient FNE1 subclones (Baker et al., 1990). As described in the previous section, *CDKN1A* is downregulated in P versus FNE1 cells and a number of other genes are upregulated. This offers a unique opportunity to ectopically express *CDKN1A* and suppress some or all of the other genes by RNAi to probe if their down- or up-regulation is the underlying cause of CIN observed in P1 cells. Indeed, a separation of function mutation in p53, which renders it apoptosis deficient but cell cycle arrest proficient, was shown to prevent CIN in a p21-proficient background that was overcome by ablation of p21 (Barboza et al., 2006). The readout for such experiments could be two-fold (i) measuring CIN directly or indirectly and (ii) analysing transcriptomes of p53-deficient cells expressing p21 and not expressing p21.

In summary, p53-loss drives CIN by transcriptional rewiring of cell cycle regulators. This effect is most likely combinatorial in nature resulting from direct derepression of cell cycle drivers like *FOXM1* as well as indirect activation of the cell cycle by mechanisms such as downregulation of its canonical targets, e.g., p21.

7.6: *BRCA1* mutagenesis led to MYC target enrichment

I alluded to MYC's role in CIN in *7.4: Ectopic MYC does not affect ploidy profiles in BRCA1-deficient background* and while I did not observe an increase in CIN as would have been expected, nonetheless, I found that the ectopic overexpression of *MYC* cDNA resulted in the expected transcriptional activation in a MYC-specific manner. MYC target genes were found to be enriched in most samples overexpressing *MYC* and when contrasting P with FNE1 samples and PM with FNE1 samples, the number of differentially expressed genes was greater in the PM versus FNE1 contrast than in the P versus FNE1 contrast. This observation rules out the possibility that the ectopically expressed *MYC* cDNA is dysfunctional.

On the transcription level, PM samples showed the highest enrichment of cell cycle and DNA replication gene sets which suggests that these cells would have even higher levels of CIN than P samples, however, I did neither directly nor indirectly assess CIN in those cells. Therefore, my conclusions are limited to what I observed in PB2/E and PB3/E versus PB2M and PB3M cells, respectively. However, all PB2/E/M and PB3/E/M samples showed enrichment of MYC target gene sets and compared to P samples their enrichment scores were higher which suggests that *MYC* or its downstream targets were up-regulated as a result of *BRCA1* mutagenesis. In PB2M

cells, ectopic *MYC* expression was detected and in comparison to PB2/E it is one log-fold increased. Nonetheless, PB2/E samples showed an increase in MYC targets V1 compared with P samples. This distinction dissipates when looking at MYC targets V2, in that case ectopic MYC expression distinguishes PB2/E samples from PB2M and their enrichment scores are closer to P samples, yet greater than the mean of the P group. PB3/E/M cells displayed higher levels of *MYC* than the other subclones and FNE1 cells altogether. In fact, ectopic expression of *MYC* did not increase total *MYC* expression in PB3M cells compared with PB3/E. These observations further limit the analysis of *MYC*-dependent CIN in PB2 and PB3 cells due to the underlying enrichment of MYC target genes.

Despite these observations being limited by only six samples, only two of which express MYC ectopically, it has to be noted that *MYC* gain and amplification have been found to be enriched in the HRD group of HGSOC defined by *BRCA1*/*2* mutations (Wang et al., 2017). Therefore, the observed enrichment of MYC target gene sets in PB2/E/M and PB3/E/M samples might reflect positive selection of cells that express high levels of MYC or its target genes. Alternatively, since gene expression follows DNA copy number on the mRNA level, MYC target genes might be overrepresented on chromosomes that are not affected by the monosomies in PB2/E/M and disomies in PB3/E/M cells (Upender et al., 2004). To investigate the role of MYC in PB2/E/M and PB3/E/M cells more carefully, one would need to confirm that MYC protein levels are increased in PB2/E and PB3/E cells first. For instance, following a confirmation of mRNA expression levels by immunoblotting, RNAi-mediated suppression of MYC to levels comparable with P or FNE1 cells could lend insight to MYC's role in CIN in these cells. Assessment of aneuploidy and CIN could be performed in the same manners as described in this thesis.

7.7: The utility of isogenic, mutant FNE1 subclones and outlook

Using FNE1 cells as a baseline, I have illustrated their utility for (i) CRISPR/Cas9 gene-editing and (ii) the study of a cell biological mechanism pertinent to HGSOC. Unfortunately, their utility is limited by poor tumourigenic potential as shown and discussed in *Chapter 6: Probing tumourigenicity of mutant FNE1 subclones*.

Nonetheless, FNE1 TO Cas9 cells and derived P1 cells are valuable tools for the study of additional genetic perturbations in a p53-proficient and -deficient background, respectively. In light of the consistent developments and updates of the CRISPR/Cas9 technology and new tools becoming available either as shared resources or commercially, laborious work relying on the generation and production of

lentiviral constructs and lengthy cell expansions might be overcome. One limiting factor in the work with FNE1 cells was poor efficiency of transient transfection of CRISPR/Cas9 vectors using lipid-based reagents, however, smaller non-plasmid gRNAs could potentially be transfected into FNE1 TO Cas9 cells with better efficiency. The combination of such an approach with a fluorescently detectable conjugate could efficiently be used for FACS-based enrichment of engineered cells. So far, only *TP53*^{mut} and *BRCA1*^{mut} double-mutant FNE1 cells were generated, however, *RB1* is also frequently lost in the HRD group (Wang et al., 2017). Therefore, mutagenizing *RB1* in P, PM, PB or PBM cells to better understand its role in the HRD group of HGSOC is an obvious next step, especially since isogenic *TP53*^{mut}*/RB1*^{mut}, *TP53*^{mut}*/BRCA1*^{mut}*/RB1*^{mut}, *TP53*^{mut}*/RB1*^{mut}*/MYC*^{OE} or *TP53*^{mut}*/BRCA1*^{mut}*/RB1*^{mut}*/MYC*^{OE} fallopian tube-derived models are lacking. Of course, the current subclones are built on the knockout of *BRCA1* although HRD can also result from BRCA2-loss. While perturbations in both genes result in HRD, their functions are distinct and dissecting their difference in an isogenic setting of HGSOC could provide important understanding of cell biological processes such as DNA replication and mitosis but also yield insight for PARPi treatments which are becoming routine clinically (Chen et al., 2018). Indeed, isogenic models of BRCA1/2-deficient mouse breast cancer cell lines have revealed differences in response to immune checkpoint blockade illustrating that their distinct function impacts treatment responses (Samstein et al., 2020). Strikingly, isogenic models for the other group of HGSOC defined by Wang et al. (2017), based on foldback inversions, are currently lacking. Since the truncal *TP53* mutation is ubiquitous, mutagenesis of *PTEN* and/or overexpression of *CCNE1* in P cells would elegantly complement the HRD group subclones by representing the FBI group.

A thus far unexplored application of the sequentially mutagenized FNE1 subclones and the RNA sequencing dataset is the discovery of previously unappreciated drug targets. Based on the RNA sequencing data it is possible to identify genes which are differentially expressed in mutant cells in contrast to FNE1 cells. This way genes for which known inhibitors exist can be identified and probed directly in combination with standard chemotherapeutics used for the treatment of HGSOC or by themselves. The direct comparison of these combinations between mutant subclones of choice and FNE1 cells would allow for the exclusion of combinations that are potentially toxic for wildtype cells. Indeed, *TP53* is one of the most frequently mutated genes in cancer thus combinations identified in FNE1 cells and mutant subclones have wide-reaching potential. In addition to combinations of one targeted gene and standard of care chemotherapy, this approach could reasonably be used to identify multiple target

genes whose simultaneous targeting could be exploited either alone or again in combination.

Chapter 8: References

Adli, M. (2018). The CRISPR tool kit for genome editing and beyond. Nat Commun 9, 1911.

Ahmed, A.A., Etemadmoghadam, D., Temple, J., Lynch, A.G., Riad, M., Sharma, R., Stewart, C., Fereday, S., Caldas, C., Defazio, A., et al. (2010). Driver mutations in TP53 are ubiquitous in high grade serous carcinoma of the ovary. J Pathol 221, 49-56.

Alexandrov, L.B., Kim, J., Haradhvala, N.J., Huang, M.N., Tian Ng, A.W., Wu, Y., Boot, A., Covington, K.R., Gordenin, D.A., Bergstrom, E.N., et al. (2020). The repertoire of mutational signatures in human cancer. Nature 578, 94-101.

Alexandrov, L.B., Nik-Zainal, S., Wedge, D.C., Aparicio, S.A., Behjati, S., Biankin, A.V., Bignell, G.R., Bolli, N., Borg, A., Borresen-Dale, A.L., et al. (2013). Signatures of mutational processes in human cancer. Nature 500, 415-421.

Auslander, N., Heselmeyer-Haddad, K., Patkar, S., Hirsch, D., Camps, J., Brown, M., Bronder, D., Chen, W.-D., Lokanga, R., Wangsa, D., et al. (2019). Cancer-type specific aneuploidies hard-wire chromosome-wide gene expression patterns of their tissue of origin. bioRxiv.

Auslander, N., Wolf, Y.I., and Koonin, E.V. (2020). Interplay between DNA damage repair and apoptosis shapes cancer evolution through aneuploidy and microsatellite instability. Nat Commun 11, 1234.

Baker, S.J., Markowitz, S., Fearon, E.R., Willson, J.K., and Vogelstein, B. (1990). Suppression of human colorectal carcinoma cell growth by wild-type p53. Science 249, 912-915.

Bakhoum, S.F., and Cantley, L.C. (2018). The Multifaceted Role of Chromosomal Instability in Cancer and Its Microenvironment. Cell 174, 1347-1360.

Bakhoum, S.F., Ngo, B., Laughney, A.M., Cavallo, J.A., Murphy, C.J., Ly, P., Shah, P., Sriram, R.K., Watkins, T.B.K., Taunk, N.K., et al. (2018). Chromosomal instability drives metastasis through a cytosolic DNA response. Nature 553, 467-472.

Bakker, B., Taudt, A., Belderbos, M.E., Porubsky, D., Spierings, D.C., de Jong, T.V., Halsema, N., Kazemier, H.G., Hoekstra-Wakker, K., Bradley, A., et al. (2016). Single-cell sequencing reveals karyotype heterogeneity in murine and human malignancies. Genome Biol 17, 115.

Baluapuri, A., Wolf, E., and Eilers, M. (2020). Target gene-independent functions of MYC oncoproteins. Nat Rev Mol Cell Biol 21, 255-267.

Barboza, J.A., Liu, G., Ju, Z., El-Naggar, A.K., and Lozano, G. (2006). p21 delays tumor onset by preservation of chromosomal stability. Proc Natl Acad Sci U S A 103, 19842-19847.

Barnes, B.M., Nelson, L., Tighe, A., Morgan, R.D., McGrail, J., and Taylor, S.S. (2020). Classification of ovarian cancer cell lines using transcriptional profiles defines the five major pathological subtypes. bioRxiv.

Barsotti, A.M., and Prives, C. (2009). Pro-proliferative FoxM1 is a target of p53-mediated repression. Oncogene 28, 4295-4305.

Bastians, H. (2015). Causes of Chromosomal Instability. Recent Results Cancer Res 200, 95-113.

Beach, R.R., Ricci-Tam, C., Brennan, C.M., Moomau, C.A., Hsu, P.H., Hua, B., Silberman, R.E., Springer, M., and Amon, A. (2017). Aneuploidy Causes Non-genetic Individuality. Cell 169, 229-242.e221.

Ben-David, U., and Amon, A. (2020). Context is everything: aneuploidy in cancer. Nat Rev Genet 21, 44-62.

Bennett, A., Bechi, B., Tighe, A., Thompson, S., Procter, D.J., and Taylor, S.S. (2015). Cenp-E inhibitor GSK923295: Novel synthetic route and use as a tool to generate aneuploidy. Oncotarget 6, 20921-20932.

Bhandari, V., Li, C.H., Bristow, R.G., Boutros, P.C., and Consortium, P. (2020). Divergent mutational processes distinguish hypoxic and normoxic tumours. Nat Commun 11, 737.

Bianco, J.N., Bergoglio, V., Lin, Y.L., Pillaire, M.J., Schmitz, A.L., Gilhodes, J., Lusque, A., Mazieres, J., Lacroix-Triki, M., Roumeliotis, T.I., et al. (2019). Overexpression of Claspin and Timeless protects cancer cells from replication stress in a checkpoint-independent manner. Nat Commun 10, 910.

Bielski, C.M., Zehir, A., Penson, A.V., Donoghue, M.T.A., Chatila, W., Armenia, J., Chang, M.T., Schram, A.M., Jonsson, P., Bandlamudi, C., et al. (2018). Genome doubling shapes the evolution and prognosis of advanced cancers. Nat Genet 50, 1189-1195.

Blank, H.M., Sheltzer, J.M., Meehl, C.M., and Amon, A. (2015). Mitotic entry in the presence of DNA damage is a widespread property of aneuploidy in yeast. Mol Biol Cell 26, 1440-1451.

Bolton, H., Graham, S.J.L., Van der Aa, N., Kumar, P., Theunis, K., Fernandez Gallardo, E., Voet, T., and Zernicka-Goetz, M. (2016). Mouse model of chromosome mosaicism reveals lineage-specific depletion of aneuploid cells and normal developmental potential. Nat Commun 7, 11165.

Boutelle, A.M., and Attardi, L.D. (2021). p53 and Tumor Suppression: It Takes a Network. Trends Cell Biol.

Boveri, T. (1914). Zur Frage der Entstehung maligner Tumoren (Jena: G. Fischer).

Bowtell, D.D., Bohm, S., Ahmed, A.A., Aspuria, P.J., Bast, R.C., Jr., Beral, V., Berek, J.S., Birrer, M.J., Blagden, S., Bookman, M.A., et al. (2015). Rethinking ovarian cancer II: reducing mortality from high-grade serous ovarian cancer. Nat Rev Cancer 15, 668-679.

Boxer, L.M., and Dang, C.V. (2001). Translocations involving c-myc and c-myc function. Oncogene 20, 5595-5610.

Breast Cancer Association, C., Dorling, L., Carvalho, S., Allen, J., Gonzalez-Neira, A., Luccarini, C., Wahlstrom, C., Pooley, K.A., Parsons, M.T., Fortuno, C., et al.

(2021). Breast Cancer Risk Genes - Association Analysis in More than 113,000 Women. N Engl J Med 384, 428-439.

Bryant, H.E., Schultz, N., Thomas, H.D., Parker, K.M., Flower, D., Lopez, E., Kyle, S., Meuth, M., Curtin, N.J., and Helleday, T. (2005). Specific killing of BRCA2-deficient tumours with inhibitors of poly(ADP-ribose) polymerase. Nature 434, 913-917.

Bunz, F., Fauth, C., Speicher, M.R., Dutriaux, A., Sedivy, J.M., Kinzler, K.W., Vogelstein, B., and Lengauer, C. (2002). Targeted inactivation of p53 in human cells does not result in aneuploidy. Cancer Res 62, 1129-1133.

Burrell, R.A., McClelland, S.E., Endesfelder, D., Groth, P., Weller, M.C., Shaikh, N., Domingo, E., Kanu, N., Dewhurst, S.M., Gronroos, E., et al. (2013). Replication stress links structural and numerical cancer chromosomal instability. Nature 494, 492-496.

Callen, E., Zong, D., Wu, W., Wong, N., Stanlie, A., Ishikawa, M., Pavani, R., Dumitrache, L.C., Byrum, A.K., Mendez-Dorantes, C., et al. (2020). 53BP1 Enforces Distinct Pre- and Post-resection Blocks on Homologous Recombination. Mol Cell 77, 26-38 e27.

Campeau, E., Ruhl, V.E., Rodier, F., Smith, C.L., Rahmberg, B.L., Fuss, J.O., Campisi, J., Yaswen, P., Cooper, P.K., and Kaufman, P.D. (2009). A versatile viral system for expression and depletion of proteins in mammalian cells. PLoS One 4, e6529.

Carter, S.L., Eklund, A.C., Kohane, I.S., Harris, L.N., and Szallasi, Z. (2006). A signature of chromosomal instability inferred from gene expression profiles predicts clinical outcome in multiple human cancers. Nat Genet 38, 1043-1048.

Cerami, E., Gao, J., Dogrusoz, U., Gross, B.E., Sumer, S.O., Aksoy, B.A., Jacobsen, A., Byrne, C.J., Heuer, M.L., Larsson, E., et al. (2012). The cBio cancer genomics portal: an open platform for exploring multidimensional cancer genomics data. Cancer Discov 2, 401-404.

Chen, C.-C., Feng, W., Lim, P.X., Kass, E.M., and Jasin, M. (2018). Homology-Directed Repair and the Role of BRCA1, BRCA2, and Related Proteins in Genome Integrity and Cancer. Annual Review of Cancer Biology 2, 313-336.

Ciriello, G., Miller, M.L., Aksoy, B.A., Senbabaoglu, Y., Schultz, N., and Sander, C. (2013). Emerging landscape of oncogenic signatures across human cancers. Nat Genet 45, 1127-1133.

Cong, L., Ran, F.A., Cox, D., Lin, S., Barretto, R., Habib, N., Hsu, P.D., Wu, X., Jiang, W., Marraffini, L.A., et al. (2013). Multiplex genome engineering using CRISPR/Cas systems. Science 339, 819-823.

CRUK (2020a). Cancer mortality statistics. https://www.cancerresearchuk.org/health-professional/cancer-statistics/mortality#heading-Four Accessed 19/03/2021.

CRUK (2020b). Ovarian cancer statistics. http://www.cancerresearchuk.org/health-professional/cancer-statistics/statistics-by-cancer-type/ovarian-cancer Accessed 19/03/2021.

Cybulska, P., Stewart, J.M., Sayad, A., Virtanen, C., Shaw, P.A., Clarke, B., Stickle, N., Bernardini, M.Q., and Neel, B.G. (2018). A Genomically Characterized Collection of High-Grade Serous Ovarian Cancer Xenografts for Preclinical Testing. Am J Pathol 188, 1120-1131.

Dang, C.V. (2012). MYC on the path to cancer. Cell 149, 22-35.

Dang, C.V. (2013). MYC, metabolism, cell growth, and tumorigenesis. Cold Spring Harb Perspect Med 3.

Dankort, D., Filenova, E., Collado, M., Serrano, M., Jones, K., and McMahon, M. (2007). A new mouse model to explore the initiation, progression, and therapy of BRAFV600E-induced lung tumors. Genes Dev 21, 379-384.

Davoli, T., Uno, H., Wooten, E.C., and Elledge, S.J. (2017). Tumor aneuploidy correlates with markers of immune evasion and with reduced response to immunotherapy. Science 355.

de Almeida, B.P., Vieira, A.F., Paredes, J., Bettencourt-Dias, M., and Barbosa-Morais, N.L. (2019). Pan-cancer association of a centrosome amplification gene expression signature with genomic alterations and clinical outcome. PLoS Comput Biol 15, e1006832.

Dobin, A., Davis, C.A., Schlesinger, F., Drenkow, J., Zaleski, C., Jha, S., Batut, P., Chaisson, M., and Gingeras, T.R. (2013). STAR: ultrafast universal RNA-seq aligner. Bioinformatics 29, 15-21.

Domcke, S., Sinha, R., Levine, D.A., Sander, C., and Schultz, N. (2013). Evaluating cell lines as tumour models by comparison of genomic profiles. Nat Commun 4, 2126.

Donehower, L.A., Harvey, M., Slagle, B.L., McArthur, M.J., Montgomery, C.A., Jr., Butel, J.S., and Bradley, A. (1992). Mice deficient for p53 are developmentally normal but susceptible to spontaneous tumours. Nature 356, 215-221.

Doran, A.H.G. (1884). Clinical and pathological observations on tumours of the ovary, fallopian tube, and braod ligament (London, UK: Smith, Elder, & Co.).

Drost, J., van Jaarsveld, R.H., Ponsioen, B., Zimberlin, C., van Boxtel, R., Buijs, A., Sachs, N., Overmeer, R.M., Offerhaus, G.J., Begthel, H., et al. (2015). Sequential cancer mutations in cultured human intestinal stem cells. Nature 521, 43-47.

Ducie, J., Dao, F., Considine, M., Olvera, N., Shaw, P.A., Kurman, R.J., Shih, I.M., Soslow, R.A., Cope, L., and Levine, D.A. (2017). Molecular analysis of high-grade serous ovarian carcinoma with and without associated serous tubal intra-epithelial carcinoma. Nat Commun 8, 990.

Eckert, M.A., Pan, S., Hernandez, K.M., Loth, R.M., Andrade, J., Volchenboum, S.L., Faber, P., Montag, A., Lastra, R., Peter, M.E., et al. (2016). Genomics of Ovarian Cancer Progression Reveals Diverse Metastatic Trajectories Including Intraepithelial Metastasis to the Fallopian Tube. Cancer Discov 6, 1342-1351.

Ertych, N., Stolz, A., Stenzinger, A., Weichert, W., Kaulfuss, S., Burfeind, P., Aigner, A., Wordeman, L., and Bastians, H. (2014). Increased microtubule assembly rates influence chromosomal instability in colorectal cancer cells. Nat Cell Biol 16, 779-791.

Ertych, N., Stolz, A., Valerius, O., Braus, G.H., and Bastians, H. (2016). CHK2-BRCA1 tumor-suppressor axis restrains oncogenic Aurora-A kinase to ensure proper mitotic microtubule assembly. Proc Natl Acad Sci U S A 113, 1817-1822.

Farmer, H., McCabe, N., Lord, C.J., Tutt, A.N., Johnson, D.A., Richardson, T.B., Santarosa, M., Dillon, K.J., Hickson, I., Knights, C., et al. (2005). Targeting the DNA repair defect in BRCA mutant cells as a therapeutic strategy. Nature 434, 917-921.

Flesken-Nikitin, A., Choi, K.C., Eng, J.P., Shmidt, E.N., and Nikitin, A.Y. (2003). Induction of carcinogenesis by concurrent inactivation of p53 and Rb1 in the mouse ovarian surface epithelium. Cancer Res 63, 3459-3463.

Foijer, F., Xie, S.Z., Simon, J.E., Bakker, P.L., Conte, N., Davis, S.H., Kregel, E., Jonkers, J., Bradley, A., and Sorger, P.K. (2014). Chromosome instability induced by Mps1 and p53 mutation generates aggressive lymphomas exhibiting aneuploidy-induced stress. Proc Natl Acad Sci U S A 111, 13427-13432.

Futreal, P.A., Liu, Q., Shattuck-Eidens, D., Cochran, C., Harshman, K., Tavtigian, S., Bennett, L.M., Haugen-Strano, A., Swensen, J., Miki, Y., et al. (1994). BRCA1 mutations in primary breast and ovarian carcinomas. Science 266, 120-122.

Galipeau, P.C., Cowan, D.S., Sanchez, C.A., Barrett, M.T., Emond, M.J., Levine, D.S., Rabinovitch, P.S., and Reid, B.J. (1996). 17p (p53) allelic losses, 4N (G2/tetraploid) populations, and progression to aneuploidy in Barrett's esophagus. Proc Natl Acad Sci U S A 93, 7081-7084.

Ganem, N.J., Godinho, S.A., and Pellman, D. (2009). A mechanism linking extra centrosomes to chromosomal instability. Nature 460, 278-282.

Gao, J., Aksoy, B.A., Dogrusoz, U., Dresdner, G., Gross, B., Sumer, S.O., Sun, Y., Jacobsen, A., Sinha, R., Larsson, E., et al. (2013). Integrative analysis of complex cancer genomics and clinical profiles using the cBioPortal. Sci Signal 6, pl1.

Ghezelayagh, T.S., Pennington, K.P., Norquist, B.M., Khasnavis, N., Radke, M.R., Kilgore, M.R., Garcia, R.L., Lee, M., Katz, R., Leslie, K.K., et al. (2020). Characterizing TP53 mutations in ovarian carcinomas with and without concurrent BRCA1 or BRCA2 mutations. Gynecol Oncol.

Giuliano, C.J., Lin, A., Girish, V., and Sheltzer, J.M. (2019). Generating Single Cell-Derived Knockout Clones in Mammalian Cells with CRISPR/Cas9. Curr Protoc Mol Biol 128, e100.

Hanahan, D., and Weinberg, R.A. (2000). The hallmarks of cancer. Cell 100, 57-70.

Hanahan, D., and Weinberg, R.A. (2011). Hallmarks of cancer: the next generation. Cell 144, 646-674.

Hanks, S., Coleman, K., Reid, S., Plaja, A., Firth, H., Fitzpatrick, D., Kidd, A., Méhes, K., Nash, R., Robin, N., et al. (2004). Constitutional aneuploidy and cancer predisposition caused by biallelic mutations in BUB1B. Nat Genet 36, 1159-1161.

Hansemann, D. (1890). Ueber asymmetrische Zelltheilung in Epithelkrebsen und deren biologische Bedeutung. Archiv für pathologische Anatomie und Physiologie und für klinische Medicin 119, 299-326.

Hanzelmann, S., Castelo, R., and Guinney, J. (2013). GSVA: gene set variation analysis for microarray and RNA-seq data. BMC Bioinformatics 14, 7.

Harding, S.M., Benci, J.L., Irianto, J., Discher, D.E., Minn, A.J., and Greenberg, R.A. (2017). Mitotic progression following DNA damage enables pattern recognition within micronuclei. Nature 548, 466-470.

Harrow, J., Frankish, A., Gonzalez, J.M., Tapanari, E., Diekhans, M., Kokocinski, F., Aken, B.L., Barrell, D., Zadissa, A., Searle, S., et al. (2012). GENCODE: the reference human genome annotation for The ENCODE Project. Genome Res 22, 1760-1774.

Heijink, A.M., Talens, F., Jae, L.T., van Gijn, S.E., Fehrmann, R.S.N., Brummelkamp, T.R., and van Vugt, M. (2019). BRCA2 deficiency instigates cGAS-mediated inflammatory signaling and confers sensitivity to tumor necrosis factor-alpha-mediated cytotoxicity. Nat Commun 10, 100.

Hernandez, L., Kim, M.K., Lyle, L.T., Bunch, K.P., House, C.D., Ning, F., Noonan, A.M., and Annunziata, C.M. (2016). Characterization of ovarian cancer cell lines as in vivo models for preclinical studies. Gynecol Oncol 142, 332-340.

Heselmeyer-Haddad, K., Berroa Garcia, L.Y., Bradley, A., Ortiz-Melendez, C., Lee, W.J., Christensen, R., Prindiville, S.A., Calzone, K.A., Soballe, P.W., Hu, Y., et al. (2012). Single-cell genetic analysis of ductal carcinoma in situ and invasive breast cancer reveals enormous tumor heterogeneity yet conserved genomic imbalances and gain of MYC during progression. Am J Pathol 181, 1807-1822.

Heselmeyer-Haddad, K., Janz, V., Castle, P.E., Chaudhri, N., White, N., Wilber, K., Morrison, L.E., Auer, G., Burroughs, F.H., Sherman, M.E., et al. (2003). Detection of genomic amplification of the human telomerase gene (TERC) in cytologic specimens as a genetic test for the diagnosis of cervical dysplasia. Am J Pathol 163, 1405-1416.

Heselmeyer, K., Schrock, E., du Manoir, S., Blegen, H., Shah, K., Steinbeck, R., Auer, G., and Ried, T. (1996). Gain of chromosome 3q defines the transition from severe dysplasia to invasive carcinoma of the uterine cervix. Proc Natl Acad Sci U S A 93, 479-484.

Hoevenaar, W.H.M., Janssen, A., Quirindongo, A.I., Ma, H., Klaasen, S.J., Teixeira, A., van Gerwen, B., Lansu, N., Morsink, F.H.M., Offerhaus, G.J.A., et al. (2020). Degree and site of chromosomal instability define its oncogenic potential. Nat Commun 11, 1501.

Hoffmann, K., Berger, H., Kulbe, H., Thillainadarasan, S., Mollenkopf, H.J., Zemojtel, T., Taube, E., Darb-Esfahani, S., Mangler, M., Sehouli, J., et al. (2020). Stable expansion of high-grade serous ovarian cancer organoids requires a low-Wnt environment. EMBO J 39, e104013.

Holland, A.J., and Cleveland, D.W. (2012). Losing balance: the origin and impact of aneuploidy in cancer. EMBO Reports 13, 501-514.

Holland, A.J., Fachinetti, D., Zhu, Q., Bauer, M., Verma, I.M., Nigg, E.A., and Cleveland, D.W. (2012). The autoregulated instability of Polo-like kinase 4 limits centrosome duplication to once per cell cycle. Genes Dev 26, 2684-2689.

Holstege, H., Joosse, S.A., van Oostrom, C.T., Nederlof, P.M., de Vries, A., and Jonkers, J. (2009). High incidence of protein-truncating TP53 mutations in BRCA1-related breast cancer. Cancer Res 69, 3625-3633.

House, C.D., Hernandez, L., and Annunziata, C.M. (2014). Recent technological advances in using mouse models to study ovarian cancer. Front Oncol 4, 26.

Hua, G., Lv, X., He, C., Remmenga, S.W., Rodabough, K.J., Dong, J., Yang, L., Lele, S.M., Yang, P., Zhou, J., et al. (2016). YAP induces high-grade serous carcinoma in fallopian tube secretory epithelial cells. Oncogene 35, 2247-2265.

Ince, T.A., Sousa, A.D., Jones, M.A., Harrell, J.C., Agoston, E.S., Krohn, M., Selfors, L.M., Liu, W., Chen, K., Yong, M., et al. (2015). Characterization of twenty-five ovarian tumour cell lines that phenocopy primary tumours. Nat Commun 6, 7419.

Ischenko, I., D'Amico, S., Rao, M., Li, J., Hayman, M.J., Powers, S., Petrenko, O., and Reich, N.C. (2021). KRAS drives immune evasion in a genetic model of pancreatic cancer. Nat Commun 12, 1482.

Iyer, S., Zhang, S., Yucel, S., Horn, H., Smith, S.G., Reinhardt, F., Hoefsmit, E., Assatova, B., Casado, J., Meinsohn, M.C., et al. (2021). Genetically Defined Syngeneic Mouse Models of Ovarian Cancer as Tools for the Discovery of Combination Immunotherapy. Cancer Discov 11, 384-407.

Jackson-Cook, C. (2011). Constitutional and acquired autosomal aneuploidy. Clin Lab Med 31, 481-511, vii.

Jamal-Hanjani, M., Wilson, G.A., McGranahan, N., Birkbak, N.J., Watkins, T.B.K., Veeriah, S., Shafi, S., Johnson, D.H., Mitter, R., Rosenthal, R., et al. (2017). Tracking the Evolution of Non-Small-Cell Lung Cancer. N Engl J Med 376, 2109-2121.

Janssen, A., van der Burg, M., Szuhai, K., Kops, G.J., and Medema, R.H. (2011). Chromosome segregation errors as a cause of DNA damage and structural chromosome aberrations. Science 333, 1895-1898.

Jazaeri, A.A., Bryant, J.L., Park, H., Li, H., Dahiya, N., Stoler, M.H., Ferriss, J.S., and Dutta, A. (2011). Molecular requirements for transformation of fallopian tube epithelial cells into serous carcinoma. Neoplasia 13, 899-911.

Johnson, W.E., Li, C., and Rabinovic, A. (2007). Adjusting batch effects in microarray expression data using empirical Bayes methods. Biostatistics 8, 118-127.

Jones, L., Wei, G., Sevcikova, S., Phan, V., Jain, S., Shieh, A., Wong, J.C., Li, M., Dubansky, J., Maunakea, M.L., et al. (2010). Gain of MYC underlies recurrent trisomy of the MYC chromosome in acute promyelocytic leukemia. J Exp Med 207, 2581-2594.

Karst, A.M., and Drapkin, R. (2012). Primary culture and immortalization of human fallopian tube secretory epithelial cells. Nat Protoc 7, 1755-1764.

Karst, A.M., Jones, P.M., Vena, N., Ligon, A.H., Liu, J.F., Hirsch, M.S., Etemadmoghadam, D., Bowtell, D.D., and Drapkin, R. (2014). Cyclin E1 deregulation occurs early in secretory cell transformation to promote formation of fallopian tube-derived high-grade serous ovarian cancers. Cancer Res 74, 1141-1152.

Karst, A.M., Levanon, K., and Drapkin, R. (2011). Modeling high-grade serous ovarian carcinogenesis from the fallopian tube. Proc Natl Acad Sci U S A 108, 7547-7552.

Kersten, K., de Visser, K.E., van Miltenburg, M.H., and Jonkers, J. (2017). Genetically engineered mouse models in oncology research and cancer medicine. EMBO Mol Med 9, 137-153.

Kessler, M., Hoffmann, K., Brinkmann, V., Thieck, O., Jackisch, S., Toelle, B., Berger, H., Mollenkopf, H.J., Mangler, M., Sehouli, J., et al. (2015). The Notch and Wnt pathways regulate stemness and differentiation in human fallopian tube organoids. Nat Commun 6, 8989.

Killcoyne, S., Gregson, E., Wedge, D.C., Woodcock, D.J., Eldridge, M.D., de la Rue, R., Miremadi, A., Abbas, S., Blasko, A., Kosmidou, C., et al. (2020). Genomic copy number predicts esophageal cancer years before transformation. Nat Med 26, 1726-1732.

Klusmann, I., Rodewald, S., Muller, L., Friedrich, M., Wienken, M., Li, Y., Schulz-Heddergott, R., and Dobbelstein, M. (2016). p53 Activity Results in DNA Replication Fork Processivity. Cell Rep 17, 1845-1857.

Knouse, K.A., Wu, J., Whittaker, C.A., and Amon, A. (2014). Single cell sequencing reveals low levels of aneuploidy across mammalian tissues. Proc Natl Acad Sci U S A 111, 13409-13414.

Knutsen, T., Padilla-Nash, H.M., Wangsa, D., Barenboim-Stapleton, L., Camps, J., McNeil, N., Difilippantonio, M.J., and Ried, T. (2010). Definitive molecular cytogenetic characterization of 15 colorectal cancer cell lines. Genes Chromosomes Cancer 49, 204-223.

Kok, Y.P., Guerrero Llobet, S., Schoonen, P.M., Everts, M., Bhattacharya, A., Fehrmann, R.S.N., van den Tempel, N., and van Vugt, M. (2020). Overexpression of Cyclin E1 or Cdc25A leads to replication stress, mitotic aberrancies, and increased sensitivity to replication checkpoint inhibitors. Oncogenesis 9, 88.

Kopper, O., de Witte, C.J., Lohmussaar, K., Valle-Inclan, J.E., Hami, N., Kester, L., Balgobind, A.V., Korving, J., Proost, N., Begthel, H., et al. (2019). An organoid platform for ovarian cancer captures intra- and interpatient heterogeneity. Nat Med 25, 838-849.

Kosicki, M., Tomberg, K., and Bradley, A. (2018). Repair of double-strand breaks induced by CRISPR-Cas9 leads to large deletions and complex rearrangements. Nat Biotechnol 36, 765-771.

Kuhn, E., Kurman, R.J., Vang, R., Sehdev, A.S., Han, G., Soslow, R., Wang, T.L., and Shih Ie, M. (2012). TP53 mutations in serous tubal intraepithelial carcinoma and concurrent pelvic high-grade serous carcinoma--evidence supporting the clonal relationship of the two lesions. J Pathol 226, 421-426.

Kurman, R.J., and Shih Ie, M. (2016). The Dualistic Model of Ovarian Carcinogenesis: Revisited, Revised, and Expanded. Am J Pathol 186, 733-747.

Labidi-Galy, S.I., Papp, E., Hallberg, D., Niknafs, N., Adleff, V., Noe, M., Bhattacharya, R., Novak, M., Jones, S., Phallen, J., et al. (2017). High grade serous ovarian carcinomas originate in the fallopian tube. Nat Commun 8, 1093.

Lambrus, B.G., Daggubati, V., Uetake, Y., Scott, P.M., Clutario, K.M., Sluder, G., and Holland, A.J. (2016). A USP28-53BP1-p53-p21 signaling axis arrests growth after centrosome loss or prolonged mitosis. J Cell Biol 214, 143-153.

Lane, D., and Levine, A. (2010). p53 Research: the past thirty years and the next thirty years. Cold Spring Harb Perspect Biol 2, a000893.

Lane, D.P. (1992). Cancer. p53, guardian of the genome. Nature 358, 15-16.

Laoukili, J., Kooistra, M.R., Bras, A., Kauw, J., Kerkhoven, R.M., Morrison, A., Clevers, H., and Medema, R.H. (2005). FoxM1 is required for execution of the mitotic programme and chromosome stability. Nat Cell Biol 7, 126-136.

Lara-Gonzalez, P., Westhorpe, F.G., and Taylor, S.S. (2012). The spindle assembly checkpoint. Curr Biol 22, R966-980.

Law, C.W., Chen, Y., Shi, W., and Smyth, G.K. (2014). voom: Precision weights unlock linear model analysis tools for RNA-seq read counts. Genome Biol 15, R29.

Lee, A.J., Endesfelder, D., Rowan, A.J., Walther, A., Birkbak, N.J., Futreal, P.A., Downward, J., Szallasi, Z., Tomlinson, I.P., Howell, M., et al. (2011). Chromosomal instability confers intrinsic multidrug resistance. Cancer Res 71, 1858-1870.

Lengauer, C., Kinzler, K.W., and Vogelstein, B. (1997). Genetic instability in colorectal cancers. Nature 386, 623-627.

Li, B., and Dewey, C.N. (2011). RSEM: accurate transcript quantification from RNA-Seq data with or without a reference genome. BMC Bioinformatics 12, 323.

Liberzon, A., Subramanian, A., Pinchback, R., Thorvaldsdóttir, H., Tamayo, P., and Mesirov, J.P. (2011). Molecular signatures database (MSigDB) 3.0. Bioinformatics 27, 1739-1740.

Limas, J.C., and Cook, J.G. (2019). Preparation for DNA replication: the key to a successful S phase. FEBS Lett 593, 2853-2867.

Lin, C.Y., Loven, J., Rahl, P.B., Paranal, R.M., Burge, C.B., Bradner, J.E., Lee, T.I., and Young, R.A. (2012). Transcriptional amplification in tumor cells with elevated c-Myc. Cell 151, 56-67.

Littler, S., Sloss, O., Geary, B., Pierce, A., Whetton, A.D., and Taylor, S.S. (2019). Oncogenic MYC amplifies mitotic perturbations. Open Biol 9, 190136.

Liu, J.F., Palakurthi, S., Zeng, Q., Zhou, S., Ivanova, E., Huang, W., Zervantonakis, I.K., Selfors, L.M., Shen, Y., Pritchard, C.C., et al. (2017). Establishment of Patient-Derived Tumor Xenograft Models of Epithelial Ovarian Cancer for Preclinical Evaluation of Novel Therapeutics. Clin Cancer Res 23, 1263-1273.

Liu, S., Kwon, M., Mannino, M., Yang, N., Renda, F., Khodjakov, A., and Pellman, D. (2018). Nuclear envelope assembly defects link mitotic errors to chromothripsis. Nature 561, 551-555.

Lohmussaar, K., Kopper, O., Korving, J., Begthel, H., Vreuls, C.P.H., van Es, J.H., and Clevers, H. (2020). Assessing the origin of high-grade serous ovarian cancer using CRISPR-modification of mouse organoids. Nat Commun 11, 2660.

Lopez, S., Lim, E.L., Horswell, S., Haase, K., Huebner, A., Dietzen, M., Mourikis, T.P., Watkins, T.B.K., Rowan, A., Dewhurst, S.M., et al. (2020). Interplay between whole-genome doubling and the accumulation of deleterious alterations in cancer evolution. Nat Genet 52, 283-293.

Lourenco, C., Kalkat, M., Houlahan, K.E., De Melo, J., Longo, J., Done, S.J., Boutros, P.C., and Penn, L.Z. (2019). Modelling the MYC-driven normal-to-tumour switch in breast cancer. Dis Model Mech 12.

Ly, P., Brunner, S.F., Shoshani, O., Kim, D.H., Lan, W., Pyntikova, T., Flanagan, A.M., Behjati, S., Page, D.C., Campbell, P.J., et al. (2019). Chromosome segregation errors generate a diverse spectrum of simple and complex genomic rearrangements. Nat Genet 51, 705-715.

Ly, P., Teitz, L.S., Kim, D.H., Shoshani, O., Skaletsky, H., Fachinetti, D., Page, D.C., and Cleveland, D.W. (2017). Selective Y centromere inactivation triggers chromosome shattering in micronuclei and repair by non-homologous end joining. Nat Cell Biol 19, 68-75.

Macintyre, G., Goranova, T.E., De Silva, D., Ennis, D., Piskorz, A.M., Eldridge, M., Sie, D., Lewsley, L.A., Hanif, A., Wilson, C., et al. (2018). Copy number signatures and mutational processes in ovarian carcinoma. Nat Genet 50, 1262-1270.

Mackenzie, K.J., Carroll, P., Martin, C.A., Murina, O., Fluteau, A., Simpson, D.J., Olova, N., Sutcliffe, H., Rainger, J.K., Leitch, A., et al. (2017). cGAS surveillance of micronuclei links genome instability to innate immunity. Nature 548, 461-465.

Martin, M. (2011). Cutadapt removes adapter sequences from high-throughput sequencing reads. 2011 17, 3.

Merritt, M.A., Bentink, S., Schwede, M., Iwanicki, M.P., Quackenbush, J., Woo, T., Agoston, E.S., Reinhardt, F., Crum, C.P., Berkowitz, R.S., et al. (2013). Gene expression signature of normal cell-of-origin predicts ovarian tumor outcomes. PLoS One 8, e80314.

Michel, L.S., Liberal, V., Chatterjee, A., Kirchwegger, R., Pasche, B., Gerald, W., Dobles, M., Sorger, P.K., Murty, V.V., and Benezra, R. (2001). MAD2 haplo-insufficiency causes premature anaphase and chromosome instability in mammalian cells. Nature 409, 355-359.

Miki, Y., Swensen, J., Shattuck-Eidens, D., Futreal, P.A., Harshman, K., Tavtigian, S., Liu, Q., Cochran, C., Bennett, L.M., Ding, W., et al. (1994). A strong candidate for the breast and ovarian cancer susceptibility gene BRCA1. Science 266, 66-71.

Mirabelli, P., Coppola, L., and Salvatore, M. (2019). Cancer Cell Lines Are Useful Model Systems for Medical Research. Cancers (Basel) 11.

Moore, K., Colombo, N., Scambia, G., Kim, B.G., Oaknin, A., Friedlander, M., Lisyanskaya, A., Floquet, A., Leary, A., Sonke, G.S., et al. (2018). Maintenance Olaparib in Patients with Newly Diagnosed Advanced Ovarian Cancer. N Engl J Med 379, 2495-2505.

Morin, P.J., and Weeraratna, A.T. (2016). Genetically-defined ovarian cancer mouse models. J Pathol 238, 180-184.

Nakamura, K., Nakayama, K., Ishikawa, N., Ishikawa, M., Sultana, R., Kiyono, T., and Kyo, S. (2018). Reconstitution of high-grade serous ovarian carcinoma from primary fallopian tube secretory epithelial cells. Oncotarget 9, 12609-12619.

Nelson, L., Tighe, A., Golder, A., Littler, S., Bakker, B., Moralli, D., Murtuza Baker, S., Donaldson, I.J., Spierings, D.C.J., Wardenaar, R., et al. (2020). A living biobank of ovarian cancer ex vivo models reveals profound mitotic heterogeneity. Nat Commun 11, 822.

NHS (2019). What is Down's syndrome? https://www.nhs.uk/conditions/downs-syndrome/ Accessed 19/03/2021.

Nicholson, J.M., Macedo, J.C., Mattingly, A.J., Wangsa, D., Camps, J., Lima, V., Gomes, A.M., Doria, S., Ried, T., Logarinho, E., et al. (2015). Chromosome mis-segregation and cytokinesis failure in trisomic human cells. Elife 4.

Nie, Z., Guo, C., Das, S.K., Chow, C.C., Batchelor, E., Simons, S.S.J., and Levens, D. (2020). Dissecting transcriptional amplification by MYC. Elife 9.

Nie, Z., Hu, G., Wei, G., Cui, K., Yamane, A., Resch, W., Wang, R., Green, D.R., Tessarollo, L., Casellas, R., et al. (2012). c-Myc is a universal amplifier of expressed genes in lymphocytes and embryonic stem cells. Cell 151, 68-79.

Nigg, E.A., and Holland, A.J. (2018). Once and only once: mechanisms of centriole duplication and their deregulation in disease. Nat Rev Mol Cell Biol 19, 297-312.

Nik-Zainal, S., Alexandrov, L.B., Wedge, D.C., Van Loo, P., Greenman, C.D., Raine, K., Jones, D., Hinton, J., Marshall, J., Stebbings, L.A., et al. (2012). Mutational processes molding the genomes of 21 breast cancers. Cell 149, 979-993.

Ogino, S., Gulley, M.L., den Dunnen, J.T., Wilson, R.B., Association for Molecular Patholpogy, T., and Education, C. (2007). Standard mutation nomenclature in molecular diagnostics: practical and educational challenges. J Mol Diagn 9, 1-6.

Oromendia, A.B., Dodgson, S.E., and Amon, A. (2012). Aneuploidy causes proteotoxic stress in yeast. Genes Dev 26, 2696-2708.

Orsulic, S., Li, Y., Soslow, R.A., Vitale-Cross, L.A., Gutkind, J.S., and Varmus, H.E. (2002). Induction of ovarian cancer by defined multiple genetic changes in a mouse model system. Cancer Cell 1, 53-62.

Otto, T., and Sicinski, P. (2017). Cell cycle proteins as promising targets in cancer therapy. Nat Rev Cancer 17, 93-115.

Padilla-Nash, H.M., Barenboim-Stapleton, L., Difilippantonio, M.J., and Ried, T. (2006). Spectral karyotyping analysis of human and mouse chromosomes. Nat Protoc 1, 3129-3142.

Perera, D., Tilston, V., Hopwood, J.A., Barchi, M., Boot-Handford, R.P., and Taylor, S.S. (2007). Bub1 maintains centromeric cohesion by activation of the spindle checkpoint. Dev Cell 13, 566-579.

Perets, R., Wyant, G.A., Muto, K.W., Bijron, J.G., Poole, B.B., Chin, K.T., Chen, J.Y., Ohman, A.W., Stepule, C.D., Kwak, S., et al. (2013). Transformation of the fallopian tube secretory epithelium leads to high-grade serous ovarian cancer in Brca;Tp53;Pten models. Cancer Cell 24, 751-765.

Pfister, K., Pipka, J.L., Chiang, C., Liu, Y., Clark, R.A., Keller, R., Skoglund, P., Guertin, M.J., Hall, I.M., and Stukenberg, P.T. (2018). Identification of Drivers of Aneuploidy in Breast Tumors. Cell Rep 23, 2758-2769.

Priestley, P., Baber, J., Lolkema, M.P., Steeghs, N., de Bruijn, E., Shale, C., Duyvesteyn, K., Haidari, S., van Hoeck, A., Onstenk, W., et al. (2019). Pan-cancer whole-genome analyses of metastatic solid tumours. Nature 575, 210-216.

Przewrocka, J., Rowan, A., Rosenthal, R., Kanu, N., and Swanton, C. (2020). Unintended on-target chromosomal instability following CRISPR/Cas9 single gene targeting. Ann Oncol 31, 1270-1273.

Putkey, F.R., Cramer, T., Morphew, M.K., Silk, A.D., Johnson, R.S., McIntosh, J.R., and Cleveland, D.W. (2002). Unstable kinetochore-microtubule capture and chromosomal instability following deletion of CENP-E. Dev Cell 3, 351-365.

Rayner, E., Durin, M.A., Thomas, R., Moralli, D., O'Cathail, S.M., Tomlinson, I., Green, C.M., and Lewis, A. (2019). CRISPR-Cas9 Causes Chromosomal Instability and Rearrangements in Cancer Cell Lines, Detectable by Cytogenetic Methods. CRISPR J 2, 406-416.

Ried, T., Knutzen, R., Steinbeck, R., Blegen, H., Schrock, E., Heselmeyer, K., du Manoir, S., and Auer, G. (1996). Comparative genomic hybridization reveals a specific pattern of chromosomal gains and losses during the genesis of colorectal tumors. Genes Chromosomes Cancer 15, 234-245.

Robinson, J.T., Thorvaldsdottir, H., Winckler, W., Guttman, M., Lander, E.S., Getz, G., and Mesirov, J.P. (2011). Integrative genomics viewer. Nat Biotechnol 29, 24-26.

Rohrberg, J., Van de Mark, D., Amouzgar, M., Lee, J.V., Taileb, M., Corella, A., Kilinc, S., Williams, J., Jokisch, M.L., Camarda, R., et al. (2020). MYC Dysregulates Mitosis, Revealing Cancer Vulnerabilities. Cell Rep 30, 3368-3382 e3367.

Rutledge, S.D., Douglas, T.A., Nicholson, J.M., Vila-Casadesus, M., Kantzler, C.L., Wangsa, D., Barroso-Vilares, M., Kale, S.D., Logarinho, E., and Cimini, D. (2016). Selective advantage of trisomic human cells cultured in non-standard conditions. Sci Rep 6, 22828.

Sack, L.M., Davoli, T., Li, M.Z., Li, Y., Xu, Q., Naxerova, K., Wooten, E.C., Bernardi, R.J., Martin, T.D., Chen, T., et al. (2018). Profound Tissue Specificity in Proliferation Control Underlies Cancer Drivers and Aneuploidy Patterns. Cell 173, 499-514 e423.

Salehi, S., Kabeer, F., Ceglia, N., Andronescu, M., Williams, M., Campbell, K.R., Masud, T., Wang, B., Biele, J., Brimhall, J., et al. (2020). Single cell fitness landscapes induced by genetic and pharmacologic perturbations in cancer. bioRxiv, 2020.2005.2008.081349.

Salk, J.J., Loubet-Senear, K., Maritschnegg, E., Valentine, C.C., Williams, L.N., Higgins, J.E., Horvat, R., Vanderstichele, A., Nachmanson, D., Baker, K.T., et al. (2019). Ultra-Sensitive TP53 Sequencing for Cancer Detection Reveals Progressive

Clonal Selection in Normal Tissue over a Century of Human Lifespan. Cell Rep 28, 132-144 e133.

Salvador, S., Rempel, A., Soslow, R.A., Gilks, B., Huntsman, D., and Miller, D. (2008). Chromosomal instability in fallopian tube precursor lesions of serous carcinoma and frequent monoclonality of synchronous ovarian and fallopian tube mucosal serous carcinoma. Gynecol Oncol 110, 408-417.

Samstein, R.M., Krishna, C., Ma, X., Pei, X., Lee, K.-W., Makarov, V., Kuo, F., Chung, J., Srivastava, R.M., Purohit, T.A., et al. (2020). Mutations in BRCA1 and BRCA2 differentially affect the tumor microenvironment and response to checkpoint blockade immunotherapy. Nature Cancer 1, 1188-1203.

Sanjana, N.E., Shalem, O., and Zhang, F. (2014). Improved vectors and genome-wide libraries for CRISPR screening. Nat Methods 11, 783-784.

Sansregret, L., Vanhaesebroeck, B., and Swanton, C. (2018). Determinants and clinical implications of chromosomal instability in cancer. Nat Rev Clin Oncol 15, 139-150.

Santaguida, S., and Amon, A. (2015). Short- and long-term effects of chromosome mis-segregation and aneuploidy. Nat Rev Mol Cell Biol 16, 473-485.

Santaguida, S., Richardson, A., Iyer, D.R., M'Saad, O., Zasadil, L., Knouse, K.A., Wong, Y.L., Rhind, N., Desai, A., and Amon, A. (2017). Chromosome Mis-segregation Generates Cell-Cycle-Arrested Cells with Complex Karyotypes that Are Eliminated by the Immune System. Dev Cell 41, 638-651.e635.

Santaguida, S., Vasile, E., White, E., and Amon, A. (2015). Aneuploidy-induced cellular stresses limit autophagic degradation. Genes Dev 29, 2010-2021.

Scarlett, U.K., Rutkowski, M.R., Rauwerdink, A.M., Fields, J., Escovar-Fadul, X., Baird, J., Cubillos-Ruiz, J.R., Jacobs, A.C., Gonzalez, J.L., Weaver, J., et al. (2012). Ovarian cancer progression is controlled by phenotypic changes in dendritic cells. J Exp Med 209, 495-506.

Schrock, E., du Manoir, S., Veldman, T., Schoell, B., Wienberg, J., Ferguson-Smith, M.A., Ning, Y., Ledbetter, D.H., Bar-Am, I., Soenksen, D., et al. (1996). Multicolor spectral karyotyping of human chromosomes. Science 273, 494-497.

SEER (2020). Cancer stat facts: Ovarian cancer. https://seer.cancer.gov/statfacts/html/ovary.html Accessed 19/03/2021.

Shalem, O., Sanjana, N.E., Hartenian, E., Shi, X., Scott, D.A., Mikkelson, T., Heckl, D., Ebert, B.L., Root, D.E., Doench, J.G., et al. (2014). Genome-scale CRISPR-Cas9 knockout screening in human cells. Science 343, 84-87.

Shaw, P.A., Rouzbahman, M., Pizer, E.S., Pintilie, M., and Begley, H. (2009). Candidate serous cancer precursors in fallopian tube epithelium of BRCA1/2 mutation carriers. Mod Pathol 22, 1133-1138.

Sheltzer, J.M. (2013). A transcriptional and metabolic signature of primary aneuploidy is present in chromosomally unstable cancer cells and informs clinical prognosis. Cancer Res 73, 6401-6412.

Sheltzer, J.M., and Amon, A. (2011). The aneuploidy paradox: costs and benefits of an incorrect karyotype. Trends Genet 27, 446-453.

Sheltzer, J.M., Ko, J.H., Replogle, J.M., Habibe Burgos, N.C., Chung, E.S., Meehl, C.M., Sayles, N.M., Passerini, V., Storchova, Z., and Amon, A. (2017). Single-chromosome Gains Commonly Function as Tumor Suppressors. Cancer Cell 31, 240-255.

Sherman-Baust, C.A., Kuhn, E., Valle, B.L., Shih Ie, M., Kurman, R.J., Wang, T.L., Amano, T., Ko, M.S., Miyoshi, I., Araki, Y., et al. (2014). A genetically engineered ovarian cancer mouse model based on fallopian tube transformation mimics human high-grade serous carcinoma development. J Pathol 233, 228-237.

Sherr, C.J., and Bartek, J. (2017). Cell Cycle–Targeted Cancer Therapies. Annual Review of Cancer Biology 1, 41-57.

Shoshani, O., Brunner, S.F., Yaeger, R., Ly, P., Nechemia-Arbely, Y., Kim, D.H., Fang, R., Castillon, G.A., Yu, M., Li, J.S.Z., et al. (2020). Chromothripsis drives the evolution of gene amplification in cancer. Nature.

Shukla, A., Nguyen, T.H.M., Moka, S.B., Ellis, J.J., Grady, J.P., Oey, H., Cristino, A.S., Khanna, K.K., Kroese, D.P., Krause, L., et al. (2020). Chromosome arm aneuploidies shape tumour evolution and drug response. Nat Commun 11, 449.

Siegel, R.L., Miller, K.D., and Jemal, A. (2020). Cancer statistics, 2020. CA Cancer J Clin 70, 7-30.

Silkworth, W.T., Nardi, I.K., Scholl, L.M., and Cimini, D. (2009). Multipolar spindle pole coalescence is a major source of kinetochore mis-attachment and chromosome mis-segregation in cancer cells. PLoS One 4, e6564.

Simoes-Sousa, S., Littler, S., Thompson, S.L., Minshall, P., Whalley, H., Bakker, B., Belkot, K., Moralli, D., Bronder, D., Tighe, A., et al. (2018). The p38alpha Stress Kinase Suppresses Aneuploidy Tolerance by Inhibiting Hif-1alpha. Cell Rep 25, 749-760 e746.

Skuse, D., Printzlau, F., and Wolstencroft, J. (2018). Sex chromosome aneuploidies. Handb Clin Neurol 147, 355-376.

Smyth, G.K. (2004). Linear models and empirical bayes methods for assessing differential expression in microarray experiments. Stat Appl Genet Mol Biol 3, Article3.

Snape, K., Hanks, S., Ruark, E., Barros-Nunez, P., Elliott, A., Murray, A., Lane, A.H., Shannon, N., Callier, P., Chitayat, D., et al. (2011). Mutations in CEP57 cause mosaic variegated aneuploidy syndrome. Nat Genet 43, 527-529.

Soto, M., Raaijmakers, J.A., Bakker, B., Spierings, D.C.J., Lansdorp, P.M., Foijer, F., and Medema, R.H. (2017). p53 Prohibits Propagation of Chromosome Segregation Errors that Produce Structural Aneuploidies. Cell Rep 19, 2423-2431.

Speicher, M.R., Gwyn Ballard, S., and Ward, D.C. (1996). Karyotyping human chromosomes by combinatorial multi-fluor FISH. Nat Genet 12, 368-375.

Stewart-Ornstein, J., Iwamoto, Y., Miller, M.A., Prytyskach, M.A., Ferretti, S., Holzer, P., Kallen, J., Furet, P., Jambhekar, A., Forrester, W.C., et al. (2021). p53 dynamics vary between tissues and are linked with radiation sensitivity. Nat Commun 12, 898.

Stingele, S., Stoehr, G., Peplowska, K., Cox, J., Mann, M., and Storchova, Z. (2012). Global analysis of genome, transcriptome and proteome reveals the response to aneuploidy in human cells. Mol Syst Biol 8, 608.

Stolz, A., Ertych, N., Kienitz, A., Vogel, C., Schneider, V., Fritz, B., Jacob, R., Dittmar, G., Weichert, W., Petersen, I., et al. (2010). The CHK2-BRCA1 tumour suppressor pathway ensures chromosomal stability in human somatic cells. Nat Cell Biol 12, 492-499.

Subramanian, A., Tamayo, P., Mootha, V.K., Mukherjee, S., Ebert, B.L., Gillette, M.A., Paulovich, A., Pomeroy, S.L., Golub, T.R., Lander, E.S., et al. (2005). Gene set enrichment analysis: a knowledge-based approach for interpreting genome-wide expression profiles. Proc Natl Acad Sci U S A 102, 15545-15550.

Szabova, L., Bupp, S., Kamal, M., Householder, D.B., Hernandez, L., Schlomer, J.J., Baran, M.L., Yi, M., Stephens, R.M., Annunziata, C.M., et al. (2014). Pathway-specific engineered mouse allograft models functionally recapitulate human serous epithelial ovarian cancer. PLoS One 9, e95649.

Szabova, L., Yin, C., Bupp, S., Guerin, T.M., Schlomer, J.J., Householder, D.B., Baran, M.L., Yi, M., Song, Y., Sun, W., et al. (2012). Perturbation of Rb, p53, and Brca1 or Brca2 cooperate in inducing metastatic serous epithelial ovarian cancer. Cancer Res 72, 4141-4153.

Tamura, N., Shaikh, N., Muliaditan, D., Soliman, T.N., McGuinness, J.R., Maniati, E., Moralli, D., Durin, M.A., Green, C.M., Balkwill, F.R., et al. (2020). Specific mechanisms of chromosomal instability indicate therapeutic sensitivities in high-grade serous ovarian carcinoma. Cancer Res.

Taylor, A.M., Shih, J., Ha, G., Gao, G.F., Zhang, X., Berger, A.C., Schumacher, S.E., Wang, C., Hu, H., Liu, J., et al. (2018). Genomic and Functional Approaches to Understanding Cancer Aneuploidy. Cancer Cell 33, 676-689.e673.

TCGA (2008). Comprehensive genomic characterization defines human glioblastoma genes and core pathways. Nature 455, 1061-1068.

TCGA (2011). Integrated genomic analyses of ovarian carcinoma. Nature 474, 609-615.

Teixeira, V.H., Pipinikas, C.P., Pennycuick, A., Lee-Six, H., Chandrasekharan, D., Beane, J., Morris, T.J., Karpathakis, A., Feber, A., Breeze, C.E., et al. (2019). Deciphering the genomic, epigenomic, and transcriptomic landscapes of pre-invasive lung cancer lesions. Nat Med 25, 517-525.

Thompson, S.L., and Compton, D.A. (2010). Proliferation of aneuploid human cells is limited by a p53-dependent mechanism. J Cell Biol 188, 369-381.

Thompson, S.L., and Compton, D.A. (2011). Chromosome missegregation in human cells arises through specific types of kinetochore-microtubule attachment errors. Proc Natl Acad Sci U S A 108, 17974-17978.

Tighe, A., Johnson, V.L., Albertella, M., and Taylor, S.S. (2001). Aneuploid colon cancer cells have a robust spindle checkpoint. EMBO Reports 2, 609-614.

Torre, L.A., Trabert, B., DeSantis, C.E., Miller, K.D., Samimi, G., Runowicz, C.D., Gaudet, M.M., Jemal, A., and Siegel, R.L. (2018). Ovarian cancer statistics, 2018. CA Cancer J Clin 68, 284-296.

Torres, E.M., Sokolsky, T., Tucker, C.M., Chan, L.Y., Boselli, M., Dunham, M.J., and Amon, A. (2007). Effects of aneuploidy on cellular physiology and cell division in haploid yeast. Science 317, 916-924.

Tubbs, A., and Nussenzweig, A. (2017). Endogenous DNA Damage as a Source of Genomic Instability in Cancer. Cell 168, 644-656.

Tutt, A., Gabriel, A., Bertwistle, D., Connor, F., Paterson, H., Peacock, J., Ross, G., and Ashworth, A. (1999). Absence of Brca2 causes genome instability by chromosome breakage and loss associated with centrosome amplification. Curr Biol 9, 1107-1110.

Tuveson, D., and Clevers, H. (2019). Cancer modeling meets human organoid technology. Science 364, 952-955.

Upender, M.B., Habermann, J.K., McShane, L.M., Korn, E.L., Barrett, J.C., Difilippantonio, M.J., and Ried, T. (2004). Chromosome transfer induced aneuploidy results in complex dysregulation of the cellular transcriptome in immortalized and cancer cells. Cancer Res 64, 6941-6949.

Valente, L.J., Tarangelo, A., Li, A.M., Naciri, M., Raj, N., Boutelle, A.M., Li, Y., Mello, S.S., Bieging-Rolett, K., DeBerardinis, R.J., et al. (2020). p53 deficiency triggers dysregulation of diverse cellular processes in physiological oxygen. J Cell Biol 219.

van den Bos, H., Spierings, D.C., Taudt, A.S., Bakker, B., Porubsky, D., Falconer, E., Novoa, C., Halsema, N., Kazemier, H.G., Hoekstra-Wakker, K., et al. (2016). Single-cell whole genome sequencing reveals no evidence for common aneuploidy in normal and Alzheimer's disease neurons. Genome Biol 17, 116.

Vang, R., Levine, D.A., Soslow, R.A., Zaloudek, C., Shih Ie, M., and Kurman, R.J. (2016). Molecular Alterations of TP53 are a Defining Feature of Ovarian High-Grade Serous Carcinoma: A Rereview of Cases Lacking TP53 Mutations in The Cancer Genome Atlas Ovarian Study. Int J Gynecol Pathol 35, 48-55.

Vassilev, L.T., Vu, B.T., Graves, B., Carvajal, D., Podlaski, F., Filipovic, Z., Kong, N., Kammlott, U., Lukacs, C., Klein, C., et al. (2004). In vivo activation of the p53 pathway by small-molecule antagonists of MDM2. Science 303, 844-848.

Vasudevan, A., Baruah, P.S., Smith, J.C., Wang, Z., Sayles, N.M., Andrews, P., Kendall, J., Leu, J., Chunduri, N.K., Levy, D., et al. (2020). Single-Chromosomal Gains Can Function as Metastasis Suppressors and Promoters in Colon Cancer. Dev Cell 52, 413-428 e416.

Vasudevan, A., Schukken, K.M., Sausville, E.L., Girish, V., Adebambo, O.A., and Sheltzer, J.M. (2021). Aneuploidy as a promoter and suppressor of malignant growth. Nat Rev Cancer 21, 89-103.

Walton, J., Blagih, J., Ennis, D., Leung, E., Dowson, S., Farquharson, M., Tookman, L.A., Orange, C., Athineos, D., Mason, S., et al. (2016). CRISPR/Cas9-Mediated Trp53 and Brca2 Knockout to Generate Improved Murine Models of Ovarian High-Grade Serous Carcinoma. Cancer Res 76, 6118-6129.

Walton, J.B., Farquharson, M., Mason, S., Port, J., Kruspig, B., Dowson, S., Stevenson, D., Murphy, D., Matzuk, M., Kim, J., et al. (2017). CRISPR/Cas9-derived models of ovarian high grade serous carcinoma targeting Brca1, Pten and Nf1, and correlation with platinum sensitivity. Sci Rep 7, 16827.

Wang, Y., Bernhardy, A.J., Cruz, C., Krais, J.J., Nacson, J., Nicolas, E., Peri, S., van der Gulden, H., van der Heijden, I., O'Brien, S.W., et al. (2016). The BRCA1-Delta11q Alternative Splice Isoform Bypasses Germline Mutations and Promotes Therapeutic Resistance to PARP Inhibition and Cisplatin. Cancer Res 76, 2778-2790.

Wang, Y.K., Bashashati, A., Anglesio, M.S., Cochrane, D.R., Grewal, D.S., Ha, G., McPherson, A., Horlings, H.M., Senz, J., Prentice, L.M., et al. (2017). Genomic consequences of aberrant DNA repair mechanisms stratify ovarian cancer histotypes. Nat Genet 49, 856-865.

Wangsa, D., Quintanilla, I., Torabi, K., Vila-Casadesus, M., Ercilla, A., Klus, G., Yuce, Z., Galofre, C., Cuatrecasas, M., Lozano, J.J., et al. (2018). Near-tetraploid cancer cells show chromosome instability triggered by replication stress and exhibit enhanced invasiveness. FASEB J 32, 3502-3517.

Weaver, Z., Montagna, C., Xu, X., Howard, T., Gadina, M., Brodie, S.G., Deng, C.X., and Ried, T. (2002). Mammary tumors in mice conditionally mutant for Brca1 exhibit gross genomic instability and centrosome amplification yet display a recurring distribution of genomic imbalances that is similar to human breast cancer. Oncogene 21, 5097-5107.

Weinberg, R.A. (2014). The biology of cancer, Second edition (New York, NY: Garland Science).

Westhorpe, F.G., Diez, M.A., Gurden, M.D., Tighe, A., and Taylor, S.S. (2010). Re-evaluating the role of Tao1 in the spindle checkpoint. Chromosoma 119, 371-379.

WHO (2021). Cancer. https://www.who.int/health-topics/cancer#tab=tab_1 Accessed 19/03/2021.

Williams, B.R., Prabhu, V.R., Hunter, K.E., Glazier, C.M., Whittaker, C.A., Housman, D.E., and Amon, A. (2008). Aneuploidy affects proliferation and spontaneous immortalization in mammalian cells. Science 322, 703-709.

Wooster, R., Bignell, G., Lancaster, J., Swift, S., Seal, S., Mangion, J., Collins, N., Gregory, S., Gumbs, C., and Micklem, G. (1995). Identification of the breast cancer susceptibility gene BRCA2. Nature 378, 789-792.

Wooster, R., Neuhausen, S.L., Mangion, J., Quirk, Y., Ford, D., Collins, N., Nguyen, K., Seal, S., Tran, T., Averill, D., et al. (1994). Localization of a breast cancer susceptibility gene, BRCA2, to chromosome 13q12-13. Science 265, 2088-2090.

Xing, D., and Orsulic, S. (2006). A mouse model for the molecular characterization of brca1-associated ovarian carcinoma. Cancer Res 66, 8949-8953.

Xu, X., Wagner, K.U., Larson, D., Weaver, Z., Li, C., Ried, T., Hennighausen, L., Wynshaw-Boris, A., and Deng, C.X. (1999a). Conditional mutation of Brca1 in mammary epithelial cells results in blunted ductal morphogenesis and tumour formation. Nat Genet 22, 37-43.

Xu, X., Weaver, Z., Linke, S.P., Li, C., Gotay, J., Wang, X.W., Harris, C.C., Ried, T., and Deng, C.X. (1999b). Centrosome amplification and a defective G2-M cell cycle checkpoint induce genetic instability in BRCA1 exon 11 isoform-deficient cells. Mol Cell 3, 389-395.

Yeo, C.Q.X., Alexander, I., Lin, Z., Lim, S., Aning, O.A., Kumar, R., Sangthongpitag, K., Pendharkar, V., Ho, V.H.B., and Cheok, C.F. (2016). p53 Maintains Genomic Stability by Preventing Interference between Transcription and Replication. Cell Rep 15, 132-146.

Yost, S., de Wolf, B., Hanks, S., Zachariou, A., Marcozzi, C., Clarke, M., de Voer, R.M., Etemad, B., Uijttewaal, E., Ramsay, E., et al. (2017). Biallelic TRIP13 mutations predispose to Wilms tumor and chromosome missegregation. Nat Genet 49, 1148-1151.

Zack, T.I., Schumacher, S.E., Carter, S.L., Cherniack, A.D., Saksena, G., Tabak, B., Lawrence, M.S., Zhsng, C.Z., Wala, J., Mermel, C.H., et al. (2013). Pan-cancer patterns of somatic copy number alteration. Nat Genet 45, 1134-1140.

Zaki, B.I., Suriawinata, A.A., Eastman, A.R., Garner, K.M., and Bakhoum, S.F. (2014). Chromosomal instability portends superior response of rectal adenocarcinoma to chemoradiation therapy. Cancer 120, 1733-1742.

Zeng, M., Kwiatkowski, N.P., Zhang, T., Nabet, B., Xu, M., Liang, Y., Quan, C., Wang, J., Hao, M., Palakurthi, S., et al. (2018). Targeting MYC dependency in ovarian cancer through inhibition of CDK7 and CDK12/13. Elife 7.

Zhai, Y., Wu, R., Kuick, R., Sessine, M.S., Schulman, S., Green, M., Fearon, E.R., and Cho, K.R. (2017). High-grade serous carcinomas arise in the mouse oviduct via defects linked to the human disease. J Pathol 243, 16-25.

Zhang, C.Z., Spektor, A., Cornils, H., Francis, J.M., Jackson, E.K., Liu, S., Meyerson, M., and Pellman, D. (2015). Chromothripsis from DNA damage in micronuclei. Nature 522, 179-184.

Zhang, H., Zhang, Y., Zhao, H., Zhang, Y., Chen, Q., Peng, H., Lei, L., Qiao, J., Shi, J., Cao, Z., et al. (2013). Hormonal regulation of ovarian bursa fluid in mice and involvement of aquaporins. PLoS One 8, e63823.

Zhang, S., Dolgalev, I., Zhang, T., Ran, H., Levine, D.A., and Neel, B.G. (2019). Both fallopian tube and ovarian surface epithelium are cells-of-origin for high-grade serous ovarian carcinoma. Nat Commun 10, 5367.

Zhang, S., Iyer, S., Ran, H., Dolgalev, I., Gu, S., Wei, W., Foster, C.J.R., Loomis, C.A., Olvera, N., Dao, F., et al. (2021). Genetically Defined, Syngeneic Organoid Platform for Developing Combination Therapies for Ovarian Cancer. Cancer Discov 11, 362-383.

Additional note

The main results presented in *Chapters 3*, *4* and *5* have been prepared for publication, deposited as a preprint on bioRxiv and simultaneously submitted to the journal *Disease Models & Mechanisms* on March 11th, 2021. Said manuscript has been appended to this thesis in *Appendix 1* and contains additional data which I elected not to include in this thesis as it was generated by my colleague Dr Dali Zong.

Appendix 1

TP53 loss initiates chromosomal instability in high-grade serous ovarian cancer

Daniel Bronder, Darawalee Wangsa, Dali Zong, Thomas J. Meyer, René Wardenaar, Paul Minshall, Anthony Tighe, Daniela Hirsch, Kerstin Heselmeyer-Haddad, Louisa Nelson, Diana Spierings, Joanne C. McGrail, Maggie Cam, André Nussenzweig, Floris Foijer, Thomas Ried, Stephen S. Taylor. doi.org/10.1101/2021.03.12.435079, bioRxiv, 2021.

TITLE

TP53 loss initiates chromosomal instability in high-grade serous ovarian cancer

AUTHORS

Daniel Bronder[1,2], Darawalee Wangsa[2], Dali Zong[3], Thomas J. Meyer[4], René Wardenaar[5], Paul Minshall[1], Anthony Tighe[1], Daniela Hirsch[2], Kerstin Heselmeyer-Haddad[2], Louisa Nelson[1], Diana Spierings[5], Joanne C. McGrail[1], Maggie Cam[4], André Nussenzweig[3], Floris Foijer[5], Thomas Ried[2], Stephen S. Taylor[1]

AFFILIATIONS

[1]Division of Cancer Sciences, Faculty of Biology, Medicine and Health, University of Manchester, Manchester Cancer Research Centre, Wilmslow Road, Manchester M20 4QL, United Kingdom; [2]Genetics Branch, [3]Laboratory of Genome Integrity, [4]CCR Collaborative Bioinformatics Resource, Center for Cancer Research, National Cancer Institute, National Institutes of Health, Bethesda, MD, USA; [5]European Research Institute for the Biology of Ageing, University of Groningen, Groningen, The Netherlands.

KEY WORDS

High-grade serous ovarian cancer, fallopian tube, chromosomal instability, *TP53*, *BRCA1*, *MYC*

MANUSCRIPT DETAILS

Page numbers	43
Figures & Tables	7 Figures; 1 Table
Supplemental information	6 Figures; 7 Tables

SUMMARY STATEMENT

High-grade serous ovarian cancer is defined by *TP53* mutation and chromosomal instability, the cause of which remains poorly understood. We developed a novel model system that implicates cell cycle deregulation upon p53-loss as cause of CIN.

ABSTRACT

High-grade serous ovarian cancer (HGSOC) originates in the fallopian tube epithelium and is characterized by ubiquitous *TP53* mutation and extensive chromosomal instability (CIN). While the direct causes of CIN are errors during DNA replication and/or chromosome segregation, mutations in genes encoding DNA replication and mitotic factors are rare in HGSOC. Thus, the drivers of CIN remain undefined. We therefore asked whether the oncogenic lesions that are frequently observed in HGSOC are capable of driving CIN via indirect mechanisms. To address this question, we genetically manipulated non-transformed *hTERT*-immortalized human fallopian tube epithelial cells to model homologous recombination deficiency (HRD) and oncogenic signalling in HGSOC. Using CRISPR/Cas9-mediated gene editing, we sequentially mutagenized the tumour suppressors *TP53* and *BRCA1*, followed by overexpression of the *MYC* oncogene. Single-cell shallow-whole-genome sequencing revealed that loss of p53 function was sufficient to lead to the emergence of heterogenous karyotypes harbouring whole chromosome and chromosome arm aneuploidies, a phenomenon exacerbated by subsequent loss of BRCA1 function. In addition, whole-genome doubling events were observed in independent p53/BRCA1-deficient subclones. Global transcriptomics showed that *TP53* mutation was also sufficient to deregulate gene expression modules involved in cell cycle commitment, DNA replication, G2/M checkpoint control and mitotic spindle function, suggesting that p53-deficiency induces cell cycle distortions that could precipitate CIN. Again, loss of BRCA1 function and MYC overexpression exacerbated these patterns of transcriptional deregulation. Thus, our observations support a model whereby the initial loss of the key tumour suppressor *TP53* is sufficient to deregulate gene expression networks governing multiple cell cycle controls, and that this in turn is sufficient to drive CIN in pre-malignant fallopian tube epithelial cells.

INTRODUCTION

High-grade serous ovarian cancer (HGSOC) is the most common histological subtype of ovarian cancer, and the deadliest gynaecological malignancy (Bowtell et al., 2015). Survival statistics are dismal, with 5-year survival of ~30%, and have remained largely unchanged over the past 30 years, illustrating the need for improved therapeutic interventions, which requires a better understanding of the underlying disease biology.

HGSOC is characterised by a relatively low mutational burden at the nucleotide level (Ciriello et al., 2013). *TP53* mutations are ubiquitous and are considered to be an early, truncal event in HGSOC tumorigenesis, which are present in precursor lesions (Ahmed et al., 2010; Labidi-Galy et al., 2017; Vang et al., 2016). However, with the exception of *BRCA1/2* mutations in ~25% of cases, other common driver mutations are rare (Cancer Genome Atlas Research, 2011). By contrast, HGSOC genomes are characterized by extensive chromosomal copy number aberrations, a consequence of rampant chromosomal instability (CIN) (Cancer Genome Atlas Research, 2011; Nelson et al., 2020). Indeed, HGSOC ranks among the most chromosomally unstable tumour types (Ciriello et al., 2013; Shukla et al., 2020), a characteristic confirmed by recent live cell imaging of established cell lines and patient-derived *ex vivo* cultures, which revealed an unprecedented level of chromosome segregation errors (Nelson et al., 2020; Tamura et al., 2020).

To delineate the mechanisms responsible for CIN, HGSOC genomes have been extensively studied by whole genome sequencing, with one study defining two CIN classes, characterized either by homologous recombination deficiency (HRD) or foldback inversions (FBI) (Wang et al., 2017). While the former correlated with mutations in *BRCA1/2*, amplifications of *MECOM* and *MYC,* and loss of *RB1*, the latter correlated with *CCNE1* amplification and *PTEN* loss (Wang et al., 2017). A second study identified seven CIN signatures, including whole-genome duplication (WGD), suggesting a larger array of underlying driver mechanisms in addition to HRD and FBI (Macintyre et al., 2018).

This presents a paradox; while HGSOC appears to be driven by CIN, mutations in genes ensuring faithful cell division and DNA replication are extremely rare (Bastians, 2015). HRD, either as a consequence of *BRCA1/2* inactivation or mutation in other DNA damage repair genes is an obvious contributor to CIN, but by itself can only account for up to ~50% of cases (Cancer Genome Atlas Research, 2011; Weaver et al., 2002; Xu et al., 1999). *TP53* has consistently been shown to correlate with aneuploidy (Ciriello et al., 2013; Davoli et al., 2017; Taylor et al., 2018; Zack et al., 2013), but its role as a driver of CIN remains

controversial. Initial studies using the near-diploid colorectal cancer cell line HCT116, suggested that p53-loss is not sufficient to cause CIN (Bunz et al., 2002). More recently, however, suppressing p53 in *hTERT*-immortalized RPE-1 cells did generate abnormal karyotypes (Kok et al., 2020; Soto et al., 2017). Furthermore, p53 inactivation in transformed murine embryonic fibroblasts deregulated multiple cellular processes affecting DNA damage response, mitosis and ploidy control (Valente et al., 2020).

Here, we aimed to develop novel model systems of CIN in HGSOC, starting with *hTERT*-immortalized non-ciliated fallopian tube epithelial cells (Merritt et al., 2013). In the first instance, we set out to model the HRD CIN class, using CRISPR/Cas9-mediated gene editing to first mutate *TP53* then *BRCA1*, followed by overexpression of *MYC.* A panel of derivative subclones were subjected to functional assays, karyotyping and gene expression profiling to determine whether (a) CIN had been induced and (b) what the potential mechanisms might be.

RESULTS

FNE1 cells to model CIN in HGSOC

In addition to the truncal *TP53* mutation, *BRCA1/2* mutations and *MYC* overexpression tend to co-occur (Wang et al., 2017), suggesting that HRD and oncogene hyperactivation likely facilitate the development of CIN in HGSOC (Fig. 1A). To model these events, we set out to manipulate diploid, karyotypically stable cells, sequentially mutating *TP53* and *BRCA1* using CRISPR/Cas9-mediated gene editing, followed by ectopic overexpression of *MYC* (Fig. 1B). Since the fallopian tube epithelium is the likely origin for HGSOC we chose the human FNE1 cell line as a starting point (Ducie et al., 2017; Merritt et al., 2013). This line is derived from non-ciliated fallopian tube epithelial cells and immortalised by ectopic expression of the telomerase component *hTERT* (Merritt et al., 2013). Importantly, FNE1 cells are *TP53* proficient, evidenced by nuclear accumulation of p53 and p21 induction in response to the MDM2 inhibitor Nutlin-3 and to cisplatin (Fig. S1A,B and data not shown) (Vassilev et al., 2004). In addition, FNE1 cells are near-diploid and karyotypically stable, as confirmed by single-cell whole genome sequencing (scWGS) and spectral karyotyping (SKY). scWGS showed that the genome is largely disomic, except for monosomies at 9p, 15, and X (Fig. S1C). Consistently, SKY showed a clonal loss of chromosomes 15 and X and an unbalanced translocation between the short arm of chromosome 9 and chromosome 15 (Fig. S1D). An identical karyotype was also recently reported for FNE1 cells using multiplex fluorescence *in situ* hybridization (M-FISH) (Tamura et al., 2020). To enable CRISPR/Cas9-mediated gene editing in FNE1 cells, we transduced them with a lentivirus expressing a tetracycline-inducible Cas9 transgene. Increasing concentrations of tetracycline resulted in a dose-dependent induction of Cas9 (Fig. S1E). Importantly, in the absence of tetracycline, Cas9 was not detectable, thereby minimizing exposure of the genome to endonuclease activity during routine cell culture.

CRISPR/Cas9-mediated mutation of *TP53* and *BRCA1*

To mutate *TP53*, we introduced an sgRNA targeting exon 2, induced Cas9 then isolated subclones by limiting dilution, either with or without Nutlin-3 selection (Fig. 1B). Characterisation of three independent subclones, designated P1–3 (Fig. S2A, Table 1), showed an absence of p53 protein (Fig. 2A), and interrogation of RNAseq data showed that all three clones harboured frameshift mutations leading to premature termination codons (Table 1;

Fig. S2B). Importantly, Nutlin-3 did not exert an anti-proliferative effect in the *TP53* mutants (Fig. 2B), indicating that the subclones are indeed functionally p53-deficient.

To then mutate *BRCA1*, clone P1 was transduced with sgRNAs targeting exons 2, 3 and 11 (Fig. S2A), Cas9 induced and subclones isolated by limiting dilution (Fig. 1B). Again, we characterised three independent subclones, designated PB1–3 (Table 1). Consistent with *BRCA1* mutation, immunoblotting failed to detect full length protein (Fig. 2C), induction of RAD51 foci in response to ionizing radiation was suppressed, and sensitivity to the PARP inhibitor olaparib was increased (Fig. 2D). To define the nature of the *BRCA1* mutations, we interrogated RNAseq data and mutations identified were then confirmed by Sanger sequencing of cloned genomic DNA (Table 1; data not shown). This revealed that PB2 and PB3 harboured mutations in exon 3, while PB1 harboured a mutation in exon 11. Interestingly, we observed alternative splicing of exon 11 in PB1 (Fig. 2E), an event that may lead to the production of a truncated BRCA1 protein that retains partial function (Wang et al., 2016). Thus, although all three PB subclones harbour *BRCA1* mutations, PB1 may have the capacity to retain partial homologous recombination (HR) proficiency. Altogether, these observations confirm the successful generation of FNE1 subclones harbouring mutations in both *TP53* and *BRCA1*.

Ectopic overexpression of *MYC*

Following mutation of *TP53* and *BRCA1*, we set out to overexpress *MYC*, an oncogene frequently amplified in HGSOC. Indeed, across 18 tumour types, HGSOC displays the highest frequency of *MYC* amplification (Zeng et al., 2018). The three *TP53* mutant clones, P1–3, and the three P1-derived *TP53*/*BRCA1* double mutant clones, PB1–3, were all transduced with a lentivirus harbouring a *MYC* cDNA downstream of a constitutive CMV promoter, generating six polyclonal derivatives, designated P1–3M and PB1–3M (Fig. 1B, Fig. S2A). In parallel, we transduced an '*empty*' vector control virus, generating a further six polyclonal derivatives, designated P1–3E and PB1–3E (Fig. S2A). Note that the *MYC* cDNA harboured four synonymous mutations (Littler et al., 2019), allowing us to differentiate ectopic and endogenous *MYC* transcripts. In turn, RNA sequencing revealed that ectopic *MYC* was indeed overexpressed relative to endogenous *MYC* in P1–3M and PB1M (Fig. 3A). In PB2M and PB3M, however, the situation was reversed, possibly indicating endogenous *MYC* was already overexpressed in these two lineages. Indeed, *MYC* was highly expressed in PB3 and PB3E, consistent with spontaneous upregulation prior to our efforts to

experimentally overexpress *MYC* (Table 1). However, for the PB2 lineage, *MYC* levels were only elevated in PB2M as expected following ectopic *MYC* overexpression, and not in PB2 or PB2E.

Importantly, overexpression of *MYC* modulated MYC-dependent processes, evidenced by immunoblotting of P1M cells, which revealed downregulation of the pro-survival factor BCL-XL (Fig. 3B). Consistent with MYC's role as a transcriptional amplifier (Lin et al., 2012; Nie et al., 2020; Nie et al., 2012), analysis of differentially expressed genes in pooled P and PM cells revealed more significantly upregulated and downregulated genes upon overexpression of *MYC* (Fig. 3C). Moreover, gene set enrichment analysis (GSEA) showed that *MYC* hallmark target gene sets V1 and V2 are positively enriched in pooled PM cells versus controls (Fig. 3D). Interestingly, the V1 and V2 sets are also positively enriched versus parental FNE1 cells in both the PB2 and PB3 lineages, with and without introduction of ectopic MYC (see below; Fig.S5). Therefore, whilst PB3 lineage cells have likely enriched V1 and V2 sets via direct overexpression of endogenous *MYC*, PB2 lineage cells may have also spontaneously upregulated MYC target gene expression via an alternative mechanism, for example by alteration of downstream MYC signalling as has been observed previously in HGSOC samples (Jimenez-Sanchez et al., 2020). Thus, these observations confirm successful upregulation of *MYC* activity in FNE1 subclones harbouring mutations in *TP53* and *BRCA1*.

Ploidy analysis reveals independent WGD events

Having established a panel of 18 FNE1 subclones harbouring genetic features found in HGSOC cells (Fig. S2A, Table 1), we set out to determine whether any of those displayed evidence of CIN. First, we analysed the P1 lineage by flow cytometry to explore changes in ploidy. The *TP53* mutant P1E, the *TP53*/*BRCA1* double mutant PB1E, plus their MYC-overexpressing counterparts, P1M and PB1M displayed typical 2c and 4c peaks, indicating no overt deviation from normal ploidy (Fig. S3). By contrast, the *TP53*/*BRCA1* double mutants, PB2E and PB3E, and their MYC-overexpressing counterparts, PB2M and PB3M, displayed evidence of 8c peaks, indicating cycling tetraploid cell population. In PB2E and PB2M, the 8c peak was small and accompanied by 2c and 4c peaks, suggesting that only a sub-fraction of the population was tetraploid. While in PB3E and PB3M, the 4c and 8c peaks were more apparent than in PB2E/M and an obvious 2c peak was absent, suggesting that the entire population was tetraploid, i.e., had undergone WGD.

Because P1E and P1M appeared overtly normal, mutation of *TP53* alone or in combination with overexpression of *MYC* is not sufficient to induce tetraploidization. Moreover, the presence of tetraploidy in PB2E and PB3E also suggests that it arose prior to *MYC* overexpression. Rather, the flow cytometry suggests that the *BRCA1* mutation was possibly driving the tetraploidy. And yet, PB1E and PB1M, which also harbour *BRCA1* mutations, do not show evidence of tetraploidy. Note, however, that, as described above, we observed alternative splicing of exon 11 in PB1, raising the possibility that the BRCA1-deficiency in this line may not be as penetrant as in PB2 and PB3 lineages. Nevertheless, the presence of tetraploid cells in the PB2 and PB3 lineages suggests independent WGD events in *TP53*/*BRCA1* double mutant FNE1 cells.

miFISH confirms WGD and reveals CIN

To obtain a more detailed picture of the ploidy changes observed by flow cytometry, we analysed 20 genetic loci in 100 FNE1, PB2M and PB3M cells using multiplex, interphase fluorescence *in situ* hybridization (miFISH) (Heselmeyer-Haddad et al., 2012). In parental FNE1 cells, 19 of the 20 loci analysed were predominantly present in two copies (Fig. 4A,C), consistent with a diploid and stable genome, and in line with the scWGS and SKY analysis (Fig. S1). In seven cells, we observed minor abnormalities, with one or two loci deviating from the mode; this, however, is within the margin of error of miFISH performed on cultured cells (Wangsa et al., 2018). By contrast, in every cell analysed only a single *CDKN2A* signal was detected, indicating a clonal loss of a region on chromosome 9, consistent with the karyotyping described above (Fig. S1). Note that the *CDKN2A* locus, which encodes the tumour suppressors p16 and p14ARF, is frequently altered in established cell lines, and may contribute to their unlimited proliferative potential *in vitro* (Huschtscha and Reddel, 1999).

In contrast to parental FNE1 cells, PB2M and PB3M displayed numerous deviations. As the ploidy measurements by flow cytometry suggested, PB2M harboured both 2c and 4c cells. The 2c subpopulation had the same clonal loss of *CDKN2A*, with additional clonal losses of *COX2* and *RB1* (Fig. 4B,C). These three clonal losses were also present in the 4c subpopulation, with only two foci of each detected. As expected, PB3M was confirmed by miFISH to be entirely composed of 4c cells (Fig 4.C). Like 4c PB2M cells, PB3M cells also had only two signals for some loci, i.e., *COX2*, *FBXW7*, *CDKN2A* and *CDH1*. These losses suggest that either a 4c population of PB3M cells has lost 2 copies of *COX2*, *FBXW7* and *CDH1*, but not *CDKN2A* (since its baseline is monosomic) or an elusive 2c PB3M population

has undergone WGD; we favour the latter explanation. Interestingly, PB3M cells show a pattern of dosage decrease of chromosome 17. In most cells three copies of *TP53* were detected and four copies of *NF1* and *HER2*. In a subset where only two *TP53* signals were observed, three copies of *NF1* and *HER2* are seen. Overall, a more diverse pattern of gains and losses were detected in PB2/3M than in FNE1 cells. Thus, these observations confirm independent WGD events in lineages PB2 and PB3. Moreover, the sub-clonal gains and losses in both diploid and tetraploid backgrounds indicate the acquisition of CIN.

scWGS reveals CIN in both diploid and tetraploid backgrounds

The sub-clonal gains and losses revealed by miFISH indicate CIN in the PB2M and PB3M lines. To explore this in more detail across a wider range of lines, and in particular in an unbiased, genome-wide manner, we performed scWGS-based karyotyping. In addition to parental FNE1 cells, we analysed the *TP53* mutant P1, the two *BRCA1*-deficient derivatives, PB2 and PB3, their *MYC*-expressing subclones, PB2M and PB3M, and the corresponding empty vector controls, PM2E and PB3E (Fig. S2A). Unsupervised hierarchical clustering identified four karyotype clusters (Fig. 5A). Cluster 1, which exhibited the monosomies at 9p, 15, and X described above (Fig. S1), consisted of parental FNE1 cells and the *TP53* mutant P1. Closer inspection revealed a number of partial or whole chromosome aneuploidies in P1 cells; whereas only two of 35 parental FNE1 cells (5.7%) displayed deviations, 10 of 18 P1 cells did so (55.6%), indicating that low level CIN is already present in *TP53*-deficient P1 cells.

Cluster 2 is characterised by near-diploid genomes with clonal segmental copy number losses on chromosomes 1, 2, 6, 12 and 13, a segmental gain on chromosome 6, and a variety of sub-clonal gains and losses. By contrast, cluster 3 was dominated by tetrasomies but with segmental disomies on chromosomes 1, 2, 6, 12 and 13, and various sub-clonal deviations. All the cells in clusters 2 and 3 were from the *TP53*/*BRCA2* double mutant lineage PB2, including PB2 itself, PB2M and PB2E, and thus reflect the diploid and tetraploid populations identified by miFISH analysis of PB2M. These data also corroborate the *COX2* (1q) and *RB1* (13q) losses seen in PB2M by miFISH, since the corresponding chromosome arms are monosomic in the diploid population. Importantly, because the monosomies in the diploid subpopulation are reflected as disomies in the tetraploid subpopulation, these losses likely occurred prior to the WGD event. The increasing frequency of sub-clonal deviations in the diploid and tetraploid PB2-lineage populations (68.8% and 78.3% displaying deviations,

respectively) compared with P1 indicates exacerbation of the low-level CIN induced by *TP53* loss.

Cluster 4, which is also dominated by tetrasomies, is made up exclusively of cells from the PB3 lineage, including PB3 itself, PB3M and PB3E, reflecting the tetraploid population identified by miFISH analysis of PB3M. Chromosomes 1q, 4 and 16 are disomic, suggesting clonal loss prior to WGD, while many other chromosomes display sub-clonal whole or segmental gains and losses, indicating pervasive CIN. Indeed, chromosome 5q displays features of rearrangement, loss and amplification. One particular segment is detectable as tetra-, penta- and hexasomy while the most telomeric region is present as di-, tri- and tetrasomy. A similar observation is made on chromosome 19 where 19p is predominantly detected in five or six copies and 19q is detected most frequently in three copies. Therefore, heterogeneity in the PB3 lineage also indicates that loss of BRCA1 function exacerbated low-level CIN induced by *TP53* loss.

CIN is initiated by *TP53* loss and exacerbated by *BRCA1* mutation

Taking together, the ploidy analysis, the miFISH and the scWGS data, our observations support a model whereby, in the PB2 and PB3 lineages, *TP53* mutation initiated low-level CIN on an otherwise diploid background, which was then exacerbated by *BRCA1* mutation, followed by genome doubling events leading to tetraploidy and more pervasive CIN. While both diploid and tetraploid sub-clones are present in the PB2 lineage, the PB3 lineage is exclusively tetraploid, possibly reflecting an early WGD event during the genesis of this line. Importantly, the extensive CIN generated in our model system is reflective of M-FISH and scWGS from patient-derived *ex vivo* HGSOC cultures, which display profound intercellular heterogeneity with karyotypes characterized by whole-chromosome aneuploidies, rearranged chromosomes, monosomies and tetrasomies (Nelson et al., 2020).

While we did not observe CIN in the PB1 lineage, we did not perform scWGS so may have missed low-level deviations due to *TP53* loss. Also, due to alternative splicing of exon 11, this lineage may retain partial *BRCA1* function, explaining why more pervasive CIN did not manifest. Interestingly, overexpression of *MYC* in the PB2 and PB3 lineages did not noticeably further exacerbate CIN. Note, however, that these cells may have spontaneously increased expression of MYC target genes prior to transduction with the *MYC* lentivirus (Fig. S5). Thus, it is possible that overexpression of *MYC* targets is contributing to the CIN

phenotype in the PB2 and PB3 lineages. Whether *MYC* overexpression exacerbates CIN in a *TP53*-mutant only background will require scWGS analysis of P1–3M.

TP53 loss initiates extensive transcriptional rewiring

The observation that *TP53* mutant cells accumulate aneuploidies was surprising considering the longstanding observation that p53-null HCT116 cells remain diploid (Bunz et al., 2002; Thompson and Compton, 2010). Indeed, we also found that CRISPR-generated *TP53*$^{-/-}$ HCT116 cells do not develop aneuploidies (Simões-Sousa et al., 2018). While *TP53* loss in HCT116 and RPE-1 cells can facilitate tolerance of abnormal karyotypes, p53-activation in response to aneuploidy is not consistent and is context dependent (Santaguida et al., 2017; Simões-Sousa et al., 2018; Soto et al., 2017; Thompson and Compton, 2010). Moreover, it should be noted that such aneuploidy tolerance studies utilised experimental induction of chromosome mis-segregation in cells lacking p53. However, the emergence of aneuploid clones with *TP53* loss has been observed in untreated mammary epithelial and RPE-1 cells (Kok et al., 2020; Salehi et al., 2020; Soto et al., 2017). In addition, multiple cellular processes were deregulated in response to p53 inactivation in transformed murine embryonic fibroblasts, including ploidy control (Valente et al., 2020). Therefore, the fact that *TP53* mutant FNE1 cells accumulate aneuploidies without exposure to exogenous replication stress or mitotic perturbation suggests that, in this context, p53 loss is also sufficient to initiate CIN. To explore potential underlying mechanisms, we performed global transcriptomics, analysing the panel of 18 derivatives by RNAseq. Parental FNE1, P1, P1E and P1M were analysed in triplicate, totalling 27 samples.

A principal component analysis (PCA) yielded four clusters, with cluster 1 comprised of the three parental FNE1 samples (Fig. 6A). Cluster 2 is dominated by the three independent *TP53* mutants, P1–3, and their '*empty'* vector derivatives P1–3E, thus reflecting gene expression changes induced by *TP53* loss. Cluster 3 contained the PB2 and PB3 lineages, reflecting the effect of *BRCA1* loss in the *TP53*-mutant background. Cluster 4 contained P1–3M and thus reflects gene expression changes induced by *MYC* overexpression on the *TP53*-mutant background. Note that PB1, and its empty vector derivative PB1E, are in cluster 2, rather than the *BRCA1*-deficient cluster 3. Likewise, PB1M is in cluster 4 with P1–3M. However, as described above, the PB1 lineage may not be fully BRCA1-deficient due to alternative splicing of exon 11. Note also that while overexpression of *MYC* had a marked effect on P1–3 and PB1 cells, it had little effect on the PB2 and PB3 cells. However, again,

as described above, these cells appear to have spontaneously upregulated expression of *MYC* target genes (Fig. S5), explaining why ectopic *MYC* had little additional effect. Based on these observations, we conclude that *TP53* mutation alone results in profound transcriptional rewiring, which is further amplified by either elevated MYC activity or BRCA1-loss, in the latter case spontaneous MYC upregulation and MYC-independent enrichment of target genes were observed.

TP53 loss deregulates cell cycle gene expression programmes

To determine how *TP53* and *BRCA1* loss and *MYC* overexpression deregulate the transcriptome in FNE1 cells, we performed gene set variation analysis (GSVA) using the Hallmark gene set collection, an approach that allows comparisons across multiple sample groups (Hänzelmann et al., 2013). Unsupervised hierarchical clustering of the 27 samples resulted in a similar separation as the PCA, with parental FNE1 (cluster 1) and the *TP53* mutants (cluster 2) forming one clade (Fig. S4). The *TP53* mutants overexpressing *MYC* (cluster 4) formed a separate clade, while the *BRCA1*-deficient lineages PB2 and PB3 (cluster 3) formed a further two clades. Next, we grouped the various cell lines into the four PCA clusters and interrogated specific gene sets. Consistent with p53 proficiency, the p53 pathway gene set was positively enriched in the parental FNE1 group (cluster 1) versus the *TP53*-mutant lineages (clusters 2–4, Fig. 6B, S5). *MYC* target gene sets V1 and V2 were most highly positively enriched in cluster 4, i.e., the *TP53*-mutant samples overexpressing *MYC* (Fig. 6B, S5). *MYC* targets were also enriched in the PB2 and PB3 lineages (cluster 3), despite only two of the six lines harbouring ectopic *MYC*, demonstrating spontaneous upregulation of *MYC* targets in PB2 and PB3. E2F targets, G2/M checkpoint and mitotic spindle gene sets also stand out; in all three cases, parental FNE1 cells (cluster 1) display negative enrichment, which suggests attenuation of these genes' expression in a p53-proficient background. Consequently, as genetic manipulations are introduced, the enrichment score progressively increases (clusters 2–4; Fig. 6C, S5). Importantly, because cluster 2 cells showed significant increases in enrichment score versus parental FNE1 cells for E2F targets, MYC targets, G2/M checkpoint and mitotic spindle gene sets, these observations indicate that loss of p53 is sufficient to deregulate multiple aspects of cell cycle control (Fig. 6C, S5). Conversely, this reveals a surprising role for wildtype p53; in the absence of cellular stresses predicted to hyper-stabilize p53, basal levels of p53 appear to be, either directly or indirectly, repressing expression of genes governing a range of cell cycle controls.

TP53 loss deregulates expression profiles of DNA replication genes

As replication stress is an established CIN driver (Burrell et al., 2013; Tamura et al., 2020), we next asked whether evidence of replication stress manifested in the RNAseq data. Indeed, upregulation of DNA replication genes is an established mechanism to tolerate replication stress (Bianco et al., 2019). However, because the Hallmark collection does not contain a DNA replication gene set, we analysed the DNA replication gene sets from the Kyoto Encyclopedia of Genes and Genomes (KEGG) and Reactome collections. GSVA revealed that the DNA replication gene sets showed significant increases in enrichment score versus parental FNE1 cells (Fig. 6D). While the enrichment score remains negative for the *TP53*-mutants (cluster 2), it is significantly increased compared with parental FNE1 cells, indicating that p53 loss is perhaps sufficient to induce replication stress.

Taken together, our observations indicate that *TP53* mutation is sufficient to deregulate multiple cell cycle gene expression programmes and trigger transcriptional alterations consistent with a response to replication stress, and that these changes are exacerbated by mutation of *BRCA1* and overexpression of *MYC*. Coupled with the ploidy and karyotype analysis, these observations provide a plausible mechanism by which *TP53* loss is sufficient to initiate CIN in FNE1 cells.

p53-deficient mouse fallopian tube organoids display cell cycle deregulation

Our finding that *TP53* loss is sufficient to deregulate gene expression programmes governing cell cycle progression, DNA replication and mitosis was surprising. Therefore, we asked whether data from an independent model system supported our observation. Recently, a series of mouse fallopian tube organoids have been developed harbouring conditional alleles designed to inactivate *Trp53* and express an SV40 Large T antigen, which in turn suppresses Rb1 function. Utilising the publicly available RNAseq data, we analysed differentially expressed genes and performed GSEA analysis. PCA shows that the wildtype and mutant organoids form two distinct clusters, indicating divergent gene expression profiles (Fig. S6A), and unsupervised hierarchical clustering analysing E2F, G2/M and mitotic spindle-related genes clearly separated wildtype from mutant (Fig. S6B). Finally, we correlated the normalized enrichment scores for various gene sets in our human FNE1-derived *TP53*-deficient P cells with the mouse organoid samples. This showed that MYC targets, E2F targets, G2/M checkpoint genes and mitotic spindle genes were all positively correlated

in both samples. Thus, although the mouse organoids are deficient for both p53 and Rb1 function, the gene expression changes are mirrored in human FNE1 cells harbouring mutant *TP53*, further supporting our notion that p53 loss in human FNE1 cells is sufficient to drive profound transcriptional deregulation of cell cycle regulators.

TP53 loss confers tolerance to pharmacologically induced mitotic perturbation

Our observations show that in FNE1 cells, *TP53* mutation is sufficient to induce CIN, and that this is accompanied by deregulation of gene expression networks required to maintain chromosomal stability. As gene expression profiling only indirectly reflects cell function, we asked whether *TP53* mutation does indeed modulate the functionality of chromosome stability pathways. To do this, we challenged parental FNE1 cells and *TP53*-deficient P1 cells with GSK923295, an inhibitor of the mitotic kinesin CENP-E (henceforth CENP-Ei), and analysed the effects by time-lapse microscopy, using cell confluency as a proxy for proliferation. Note that pharmacological inhibition of CENP-E prevents congression of a small number of chromosomes, thus preventing satisfaction of the spindle assembly checkpoint (SAC), in turn inducing a mitotic arrest. Eventually, 'SAC exhaustion' results in anaphase onset and mitotic exit in the presence of polar chromosomes, leading to aneuploidy (Bennett et al., 2015; Wood et al., 2010).

In the absence of inhibitor, both populations proliferated and then reached a confluency plateau after 48 hours (Fig. 7A). Upon exposure to CENP-Ei, both parental FNE1 and P1 cells underwent mitotic arrest, evidenced by a static confluence during the first 12 hours and an increase in mitotic index (Fig. 7A,B). They eventually divided and flattened out, resulting in a confluence increase. Parental FNE1 cells failed to divide again, yielding a long second plateau and progressive decrease in mitotic index. By contrast, *TP53*-mutant P1 cells entered and exited a second mitosis, indicated by a short second plateau followed by sustained confluency increase and consistently increased mitotic index (Fig. 7A,B). To confirm this, we performed cell fate profiling, analysing 25 individual cell divisions and tracking the fate of the daughters. In the absence of CENP-Ei, cells in both populations completed multiple rounds of cell division (Fig. 7C). Upon exposure to CENP-Ei, both parental FNE1 and P1 cells underwent prolonged mitotic delays (Fig. 7C, compare the length of black bars), but, following eventual exit, while the parental FNE1 cells were then blocked in the subsequent interphase, the vast majority of the p53-deficient P1 cells entered second mitoses, indicating continued cell cycle progression.

Consistent with the interphase block, p53 was stabilised in parental FNE1 cells (Fig. 7D) and longer-term viability was diminished (Fig. 7E). Thus, we conclude that loss of *TP53* in FNE1 cells is sufficient to compromise the post-mitotic cell cycle blocks that would normally prevent proliferation of aneuploid daughter cells following a prolonged mitosis and chromosome mis-segregation event. While we have not analysed the effect of p53-loss on replication stress and G2/M checkpoint controls directly, these observations are consistent with the notion that *TP53* disruption is sufficient to compromise cell biological processes that would otherwise function to minimise CIN.

DISCUSSION

HGSOC is characterized by ubiquitous mutations in *TP53* and high levels of aneuploidy as a consequence of CIN (Cancer Genome Atlas Research, 2011; Ciriello et al., 2013). However, a genetic basis for CIN in HGSOC remains elusive. In this study, we set out to investigate whether the genetic alterations commonly observed in HGSOC are sufficient to drive CIN, in particular in the HRD group characterized by *BRCA1/2* mutation and *MYC* amplification (Wang et al., 2017). As HGSOC predominately originates from the fallopian tube, we generated a panel of CRISPR/Cas9-mutant, fallopian tube-derived subclones based on the *hTERT*-immortalized, non-transformed cell line FNE1 (Labidi-Galy et al., 2017; Merritt et al., 2013). We first showed that FNE1 cells mount a robust p53 response indicating pathway proficiency, in contrast to other model cell lines which rely on p53 suppression for immortalization (Fig. S1A,B) (Karst and Drapkin, 2012; Karst et al., 2011; Nakamura et al., 2018). Importantly, parental FNE1 p53 proficiency allowed us to directly test the impact of p53 loss of function alone, and in combination with BRCA1 deficiency and MYC overexpression, in an isogenic model system. Using this system, we find that p53 loss alone is sufficient to cause aneuploidy in FNE1 cells, which is exacerbated in the absence of functional BRCA1. Analysing the transcriptome revealed that cell cycle deregulation was apparent in *TP53* single mutants and amplified in *TP53*/*MYC* double mutants. The most highly enriched gene sets compared with the parental FNE1 cells were G2/M checkpoint, E2F targets, DNA replication and mitotic spindle, which were enriched in cells deficient for p53 alone and progressively more enriched with additional genetic manipulations. These findings, which were consistent with publicly available data from mutant mouse fallopian tube organoids (Fig. S6) (Zhang et al., 2019), therefore indicate that p53 loss alone results in transcriptional changes that can deregulate the cell cycle and promote low-level CIN. Since truncating mutations that lead to a loss-of-function only account for 35% of HGSOC (Cancer Genome Atlas Research, 2011), future work will require to look into other, missense and potential gain-of-function, *TP53* mutations in this context.

TP53 mutations have been firmly established as early and ubiquitous events in HGSOC development. However, the implications of *TP53* mutation on fallopian tube epithelial cells remain poorly understood and have thus been highlighted as key to understanding the development of HGSOC (Bowtell et al., 2015). Although p53 has been established as suppressor of proliferation in response to aneuploidy, mutations in *TP53* correlate consistently and most strongly with aneuploidy and WGD in multiple tumour types (Bielski et al.,

2018; Ciriello et al., 2013; Davoli et al., 2017; Taylor et al., 2018; Thompson and Compton, 2010; Zack et al., 2013). While evaluation of fallopian tube-derived models with suppressed p53 has previously suggested that additional p53-independent mechanisms act as barriers to proliferation of aneuploid cells, the same study found increased potential of transformation with p53 suppression in combination with pharmacologically induced aneuploidy in soft agar assays (Chui et al., 2019). Conflicting observations have also been reported regarding the relationship between p53 loss and the emergence of aneuploidy in studies utilizing colorectal cancer cell lines (Bunz et al., 2002; Simões-Sousa et al., 2018). Indeed, we observed an increase in structural and numerical aneuploidy by scWGS when comparing parental FNE1 with p53-deficient P1 cells. Although the magnitude of this change is moderate quantitatively, on a qualitative level it is evident that P1 cells harbour more whole chromosome or chromosome arm aneuploidies than parental FNE1 cells from two different passages (Fig. 5). Therefore, mounting evidence from us and others suggests that p53 loss alone may be sufficient to induce low levels of CIN, permitting cells to explore karyotypic heterogeneity. However, the importance of environmental factors such as O_2 levels has only recently been brought to light which might impact both chromosome segregation and the processes preceding mitosis as well as the selection of explorable karyotypes. It is conceivable that growth conditions at atmospheric O_2 levels may previously have masked the emergence of aneuploidy as euploid cells would outcompete aneuploid cells more rapidly than under normoxic or hypoxic conditions (Rutledge et al., 2016).

The development of isogenic, *bona fide* mutant cell lines allowed us to study mitotic perturbations side-by-side in p53-proficient and -deficient cells. HGSOC is appreciated as one of the most chromosomally unstable cancer entities based on *in silico* analyses of cancer genomes, which were backed up by cell biological studies of mitosis in HGSOC models (Nelson et al., 2020; Tamura et al., 2020). Primary cultures established from HGSOC patients' ascitic fluid can take more than six hours to complete mitosis in extreme cases, and up to 24 hours in select examples of individual cells (Nelson et al., 2020). This dramatically increased mitotic duration compared with non-transformed cells has been shown to be limited in a p53-dependent manner termed the 'mitotic timer'. Indeed, knock-out of *TP53* and its upstream regulators in this specific context, *USP28* and *53BP1*, rescued growth arrest following prolonged mitosis of up to six hours (Lambrus et al., 2016). Inhibiting the mitotic kinesin CENP-E pharmacologically, we could achieve a comparable increase in mitotic duration and were able to show that p53 was stabilized in response to CENP-E inhibition.

Furthermore, we show that P1 cells tolerate this stress better than parental FNE1 cells in short-term as well as long-term assays (Fig. 7). Thus, we show that p53 loss precipitates low levels of CIN and also partially rescues viability upon mitotic delay and chromosome mis-segregation; this dual- or potentially multi-functionality of p53 provides an explanation as to why one of the most chromosomally unstable tumour entities is characterized by ubiquitous *TP53* mutations.

Beyond mutations in *TP53*, mutations in *BRCA1/2* are the second most common mutation in HGSOC (12% of cases each). In genetically engineered mouse models of mammary epithelial cancer, deletion of exon 11 of *BRCA1* was shown to cause functional G2/M checkpoint disruption and tumorigenesis (Weaver et al., 2002; Xu et al., 1999). Based on these two observations, and the fact that human BRCA1-deficient fallopian tube-derived cell line models are lacking, we mutated *BRCA1* to create a model of more pronounced CIN and HRD. We found that our three cell lines deficient in full length BRCA1 are distinct from one another; based on the analysis of gene expression profiles by PCA and GSVA, PB1 clusters with P cells and PB2 and PB3 each form independent clusters. This distinction likely reflects biological heterogeneity following *BRCA1* mutagenesis that led to exacerbation of CIN. Indeed, PB1 cells are largely 2c, while PB2 cells harbour a 2c and 4c population and PB3 cells are 4c. Interrogation of our RNAseq data on the nucleotide level found that PB2 and PB3 have an identical exon 3 mutation, however, PB1 cells express a splice variant of exon 11 as a consequence of a mutation in the same exon, which is known to diminish PARPi sensitivity versus other BRCA1-mutants (Wang et al., 2016). Our findings are in agreement with this *BRCA1* variant having some functionality, as we find that, despite the absence of full-length *BRCA1*, its retained expression might be sufficient to protect against aneuploidy. As flow cytometric and miFISH evidence suggested aneuploidy, PB2 and PB3 were subjected to scWGS and indeed the extent of copy number heterogeneity observed exceeded that of P1 cells. Interestingly, we observed a propensity for WGD in both PB2 and PB3, despite *BRCA1* mutations not being reported to correlate with whole genome doubling (Bielski et al., 2018). This could reflect an *in vitro* selection pressure permitting the detection of 4c PB2 and PB3 cells in our system. Nevertheless, we conclude that the combination of p53- and BRCA1-deficiency can drive CIN in a context-dependent manner, where low levels of BRCA1 activity such as observed in PB1 remain protective.

Several non-genetic causes of CIN such as increased microtubule assembly rates, centrosome amplification and replication stress have been identified in colorectal cancer

and HGSOC cell lines (Bastians, 2015; Tamura et al., 2020). To try and decipher the causes of CIN in our mutant subclones we turned to analysis of transcriptomics, which enabled us to take an agnostic, genome-wide approach. We observed that loss of p53 alone resulted in an enrichment of gene sets comprised of genes regulating the cell cycle and DNA replication. We suggest that this effect is a consequence of the downregulation of canonical p53-targets such as *MDM2* and *CDKN1A*, which encodes the CDK inhibitor p21 (Fig. 4C). p21 plays an important role in suppressing S-phase entry by negatively regulating cyclin E and CDK2. The absence of this negative regulation thus permits cyclin E and CDK2 to hyperphosphorylate RB1 more rapidly, which results in de-sequestration of E2F, a key transcription factor controlling S-phase entry (Sullivan et al., 2018). Indeed, the E2F targets gene set is significantly less negatively enriched in P samples than in parental FNE1 samples (Fig. 6C). To contextualize, p21 has been shown to protect cells from CIN. In a genetically engineered mouse model of p53 separation-of-function, which was apoptosis-deficient but partially functional to suppress cell cycle progression, deletion of p21 led to an increase in CIN (Barboza et al., 2006). Moreover, three of the four sample groups showed significantly different and more positive enrichment scores in cell cycle related gene sets compared with parental FNE1 cells.

With the exception of the mitotic spindle gene set, overexpression of *MYC* consistently amplified the already observed enrichment in p53-deficient P samples, likely reflecting MYC's role as transcriptional amplifier (Lin et al., 2012; Nie et al., 2020; Nie et al., 2012). This held true also for the negative enrichment of the p53 pathway gene set where P samples displayed an already negative enrichment score that was even more negative in the PM samples (Fig. S5). In contrast to P samples, *MYC* overexpression did not seem to have the same impact on the transcriptome in PB2 and PB3 as it did in PM samples (Fig. 6A). In fact, PB2 and PB3 showed more positive enrichment of MYC targets V1 and V2 than P samples even without *MYC* overexpression; this is consistent, at least in PB3 samples, with higher endogenous *MYC* transcript levels (Table 1). Interestingly, the PB2M sample reaches the highest enrichment score of the PB2 lineage suggesting that ectopic MYC is active in this sample, but perhaps to a lesser extent than in PM samples. Consistent with our findings, proteogenomic analyses of HGSOC had suggested a causal role for the deregulation of mitotic and DNA replication genes in the high levels of CIN observed in this disease, however, the causes for this deregulation could not be definitively dissected in patient samples (McDermott et al., 2020). Taking these data into account, we suggest that CIN is caused by

the cumulative changes in cell cycle regulators' expression, rather than a single causative gene, as a consequence of, e.g., loss of p53-signalling through its downstream effector p21, which promotes transcriptional programs of cell cycle progression. Future work should focus on genetic add-back experiments of down-regulated *CDKN1A* (encodes p21) to investigate if this rescues the observed deregulated expression of cell cycle genes and low-level CIN.

In summary, we provide evidence, based on a novel human, fallopian tube-derived cell line panel that p53 loss leads to transcriptomic deregulation of cell cycle regulators, which is amplified by the overexpression of the oncogene *MYC*. We propose that the sum of these transcriptional changes causes CIN in HGSOC and show that P1 cells display low levels of aneuploidy. Furthermore, we show that additional genetic manipulation of *BRCA1* exacerbated both the enrichment of cell cycle regulators and aneuploidy. Finally, p53 loss increased tolerance of pharmacological perturbation of mitosis using an inhibitor of CENP-E, further supporting its potential role in the development of CIN in HGSOC. Our data point to the dual- or multi-functional role of p53 whereby its loss precipitates CIN by causing cell cycle and DNA replication deregulation while simultaneously also promoting the survival of aneuploid cells that experienced those stresses in the previous cell cycle.

MATERIALS AND METHODS

Details of critical commercial reagents and kits, drugs, antibodies, recombinant DNA, oligonucleotides, FISH probes and software are contained in Table S1.

Cell culture

FNE1 cells (a kind gift from Dr Tan A. Ince) were cultured in WIT-Fo Culture Media (FOMI) at 5% O_2 and 5% CO_2 at 37°C, as described previously (Merritt et al., 2013). AAV293T cells (ATCC) were cultured in DMEM supplemented with 10% FBS and 100 U ml^{-1} penicillin-streptomycin, at atmospheric O_2 and 5% CO_2 at 37°C. All cell lines were authenticated using the Promega Powerplex 21 System and regularly tested for Mycoplasma either by PCR (both at CRUK Manchester Institute Molecular Biology Core Facility) or the Lonza enzymatic test (Animal Molecular Diagnostics Laboratory at NCI Frederick, MD).

Lentiviruses were produced by co-transfection of AAV293T cells at 5×10^4 cells per well in a 24-well microplate with recombinant DNA at 0.375 µg lentivirus of interest, 0.5 µg psPAX2 and 0.125 µg pMD2.G (both kind gifts from Dr Didier Trono) using the Promega ProFection Mammalian Transfection System kit according to manufacturer instructions. Transfection media was replaced after overnight incubation and lentivirus was harvested every other day for four days. Supernatant containing lentivirus was centrifuged, filtered (0.45 µm) and frozen for storage at -80°C.

CRISPR/Cas9-expressing FNE1 cells were generated by transduction with Dharmacon Edit-R Inducible Lentiviral Cas9 particles followed by selection with blasticidin S at 8 µg ml^{-1}. Cas9 expression was assessed by titrating tetracycline and induced using 15 µg ml^{-1} in subsequent experiments. To mutate *TP53*, FNE1 cells expressing inducible Cas9 were transduced with lentiGuide-Puro (a kind gift from Dr Feng Zhang (Sanjana et al., 2014)) containing a guide RNA (gRNA) targeting *TP53* (Table S2) and selected in 0.7 µg ml^{-1} puromycin. Cas9 was then induced for five days before isolation of single-cell clones by limiting dilution (either immediately or following five days further selection in Nutlin-3). Taking P1 cells forward, cells were transduced with six different lentiGuide-Neo (see 'Molecular Biology' for details) lentiviruses each containing a unique gRNA targeting *BRCA1* (Table S2). After neomycin selection at 0.8 mg ml^{-1}, Cas9 was induced as above before isolation of single-cell derived subclones by limiting dilution. Clones were screened by immunoblotting (see 'Biochemistry' for details). Mutations in targeted genes were assessed in the RNA sequencing dataset using Integrative Genomics Viewer (Version 2.8.0) and annotated according to standard practices (Ogino et al., 2007; Robinson et al., 2011). Mutations in *BRCA1* in

PB1 and PB2 cells were confirmed using Sanger sequencing. *MYC* overexpressing and cognate 'E' cells were generated by transduction with pLenti CMV Hygro DEST or MYC lentiviruses (a kind gift from Drs Eric Campeau and Paul Kaufman (Campeau et al., 2009)) and selection with 25 µg ml^{-1} hygromycin, maintaining a polyclonal cell population. Immunoblotting and RNA sequencing were employed to confirm functionality of *MYC* overexpression. All lentiviral transductions were performed in 4 µg ml^{-1} polybrene.

Functional deficiency of p53 and BRCA1 in putative clones was confirmed by exploiting the known synthetic-viable and -lethal relationships with Nutlin-3 and PARPi treatment, respectively. Nutlin-3 assays were performed by seeding 30,000 cells (parental FNE1, P1 and P3 transduced with pLVX mCherry-H2B Puro) into Primaria 24-well microplates. The next day, either vehicle (DMSO) or 10 µM Nutlin-3 (Selleck Chem, TX) were added in phenol red-free media and the cells imaged for 96 hours on an IncuCyte® ZOOM (Satorius AG, Germany) time-lapse microscope housed in a low-oxygen incubator (5% O_2, 5% CO_2). IncuCyte® ZOOM custom software was used in real-time to measure confluency and red fluorescent object count and for data analysis. Population doubling for each culture was calculated by performing a log_2 transformation of the fold-change nuclear count from T_0 and plotted against time. PARPi (Olaparib, Selleck Chem, TX) sensitivity was assessed by seeding 100 cells directly into drug or vehicle containing media in collagen-coated, black 96-well microplates (Greiner Bio-One North America Inc., NC). Media and drug were replenished every three days. On day seven, 30 µl CellTiter-Blue® (Promega, WI) reagent were added to 150 µl of media and incubated for four hours followed by fluorescence signal measurement on a SpectraMax M2 plate reader (Molecular Devices, CA).

Assays studying the response to CENP-E inhibition were performed using GSK923295 (Selleck Chem, TX). For live-cell imaging, 30,000 cells were seeded into Primaria 24-well microtiter plates, allowed to adhere overnight, vehicle or drug (250 nM) were added the next day and imaging on an IncuCyte® ZOOM time-lapse microscope was performed as described above. Cell fate profiles were analysed manually based on exported MPEG-4 videos. Long-term viability assays were performed by seeding 2,000 cells into Primaria 6-well microtiter plates, allowing the cells to adhere overnight and adding vehicle or drug the next day. Drug washout was performed at indicated timepoints and media replenished every 36–48 hours. Experiments were concluded after 14 days, cells were washed, fixed with 1% formaldehyde (in PBS) and stained with crystal violet (0.05% in dH_2O).

Quantitation was achieved by extracting crystal violet with acetic acid and measuring absorbance on a SpectraMax M2 plate reader.

A summary of all cell lines generated is provided in Table 1 and Figure S2A.

Cell biology

Cells were harvested normally or *in situ*, lysed in sample buffer (0.35 M Tris pH 6.8, 0.1 g/ml sodium dodecyl sulphate, 93 mg/ml dithiothreitol, 30% glycerol, 50 mg/ml bromophenol blue) and boiled for five minutes. Proteins were resolved by SDS-PAGE and electroblotted by wet transfer onto Immobilion-P membranes (Millipore Sigma, MA). Membranes were blocked in 5% milk in TBS-T (50 mM Tris pH 7.6, 150 mM NaCl, 0.1% Tween-20) and incubated with primary antibodies at indicated concentrations (Table S1) overnight at 4°C. Membranes were then washed with TBS-T and incubated with horseradish-peroxidase-conjugated secondary antibodies (Table S1) for two hours at room temperature. After further washes with TBS-T, detection was performed using EZ-ECL Chemiluminescence Substrate (Biological Industries, Israel) or Luminata Forte Western HRP Substrate (Millipore Sigma, MA). Membranes were imaged on Biospectrum 500 (UVP, CA) imaging system.

For p53 immunofluorescence, parental FNE1 cells were seeded onto collagen-coated 19 mm coverslips, incubated overnight and treated with 10 μM Nutlin-3 for 8 hours. Cells were then washed with PBS, fixed (1% formaldehyde in PBS), quenched with glycine, permeabilized with PBS-T (PBS, 0.1% Triton X-100), incubated consecutively with primary (mouse anti-p53, DO-1, Santa Cruz Biotechnology, TX) and secondary (donkey anti-mouse conjugated with Cy3, Jackson ImmunoResearch Laboratories Inc., PA) antibodies for 30 minutes each with a wash step in between (Table S1). Coverslips were then washed with PBS-T, stained with Hoechst 33258 (Millipore Sigma, MA), washed with PBS-T and mounted onto slides (90% glycerol, 20 mM Tris, pH 9.2). Slides were imaged on an Axioskop2 microscope fitted with a 40× oil immersion objective (both from Zeiss Inc., Germany) and a CoolSNAP HQ camera (Photometrics, AZ) operated by MetaMorph software (Molecular Devices, CA). Image analysis was performed with Adobe Photoshop® CC 2015 (Adobe Systems Inc., CA). Microtiter plates were imaged after addition of PBS on Lionhart FX automated microscope fitted with a 40× objective operated by custom Gen5 (all BioTek, VT) software, which was also utilized for image analysis. RAD51 immunofluorescence was performed as described previously (Callen et al., 2020). Briefly, cells were seeded into a black 96-well microplate (Greiner Bio-One North America Inc., NC) coated with gelatine. Prior to γ-irradiation (5 Gy, ^{137}Cs Mark 1 irradiator, JL Shepherd, CA), cells were incubated with 10

683 μM EdU for 30 minutes. Four hours post-irradiation, cells were pre-extracted (20 mM
684 HEPES, 50 mM NaCl, 3 mM $MgCl_2$, 0.3 M sucrose, 0.2% Triton X-100) on ice for 5 minutes
685 to remove soluble nuclear proteins. Pre-extracted samples were fixed (4% paraformalde-
686 hyde in PBS), permeabilized (PBS, 0.5% Triton X-100), and incubated with anti-RAD51 an-
687 tibody (rabbit anti-RAD51, 1:250, Abcam). Detection of RAD51 and EdU was accomplished
688 by incubating samples with Alexa Fluor 568-conjugated secondary antibodies (goat anti-
689 rabbit, Thermo Fisher Scientific, MA) followed by a click-IT reaction as per manufacturer's
690 instructions (Thermo Fisher Scientific, MA). Finally, DNA was counterstained with DAPI
691 (Thermo Fisher Scientific, MA). Microtiter plates were imaged at 40× magnification on a
692 Lionheart LX automated microscope (BioTek Instruments, Inc.). Quantification of nuclear
693 RAD51 foci was performed using the Gen5 spot analysis software (BioTek Instruments,
694 Inc.).

695 **Molecular biology**

696 pLenti CMV Hygro DEST (w117-1) was digested with SalI and BamHI (New England Bi-
697 oLabs Inc., MA) according to manufacturer instructions. *MYC* cDNA was PCR-amplified
698 from pcDNA5 FRT/TO CR MYC and cloned into pLenti CMV Hygro DEST, creating pLenti
699 CMV Hygro MYC (Littler et al., 2019). pLVX mCherry N1 (Clonetech Laboratories Inc., CA)
700 was digested with XhoI and BamHI (New England BioLabs Inc., MA) according to manufac-
701 turer instructions. H2B cDNA was PCR-amplified from pcDNA5 FRT/TO GFP-H2B and
702 cloned into pLVX mCherry N1, creating pLVX mCherry-H2B Puro (Morrow et al., 2005).
703 Gibson Assembly was utilized to create lentiGuide Neo. Briefly, lentiGuide Puro was PCR-
704 amplified, omitting the puromycin-resistance cassette. Separately, the neomycin-resistance
705 cassette was PCR-amplified from pLXV MYC-mCherry Neo. Fragments were then assem-
706 bled into lentiGuide Neo using Gibson Assembly Master Mix (New England BioLabs Inc.,
707 MA) according to manufacturer instructions. gRNAs were introduced into lentiGuide
708 Puro/Neo by ligating the annealed forward and reverse oligonucleotides into BsmBI-di-
709 gested target vectors (Sanjana et al., 2014). All recombinant vectors were grown in XL1-
710 Blue competent cells and extracted using QIAprep Spin Miniprep kit (Qiagen, Germany)
711 according to manufacturer instructions. Oligonucleotide sequences are described in Table
712 S2. Recombinant vectors were validated functionally *in vitro* or by Sanger sequencing.

713 **Molecular cytogenetics**

714 For SKY, cells were cultured as normal and incubated in 100 ng ml^{-1} Colcemid (Roche, MA)
715 for 2 hours prior to harvest. Subsequently, for SKY and miFISH, cells were harvested,

swelled in hypotonic buffer (0.075 M KCl) for 30 minutes at 37°C, fixed in methanol/acetic acid (3:1) in three wash steps, dropped onto glass slides and aged for 2 weeks at 37°C. Four probe panels containing five probes each were assembled totalling one centromere probe (CCP10) and 19 gene probes (all custom ordered from CytoTest, MD): *COX2* (1q31.1), *PIK3CA* (3q26.32), *FBXW7* (4q31.3), *CCNB1* (5q13.2), *DBC2* (8p21.3), *MYC* (8q24.21), *CDKN2A* (9p21.3), *PTEN* (10q23.31), *CCND1* (11q13.3), *KRAS* (12p12.1), *RB1* (13.14.2), *CDH1* (16q22.1), *TP53* (17p13.1), *NF1* (17q11.2), *HER2* (17q12), *SMAD4* (18q21.2), *CCNE1* (19q12), *ZNF217* (20q13.2) and *NF2* (22q12.2). Images were taken on an automated fluorescence microscope fitted with a 40× oil immersion objective (BX63, Olympus, Japan), custom optical filters (Chroma, VT) and a motorized stage. Custom software was used for operation and analysis (BioView, Israel). A total of 100 nuclei were analysed per sample for miFISH and 15 metaphases were analysed per sample for SKY. Procedures pertaining to SKY and miFISH hybridization, stripping and rehybridization were as described previously (Heselmeyer-Haddad et al., 2012; Padilla-Nash et al., 2006; Wangsa et al., 2018).

Next generation sequencing

RNA was extracted from logarithmically growing cells *in situ* using the RNeasy Plus Mini kit (Qiagen, Germany) according to manufacturer instructions. RNA integrity and quality were assessed using a 2200 TapeStation (Agilent Technologies, CA; performed by the CCR Genomics Core, Bethesda, MD). Libraries were prepared using Illumina TruSeq® Stranded mRNA Library Prep (Illumina Inc., CA), pooled and paired-end sequenced on Illumina NovaSeq using an SP flow cell according to manufacturer instructions (Sequencing Facility at NCI Frederick, MD). Samples returned 37 to 51 million pass filter reads with more than 91% of bases above the quality score of Q30.

scWGS was performed on single cells sorted for a 2c (parental FNE1, P1) or 4c (PB3, PB3E, PB3M) genome content (for PB2, PB2E and PB2M 12 cells from each population were included) as described previously (Bakker et al., 2016; Nelson et al., 2020; van den Bos et al., 2016).

Bioinformatics

For RNA sequencing, sample reads were processed using the CCBR Pipeliner utility (https://github.com/CCBR/Pipeliner). Briefly, reads were trimmed for adapters and low-quality bases using Cutadapt (version 1.18) (http://gensoft.pasteur.fr/docs/cutadapt/1.18) before alignment to the human reference genome (hg38/Dec. 2013/GRCh38) from the UCSC

browser and the transcripts annotated using STAR v2.4.2a in 2-pass mode (Dobin et al., 2013; Martin, 2011). Expression levels were quantified using RSEM (version 1.3.0) (Li and Dewey, 2011) with GENCODE annotation version 30 (Harrow et al., 2012). The same approach was used for mouse model data downloaded from Gene Expression Omnibus (GEO, accession number GSE125016), with alignment to the mouse reference genome (mm10).

Raw read counts (expected counts from RSEM) were imported to the NIH Integrated Data Analysis Platform for downstream analysis. Low count genes (counts-per-million [CPM] <0.5), ≥ three samples were filtered prior to the analysis. Counts were normalized to library size as CPM and the voom algorithm (Law et al., 2014) from the Limma R package (version 3.40.6) (Smyth, 2004) was used for quantile normalization (Tables S4 and S7). Batch correction was performed prior to analysis using the ComBat function in the sva package (Johnson et al., 2007). Differentially expressed genes (DEG) using Limma and pre-ranked gene set enrichment analysis (GSEA) were computed between each genotype using the molecular signatures database (Liberzon et al., 2011; Subramanian et al., 2005). And gene set variation analysis (GSVA) was performed using the GSVA package (Hänzelmann et al., 2013). Genes or gene sets with an adjusted p-value ≤0.05 were considered statistically significant. Preparation of heatmaps was performed in R Studio (Subramanian et al., 2005).

Analysis of copy-number changes based on scWGS was executed according to previous reports (Bakker et al., 2016; Nelson et al., 2020; van den Bos et al., 2016).

Quantification and statistical analysis

Prism 8 (GraphPad, CA) was used to generate graphs and perform statistical analyses. RStudio (R Project for Statistical Computing) was used to perform sequencing analyses and generate heatmaps (R packages Complex Heatmaps and AneuFinder) and volcano plots (R package Enhanced Volcano).

ACKNOWLEDGEMENTS

We thank members of the Ried and Taylor laboratories for advice. We thank the following facilities: Molecular Biology Core, Imaging and Flow Cytometry Core (both Cancer Research UK Manchester Institute), OSTR Sequencing, Animal Diagnostics Laboratory (both NCI at Frederick, MD), CCR Genomics Core and Laboratory of Genome Integrity Flow Cytometry Core (both NCI at Bethesda, MD).

COMPETING INTERESTS

We report no competing interests.

FUNDING

DB was supported by a Wellcome Trust-NIH PhD Studentship (200932/Z/16/Z) and the NIH-OxCam program. DH was supported by a Mildred Scheel postdoctoral fellowship from the Deutsche Krebshilfe. This study was in part supported by the intramural research program of the National Institutes of Health, the National Cancer Institute. This study was also in part supported by a Cancer Research UK Program grant to SST (C1422/A19842) and a Cancer Research UK Centre Award (C5759/A25254).

DATA AVAILABILITY

Next generation sequencing data will be made available without restriction through GEO or the EMBL-EBI's repository upon publication in accordance with the journal's publishing policy.

AUTHOR CONTRIBUTIONS STATEMENT

All experiments and analyses were performed by DB except for the following: Fig. S1C and Fig. 5 were performed by RW, DS and supervised by FF; Fig. S1D was performed by DW; Fig. 2D was performed in part by DZ and supervised by AN; Fig. 2E, 3A,C,D, 6, S2B, S4, S5 and S6 were performed with help from TJM and supervised by MC. All other authors provided reagents and/or technical support. TR and SST provided additional funding and supervision. DB interpreted the data and wrote this manuscript, both with support from JM, TR and SST. All authors read the manuscript and provided feedback.

Table 1. Summary of mutant cell lines generated in this study including mutation status and *MYC* RNA levels.

Cell line	*TP53*			*BRCA1*					*MYC* RNA§		
	Nucleotide sequence	Protein sequence	Full length protein expression	Nucleotide sequence	Protein sequence	Full length protein expression	HRP/D	PARPi	4 Sites End	4 Sites Ect	CPM
FNE1	WT	WT	Pres	WT	WT	Pres*	HRP†	-	149	0	6.11
P1	r.40_44delCTGAG	p.Leu14Serfs*12	Abs	WT	WT	Pres	HRP	Res	127	0	6.06
PE1								-	133	0	6.16
PM1								-	54	307	8.37
P2	r.40_41delCT	p.Leu14Glufs*13	Abs*	WT	WT	Pres*	HRP‡	-	176	0	6.26
PE2								-	119	0	6.05
PM2								-	85.4	321	8.42
P3	r.40_41delCT	p.Leu14Glufs*13	Abs	WT	WT	Pres*	HRP‡	-	123	0	6.46
PE3								-	167	0	6.35
PM3								-	32	154	8.33
PB1	r.40_44delCTGAG	p.Leu14Serfs*12	Abs	c.4038_4039insA	p.Glu1346Glufs*10	Abs	HRD‡	Sen	120	0	6.32
PBE1								-	174	0	6.39
PBM1								-	47.2	202	8.02
PB2	r.40_44delCTGAG	p.Leu14Serfs*12	Abs	c.90_91insA	p.Ile31Asnfs*10	Abs	HRD	Sen	143	0	6.53
PBE2								-	157	0	6.23
PBM2								-	180	159	7.53
PB3	r.40_44delCTGAG	p.Leu14Serfs*12	Abs	r.90_91insA	p.Ile31Asnfs*10	Abs	HRD‡	Sen	308	0	7.17
PBE3								-	396	0	7.13
PBM3								-	184	30	7.25

Mutation status detected by RNA sequencing for *TP53* and Sanger sequencing for *BRCA1*. *Assumed based on nucleotide/protein sequence (immunoblot not completed). †Shown by Tamura et al. (2020). ‡Assumed based on overall clone characteristics (RAD51 assay not completed). §Normalized RNAseq read counts are mean values across four sites with synonymous mutations in ectopic *MYC* (colour/shading indicates relative expression whereby white is lower and purple is higher). Where RNAseq was done in triplicate (parental FNE1, P1, P1E and P1M) the mean across the three replicates is given. CPM=counts-per-million reads mapped; Pres=Present; Abs=Absent; HRP=Homologous recombination proficient; HRD=Homologous recombination deficient; Res=Resistant; Sen=Sensitive.

LEGENDS

Figure 1: Intellectual Framework and Experimental Strategy

A Schematic of modelled high-grade serous ovarian cancer (HGSOC) development from the fallopian tube secretory epithelium including ubiquitous *TP53* mutation, grouping based on foldback inversions (FBI) or homologous recombination deficiency (HRD) and associated genomic changes in key tumour suppressors and oncogenes (Wang et al., 2017).

B Experimental approach using *hTERT*-immortalized, fallopian tube-derived FNE1 cells to generate tet-inducible Cas9-expressing cells, which were then mutagenized to generate isogenic p53-deficient (P), p53/BRCA1-deficient (PB) and MYC-overexpressing double- (PM) and triple-(PBM) mutant subclones. MYC-overexpressing cells are co-isogenic, polyclonal populations of the parental subclones. Single- (PE) and double-mutant (PBE) control cells were also generated via transduction with an '*empty'* virus vector. See also Figure S2A.

Figure 2: Generation and Functional Validation of *TP53* and *TP53/BRCA1*-mutant Subclones

A Representative immunoblot of p53 expression in CRISPR/Cas9-derived *TP53*-mutant (P1) cells and parental FNE1 cells treated with either DMSO (vehicle) or Nutlin-3. TAO1 serves as loading control.

B Nuclear proliferation curves of parental FNE1 and P1 cells expressing an mCherry-tagged histone in the presence of DMSO or Nutlin-3. Normalised red object count (ROC) was calculated as fold change from T_0. Results from three technical replicates are shown as mean with error bars indicating standard deviation.

C Representative immunoblot of full-length BRCA1 expression in CRISPR/Cas9-derived *TP53/BRCA1* double-mutant (PB2) cells. Here, P1 reflects a BRCA1-proficient (p53-deficient) subclone recovered after Cas9 induction. TAO1 serves as loading control.

D Left panel, Quantitation of RAD51 foci formation in EdU-positive *TP53*-mutant (P1; 111 nuclei) and *TP53*/*BRCA1* double-mutant (PB2; 114 nuclei) cells following 5 Gy ionizing radiation. Results from single experiment are shown. Statistical analysis was performed using a student's t-test. Right panel, CellTiter-Blue® viability assay of P1 and PB1–3 cells treated with indicated concentrations of the PARPi olaparib over the course of one week. Viability was normalized to DMSO (vehicle)-treated cells. Results from three technical replicates, error bars represent standard deviation.

E Representative Sashimi plot depicting alternative splicing of *BRCA1* exon 11 observed in P1 and PB1 subclones. Numbers indicate raw junction reads attesting to the splice events indicated by the arcs. The minimum of splice junction reads was three. Note that junction reads mapping 3' terminally of exon 11 and 5' terminally of exon 12 in PB1 are not detected in PB1. See also Figures S1, S2 and Table 1.

Figure 3: Generation and Functional Validation of *MYC*-overexpressing *TP53*-mutant and *TP53/BRCA1*-mutant Subclones

A Normalized read count of endogenous (circle) and ectopic (triangle) *MYC* RNA was determined by interrogating RNA sequencing data at the nucleotide level. Read counts at four sites of synonymous mutations in ectopic *MYC* were enumerated, with each mutation site reflected by one of the four circles/triangles per cell line in the graph. Reads were normalized to uniquely mapped reads. P1M was sequenced in triplicate thus the average of the three replicates is plotted for each locus. Note, endogenous *MYC* levels may be elevated in PB2M and PB3M relative to other samples (see results text).

B Representative immunoblot of P1 cells transduced with empty vector (EV) or MYC-overexpressing (MYC) lentiviruses showing MYC and BCL-XL expression. TAO1 serves as loading control.

C Volcano plots showing differentially expressed genes in P (pooled P1–3 and P1–3E) and PM (pooled P1–3M) samples, compared with parental FNE1 samples. Each point reflects a single gene where blue indicates differential down-regulation and red indicates differential up-regulation. Black means that the significance threshold of adj. p-value ≤0.05 was not reached. The canonical p53 target genes *CDKN1A* and *MDM2* as well as *MYC* are indicated. The number of differentially down- and up-regulated genes is shown in blue and red font, respectively.

D Enrichment of Hallmark MYC Targets V1 and V2 comparing PM (pooled P1–3M) with P (pooled P1–3 and P1–3E). Black font indicates normalized enrichment score, and grey font indicates adj. p-value.

The adj. p-value for differentially expressed genes in C–D was determined using the Benjamini-Hochberg algorithm. Results are from a single experiment with pooled clones as described (with the exception of parental FNE1, P1, P1E and P1M, for which 3 technical replicates are included). P=*TP53*-mutant; B=*BRCA1*-mutant; E=Empty vector lentivirus; M=*MYC*-overexpressing lentivirus. See also Figure S2 and Table 1.

Figure 4: miFISH Implicates On-Going Chromosomal Instability, Aneuploidy and Whole Genome Doubling in Two Triple Mutant Subclones

A–B Representative composite multiplex, interphase fluorescence *in situ* hybridization (miFISH) images of all 20 probes hybridized in succession on parental FNE1 and PB2M cells, respectively. Note the reduced signal count of *COX2* and *RB1* in PB2M versus parental FNE1.

C Copy number aberrations of centromere 10 (CCP10) and 19 indicated gene loci in parental FNE1 and the two aneuploid triple-mutant subclones assessed by miFISH. Blue and red indicate copy number loss and gain, respectively, relative to the diploid, parental FNE1. Columns indicate single cells (n=100, each for parental FNE1, PB1M and PB3M). P=*TP53*-mutant; B=*BRCA1*-mutant; M=*MYC*-overexpressing lentivirus. See also Figure S3.

Figure 5: Single-cell Shallow-depth Whole-genome Sequencing Finds Ongoing CIN and Whole-Genome Doubling in Mutant Subclones

A Single cells from indicated genetic backgrounds were subjected to scWGS and subsequent unsupervised hierarchical clustering analysis, which first clusters cells by ploidy and then in a genotype-dependent manner. Autosomes from 1–22 and the X chromosome are displayed as columns. Each row represents a single cell of indicated genetic background (middle box). The colour in each row at a defined genomic location indicates the copy number (top box). Note FNE1_2 is a reproduction of data from Fig. S1C.

B Aneuploidy, structural and heterogeneity scores were calculated from scWGS data in A. The structural score is defined as the number of copy number state transitions (within a single chromosome) per Mb, normalized to the number of cells analysed. Generation of the heterogeneity and aneuploidy scores are described previously (Bakker et al., 2016). Based on structural and aneuploidy scores samples separate into a diploid and tetraploid cluster. Note, one of the parental FNE1 samples contained a tetraploid cell (FNE1_1), which resulted in an increase in all three scores, which was reduced if the scores were recalculated omitting that cell (dotted arrow).

Figure 6: Transcriptome Profiling Reveals Cell Cycle Deregulation Upon p53 Loss

A Principal component analysis (PCA) of 27 cell lines analysed by RNA sequencing separates parental FNE1 samples from mutant subclones and BRCA1-deficient subclones from

those with fully or partially functioning BRCA1. Indicated colours correspond to sample genotype. Dotted lines capture four clusters defined by similarity of transcriptomes that broadly follow sample genotype with the exception of PB1 and PB1E/M (see text). Samples derived from the PB3 lineage are depicted as squares. Percent variance of principle components 1 (PC1) and 2 (PC2) are indicated in parenthesis along axes. See corresponding Table S3 for input data.

B Gene set variation analysis (GSVA) was performed on samples grouped according to each of the four distinct PCA clusters and the mean was used to perform unsupervised hierarchical clustering. The 50 Hallmark gene sets are indicated, and the enrichment score (ES) is depicted in blue or red for negative or positive enrichment, respectively. See also Figure S4 and Table S4.

C–D Results from two representative Hallmark gene sets from B, and the DNA replication gene sets from the KEGG and Reactome collections are shown. Samples were grouped based on PCA cluster allocation and the colour of individual data points corresponds to sample genotype as in A. Samples derived from the PB3 lineage are depicted as squares. For cluster 1 (FNE1): n=3 samples; cluster 2 (P): n=12; and clusters 3 and 4 (PB and PM): n=6. Horizontal bar and error bars indicate mean and standard deviation, respectively. Asterisks depict adj. p-value between indicated groups compared with cluster 1 (FNE1) by Brown-Forsythe and Welsh ANOVA where * adj. p-value ≤ 0.05, ** adj. p-value ≤ 0.005, *** adj. p-value ≤ 0.0005, **** adj. p-value < 0.0001. See Figure S5 and Table S5.

P=*TP53*-mutant; B=*BRCA1*-mutant; E=empty vector lentivirus; M=*MYC*-overexpressing lentivirus.

Figure 7: p53 Loss Alone Permits Pharmacologically Induced CIN

A Confluence curves of parental FNE1 and *TP53*-mutant (P1) cells in the presence of DMSO (vehicle) or CENP-Ei (GSK923295). Confluence was normalized to T_0 by subtraction. Arrow indicates mitotic arrest. Representative results from three technical replicates of at least three independent experiments are shown. Error bars represent standard deviation.

B Mitotic index was profiled in parental FNE1 and P1 cells in the presence of DMSO or CENP-Ei at indicated time points. Results shown are from three fields of view from three technical replicates shown in A.

C Cell fate profiling by time-lapse microscopy of parental FNE1 and P1 cells in the presence of DMSO or CENP-Ei. 25 cells and both daughters of the first mitosis were profiled per condition.

D Immunoblot of p53 expression in parental FNE1 cells treated with DMSO or CENP-Ei for 24 and 48 hours. TAO1 serves as loading control.

E Crystal violet-based viability assay of parental FNE1 and P1 cells treated with DMSO or CENP-Ei for indicated time period followed by drug washout. Experiment was concluded 14 days after drug addition and viability was normalized to DMSO-treated cells. Two independent experiments are shown for the 24- and 72-hour washouts and three for 0- and 48-hour washouts. Error bars represent standard deviation.

Figure S1: FNE1 Characterization

A Immunofluorescence imaging of DMSO (vehicle) and Nutlin-3-treated parental FNE1 cells shows stabilization of p53 in response to Nutlin-3. Representative images from one of three experiments. Scale bars, 10 µm.

B Immunoblot of cells treated with Nutlin-3 over a time course of 8 hours to analyse p53 and p21 expression. TAO1 serves as loading control.

C Shallow-depth whole-genome sequencing analysis of copy number aberrations in single parental FNE1 cells (rows) where columns reflect chromosomes 1–22 and X. Colour indicates detected copy number level (box).

D Spectral karyotyping image of a representative metaphase spread shows a near-diploid genome with loss of chromosomes 15 and X and translocation between 9p and 15q (red boxes).

E Immunoblot of tet-inducible Cas9 expression in parental FNE1 cells after transduction with Edit-R Inducible Lentiviral Cas9 and selection. Subsequent experiments utilized 15 µg ml^{-1} tet for Cas9 induction. TAO1 serves as loading control. Tet= µg ml^{-1} tetracycline.

Figure S2: Pedigree of Mutant Subclones and *TP53* Locus Mutation

A Pedigree of FNE1 cells and sequentially CRISPR/Cas9-mediated genome-engineered subclones with introduction of MYC overexpression or empty lentiviral construct.

B Coverage of RNA sequencing reads of *TP53* exon 2 in indicated subclones. Deletion of 2–5 nucleotides in the three mutagenized subclones is shown, resulting in a downstream premature termination codon.

P=*TP53*-mutant; B=*BRCA1*-mutant; E=empty vector lentivirus; M=*MYC*-overexpressing lentivirus.

Figure S3: Genome Content of PB2 and PB3 Clones Suggests Aneuploidy

Flow cytometric analysis of genome content in control (empty vector) and MYC overexpressing cells of the same genotype. 2c, 4c and 8c correspond to a diploid, tetraploid and octoploid genome.

P=*TP53*-mutant; B=*BRCA1*-mutant; E=empty vector lentivirus; M=*MYC*-overexpressing lentivirus.

Figure S4: Gene Set Variation Analysis Separates Parental and Mutant Samples

Unsupervised hierarchical clustering of 27 cell lines based on enrichment scores calculated for Hallmark gene sets by gene set variation analysis (GSVA) from RNAseq. The top row indicates the PCA cluster of the respective sample, see Fig. 7A. Orange and blue shading indicate positive and negative enrichment scores, respectively.

Figure S5: Gene Set Variation Analysis Corroborates Genotypic Transcriptomic Features

Results from four representative Hallmark gene sets from Fig. 6B are shown. Samples were grouped based on PCA cluster allocation and the colour of individual data points corresponds to sample genotype as in Fig. 6A. For cluster 1 (FNE1): n=3 samples; cluster 2 (P): n=12; and clusters 3 and 4 (PB and PM): n=6. Note PB1 and PB1E/M samples are included in clusters 2 and 4, respectively, rather than 3 (see text). Samples from the PB3 lineage are depicted as squares. Horizontal bar and error bars indicate mean and standard deviation, respectively. Asterisks depict adj. p-value between indicated groups compared with cluster 1 (FNE1) by Brown-Forsythe and Welsh ANOVA where * adj. p-value ≤ 0.05, ** adj. p-value ≤ 0.005, *** adj. p-value ≤ 0.0005, **** adj. p-value < 0.0001. See Table S5.

Figure S6: Differential Expression of Cell Cycle Regulators in *TP53*-mutant Mouse Fallopian Tube Organoids Correlates with that of Human *TP53*-mutant Fallopian Tube-derived Subclones

A Principal component analysis (PCA) of publicly available RNA sequencing data from eight murine wildtype (Wt) and *Trp53*-mutant (Mut) organoids (Zhang et al., 2019). Percent

variance of principle components 1 (PC1) and 2 (PC2) are indicated in parenthesis along axes. See also Table S6.

B Unsupervised hierarchical clustering based on the expression of 468 cell cycle regulators in the eight available mouse organoid samples. See also Table S7.

C Correlation of positively and negatively enriched gene sets when *TP53* is mutated in our human FNE1 model and the *Trp53*-mutant mouse organoids versus corresponding control cells. The size and the colour of the bubbles indicate significance in the mouse and human contrasts with wildtype, respectively. NES=normalized enrichment score.

Table S1

Summary of reagents and critical commercial kits, experimental models and software.

Table S2

Summary of oligonucleotides used in this study. Blue font indicates gRNA sequence.

Table S3

Filtered, quantile normalized, batch corrected, Log_2 transformed RNA sequencing reads for cell line samples used as basis for all human RNA sequencing analyses downstream used to generate Fig. 7.

Table S4

Mean enrichment scores for Hallmark gene sets calculated by gene set variation analysis of parental FNE1, P, PB and PM samples used to generate Fig. 7B.

Table S5

Enrichment scores calculated in gene set variation analysis (GSVA) of all samples used to generate data in Table S4, Fig. 7B,C, S4, S5.

Table S6

Filtered, quantile normalized, batch corrected, Log_2 transformed RNA sequencing reads for organoid samples used as basis for all mouse RNA sequencing analyses downstream used to generate Fig. S6.

Table S7

Z-scores calculated sample-wise for mouse organoid samples used to generate Fig. S6B.

REFERENCES

Ahmed, A.A., Etemadmoghadam, D., Temple, J., Lynch, A.G., Riad, M., Sharma, R., Stewart, C., Fereday, S., Caldas, C., Defazio, A.*, et al.* (2010). Driver mutations in TP53 are ubiquitous in high grade serous carcinoma of the ovary. J Pathol *221*, 49-56.

Bakker, B., Taudt, A., Belderbos, M.E., Porubsky, D., Spierings, D.C., de Jong, T.V., Halsema, N., Kazemier, H.G., Hoekstra-Wakker, K., Bradley, A.*, et al.* (2016). Single-cell sequencing reveals karyotype heterogeneity in murine and human malignancies. Genome Biol *17*, 115.

Barboza, J.A., Liu, G., Ju, Z., El-Naggar, A.K., and Lozano, G. (2006). p21 delays tumor onset by preservation of chromosomal stability. Proc Natl Acad Sci U S A *103*, 19842-19847.

Bastians, H. (2015). Causes of Chromosomal Instability. Recent Results Cancer Res *200*, 95-113.

Bennett, A., Bechi, B., Tighe, A., Thompson, S., Procter, D.J., and Taylor, S.S. (2015). Cenp-E inhibitor GSK923295: Novel synthetic route and use as a tool to generate aneuploidy. Oncotarget *6*, 20921-20932.

Bianco, J.N., Bergoglio, V., Lin, Y.L., Pillaire, M.J., Schmitz, A.L., Gilhodes, J., Lusque, A., Mazieres, J., Lacroix-Triki, M., Roumeliotis, T.I.*, et al.* (2019). Overexpression of Claspin and Timeless protects cancer cells from replication stress in a checkpoint-independent manner. Nat Commun *10*, 910.

Bielski, C.M., Zehir, A., Penson, A.V., Donoghue, M.T.A., Chatila, W., Armenia, J., Chang, M.T., Schram, A.M., Jonsson, P., Bandlamudi, C.*, et al.* (2018). Genome doubling shapes the evolution and prognosis of advanced cancers. Nat Genet *50*, 1189-1195.

Bowtell, D.D., Bohm, S., Ahmed, A.A., Aspuria, P.J., Bast, R.C., Jr., Beral, V., Berek, J.S., Birrer, M.J., Blagden, S., Bookman, M.A.*, et al.* (2015). Rethinking ovarian cancer II: reducing mortality from high-grade serous ovarian cancer. Nat Rev Cancer *15*, 668-679.

Bunz, F., Fauth, C., Speicher, M.R., Dutriaux, A., Sedivy, J.M., Kinzler, K.W., Vogelstein, B., and Lengauer, C. (2002). Targeted inactivation of p53 in human cells does not result in aneuploidy. Cancer Res *62*, 1129-1133.

Burrell, R.A., McClelland, S.E., Endesfelder, D., Groth, P., Weller, M.C., Shaikh, N., Domingo, E., Kanu, N., Dewhurst, S.M., Gronroos, E.*, et al.* (2013). Replication stress links structural and numerical cancer chromosomal instability. Nature *494*, 492-496.

Callen, E., Zong, D., Wu, W., Wong, N., Stanlie, A., Ishikawa, M., Pavani, R., Dumitrache, L.C., Byrum, A.K., Mendez-Dorantes, C.*, et al.* (2020). 53BP1 Enforces Distinct Pre- and Post-resection Blocks on Homologous Recombination. Mol Cell *77*, 26-38 e27.

Campeau, E., Ruhl, V.E., Rodier, F., Smith, C.L., Rahmberg, B.L., Fuss, J.O., Campisi, J., Yaswen, P., Cooper, P.K., and Kaufman, P.D. (2009). A versatile viral system for expression and depletion of proteins in mammalian cells. PLoS One *4*, e6529.

Cancer Genome Atlas Research, N. (2011). Integrated genomic analyses of ovarian carcinoma. Nature *474*, 609-615.

Chui, M.H., Doodnauth, S.A., Erdmann, N., Tiedemann, R.E., Sircoulomb, F., Drapkin, R., Shaw, P., and Rottapel, R. (2019). Chromosomal Instability and mTORC1 Activation through PTEN Loss Contribute to Proteotoxic Stress in Ovarian Carcinoma. Cancer Res *79*, 5536-5549.

Ciriello, G., Miller, M.L., Aksoy, B.A., Senbabaoglu, Y., Schultz, N., and Sander, C. (2013). Emerging landscape of oncogenic signatures across human cancers. Nat Genet *45*, 1127-1133.

Davoli, T., Uno, H., Wooten, E.C., and Elledge, S.J. (2017). Tumor aneuploidy correlates with markers of immune evasion and with reduced response to immunotherapy. Science *355*.

Dobin, A., Davis, C.A., Schlesinger, F., Drenkow, J., Zaleski, C., Jha, S., Batut, P., Chaisson, M., and Gingeras, T.R. (2013). STAR: ultrafast universal RNA-seq aligner. Bioinformatics *29*, 15-21.

Ducie, J., Dao, F., Considine, M., Olvera, N., Shaw, P.A., Kurman, R.J., Shih, I.M., Soslow, R.A., Cope, L., and Levine, D.A. (2017). Molecular analysis of high-grade serous ovarian carcinoma with and without associated serous tubal intra-epithelial carcinoma. Nat Commun *8*, 990.

Hänzelmann, S., Castelo, R., and Guinney, J. (2013). GSVA: gene set variation analysis for microarray and RNA-seq data. BMC Bioinformatics *14*, 7.

Harrow, J., Frankish, A., Gonzalez, J.M., Tapanari, E., Diekhans, M., Kokocinski, F., Aken, B.L., Barrell, D., Zadissa, A., Searle, S.*, et al.* (2012). GENCODE: the reference human genome annotation for The ENCODE Project. Genome Res *22*, 1760-1774.

Heselmeyer-Haddad, K., Berroa Garcia, L.Y., Bradley, A., Ortiz-Melendez, C., Lee, W.J., Christensen, R., Prindiville, S.A., Calzone, K.A., Soballe, P.W., Hu, Y.*, et al.* (2012). Single-cell genetic analysis of ductal carcinoma in situ and invasive breast cancer reveals enormous tumor heterogeneity yet conserved genomic imbalances and gain of MYC during progression. Am J Pathol *181*, 1807-1822.

Huschtscha, L.I., and Reddel, R.R. (1999). p16(INK4a) and the control of cellular proliferative life span. Carcinogenesis *20*, 921-926.

Jimenez-Sanchez, A., Cybulska, P., Mager, K.L., Koplev, S., Cast, O., Couturier, D.L., Memon, D., Selenica, P., Nikolovski, I., Mazaheri, Y.*, et al.* (2020). Unraveling tumor-

immune heterogeneity in advanced ovarian cancer uncovers immunogenic effect of chemotherapy. Nat Genet *52*, 582-593.

Johnson, W.E., Li, C., and Rabinovic, A. (2007). Adjusting batch effects in microarray expression data using empirical Bayes methods. Biostatistics *8*, 118-127.

Karst, A.M., and Drapkin, R. (2012). Primary culture and immortalization of human fallopian tube secretory epithelial cells. Nat Protoc *7*, 1755-1764.

Karst, A.M., Levanon, K., and Drapkin, R. (2011). Modeling high-grade serous ovarian carcinogenesis from the fallopian tube. Proc Natl Acad Sci U S A *108*, 7547-7552.

Kok, Y.P., Guerrero Llobet, S., Schoonen, P.M., Everts, M., Bhattacharya, A., Fehrmann, R.S.N., van den Tempel, N., and van Vugt, M. (2020). Overexpression of Cyclin E1 or Cdc25A leads to replication stress, mitotic aberrancies, and increased sensitivity to replication checkpoint inhibitors. Oncogenesis *9*, 88.

Labidi-Galy, S.I., Papp, E., Hallberg, D., Niknafs, N., Adleff, V., Noe, M., Bhattacharya, R., Novak, M., Jones, S., Phallen, J.*, et al.* (2017). High grade serous ovarian carcinomas originate in the fallopian tube. Nat Commun *8*, 1093.

Lambrus, B.G., Daggubati, V., Uetake, Y., Scott, P.M., Clutario, K.M., Sluder, G., and Holland, A.J. (2016). A USP28-53BP1-p53-p21 signaling axis arrests growth after centrosome loss or prolonged mitosis. J Cell Biol *214*, 143-153.

Law, C.W., Chen, Y., Shi, W., and Smyth, G.K. (2014). voom: Precision weights unlock linear model analysis tools for RNA-seq read counts. Genome Biol *15*, R29.

Li, B., and Dewey, C.N. (2011). RSEM: accurate transcript quantification from RNA-Seq data with or without a reference genome. BMC Bioinformatics *12*, 323.

Liberzon, A., Subramanian, A., Pinchback, R., Thorvaldsdóttir, H., Tamayo, P., and Mesirov, J.P. (2011). Molecular signatures database (MSigDB) 3.0. Bioinformatics *27*, 1739-1740.

Lin, C.Y., Loven, J., Rahl, P.B., Paranal, R.M., Burge, C.B., Bradner, J.E., Lee, T.I., and Young, R.A. (2012). Transcriptional amplification in tumor cells with elevated c-Myc. Cell *151*, 56-67.

Littler, S., Sloss, O., Geary, B., Pierce, A., Whetton, A.D., and Taylor, S.S. (2019). Oncogenic MYC amplifies mitotic perturbations. Open Biol *9*, 190136.

Macintyre, G., Goranova, T.E., De Silva, D., Ennis, D., Piskorz, A.M., Eldridge, M., Sie, D., Lewsley, L.A., Hanif, A., Wilson, C.*, et al.* (2018). Copy number signatures and mutational processes in ovarian carcinoma. Nat Genet *50*, 1262-1270.

Martin, M. (2011). Cutadapt removes adapter sequences from high-throughput sequencing reads. 2011 *17*, 3.

McDermott, J.E., Arshad, O.A., Petyuk, V.A., Fu, Y., Gritsenko, M.A., Clauss, T.R., Moore, R.J., Schepmoes, A.A., Zhao, R., Monroe, M.E.*, et al.* (2020). Proteogenomic Characterization of Ovarian HGSC Implicates Mitotic Kinases, Replication Stress in Observed Chromosomal Instability. Cell Reports Medicine *1*.

Merritt, M.A., Bentink, S., Schwede, M., Iwanicki, M.P., Quackenbush, J., Woo, T., Agoston, E.S., Reinhardt, F., Crum, C.P., Berkowitz, R.S.*, et al.* (2013). Gene expression signature of normal cell-of-origin predicts ovarian tumor outcomes. PLoS One *8*, e80314.

Morrow, C.J., Tighe, A., Johnson, V.L., Scott, M.I., Ditchfield, C., and Taylor, S.S. (2005). Bub1 and aurora B cooperate to maintain BubR1-mediated inhibition of APC/CCdc20. J Cell Sci *118*, 3639-3652.

Nakamura, K., Nakayama, K., Ishikawa, N., Ishikawa, M., Sultana, R., Kiyono, T., and Kyo, S. (2018). Reconstitution of high-grade serous ovarian carcinoma from primary fallopian tube secretory epithelial cells. Oncotarget *9*, 12609-12619.

Nelson, L., Tighe, A., Golder, A., Littler, S., Bakker, B., Moralli, D., Murtuza Baker, S., Donaldson, I.J., Spierings, D.C.J., Wardenaar, R.*, et al.* (2020). A living biobank of ovarian cancer *ex vivo* models reveals profound mitotic heterogeneity. Nat Commun *11*, 822.

Nie, Z., Guo, C., Das, S.K., Chow, C.C., Batchelor, E., Simons, S.S.J., and Levens, D. (2020). Dissecting transcriptional amplification by MYC. Elife *9*.

Nie, Z., Hu, G., Wei, G., Cui, K., Yamane, A., Resch, W., Wang, R., Green, D.R., Tessarollo, L., Casellas, R.*, et al.* (2012). c-Myc is a universal amplifier of expressed genes in lymphocytes and embryonic stem cells. Cell *151*, 68-79.

Ogino, S., Gulley, M.L., den Dunnen, J.T., Wilson, R.B., Association for Molecular Patholpogy, T., and Education, C. (2007). Standard mutation nomenclature in molecular diagnostics: practical and educational challenges. J Mol Diagn *9*, 1-6.

Padilla-Nash, H.M., Barenboim-Stapleton, L., Difilippantonio, M.J., and Ried, T. (2006). Spectral karyotyping analysis of human and mouse chromosomes. Nat Protoc *1*, 3129-3142.

Robinson, J.T., Thorvaldsdottir, H., Winckler, W., Guttman, M., Lander, E.S., Getz, G., and Mesirov, J.P. (2011). Integrative genomics viewer. Nat Biotechnol *29*, 24-26.

Rutledge, S.D., Douglas, T.A., Nicholson, J.M., Vila-Casadesus, M., Kantzler, C.L., Wangsa, D., Barroso-Vilares, M., Kale, S.D., Logarinho, E., and Cimini, D. (2016). Selective advantage of trisomic human cells cultured in non-standard conditions. Sci Rep *6*, 22828.

Salehi, S., Kabeer, F., Ceglia, N., Andronescu, M., Williams, M., Campbell, K.R., Masud, T., Wang, B., Biele, J., Brimhall, J.*, et al.* (2020). Single cell fitness landscapes induced by genetic and pharmacologic perturbations in cancer. bioRxiv, 2020.2005.2008.081349.

Sanjana, N.E., Shalem, O., and Zhang, F. (2014). Improved vectors and genome-wide libraries for CRISPR screening. Nat Methods *11*, 783-784.

Santaguida, S., Richardson, A., Iyer, D.R., M'Saad, O., Zasadil, L., Knouse, K.A., Wong, Y.L., Rhind, N., Desai, A., and Amon, A. (2017). Chromosome Mis-segregation Generates Cell-Cycle-Arrested Cells with Complex Karyotypes that Are Eliminated by the Immune System. Dev Cell *41*, 638-651.e635.

Shukla, A., Nguyen, T.H.M., Moka, S.B., Ellis, J.J., Grady, J.P., Oey, H., Cristino, A.S., Khanna, K.K., Kroese, D.P., Krause, L.*, et al.* (2020). Chromosome arm aneuploidies shape tumour evolution and drug response. Nat Commun *11*, 449.

Simões-Sousa, S., Littler, S., Thompson, S.L., Minshall, P., Whalley, H., Bakker, B., Belkot, K., Moralli, D., Bronder, D., Tighe, A.*, et al.* (2018). The p38alpha Stress Kinase Suppresses Aneuploidy Tolerance by Inhibiting Hif-1alpha. Cell Rep *25*, 749-760 e746.

Smyth, G.K. (2004). Linear models and empirical bayes methods for assessing differential expression in microarray experiments. Stat Appl Genet Mol Biol *3*, Article3.

Soto, M., Raaijmakers, J.A., Bakker, B., Spierings, D.C.J., Lansdorp, P.M., Foijer, F., and Medema, R.H. (2017). p53 Prohibits Propagation of Chromosome Segregation Errors that Produce Structural Aneuploidies. Cell Rep *19*, 2423-2431.

Subramanian, A., Tamayo, P., Mootha, V.K., Mukherjee, S., Ebert, B.L., Gillette, M.A., Paulovich, A., Pomeroy, S.L., Golub, T.R., Lander, E.S.*, et al.* (2005). Gene set enrichment analysis: a knowledge-based approach for interpreting genome-wide expression profiles. Proc Natl Acad Sci U S A *102*, 15545-15550.

Sullivan, K.D., Galbraith, M.D., Andrysik, Z., and Espinosa, J.M. (2018). Mechanisms of transcriptional regulation by p53. Cell Death Differ *25*, 133-143.

Tamura, N., Shaikh, N., Muliaditan, D., Soliman, T.N., McGuinness, J.R., Maniati, E., Moralli, D., Durin, M.A., Green, C.M., Balkwill, F.R.*, et al.* (2020). Specific mechanisms of chromosomal instability indicate therapeutic sensitivities in high-grade serous ovarian carcinoma. Cancer Res.

Taylor, A.M., Shih, J., Ha, G., Gao, G.F., Zhang, X., Berger, A.C., Schumacher, S.E., Wang, C., Hu, H., Liu, J.*, et al.* (2018). Genomic and Functional Approaches to Understanding Cancer Aneuploidy. Cancer Cell *33*, 676-689.e673.

Thompson, S.L., and Compton, D.A. (2010). Proliferation of aneuploid human cells is limited by a p53-dependent mechanism. J Cell Biol *188*, 369-381.

Valente, L.J., Tarangelo, A., Li, A.M., Naciri, M., Raj, N., Boutelle, A.M., Li, Y., Mello, S.S., Bieging-Rolett, K., DeBerardinis, R.J.*, et al.* (2020). p53 deficiency triggers dysregulation of diverse cellular processes in physiological oxygen. J Cell Biol *219*.

van den Bos, H., Spierings, D.C., Taudt, A.S., Bakker, B., Porubsky, D., Falconer, E., Novoa, C., Halsema, N., Kazemier, H.G., Hoekstra-Wakker, K.*, et al.* (2016). Single-cell whole genome sequencing reveals no evidence for common aneuploidy in normal and Alzheimer's disease neurons. Genome Biol *17*, 116.

Vang, R., Levine, D.A., Soslow, R.A., Zaloudek, C., Shih Ie, M., and Kurman, R.J. (2016). Molecular Alterations of TP53 are a Defining Feature of Ovarian High-Grade Serous Carcinoma: A Rereview of Cases Lacking TP53 Mutations in The Cancer Genome Atlas Ovarian Study. Int J Gynecol Pathol *35*, 48-55.

Vassilev, L.T., Vu, B.T., Graves, B., Carvajal, D., Podlaski, F., Filipovic, Z., Kong, N., Kammlott, U., Lukacs, C., Klein, C.*, et al.* (2004). In vivo activation of the p53 pathway by small-molecule antagonists of MDM2. Science *303*, 844-848.

Wang, Y., Bernhardy, A.J., Cruz, C., Krais, J.J., Nacson, J., Nicolas, E., Peri, S., van der Gulden, H., van der Heijden, I., O'Brien, S.W.*, et al.* (2016). The BRCA1-Delta11q Alternative Splice Isoform Bypasses Germline Mutations and Promotes Therapeutic Resistance to PARP Inhibition and Cisplatin. Cancer Res *76*, 2778-2790.

Wang, Y.K., Bashashati, A., Anglesio, M.S., Cochrane, D.R., Grewal, D.S., Ha, G., McPherson, A., Horlings, H.M., Senz, J., Prentice, L.M.*, et al.* (2017). Genomic consequences of aberrant DNA repair mechanisms stratify ovarian cancer histotypes. Nat Genet *49*, 856-865.

Wangsa, D., Braun, R., Schiefer, M., Gertz, E.M., Bronder, D., Quintanilla, I., Padilla-Nash, H.M., Torres, I., Hunn, C., Warner, L.*, et al.* (2018). The evolution of single cell-derived colorectal cancer cell lines is dominated by the continued selection of tumor-specific genomic imbalances, despite random chromosomal instability. Carcinogenesis *39*, 993-1005.

Weaver, Z., Montagna, C., Xu, X., Howard, T., Gadina, M., Brodie, S.G., Deng, C.X., and Ried, T. (2002). Mammary tumors in mice conditionally mutant for Brca1 exhibit gross genomic instability and centrosome amplification yet display a recurring distribution of genomic imbalances that is similar to human breast cancer. Oncogene *21*, 5097-5107.

Wood, K.W., Lad, L., Luo, L., Qian, X., Knight, S.D., Nevins, N., Brejc, K., Sutton, D., Gilmartin, A.G., Chua, P.R.*, et al.* (2010). Antitumor activity of an allosteric inhibitor of centromere-associated protein-E. Proc Natl Acad Sci U S A *107*, 5839-5844.

Xu, X., Weaver, Z., Linke, S.P., Li, C., Gotay, J., Wang, X.W., Harris, C.C., Ried, T., and Deng, C.X. (1999). Centrosome amplification and a defective G2-M cell cycle checkpoint induce genetic instability in BRCA1 exon 11 isoform-deficient cells. Mol Cell *3*, 389-395.

Zack, T.I., Schumacher, S.E., Carter, S.L., Cherniack, A.D., Saksena, G., Tabak, B., Lawrence, M.S., Zhsng, C.Z., Wala, J., Mermel, C.H.*, et al.* (2013). Pan-cancer patterns of somatic copy number alteration. Nat Genet *45*, 1134-1140.

Zeng, M., Kwiatkowski, N.P., Zhang, T., Nabet, B., Xu, M., Liang, Y., Quan, C., Wang, J., Hao, M., Palakurthi, S.*, et al.* (2018). Targeting MYC dependency in ovarian cancer through inhibition of CDK7 and CDK12/13. Elife *7*.

Zhang, S., Dolgalev, I., Zhang, T., Ran, H., Levine, D.A., and Neel, B.G. (2019). Both fallopian tube and ovarian surface epithelium are cells-of-origin for high-grade serous ovarian carcinoma. Nat Commun *10*, 5367.

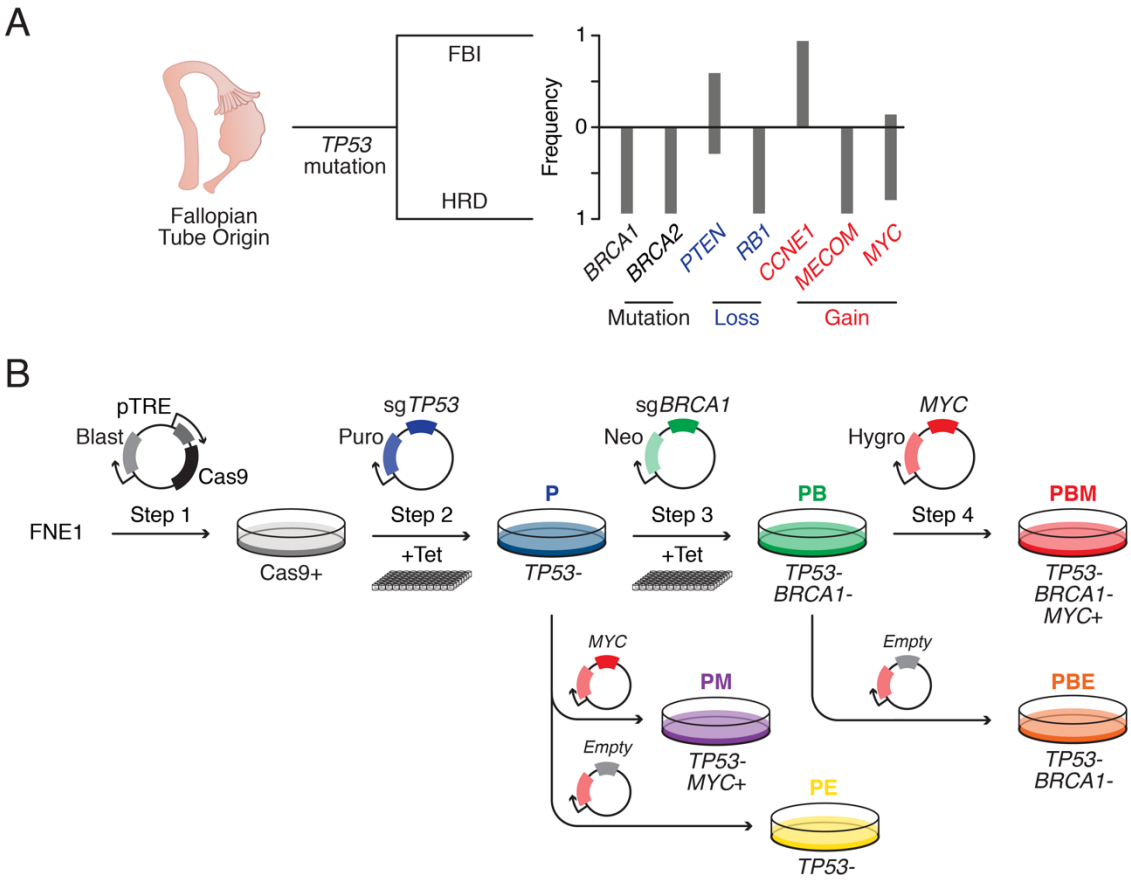

Figure 1

1256

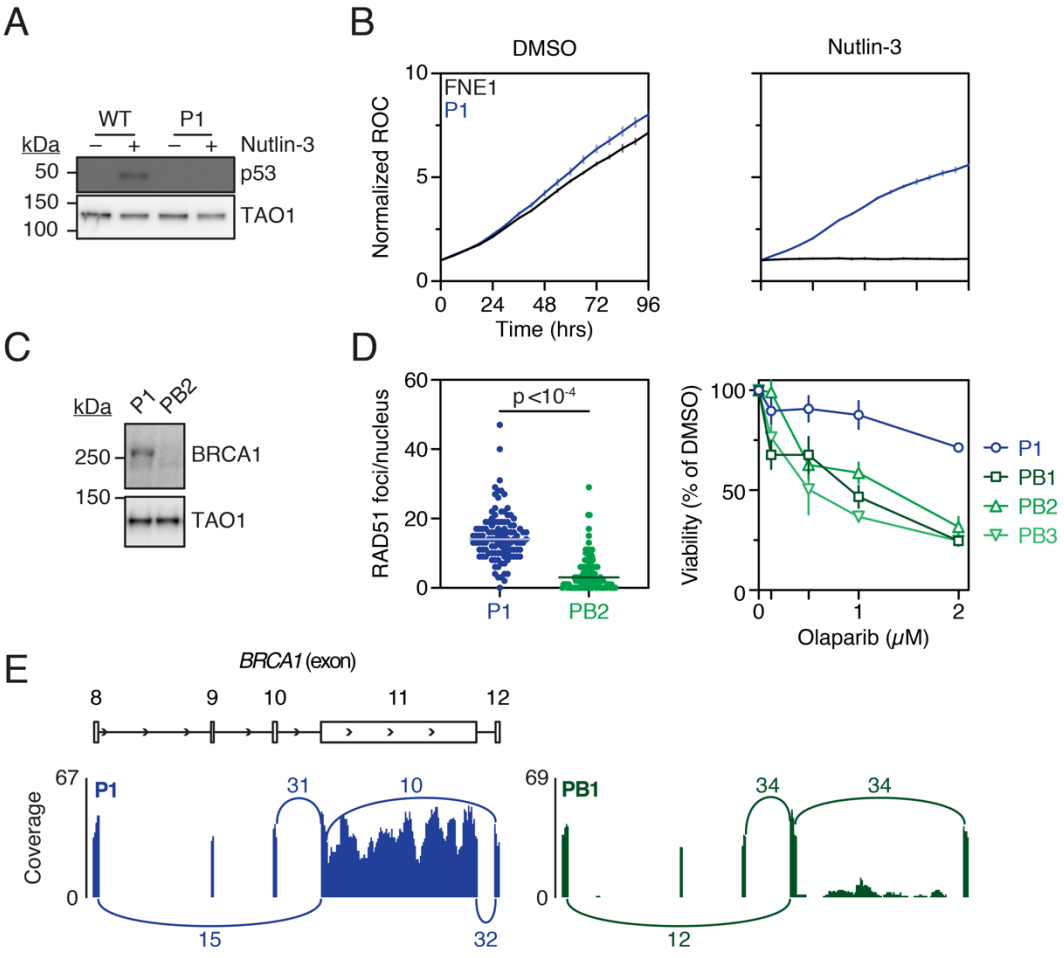

Figure 2

1257

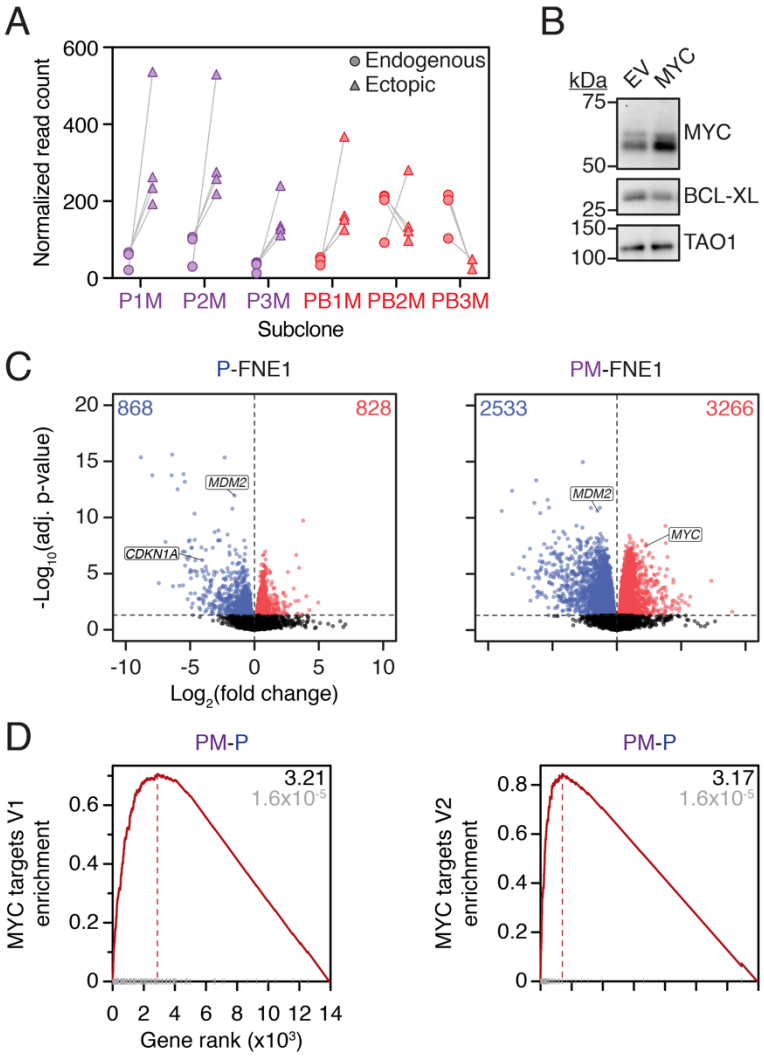

Figure 3

1258

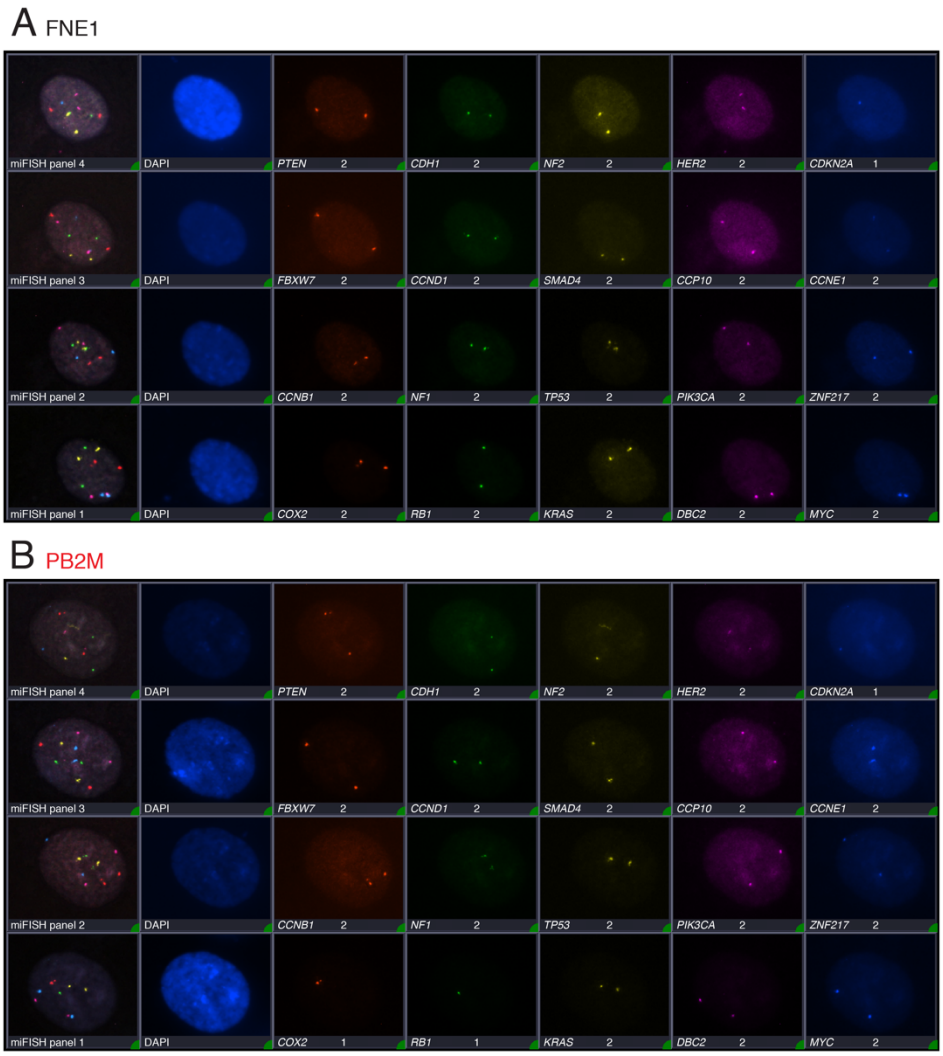
A FNE1
miFISH panel 4
DAPI
PTEN 2
CDH1 2
NF2 2
HER2 2
CDKN2A 1
miFISH panel 3
DAPI
FBXW7 2
CCND1 2
SMAD4 2
CCP10 2
CCNE1 2
miFISH panel 2
DAPI
CCNB1 2
NF1 2
TP53 2
PIK3CA 2
ZNF217 2
miFISH panel 1
DAPI
COX2 2
RB1 2
KRAS 2
DBC2 2
MYC 2
B PB2M
miFISH panel 4
DAPI
PTEN 2
CDH1 2
NF2 2
HER2 2
CDKN2A 1
miFISH panel 3
DAPI
FBXW7 2
CCND1 2
SMAD4 2
CCP10 2
CCNE1 2
miFISH panel 2
DAPI
CCNB1 2
NF1 2
TP53 2
PIK3CA 2
ZNF217 2
miFISH panel 1
DAPI
COX2 1
RB1 1
KRAS 2
DBC2 2
MYC 2
C
FNE1
PB2M
PB3M
Signal count
10
8
6
4
2
0
CCP10
COX2
PIK3CA
FBXW7
CCNB1
DBC2
MYC
CDKN2A
PTEN
CCND1
KRAS
RB1
CDH1
TP53
NF1
HER2
SMAD4
CCNE1
ZNF217
NF2

Figure 4

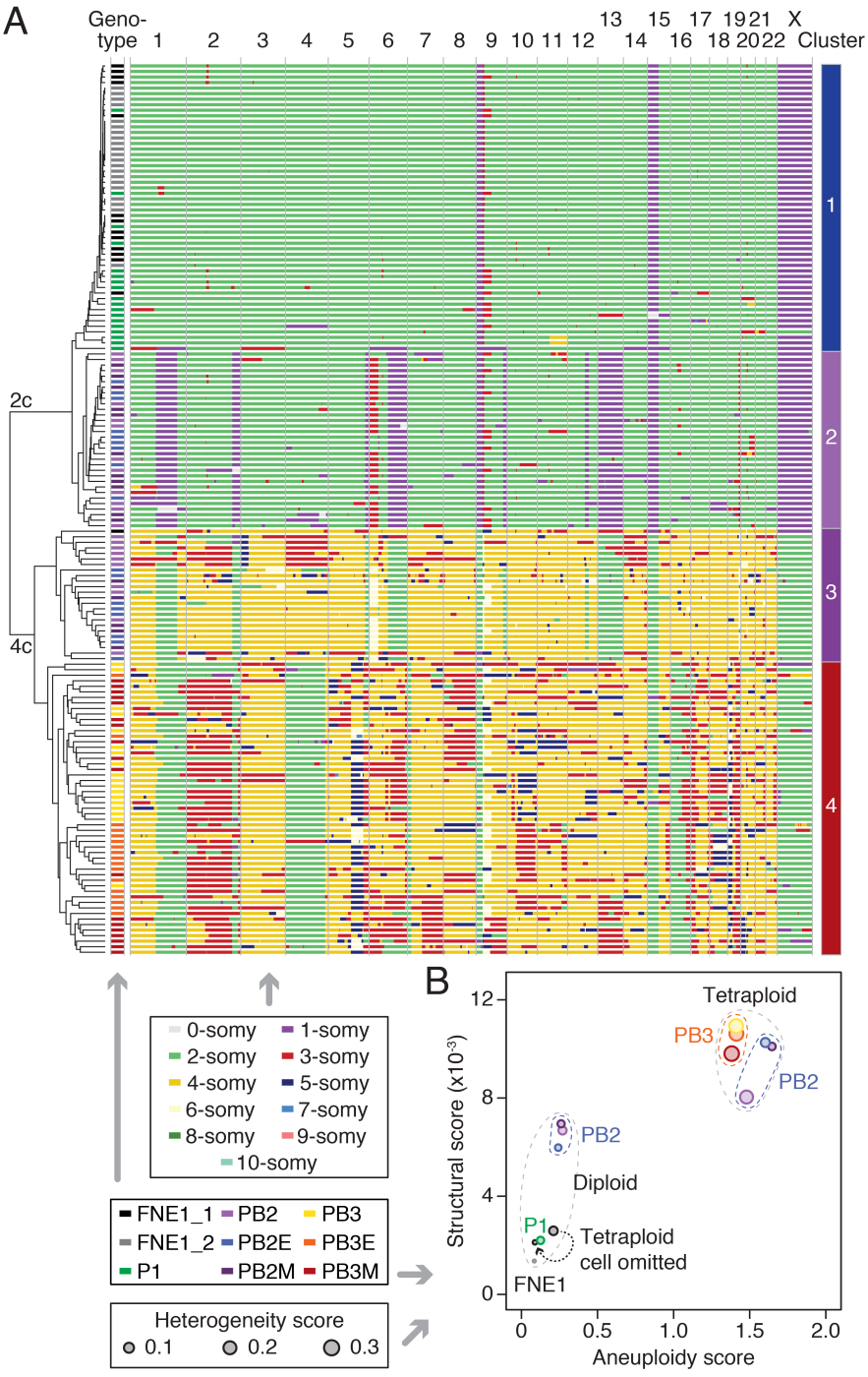

Figure 5

1260

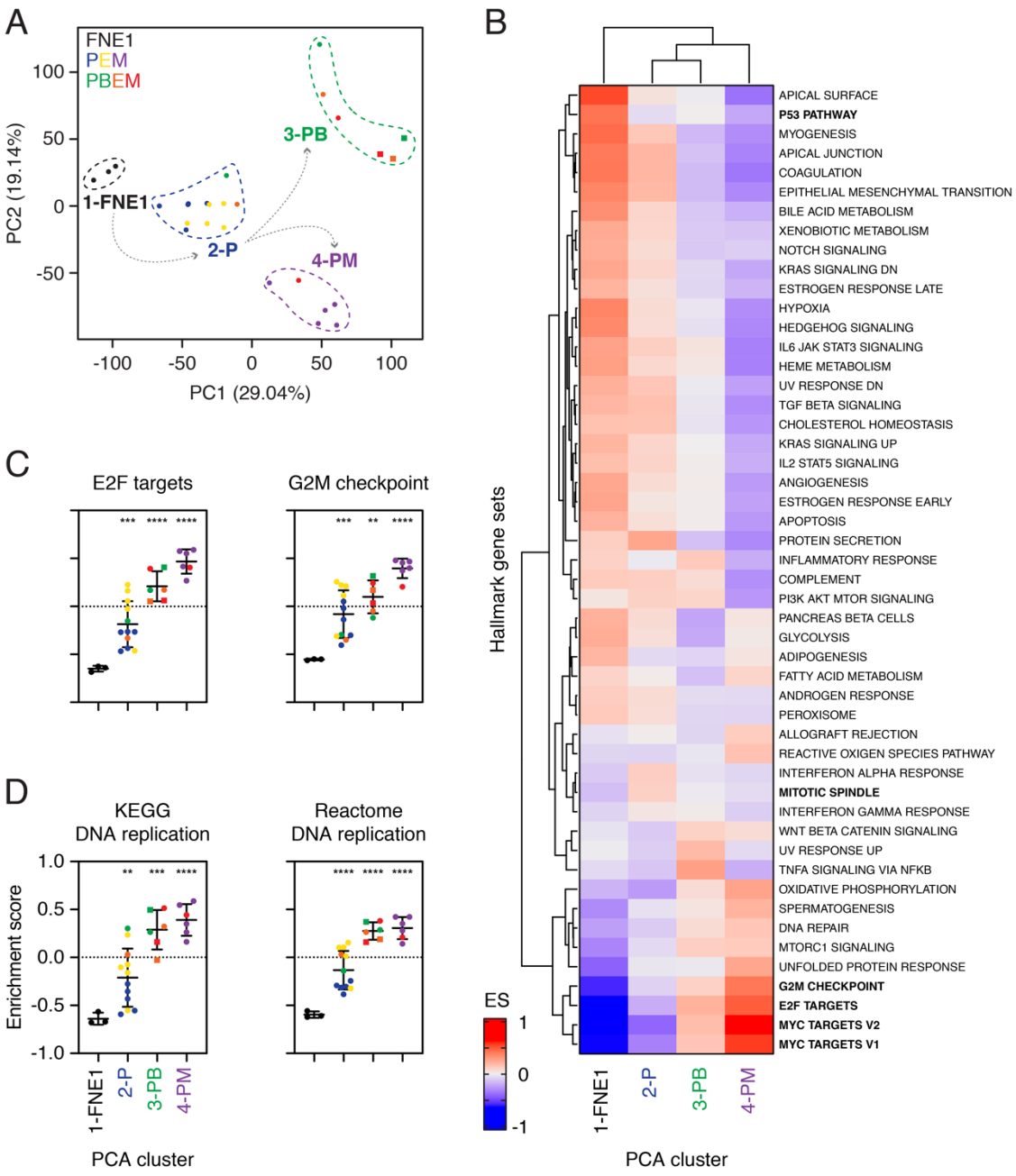
A
FNE1
PEM
PBEM
1-FNE1
2-P
3-PB
4-PM
PC2 (19.14%)
PC1 (29.04%)
B
Hallmark gene sets
APICAL SURFACE
P53 PATHWAY
MYOGENESIS
APICAL JUNCTION
COAGULATION
EPITHELIAL MESENCHYMAL TRANSITION
BILE ACID METABOLISM
XENOBIOTIC METABOLISM
NOTCH SIGNALING
KRAS SIGNALING DN
ESTROGEN RESPONSE LATE
HYPOXIA
HEDGEHOG SIGNALING
IL6 JAK STAT3 SIGNALING
HEME METABOLISM
UV RESPONSE DN
TGF BETA SIGNALING
CHOLESTEROL HOMEOSTASIS
KRAS SIGNALING UP
IL2 STAT5 SIGNALING
ANGIOGENESIS
ESTROGEN RESPONSE EARLY
APOPTOSIS
PROTEIN SECRETION
INFLAMMATORY RESPONSE
COMPLEMENT
PI3K AKT MTOR SIGNALING
PANCREAS BETA CELLS
GLYCOLYSIS
ADIPOGENESIS
FATTY ACID METABOLISM
ANDROGEN RESPONSE
PEROXISOME
ALLOGRAFT REJECTION
REACTIVE OXIGEN SPECIES PATHWAY
INTERFERON ALPHA RESPONSE
MITOTIC SPINDLE
INTERFERON GAMMA RESPONSE
WNT BETA CATENIN SIGNALING
UV RESPONSE UP
TNFA SIGNALING VIA NFKB
OXIDATIVE PHOSPHORYLATION
SPERMATOGENESIS
DNA REPAIR
MTORC1 SIGNALING
UNFOLDED PROTEIN RESPONSE
G2M CHECKPOINT
E2F TARGETS
MYC TARGETS V2
MYC TARGETS V1
ES
PCA cluster
C
E2F targets
G2M checkpoint
D
KEGG
DNA replication
Reactome
DNA replication
Enrichment score
PCA cluster

Figure 6

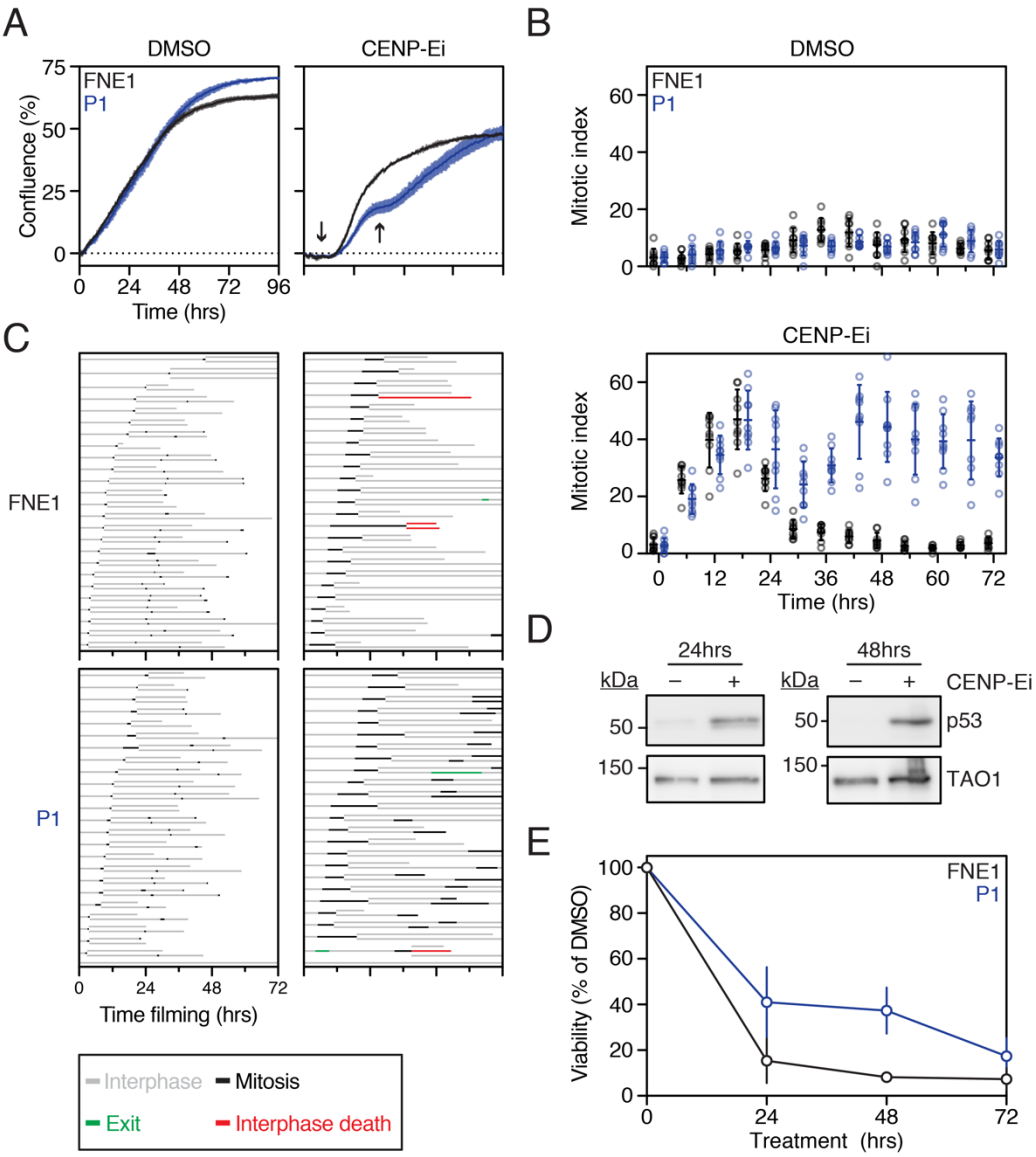

Figure 7

1262

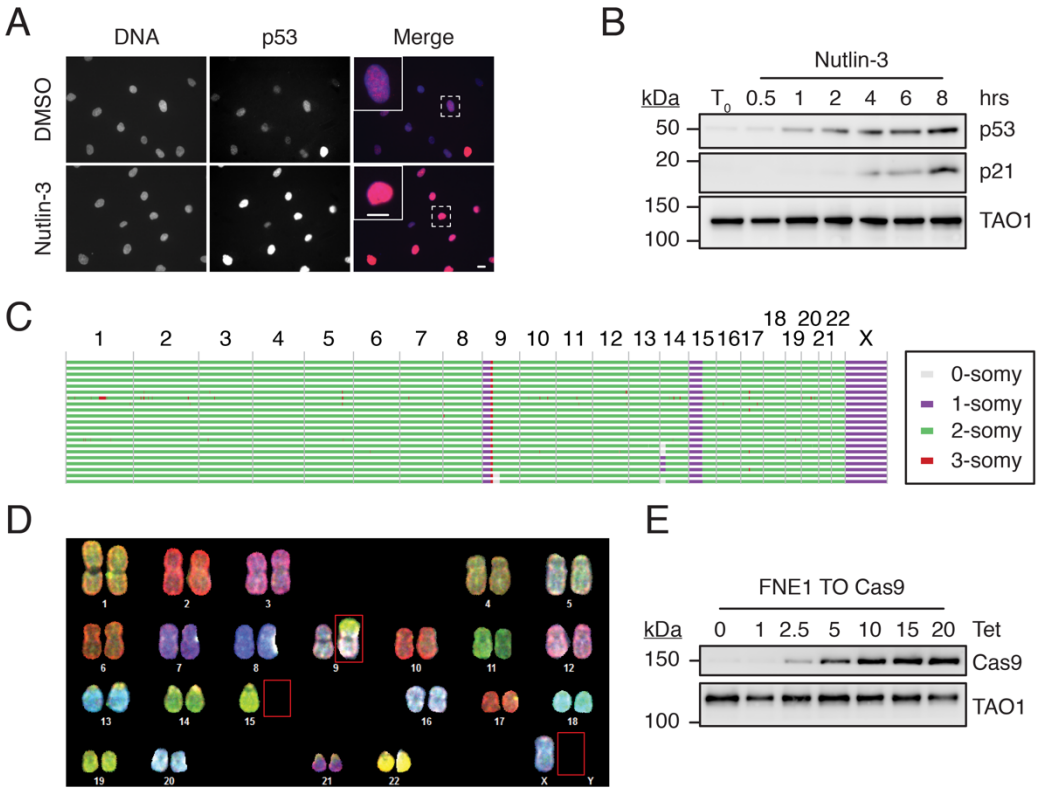

Figure S1

1263

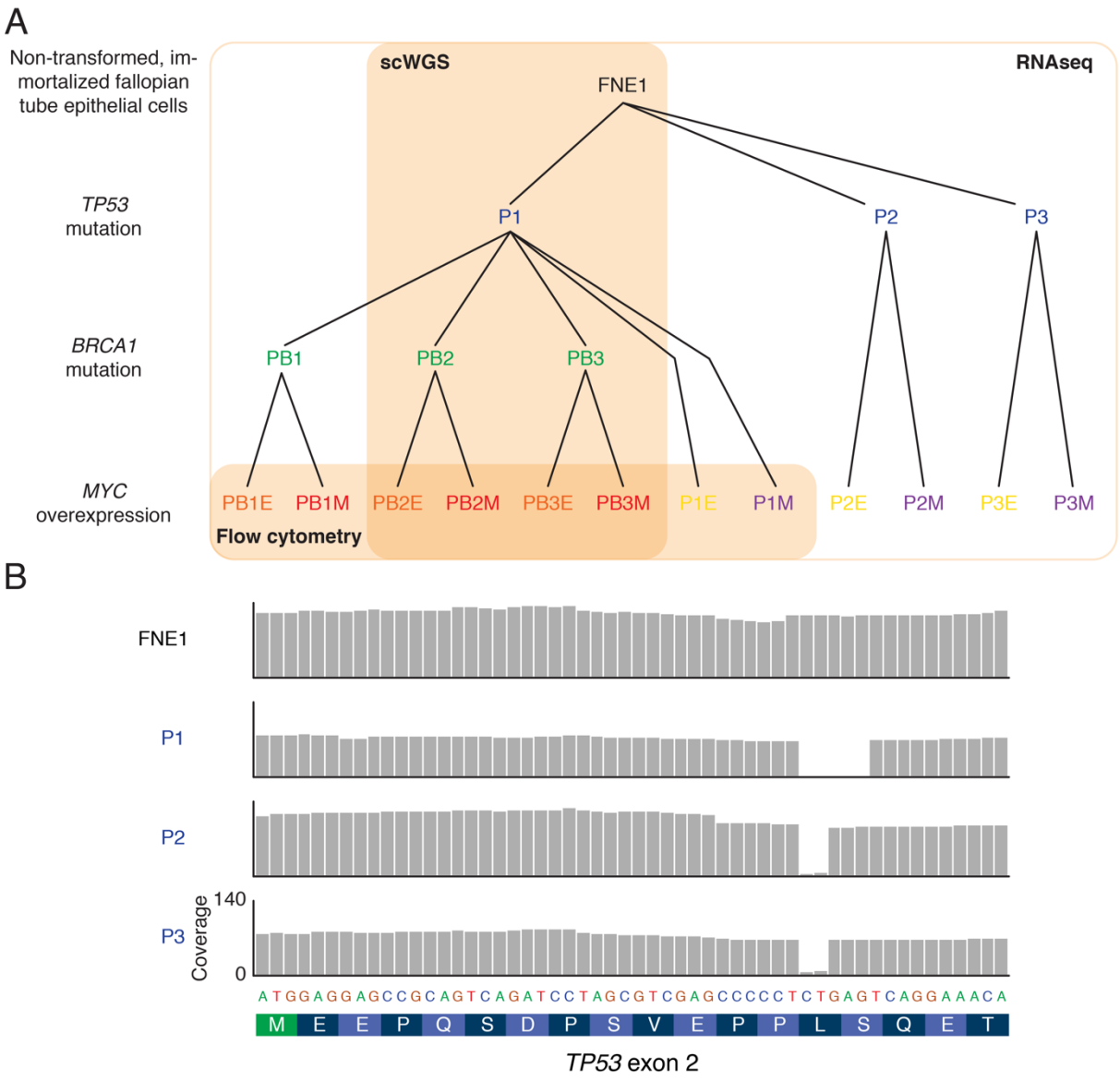
A
Non-transformed, immortalized fallopian tube epithelial cells
TP53 mutation
BRCA1 mutation
MYC overexpression
scWGS
RNAseq
FNE1
P1
P2
P3
PB1
PB2
PB3
PB1E
PB1M
PB2E
PB2M
PB3E
PB3M
P1E
P1M
P2E
P2M
P3E
P3M
Flow cytometry
B
FNE1
P1
P2
P3
Coverage
140
0
ATGGAGGAGCCGCAGTCAGATCCTAGCGTCGAGCCCCCTCTGAGTCAGGAAACA
M E E P Q S D P S V E P P L S Q E T
TP53 exon 2

Figure S2

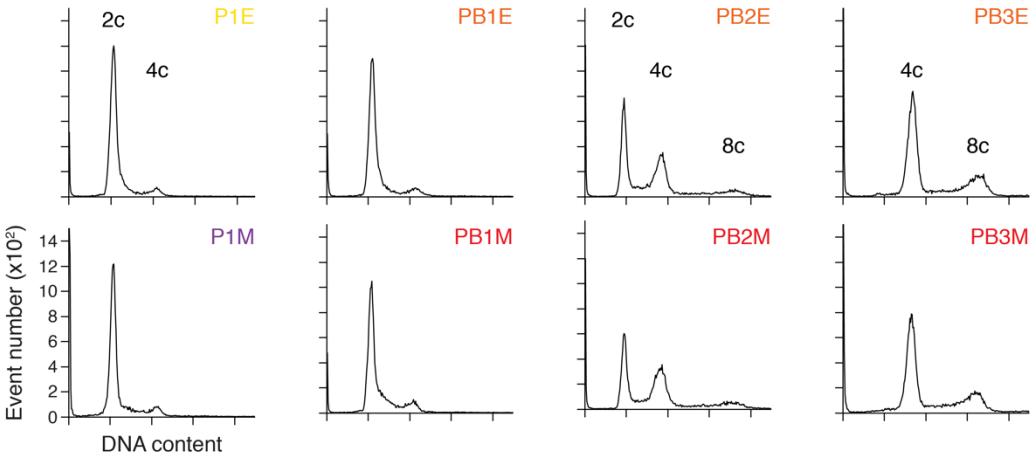

Figure S3

1265

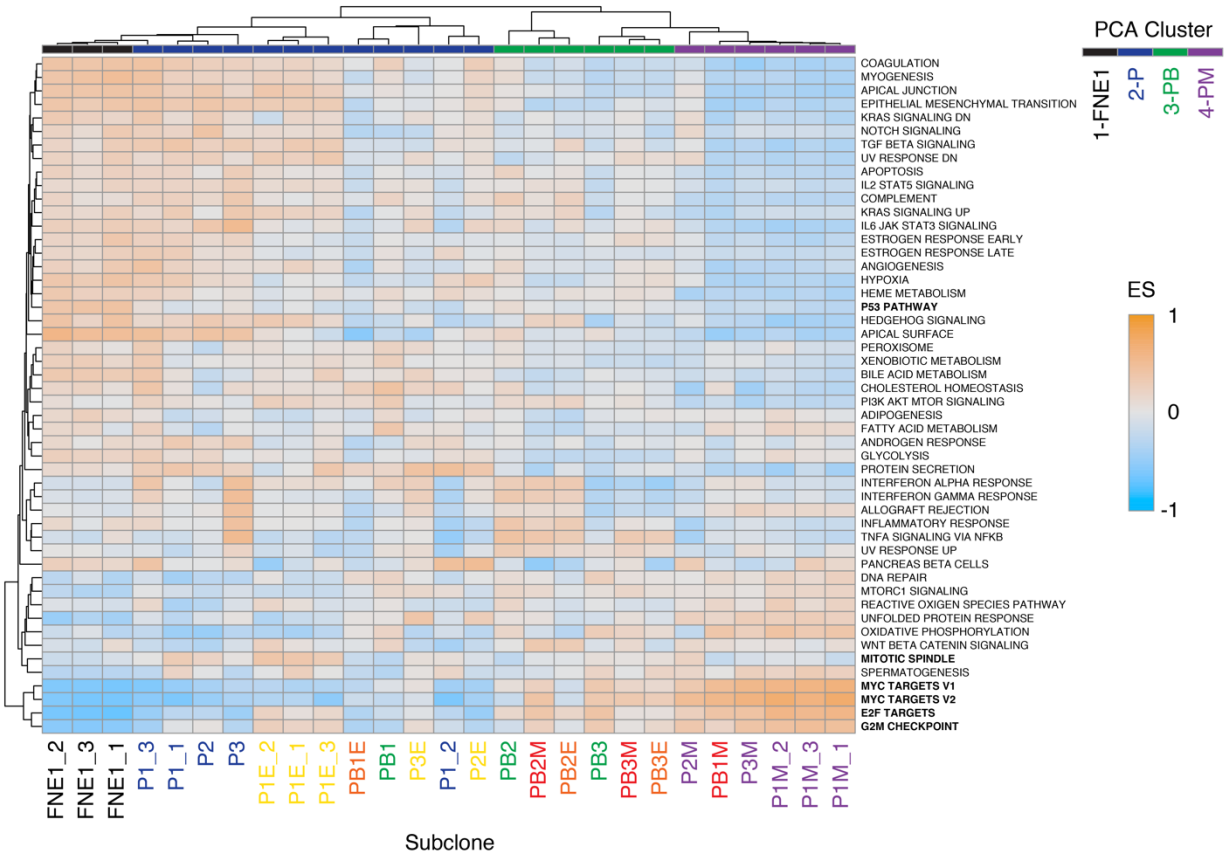

Figure S4

1266

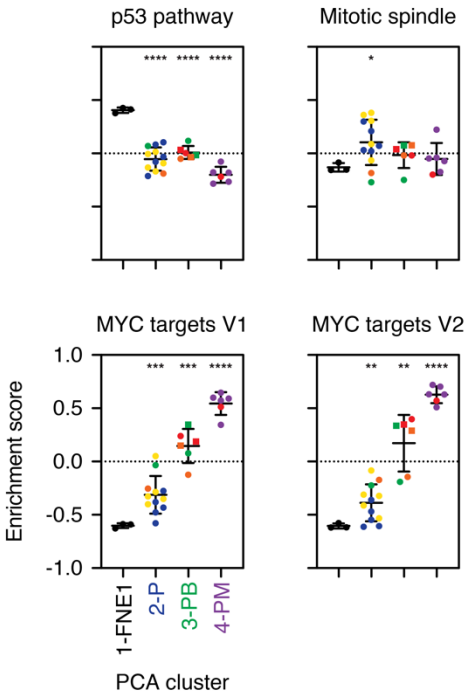
p53 pathway
Mitotic spindle
MYC targets V1
MYC targets V2
Enrichment score
1.0
0.5
0.0
-0.5
-1.0
1-FNE1
2-P
3-PB
4-PM
PCA cluster

Figure S5

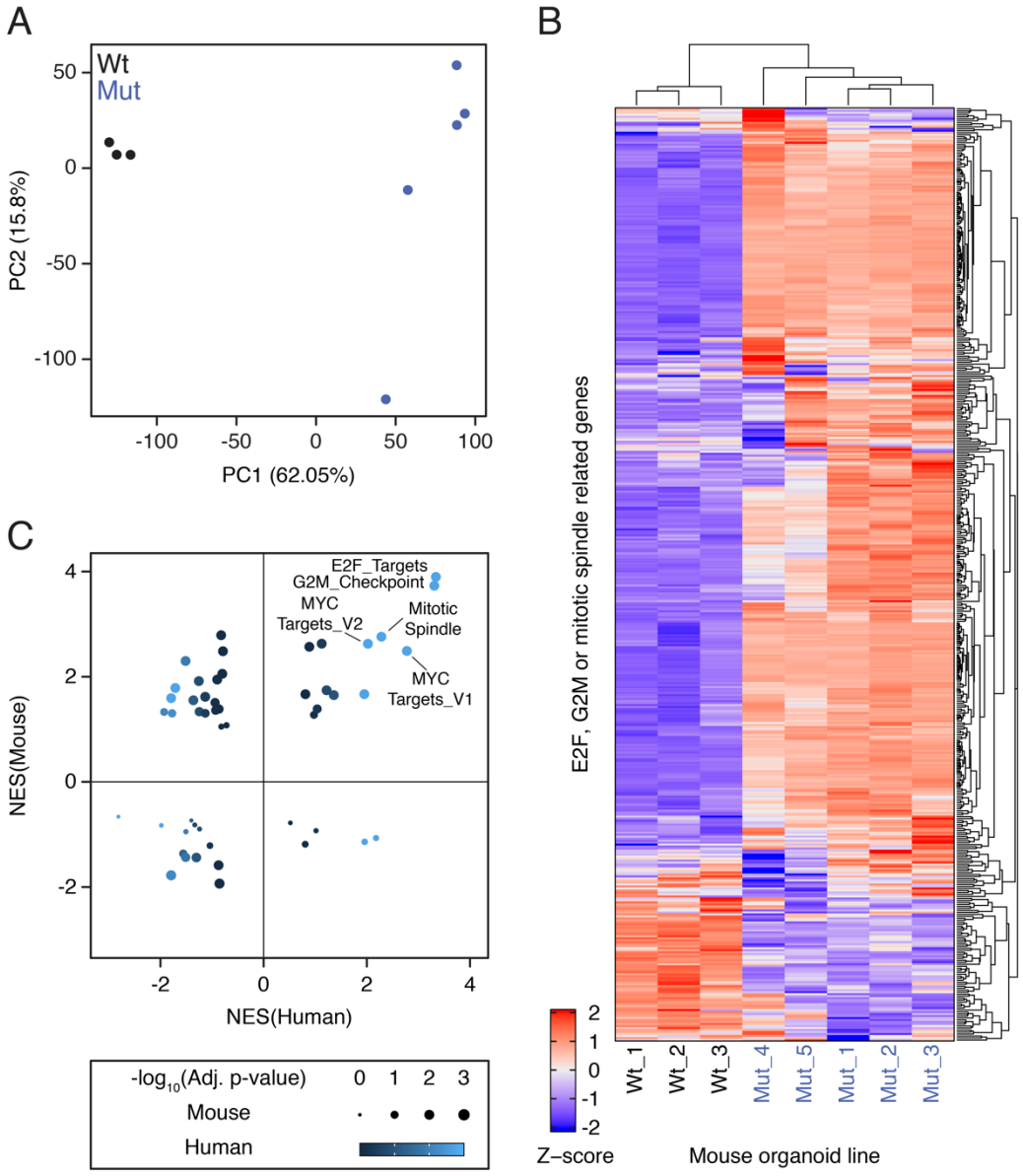
A
Wt
Mut
PC2 (15.8%)
PC1 (62.05%)
B
E2F, G2M or mitotic spindle related genes
Wt_1
Wt_2
Wt_3
Mut_4
Mut_5
Mut_1
Mut_2
Mut_3
Z−score
Mouse organoid line
C
E2F_Targets
G2M_Checkpoint
MYC
Targets_V2
Mitotic
Spindle
MYC
Targets_V1
NES(Mouse)
NES(Human)
-log10(Adj. p-value)
Mouse
Human

Figure S6